Surfactant-Free Synthesis of Metal Chalcogenides and their Role as Catalyst for Environmental Remediation and Electrochemical Oxygen Evolution reaction (OER)

A thesis submitted for the degree of

DOCTOR OF PHILOSOPHY

In

CHEMISTRY

By

Manzoor Ahmad Pandit

Reg. No. 15CHPH03

School of Chemistry

University of Hyderabad

Hyderabad - 500046

India

September 2020

Surfactant-Free Synthesis of Metal Chalcogenides and their Role as Catalyst for Environmental Remediation and Electrochemical Oxygen Evolution reaction (OER)

A thesis submitted for the degree of

DOCTOR OF PHILOSOPHY

In

CHEMISTRY

By

Manzoor Ahmad Pandit

Reg. No. 15CHPH03

School of Chemistry

University of Hyderabad

Hyderabad - 500046

India

September 2020

Dedicated

to

My Parents

प्रतिष्ठित संस्थान
INSTITUTION OF EMINENCE

DECLARATION

I hereby declare that the matter embodied in the thesis entitled "**Surfactant-Free Synthesis of Metal Chalcogenides and their Role as Catalyst for Environmental Remediation and Electrochemical Oxygen Evolution Reaction (OER)"** is the result of investigations carried out by me in the School of Chemistry, University of Hyderabad, India, under the supervision of Prof. K. Muralidharan.

In keeping with the general practice of reporting scientific investigations, due acknowledgements have been made wherever the work described is based on the findings of other investigators. Any omission, which might have occurred by oversight or error, is regretted.

K. MU 16/9/2020

Signature of Supervisor

.K. MURALIDHARAN
Professor
School of Chemistry
University of Hyderabad
Hyderabad - 500 046.

Manzoor

Manzoor Ahmad Pandit

Reg. No.: 15CHPH03

प्रतिष्ठित संस्थान
INSTITUTION OF EMINENCE

CERTIFICATE

This is to certify that the thesis entitled **"Surfactant-Free Synthesis of Metal Chalcogenides and their Role as Catalyst for Environmental Remediation and Electrochemical Oxygen Evolution Reaction (OER)"** submitted by **Manzoor Ahmad Pandit** with registration number **15CHPH03** in partial fulfillment of the requirements for the award of Doctor of Philosophy (Ph.D.) in the School of Chemistry is a bonafide work carried out by him under my supervision and guidance. This thesis is free from plagiarism and has not been submitted previously in part or full to this or any other University/Institution for any degree or diploma. Further the student has three publications before submission of the thesis for adjudication and has produced evidences for the same in the form of reprints.

Further Part of this thesis has been:

A. Published as the following article:

1. Billakanti Srinivas, **Manzoor Ahmad Pandit**, and Krishnamurthi Muralidharan, Importance of Clean Surfaces on the Catalyst: SnS_2 Nanorings for Environmental Remediation. *ACS Omega* **2019**, *4*, 14970−14980. **(Chapter 2)**
2. **Manzoor Ahmad Pandit**, Srinivas Billakanti, and Krishnamurthi Muralidharan, A simplistic approach for the synthesis of CuS-CdS heterostructure: A novel photocatalyst for oxidative dye degradation. *J. Environ. Chem. Eng.* **2020**, *8*, 103542. **(Chapter 3)**
3. **Manzoor Ahmad Pandit**, Dasari Sai Hemanth Kumar, Srinivas Billakanti, Manigandan Ramadoss, and Krishnamurthi Muralidharan, Chalcopyrite with Magnetic and Dielectric Properties: An Introductory Catalyst for 4-Nitrophenol Reduction. *J. Phys. Chem. C* **2020**, *124*, 33, 18010−18019. **(Chapter 4)**

B. Presented in the following conferences:

1. **Poster** in International Conference on Materials Science and Technology **(ICMST), 2019**, held at VSSC ISRO, Trivandrum Kerala, from 10-13 October, 2018.
2. **Oral talk**, "A simplistic approach for the synthesis of CuS-CdS heterostructure: A novel photocatalyst for oxidative dye degradation" in **Chem Fest-2019**, held at School of Chemistry, University of Hyderabad, from 22-23 February, 2019.

Further, the student has passed the following courses towards the fulfillment of coursework requirement for Ph.D.:

S.No.	Course Code	Title	Credits	Pass/Fail
1.	CY-801	Research Proposal	3	Pass
2.	CY-805	Instrumental Methods-A	3	Pass
3.	CY-806	Instrumental Methods-B	3	Pass
4.	CY-504	Chemistry of Materials	3	Pass

K. Mu 9/9/2020

Prof. K. Muralidharan
(Thesis Supervisor)

K. MURALIDHARAN
Professor
School of Chemistry
University of Hyderabad
Hyderabad - 500 046.

Dean
School of Chemistry

Dean
SCHOOL OF CHEMISTRY
University of Hyderabad
Hyderabad-500 046

CONTENTS

CHAPTER – 2

Importance of Clean Surfaces on the Catalyst: SnS_2 Nanorings for Environmental Remediation

CHAPTER – 5

Boosting the Bifunctional Catalytic Role of Cobalt Iron Chalcogenide- $Co_{0.8}Fe_{0.2}L_2$ (L = S and Se) as an Electrochemical OER Performer and a Photocatalyst for Cr(VI) Reduction

CHAPTER – 6

Summary and Conclusions

ACKNOWLEDGMENT

All praises to the Almighty Allah who has bestowed me health and wisdom, which enabled me to complete this study successfully.

In pursuing this study, I owe intellectual as well as personal debts to several people; it would have been impossible to complete this work without their invaluable support and guidance. First and foremost, I would like to express my deepest gratitude to my Supervisor **Prof. K. Muralidharan**, for his advice, patience, encouragement and invaluable guidance throughout the course. His guidance was the beacon light for my research and writing of this thesis. I could not have imagined better supervisor and mentor for my Ph.D. than him. I owe my personal gratitude to my supervisor for giving me time and space to work under his supervision; it was great life experience to owe his thoughts and mentorship. Thank you so much sir.

I would like to thank and owe my personal appreciation to my doctoral committee members **Prof. Samar Kumar Das** and **Prof. Viswanathan Baskar** for their constant support, inspiration and ideas throughout my research career. Besides this I pay my honor to present and former Deans of School of Chemistry for their valor and support on various occasions. I am highly thankful to all the faculty members of the school for their timely support and as a source of inspiration and motivation towards carrying my research to new and achievable heights and acting as a torch bearer for students with the aim for pursuing research in their carrier. My acknowledgement would seem to be incomplete if I wouldn't mention and thank non-teaching and technical staff especially Dr. Muvva Durga Prasad (specially known as DP anna), Sunil anna, S. Thurabuddin, Durgesh Singh, Pankaj, B. Anandam, Asia Pervaz and Jyoti. I sincerely thank to UGC-BSR for fellowship. I thank and acknowledge University Grants Commission, New Delhi, India (through the UPE and CAS programs) and the Department of Science and Technology, New Delhi, India (through the PURSE and FIST programs) for financial and infrastructure support.

I feel utmost pride in acknowledging the love and support of my parents (**Abdul Salam Pandit** and **Haleema Akhter**), without their affections and constant support I was supposed to be nothing. I thank them for always showering me with their prayers which had made me capable to stand against all the challenges that I have faced in my life. Thank you Dad and Mom for your unconditional love. The love and consistent support of not only my parents but also my siblings give me courage on each step of my life. I ought to subject my sincere feelings to my family members **Tanveer Pandit**, **Ashaq Pandit**, **Tariq Pandit**, **Naseer Pandit**, **Shaheena Akhter**, **Mehmooda Salam** and to my brother in-law **Nazir Ahmad Naik**. I would like to thank my family for an inherent debt in the form of emotional, moral and intellectual support that continue to inspire me attain my dreams. Their unconditional love and faith in my stature always boosted me towards the excellence. The unconditional love of bacha party including **Tehseen**, **Sidra**, **Irtiza, Zohra**, **Sadia**, **Fatima**, **Aariz** and the newly made entry by **Shahveer** whom I miss during this tenure of five years will not exclude from this special part of my life. I also thank to **Shakeela**, **Mymoona** and **Shaista** for their wishes and prayers.

I extend my special thanks to my dear fellows here at HCU and at other places (**Nayeem Pandit** and **Ashiq Pandit** from Jamia Millia Islamia) for their immense support and guidance from academic to personal sphere. I will be always indebted to you people. My special appreciation goes to **Miss Kiran Zahra** for her valuable support through the hard times of my program and for being there always as an inspiration and source of motivation.

My deep gratitude goes to my friends especially **Dr. Aaqib**, **Dr. Ishfaq**, **Dr Javaid**, **Dr. Showkat**, **Dr Junaid**, **Dr. Junaid Sofi**, **Mr. Ishfaq** and **Mr. Irfan** for their encouraging and guiding attitude. My profound regards and gratitude goes to my Kashmiri fraternity of HCU from various departments including Dr. Sajad, Dr. Tawfeeq, Dr. yaseen, Dr. Bilal, Dr. Jamsheed, Dr. Ishfaq, Dr. Layeek, Dr. Owais, Dr. Sarwar, Mr. Owais Sopori, Mr. Sareer, Mr. Rafiq, Mr. Saleem and Mr. Gulzar Madni for their support and cooperation throughout the programme.

I would like to pay pay special thanks to my seniors and lab members especially **Dr. Srinivas Billakanti**, Dr. Sanyasi Naidu, **Dr. Manigandan Ramadoss**, Dr. Hanumanth

Rao, Dr. Ramu Guda, Venky Velpuri, Anjana K. O, Anju Joseph, **Hemanth Kumar**, Ramakrishna and Prachuritha for their support, valuable discussion and encouragement. I am also thankful to my batchmates who joined with me in the school of chemistry 2015 for Ph. D for their timely support and encouragement, especially my special thanks to **Senthil Nathan**. I owe my sincere thanks to **Dr. Dhanasekar** who always made himself available to put his valuable efforts for helping me whenever I felt. I also feel positive in thanking to my juniors who showed their love, respect and affection towards me during this tenure.

Finally I express my sincere regards to all my friends and well-wishers for their moral support, motivation and encouragement.

Manzoor

List of Schemes

List of Figures

List of Tables

List of Acronyms

NPs	Nanoparticles
NMS	Nanomaterials
OER	Oxygen evolution reaction
Rh B	Rhodamine B
MB	Methylene blue
MO	Methyl orange
NP	Nitrophenol
AP	Aminophenol
PANI	Polyaniline
PEDOT	Poly(3,4-ethylenedioxythiophene)
POPD	Poly(O-Phenylenediamine)
PMMA	Polymethylmethaacrylate
RGO	Reduced graphene oxide
PEG	Polyethyleneglycol
DNA	Deoxyribonucleic acid
RNA	Ribonucleic acid
CNT	Carbon nanotubes
C_3N_4	Carbonnitride
CTAB	Cetyl trimethyl ammonium bromide
QDs	Quantum Dots
TMC	Transition metal chalcogenide
CVD	Chemical vapor deposition
PACVD	Plasma-assisted chemical vapor deposition

LCVD	Laser chemical vapor deposition
LIBs	Lithium ion batteries
HMDS	Hexamethyldisilazane
MNP	Magnetic nanoparticles
HER	Hydrogen evolution reaction
OER	Oxygen evolution reaction
PXRD	Powder X-ray diffraction
AFM	Atomic force microscopy
SEM	Scanning electron microscopy
FESEM	Field emission scanning electron microscopy
EDS	Energy dispersive spectroscopy
TEM	Transmission electron microscopy
HRTEM	High resolution transmission electron microscopy
SAED	Selected Area electron diffraction
XPS	X-ray photoelectron spectroscopy
FT-IR	Fourier transform infra-red spectroscopy
JCPDS	Joint committee on powder diffraction standards
UV-vis	Ultraviolet visible spectroscopy
DSSS	Dye sensitized solar cell

SYNOPSIS

The thesis entitled "**Surfactant-Free Synthesis of Metal Chalcogenides and their Role as Catalyst for Environmental Remediation and Electrochemical Oxygen Evolution Reaction (OER)**" comprises of five chapters

Chapter 1: Introduction

The introduction chapter is a combination of a literature survey for nanomaterials comprising the definition of nanomaterials, classification, modes of synthesis, and applications. Various methods used for the synthesis of nanomaterials and their merits and demerits are discussed. Other than the reported methods used for the synthesis of nonomaterials, the method developed in our lab, pronounced as hexamethyldisilazane (HMDS) assisted method, has been discussed, and its advantages are compared to other reported methods. Besides these, their different properties, including catalytic, optical, dielectric, and magnetic properties, have also been discussed. Various kinds of suitable applications for environmental remediation and oxygen evolution purposes have been explained. The implications of the use of surfactants on catalytic properties and their remedy involving the surfactant-free synthesis of nanocatalysts have been discussed.

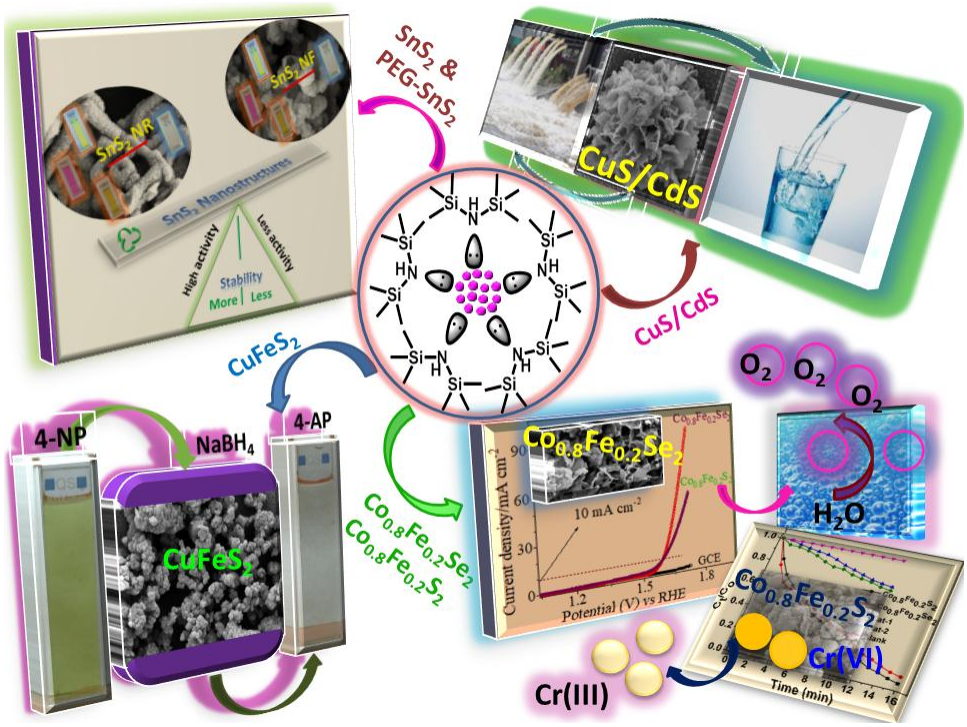

Chapter 2: Importance of Clean Surfaces on the Catalyst: SnS_2 Nanorings for Environmental Remediation

Chapter 2 describes the synthesis of SnS_2 nanocrystals and the effect of surfactants on the catalyst's surface and its catalytic activities. We have produced SnS_2 nanomaterials in two ways, without surfactant and with surfactant polyethyleneglycol (PEG). The presence and absence of surfactant molecules had significant effects on the morphology of particles produced. We have obtained ring-type morphology for surfactant-free (sf-SnS_2NRs), and flowers-like for PEG stabilized SnS_2 (peg-SnS_2NF). In both cases, the synthesis was performed in a single step by HMDS-assisted method under inert conditions in the presence or absence of PEG. The nanomaterials synthesized were characterized by different analytical and spectroscopic techniques, including PXRD, FESEM, TEM, BET, RAMAN, UV-visible, and XPS. The average sizes of particles calculated for sf-SnS_2NR and peg-SnS_2NF were estimated to be ~50 nm and ~100 nm, respectively. The influence of surfactants was conveyed by carrying photocatalysis for the degradation of toxic organic dyes (Rh B and MB) and inorganic chemical Cr(VI). In both cases, the sf-SnS_2 NRs showed supremacy in its catalytic behavior, degrading more than 95% of both the contaminants in a short period compared to peg-SnS_2NF. The overall enhancement in photocatalysis for sf-SnS_2NRs is because of open access to active sites and an enhancement in interfacial charge transfer on its surface compared to peg-SnS_2NF. The catalysts stability performed upto a certain number of cycles predicted a long shelf life with retaining its structure and morphology.

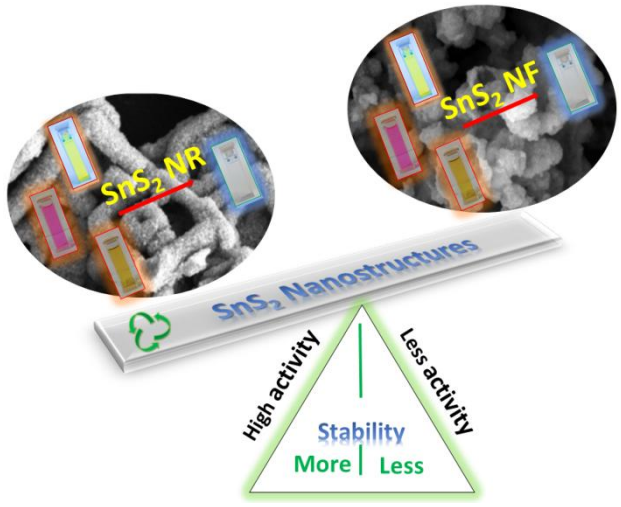

Chapter 3: A Simplistic Approach for the Synthesis of CuS-CdS Heterostructure: A Novel Photocatalyst for Oxidative Dye Degradation

This chapter explains the possibility of improving the catalytic performance by the formation of heterostructures between nanomaterials. From this perceptive, we have designed and developed CuS-CdS heterostructures. Thus, in this chapter, the direct synthesis of CuS-CdS based mesoporous composite materials and their photocatalytic activity are described. In this study, a series of CuS micro flowers (mf) decorated with varying amounts of CdS nanoparticles (NP) have been synthesized successfully in a controlled manner. Relatively easy synthesis of material along with its surfactant-free clean surfaced heterojunction accentuates the reliability of the protocol described here. Full characterization of these semiconducting materials was accomplished with a series of analytical techniques, which include powder x-ray diffraction (PXRD), scanning electron microscopy (SEM), tunnelling electron microscopy (TEM), x-ray photoelectron spectroscopy (XPS), UV-Vis, IR, BET and lifetime studies. Upon varying the concentration of precursor of Cd in the reactions, the resulting materials exhibited a well-demarcated change in morphologies ranging from undifferentiated mass to well-differentiated flower-like architectures. The thoroughly characterized composite was accessed finally for its potential photocatalytic activity for the degradation of organic dyes. The results showed 96.0% degradation of rhodamine B (RhB) over 10 minutes and 94.7% degradation of methylene blue (MB) over 9 minutes. This observed rate of degradation was much higher than that observed in the case of pure CuS (62.0% of RhB and 50.2% of MB).

Chapter 4: Chalcopyrite with Magnetic and Dielectric Properties: An Introductory Catalyst for 4-Nitrophenol Reduction

The progress for the development of active, stable, and economic catalysts for the chemical transformation of noxious chemicals to benign is of primary importance. In this chapter, we have explored the formation of a ternary transition metal chalcogenide-$CuFeS_2$ for the first time using the HMDS-assisted synthetic method and its catalysis for 4-nitrophenol (4-NP) reduction to 4-aminophenol (4-AP) by this material for the first time. The synthesis of surfactant-free chalcopyrite, sf-$CuFeS_2$ by wet-chemical one-pot HMDS-assisted synthetic method was accomplished. Various analytical and spectroscopic techniques carried on for the physical characterization of the material produced. From the observation of magnetic properties, the material chalcopyrite was found to be paramagnetic. The dielectric constant and dielectric loss were also determined, and they were decreasing with an increase in frequency. The dielectric behavior of the material was explained by Maxwell-Wagner theory of polarization, and the dielectric constant of the as-synthesized sample was found to be 3.176 at 100 ºC and 500 kHz. The potential catalytic activity was confirmed by performing the reduction of 4-nitrophenol (4-NP) to 4-amino phenol (4-AP) in the presence of sodium borohydride ($NaBH_4$) in aqueous medium at room temperature. The catalyst showed about 90% yields in the reduction reactions, which can be attributed to easy-access to active sites invigorated by the absence of surfactant molecules. Reusability tests performed upto five cycles, determined the well stability and retention of activity for catalyst.

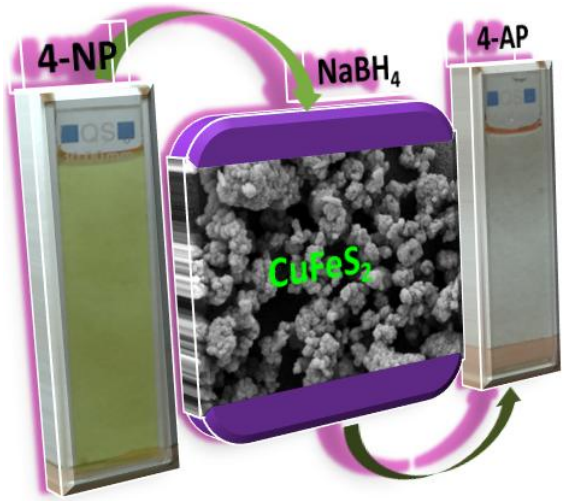

Chapter 5: Boosting the Bifunctional Catalytic Role of Cobalt Iron Chalcogenide-$Co_{0.8}Fe_{0.2}L_2$ (L = S and Se) as an Electrochemical OER Performer and a Photocatalyst for Cr(VI) Reduction

In this segment of the thesis, we have described the development of two novel series of ternary transition metal chalcogenides-$Co_{0.8}Fe_{0.2}L_2$ (L = S, Se) [$Co_{0.8}Fe_{0.2}S_2$ and $Co_{0.8}Fe_{0.2}Se_2$] using HMDS-assisted approach. The bifunctional role of these materials is explored for electrochemical OER performance and photocatalytic reduction of Cr(VI). The $Co_{0.8}Fe_{0.2}S_2$ and $Co_{0.8}Fe_{0.2}Se_2$ were synthesized by taking two different chalcogenide sources, thiourea and selenium powder. The different physicochemical properties of $Co_{0.8}Fe_{0.2}S_2$ and $Co_{0.8}Fe_{0.2}Se_2$ were scrutinized by various analytical and spectroscopic techniques, including PXRD, FESEM, TEM, BET, XPS, and UV-visible. As an electrocatalyst, the materials depicted well electrochemical water splitting properties for OER (345 and 350 mV @η_{10} as overpotential value and 52.4 and 84.5 mV/dec Tafel values for $Co_{0.8}Fe_{0.2}Se_2$ and $Co_{0.8}Fe_{0.2}S_2$, respectively). Comprehensive catalytic properties showed $Co_{0.8}Fe_{0.2}Se_2$ as a superior electrocatalyst than $Co_{0.8}Fe_{0.2}S_2$. When tested for photocatalytic reduction of Cr(VI) at pH value 3, $Co_{0.8}Fe_{0.2}S_2$ showed its best performance with a 96% reduction of Cr(VI) and 91% for $Co_{0.8}Fe_{0.2}Se_2$. The difference in catalytic properties is probably because of the dissimilarity in morphology. The catalysts retained their catalytic ability for 1500 CV cycles for OER performance and five cycles in Cr(VI) reduction.

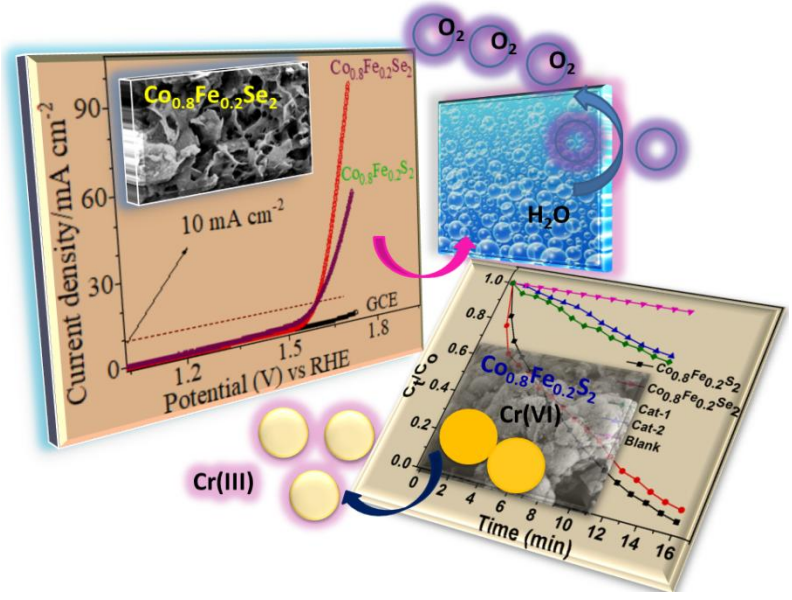

CHAPTER – 1

Abstract

The introduction chapter comprises a general discussion about the nanomaterials and their applications, and chalcogenides of main-group and transition metals. The metal chalcogenides include the binary and ternary compositions, also their composites. Further, the methods used for the synthesis of nanomaterials, particularly metal chalcogenides and their catalytic applications, have been discussed. The chapter also included the description of the widely practiced synthetic methods such as the hydrothermal method, sol-gel process, precipitation technique, microwave approach, chemical-vapor deposition method, and the electrochemical deposition method. Various types of applications discussed are; catalysis (4-nitrophenol reduction), photocatalysis (oxidation of dyes and detoxification of Cr(VI) to Cr(III)), and electrocatalytic water splitting (OER). The chapter also included a description of some crucial properties like optical, magnetic, and dielectric properties. The introduction chapter also explains the problems associated with surfactants on the catalytic properties and our synthetic approach (HMDS -assisted synthetic approach) to produce surfactant-free catalysts. In the end, the primary purpose of the work included in this thesis has been highlighted.

Introduction

1.1. Nanomaterials and Nanotechnology

The materials distinguished from their bulk counterparts in having at least one of the dimensions in the nanoscale range or the order of 10^{-9} m are called nanomaterials. The nanomaterials mostly vary in size between 1-100 nm and are ultrasmall particles. This small size gives them properties entirely different from their bulk. The branch of science which deals with the nanomaterials, including their synthesis, characterization, and properties, is called nanoscience. The technology involved in this whole process, which is the integration of chemistry, physics, and biology, accompanied by the fundamentals of science and engineering, is termed as nanotechnology.

The advancement in science and technology provided new ways to design and characterize the nanoscale range materials. The materials synthesized at the nanoscale, for example, possess excellent optical, thermal, biological, magnetic, and electrical properties that make them usable in advanced applications. In the nanoscale regime, alteration of some physical and chemical properties occurs, and this change introduces new properties to the materials. The objects surrounding a human are mostly on the macro scale, it is only through high-resolution microscopes they deal with the nano-objects, so it is the contact tip surface which acts as a medium of communication between these two worlds. Nanotechnology never overpowers microtechnology; instead, it always remained close to microtechnology, making its studies deeper and more explored.

Nanomaterials can be obtained from different sources like natural or human efforts. They can be engineered into particular architecture under certain critical conditions with sophisticated instruments to have desired properties. For example, some the sources include single metallic semiconductors (e.g, Al, Cu, Ag, Au, Ni, Ti, Ce, Sr and Co etc) [1], or their combinations either with S, Se or O and/or with polymers in the form of binary, ternary or composites with different stoichiometries (CdS, ZnS, CuS, FeS, NiS) [2], (TiO_2, Fe_2O_3, CuO) [3], ($CuInS_2$, $CuFeS_2$, $NiCo_2S_4$) [4], (CuS/ZnS, CuS/CdS, CdS/ZnS) [5], (V_2O_5/PEDOT/MnO_2, graphene/PEDOT/MnO_2, PANI/CuS/RGO) [6]. The examples for the natural sources are; bio based, organic materials (e.g., collagen, gelatin, laminin, carbon nanotubes) [7] and inorganic material

(e.g., $CaCO_3$ [8], SiO_2 [9], $CaSO_4$ [10], Al_2O_3 [11]). Nanomaterials have been obtained in different shapes and morphology (Figure 1.1). The shapes vary from (nanocubes, hexapods, octahedral) [12], nanoprisms [13], urchins [14], tetrahexahedra [15], star-shaped [16], nanoplates [17], nanospheres [18]. Besides shape and morphology, the dimensions or size plays a crucial role in determining the various Physico-chemical combinations of properties of nanomaterials. Based on the dimensions, we have 0D, 1D, 2D, and 3D categories of nanomaterials.

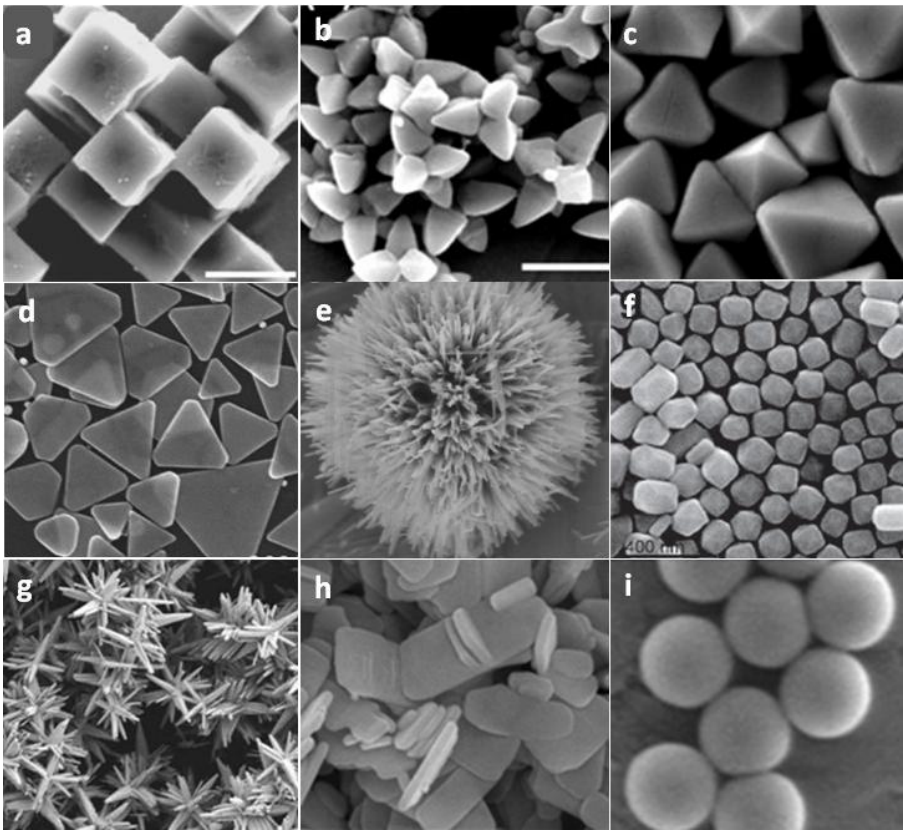

Figure 1.1. Depiction of morphological diversification of nanomaterials as reported by different literatures [Ref. 12-18].

1.2. Classification of Nanomaterials

Different perspectives were given at different times regarding the classification of nanomaterials. Some scientists classified the nanomaterials based on size or dimensions, according to shape or morphology, based on the nature of sources, while according to

suitable applications. Keeping in view the above clause of classifications, we have enlisted some classifications here and discussed them briefly.

1.2.1. On the basis of Dimensions.

Several nanomaterials with excellent properties and applications have been synthesized. So the demand to classify them is a prerequisite criterion. Gleiter et al. made the first attempt at the classification of nanomaterials [19]. Their classification was based merely on crystal structure and chemical composition. However, this classification had some shortcomings, as it did not consider aspects like dimensions [20]. Pokropivny and Skorokhod in 2007 elaborated on the classification of nanomaterials by including all the dimensions related to materials like 0D, 1D, 2D, 3D [21]. So different classifications given for nanomaterials based on dimensions are depicted in Figure 1.2.

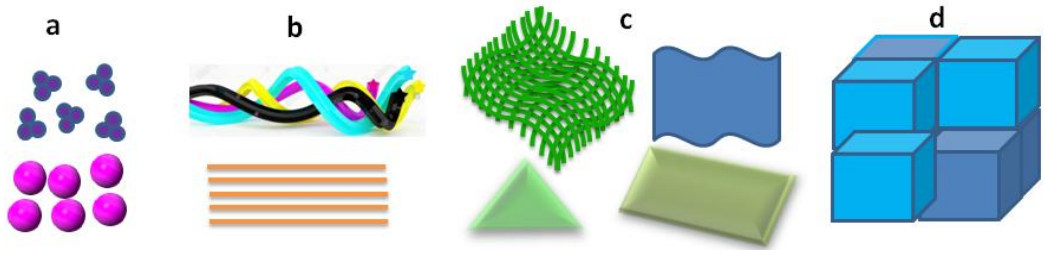

Figure 1.2. Portrayal of dimensional classification of NMs (a) nanospheres and nanoclusters illucidating zero dimensional (b) nanowires and nanorods showing one dimensional (c) networks, prisms, sheets and plates as two dimensional (d) cubes as three dimensional nanomaterials.

1.2.2. On the basis of Materials.

Based on the type of materials we have nanomaterials classified as follows

(a) Carbon based Nanomaterials.

Carbon-based nanomaterials are the materials with their skeleton entirely made up of carbon. Carbon itself exists in different polymorphs like graphene, diamond, fullerenes, carbon nanotubes, and carbon fibers. All these have been obtained in the nanoforms though some are difficult to prepare on nanoscale like diamond. These materials possess a hallow or layered structure with each layer interconnected to one another through some

non-covalent interactions like hydrogen bond, ionic forces, π-π interactions, which helps them to bind when prepared in nanoscale. It is through these interactions with the organic moieties that make them suitable adsorbent materials. They show enhancement in their properties when produced in nanoscale and perform well in different applications like electrochemical sensing, electrochemical water splitting, biological applications, and tissue engineering [22]. Some of the carbon-based nanomaterials are shown in Figure 1.3 [23].

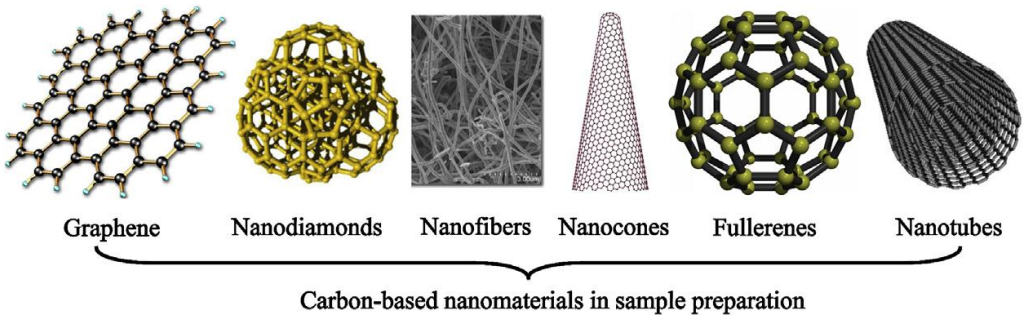

Figure 1.3. Depiction of carbon based nanomaterials [23].

(b) Organic or Bio based Nanomaterials

Organic or bio based nanomaterials have their origin wholly from natural sources like animals or plants. Through some covalent or noncovalent interactions, they get constructed into some impressive structures. The most important ones include cyanine derivatives, porphyrin, liposomes, DNAs and RNAs, chitin, and chitosan. These are having some interesting medicinal applications like in photothermal cancer therapy or imaging.

(c) Inorganic based Nanomaterials

They are mostly inorganic metals or their combinations with each other or with oxygen or sulfur, e.g., Cu, Cd, Ag, Au, Zn, Ni-Fe, ZnO, and Fe_2O. The inorganic or metal nanoparticles possess an important characteristic feature of localized surface Plasmon resonance due to which they show unique optical properties. The metallic nanoparticles showing this important property are Ag, Au, and Cu; this is because of the broadness featuring in their visible spectrum [24].

(d) Composites

The composite materials are formed by combinations of either inorganic metals or metal ions with polymers or bio based compounds. Some exciting materials are inorganic-organic hybrid perovskites, pmofs, mofs (zeolites), polymer/MX composites (where polymer = PANI (polyaniline), polypyrole, polythiophene, M = Sn, Ni, Cu, Cd, X = S, O, Cl).

1.3. General Synthetic Approach and Applications

A number of synthetic methods were adapted at different times by different people for the synthesis of nanomaterials. All these methods differ from one another either in synthetic modes or in one or two other conditions like temperature, time, ways of synthesis, feasibility of reaction, scalability etc. But overall all the synthetic methods were enlisted in two approaches namely, Top to Bottom and Bottom to Top approaches (Figure 1.4).

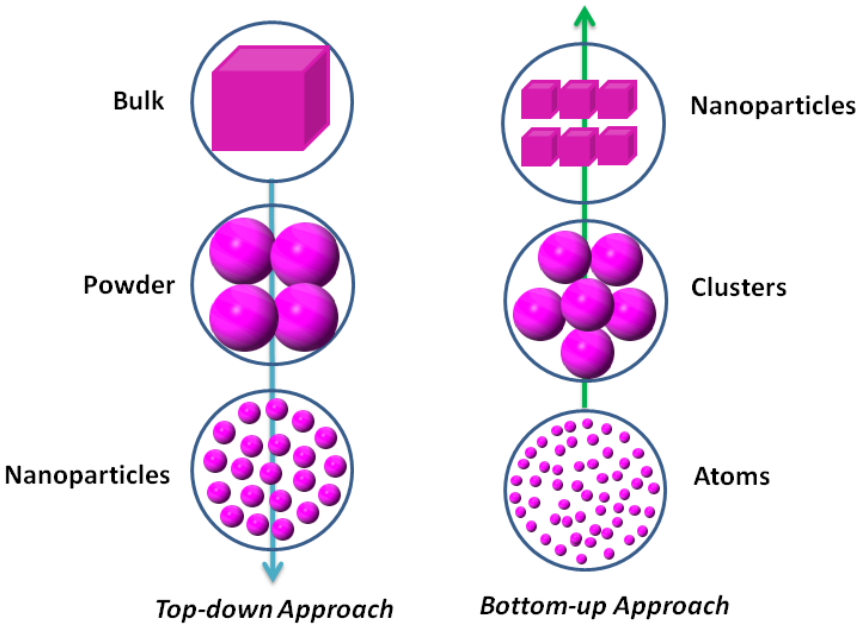

Figure 1.4. Schematic view of the two ways of synthesis for nanomaterials: top to bottom and bottom to top approach. Both the techniques involve various steps making the synthesis easy and possible.

1.3.1. Top to bottom method

Top to bottom approach can be defined as the slicing of bulk material to get it into nano dimensions. Mostly, the materials are obtained in this method by mechanical pathways like mechanical ball milling and attrition. Many nanostructures have been produced by mechanical ball milling, including both amorphous and crystalline materials under inert conditions [25]. Here some of the crystal facets are removed to introduce superior properties into the crystal. One of the hurdles in the top to bottom approach is that it leads to imperfections or defects within the material, causing crystal destruction. The crystal defects, in turn, produce challenges while designing material. By top to bottom approach, it easy to scale up the production of materials, and therefore, it played a magnificent role in the nanoworld.

1.3.2. Bottom to Top method

Bottom to top approach can be defined as the stacking or assembling of material from the bottom. It is somehow similar to the construction of a new building starting from bricks, but here stacking of atoms. Living creatures around us can be considered a perfect example of a bottom-to-top approach where scaling or assembling occurs at the cellular level. The approach has achieved unlimited feats for designing and synthesis of nanomaterials. Colloidal dispersions can achieve the production of many nanomaterials. This approach finds its practical utility for the synthesis of thermoelectric materials [26].

1.3.3. Applications of Nanomaterials

As nanotechnology advances, the materials prepared at different levels find their practical utility [27]. Nanomaterials have fascinating physical and chemical properties, allowing their special applications to be more advanced than the substances of the same structure. Application of nanomaterials covers a diversified area from natural sciences, engineering, and medical, agricultural to interdisciplinary areas [28]. Table 1.1 shows the diversified applications of differently synthesized nanomaterials.

Table 1.1. Applicability of various nanomaterials in distinct fields.

S. No.	Materials	Applications	Ref.
1.	Ag–TiO_2, Fe_2O_3, ZnO–SnO_2, ZnO–CdS@Cd.	Photocatalysts	[29]
2.	Cu(InxGa$_{1-x}$)Se_2, Co_3O_4, $CsPbBr_3$, $CH_3NH_3PbI_2Br$	Photovoltaic's	[30]
3.	Sb_2Se_3, CdTe, SnO_2, GeS, WS_2, ZnO, MoS_2	Photodetectors	[31]
4.	TiO_2, Pt–Ir, NiO–Au, PtAu/G-CNTs, CuO, ZnO	Sensors	[32]
5.	Ni/Ni_3Fe/B-CNT, CoSnS@CNT, $Co_{0.5}Fe_{0.5}S$@N-MC	Water splitting	[33]
6.	$CoFe_2O_4$–TiO_2, ZnO & CdO NPs, CdS, Ag@AgCl	Dye degradation	[34]
7.	ZY-CS, TiO_2, Pd/TiO_2, Fe_2O_3/ZrO_2@ZrO_2, Cu_2O	CO_2 conversion	[35]
8.	Ag NPs, ZnO–Au composites, AgFON, Copper NPs	SER's	[36]
9.	CuS, CuS and ZnO/$Zn(OH)_2$ NPs, ZnSe@ZnS QDs, ch-Cu composite	Medicine	[37]
10.	MoS_2–MoO_3, MWCNTs, GaN	LED's	[38]
11.	($VO_xN_{y-x}C$) NPs, $NiCo_2O_4$, $ZnCo_2O_4$, NiO/$Ni(OH)_2$	Supercapacitors	[39]
12.	Co_3O_4 NMs, $Ca(OH)_2$-coated ZnO, $NiCo_2O_4$ for Ni/Zn battery	Batteries	[40]
13.	PbTe, ZnO–TiO_2–SiO_2 Nc's, ZnS Np's, ZrS_2	Non linear optics	[41]

1.4. Metal Chalcogenides and their Synthesis

The combinations of metals (main group or transition) with any of the chalcogenides are called metal chalcogenides. The term 'chalcogenide' is mostly confined and specified for group VIA of the periodic table. Although VIA starts from oxygen to polonium but mostly combinations with sulfur, selenium, and tellurium had been studied thoroughly. Metal chalcogenides exist in different stoichiometric forms with different potential activities. Combinations of metal chalcogenides with graphene, carbon nitride, graphene oxide, nickel foam, which acts as a support for them to form various types of heterostructures, enhances their applicability.

The transition metal chalcogenides themselves are categorized as mono, di, tri, and tetra depending upon the number of transition metals present. The most common stoichiometry possible is either 1:1 or 1:2. The monochalcogenides are designated as MX (M = main group or transition metal, X = S, Se, Te). They generally crystallize in zinc blende structure. The dichalcogenides are represented as MX_2 (M = transition metal, X = a chalcogenide). The most widely studied is sulphide among these. They generally crystallize in cadmium diiodide or molybdenum disulphide crystalline structure. Some of the important examples of metal chalcogenides are enlisted as: SnS_2, Bi_2S_3, Sb_2S_3, CuS, CdS, ZnS, $CuSe_2$, WSe_2, $CoSe_2$, $NiCo_2S_4$, Cu_3BiS_3, MoS_2, $BiVO_4$, and $CuInGaSe_2$.

The research interests for designing advanced functional nanomaterials are increasing because of their size and shape dependent properties. The present-day nanomaterials are designed and fabricated in a way that they are used in different fields based on their properties [42-48]. So the design and fabrication of chalcogenide nanomaterials with controlled size and morphology are of prime importance in this era of nanotechnology. Here some of the well-practiced synthetic methods for nanomaterial synthesis have been discussed.

1.4.1. Hydrothermal method

Hydrothermal synthesis is defined as a mode of synthesis under a closed system. It is a controlled synthesis of materials in aqueous solution in a closed vessel at a temperature above 100 °C, and more than the atmospheric pressure built within [49, 50]. Proper control over the reaction parameters (including pH, duration, temperature, and pressure) in the hydrothermal approach is required for the specific application. The whole reaction set up consists of Teflon enclosed within a steel autoclave to bear high temperature and pressure [Figure 1.5]. The hydrothermal and solvothermal approaches differ from each other by the mere presence of a solvent, for hydrothermal, it is water and while for solvothermal an organic solvent other than water. The materials prepared by hydrothermal methods show high crystallinity compared to other methods. On the other side, it is a time-consuming process, and since the reaction takes place in a closed system, there is no knowledge about the physical stature of the reaction mixture. Under these conditions, the reaction mixture may develop internal complications.

Figure 1.5. Showing a picture of an autoclave used to carry a hydrothermal reaction.

Numerous nanomaterials have been synthesized by the hydrothermal approach. This method was used extensively to synthesize oxides of W, Mo, V, and some kinds of phosphates [51-60]. The much convenient hydrothermal approach provides access to those phases which are not possible by other synthetic ways [61]. Some of the functional nanomaterials prepared by hydrothermal methods reported in different pieces of literature are enlisted below.

Azam et al. synthesized zinc selenide nanoparticles by the hydrothermal method involving different surfactants (CTAB, SDS, PEG-600, and 4000) at 180 °C with various time ranges. Hydrazine played the central role as a reducing agent. [62].

$$Zn(AC)_2.2H_2O + SeCl_4 + CTAB \xrightarrow[180\ oC,\ 18\ h]{Hydrazine} ZnSe\ NPs$$

Scheme 1.1: Synthesis of zinc selenide nanoparticles

Caixin et al. by surfactant-assisted hydrothermal approach synthesized SnO_2 nanorods. Here the surfactant CTAB directed the growth of 1D nanorods of rutile phase SnO_2. The SnO_2 nanorods thus prepared have diameters of ca. 40–100 nm [63].

$$SnCl_4 + NaOH + H_2O + \underset{(CTAB)}{cetyltrimethyl\ ammonium\ bromide} \xrightarrow{160\ ^oC,\ 12\ h} SnO_2\ NPs$$

Scheme 1.2: Synthesis of tin oxide nanoparticles

Xiaodi et al. using the hydrothermal approach, ionic liquid ([BMIm][$SeO_2(OCH_3)$]) for Se source, successfully synthesized ZnSe hollow nanospheres. The hollow nanospheres

were monodispersed. The ionic liquid performs the dual role of being a precursor for Se and a stabilizer for the one-pot production of ZnSe nanostructures. [64].

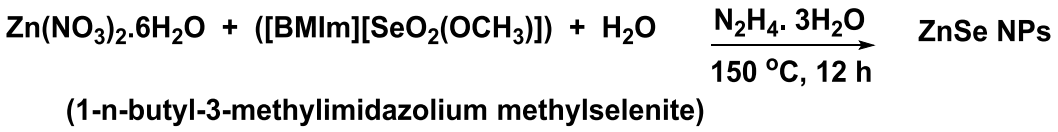

Scheme 1.3: Synthesis of zinc selenide nanoparticles

Sugarthi et al. successfully synthesized three batches of ternary chalcogenide $AgBiS_2$ by solvothermal approach within a temperature range of 140 °C to 180 °C (temperature difference of 20 °C) followed by calcination. The materials prepared presented a different morphology in all the three batches confirmed by FESEM [65].

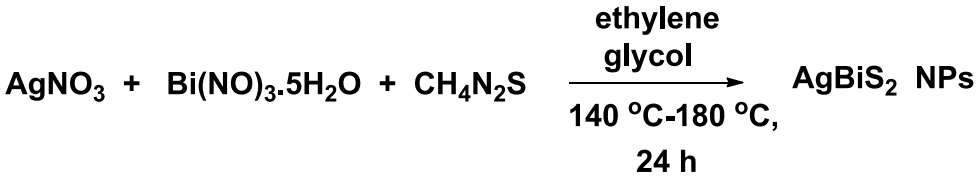

Scheme 1.4: Synthesis of silver bismuth sulphide nanoparticles

Kaiqiang et al. synthesized MoSSe nanostructures by one-pot hydrothermal assisted synthesis at a high temperature of 200 °C and 24 h duration. The ratio of selenium and thiourea were changed to give different stoichiometries of $MoS_{2(1-x)}Se_{2x}$ [66].

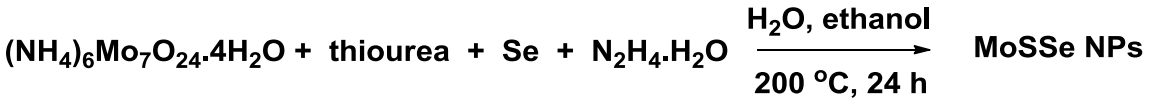

Scheme 1.5: Synthesis of molybedenum sulphide selenide nanoparticles

Subramanian et al. synthesized MnO_2 nanomaterials by hydrothermal technique. The as-synthesized materials with a mix of nanorod and plate type morphology worked as an excellent electrode material for supercapacitors [67].

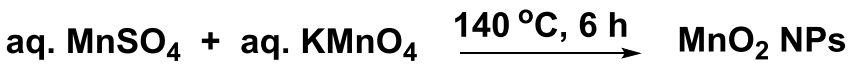

Scheme 1.6: Synthesis of manganese oxide nanoparticles

1.4.2. Sol-gel method

The sol-gel approach is one of the best ways of synthesizing nanomaterials from the precursor solutions and finally molding it to the desired shape and structure bestowed with superior properties. A suitable mixture of raw material solution acts as a precursor for the desired materials to be fabricated in this process. The frequently used materials as precursors are oxides and chlorides of metals, which subsequently undergo hydrolytic and condensation reactions. The metal oxides have either (M-O-M) or (M-OH-M) linkages, through which the metals remain intact to each other. This sort of linkage gives rise to polymeric solution formation, which results in a diphase gel-like formation in which both solid and liquid forms coexist. This gel-like material finally results in the intricate formation of either discrete particles or polymers. This technique has rapidly enlarged to different fields of science and technology [68].

The benefit of the sol-gel technique is that the material's density is enhanced at a satisfactory level compared to the other available techniques. Being a cheap and low temperature-assisted technique, we can easily control the material's chemical composition. The materials fabricated through the sol-gel approach show many potent applications in various fields like in optical and electronic areas, energy conversion, and bio-sensing and medical fields [69, 70]. Figure 1.6 gives an illustration of the nanomaterial synthesized through the sol-gel technique [71]. Some of the important functional nanomaterials prepared by sol-gel methods are itemized below.

Figure 1.6. CuO nanoparticle synthesis by sol-gel technique [71].

Vijay et al. revealed the successful synthesis of cadmium sulphide/cadmium selenide core-shell heterojunction by the sol-gel synthetic approach. The reports claim a redshift in the photoluminescence spectrum, making the materials suitable for DSSCs [72].

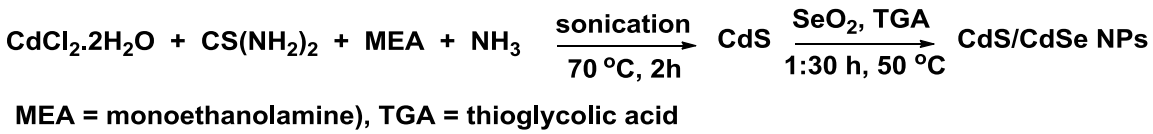

Scheme 1.7: Synthesis of cadmium sulphide/cadmium selenide nanoparticles

Lemine et al. using the sol-gel approach, successfully carried the synthesis of Fe_3O_4 nanomaterials. The magnetite nanoparticles had a size distribution of 8 nm [73].

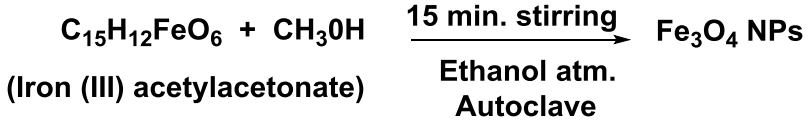

Scheme 1.8: Synthesis of magnetite nanoparticles

Jie et al. claimed the fabrication of copper-tin-sulphide film as a base material for solar cells using a sol-gel approach. Various films were prepared by changing the copper ratio to tin from 1.6 to 2.0 while keeping sulphur to metal ratio constant as 2.0 [74].

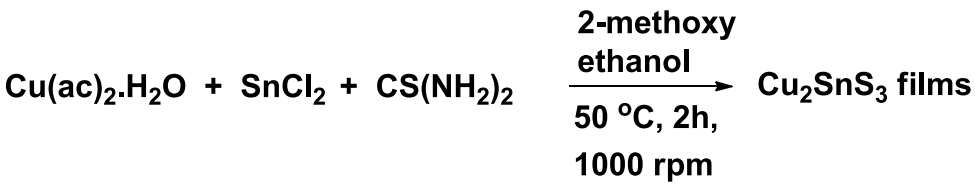

Scheme 1.9: Synthesis of copper tin sulphide nanoparticles

Man et al. claimed the synthesis of TiO_2-Ag nanoparticles through the sol-gel chemical approach using reducing agent sodium citrate tribasic dihydrate. When it is used as a catalyst, by varying the concentration of Ag in materials, the photocatalytic reduction of 4-nitrophenol was found to increase [75].

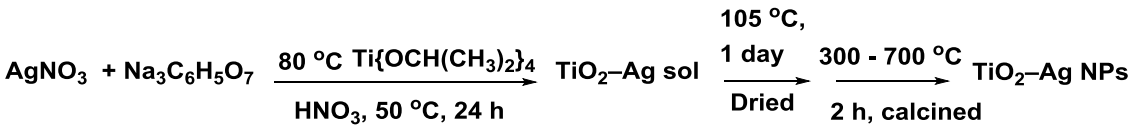

Scheme 1.10: Synthesis of titanium oxide-silver nanoparticles

Prasad et al. synthesized zinc doped cadmium sulphide nanoparticles by sol-gel method and developed their thin films using the spin coating method. The films were developed with varying concentrations of zinc. An enhancement in the thermoelectric property was observed with each incremental variation of zinc [76].

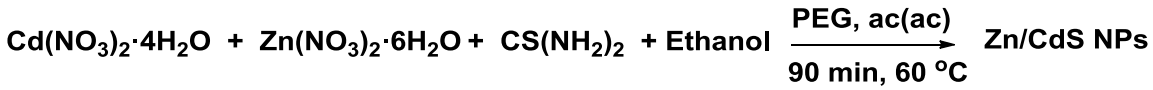

Scheme 1.11: Synthesis of zinc doped cadmium sulphide nanoparticles

1.4.3. Precipitation method

The precipitation method is used for the extraction of a solid mass from a solution. It is a process of settling down the insoluble materials under the influence of gravity or due to density. During settling, the particle size may vary from time to time. Different explanations and theories were put forward time by time to enlighten the precipitate formation. The factors affecting the particle size for precipitate formation include the precipitate's solubility, the temperature at which the precipitation reaction is carried, components amount, and the frequency of mixing of reagents. The main contributors to precipitate development are nucleation and growth. Nucleation comprises of a combination of small tiny entities together to form a stable product. The small entities can be ions, atoms, or molecules which get attracted to each other, forming a stable product. In contrast, growth involves the formation of larger size particles but in lesser numbers. A general reaction scheme for precipitation method is shown in Figure 1.7.

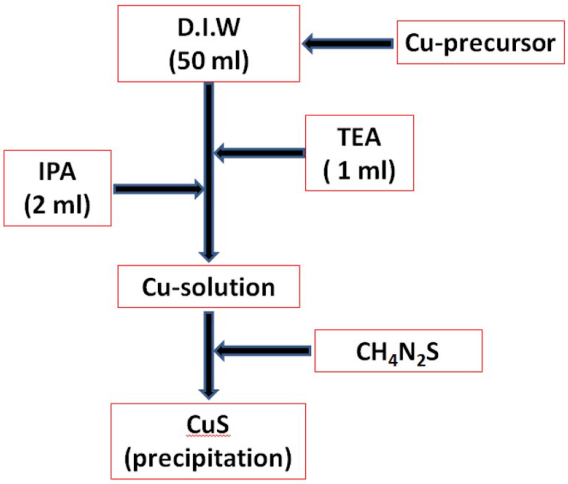

Figure 1.7. Synthethic Pathway of CuS by precipitation method [77].

Precipitation finds its practical applicability in many applications, e.g., in pigment formation and desalination of water. Some of the crucial nonomaterials produced by the precipitation route are enlisted below.

Babu et al. synthesized CuS NPs with different phases using the co-precipitation method. The CuS nanomaterial was synthesized using water as a reaction medium. The different sources of Cu (CuCl, $CuCl_2$, and $CuSO_4$) were employed to determine the effect on the properties of synthesized CuS nanoparticles [77].

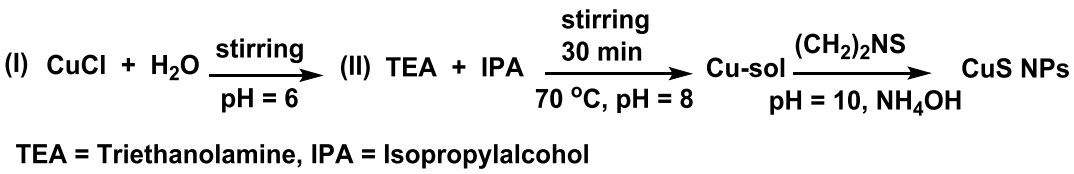

Scheme 1.12: Synthesis of copper sulphide nanoparticles

Andrade et al. synthesized magnetite Fe_3O_4 nanoparticles using the co-precipitation route. The magnetic Fe_3O_4 nanoparticles were doped with different metal cations, including Ce^{4+}, Co^{2+}, Mn^{2+}, and Ni^{2+}, and their effects on properties were studied. An enhancement in methylene blue photodecomposition was prevalent using doped Fe_3O_4 as photocatalysts. While studying the effect of doping on electrical properties, it was noticed that Co decreased the resistivity and Ce, Mn and Ni increased [78].

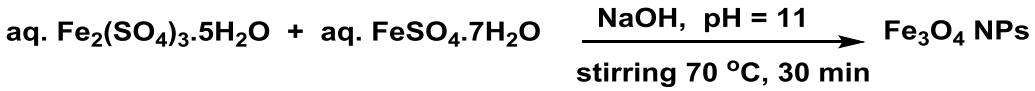

Scheme 1.13: Synthesis of magnetite nanoparticles

Tahir et al. claimed the successful synthesis of cadmium silver-sulphide heterostructures by precipitation method using polyvinylpyrrolidone as a template. The materials synthesized were tested for biological activities with different bacterial stains. An enhancement in activities was observed as the concentration of cadmium sulphide was increased [79].

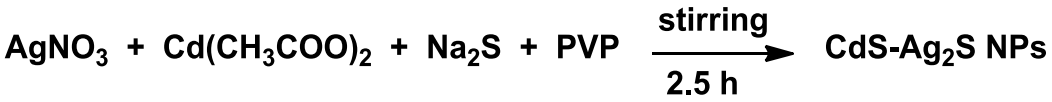

Scheme 1.14: Synthesis of cadmium sulphide-siler sulphide nanoparticles

Sharareh et al. reported the synthesis of nickel ferrites through the co-precipitation method. Mn-doped the nickel ferrite materials and its effect on structural and magnetic properties were elucidated. A preferable change in structural and magnetic properties was observed [80].

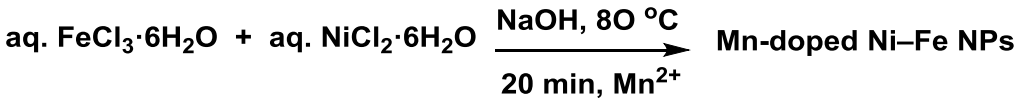

Scheme 1.15: Synthesis of manganese doped nickel ferrite nanoparticles

1.4.4. Microwave method

Microwave synthesis is the approach of synthesis in which microwaves are utilized in order to perform a reaction. Microwaves are the high-frequency radiations which will generate heat in any materials with mobile charge carriers. The heat is produced either due to collision like in the case of solvent molecules or due to electric current generation because of mobile charge carriers. This process produces heat within the materials. The heating effect produced in microwave synthesis is different from conventional heating. In conventional heating, much heat is wasted first in raising the temperature, heating the surroundings of the reaction vessel, furnace, or an oil bath while the core material initially remains unheated, due to which it takes too much time to complete a reaction. In

microwave synthesis, the radiations remain confined to the sample and in a closed system. Consequently, the loss of heat radiations is prevented hence taking lesser time, and reactions are reproducible. Microwave synthesis is most common in organic fields [81] and has been extended to synthesize inorganic nanomaterials also [82]. The microwave-assisted synthetic approach is extended easily to industrial processes like in food processing [83-86]. It is considered the most effective way to control macroscopic morphology and crystallite size [87]. Figure 1.8 gives the diagrammatic representation of the microwave technique.

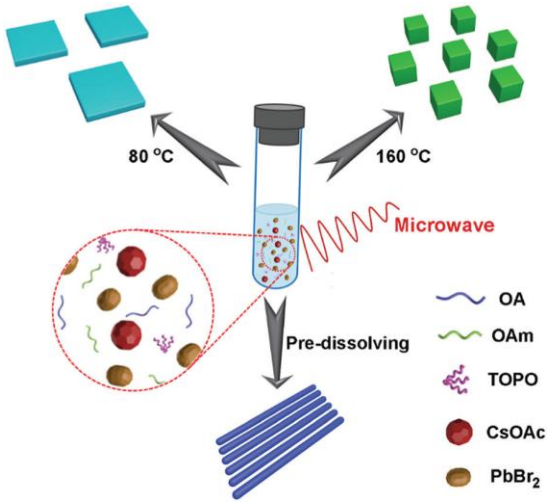

Figure 1.8. Microwave assisted synthetic approach of nanoamterials [87].

Badria et al. claimed the synthesis of silver sulphide nanomaterials by adopting the microwave technique. The materials were synthesized using different concentrations of surfactant sodium dodecyl sulfate (SDS) for time duration of 10 minutes and 700W power. The silver sulphide nanomaterials proved to be suitable photocatalysts for the degradation of methyl green dye [88].

$$AgNO_3 + Na_2S + H_2O + SDS \xrightarrow[\text{(b) Microwave 700 W, 10 min}]{\text{(a) stirring 30 min}} Ag_2S\ NPs$$

Scheme 1.16: Synthesis of silver sulphide nanoparticles

Shkir et al. successfully synthesized strontium doped PbS by adding different strontium loadings applying a microwave-assisted synthetic approach. The nanomaterials developed with different Sr amounts showed an enhancement in their physical properties

like in PL intensity, dielectric properties, and electrical properties. Overall, an enhancement in the optical properties was confirmed on doping with strontium [89].

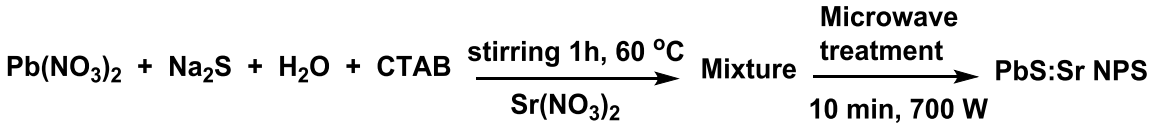

Scheme 1.17: Synthesis of strontium doped lead sulphide nanoparticles

David et al. reported the synthesis of cobalt-metal organic framework structures with platelet like morphology by microwave synthetic approach. The Co-MOF materials were transformed into cobalt-carbon nanocomposite discs by heating them above 800 °C. The materials performed the role of an electrode in sodium-ion batteries [90].

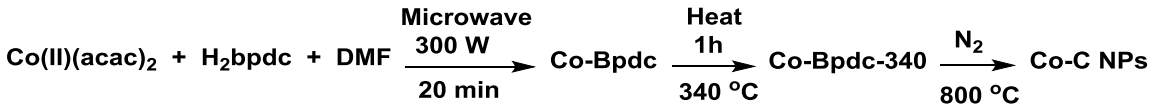

Scheme 1.18: Synthesis of cobalt-carbon nanoparticles

Iqbal et al. highlighted the synthesis of zinc vanadate nanoparticles by applying microwave. The nanoparticles thus synthesized were utilized for the photolysis of methylene blue dye degradation [91].

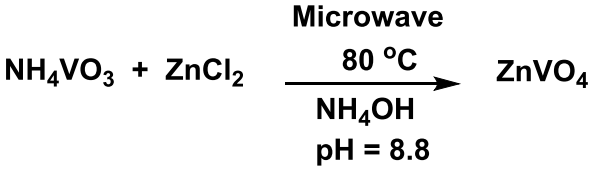

Scheme 1.19: Synthesis of zinc vanadate nanoparticles

Luo et al. utilized microwave synthetic approach to successfully synthesize Sb_2Se_3 nanostructures by a simple variation of solvents volume in EG and water. The synthesized materials with nanowires and microrod type morphology performed the best role as the anode in LIBs [92].

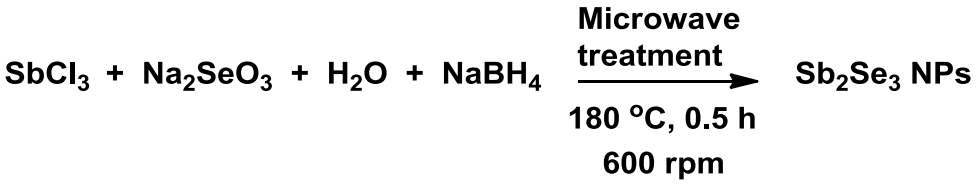

Scheme 1.20: Synthesis of antimony selenide nanoparticles

Zhang et al. claimed the successful synthesis of carbon nitride-copper oxide heterojunctions by microwave synthetic pathways. The heterojunctions were studied for their catalytic applications to decompose NH_4ClO_4 while heating them at different temperatures. An overall high value of thermal decomposition was achieved under the influence of carbon nitride-copper oxide heterojunctions [93].

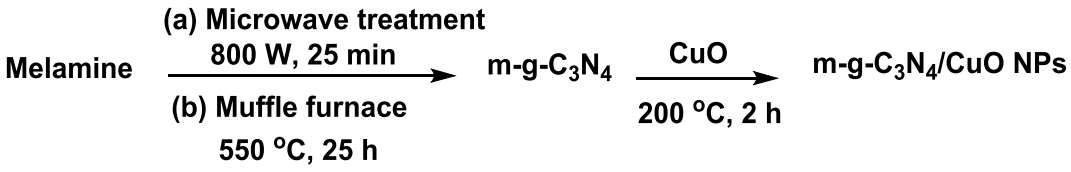

Scheme 1.21: Synthesis of carbon nitride-copper oxide nanoparticles

1.4.5. Chemical-Vapour Deposition method

The Chemical-Vapour Deposition (CVD) process involves heating the precursor substrates to a high-temperature vapor phase and depositing the required materials on a solid stratum. The CVD method has good commercial acceptance for the formation of thin films or coatings necessary for semiconductor formation on an industrial scale. By CVD, films of micrometers range can be deposited, which is advantageous for this method. This technique can achieve reasonable control over morphology, crystalline nature, and stoichiometries. PACVD (plasma-assisted chemical vapor deposition) and LCVD (laser chemical vapor deposition) variants of CVD have received special attention. [94].

Siyuan et al. claimed a successful production of mono and bi-layered molybdenum selenide and their films by adopting a modified version of the chemical vapor deposition technique by introducing a reverse flow strategy. Good control over nucleation and morphology was reported by merely controlling the temperature and time. The technique

is recognized as a way to synthesize transition metal dichalcogenide crystals on a large scale and consistent. [95].

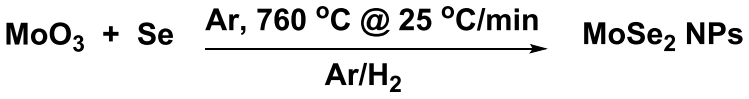

Scheme 1.22: Synthesis of molybedenum selenide nanoparticles

Zhao et al. successfully synthesized $MoTe_xSe_{2-x}$ films by using the CVD approach. The group claimed that a well-tuning of band edge could be achieved by merely changing the Te concentration. The synthesized materials based on Raman spectra were confirmed in having 2H-phase [96].

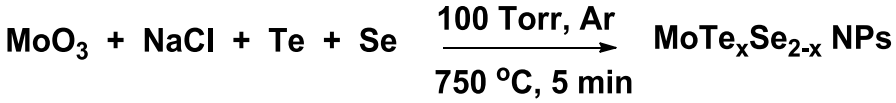

Scheme 1.23: Synthesis of telurim doped molybedenum sulphide nanoparticles

Giannazzo et al. successfully synthesized the molybdenum sulphide monolayer by using the chemical vapor deposition approach. The MoS_2 monolayers were studied by conductive force AFM to find their contribution in grain boundaries resistance measurements using SiO_2/Si as support. [97].

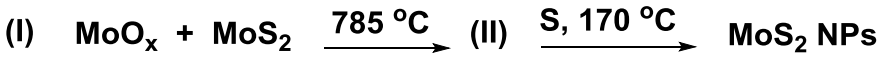

Scheme 1.24: Synthesis of molybedenum sulphide nanoparticles

Chen et al. successfully utilized the CVD approach to lead the synthesis of layered $MoSe_2$ by bringing variations in Mo to Se ratio, hydrogen flux, and the temperature at which layer formation occurs. The group also reported the synthesis of $MoSe_2$ nanoribbons utilizing different substrates by this ambient pressure CVD approach. [98].

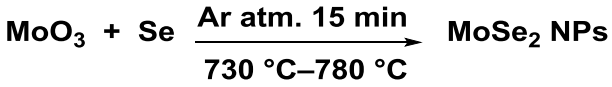

Scheme 1.25: Synthesis of molybedenum selenide nanoparticles

1.4.6. Electrochemical Deposition Technique

An electrochemical deposition involves depositing a thin and compact coating on a conductive material as a substrate. The coating is done with the desired material, i.e., a metal, metal oxide, or a salt. The process is carried in an electrochemical cell (Figure 1.9) containing an electrolyte of the desired coated material or its complex form [99]. The metaphysical and optical properties like morphology, stoichiometry, conducting behavior of the semiconductor materials can be controlled well by the electrochemical deposition approach [100]. The electrochemical deposition technique involves an electrolyte solution containing ions in continuous motion by applying an electric field. The ions are involved in exchanging electrons and holes at their respective electrodes and hence getting deposited there [100].

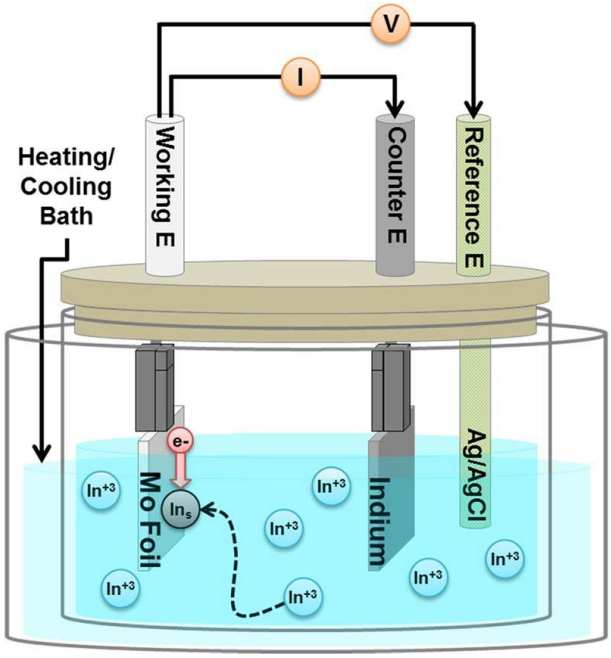

Figure 1.9. The electrochemical set up showing the deposition of indium films using a three electrode system [99].

Waldiya et al. achieved the electrochemical deposition of CdTe using an ionic liquid-([BMIM][Ac]) at an elevated temperature of 90 °C, and with Cd:Te ratio equals to 2. The prepared material served as a superior catalyst for photoelectrochemical water splitting for hydrogen evolution reactions [101].

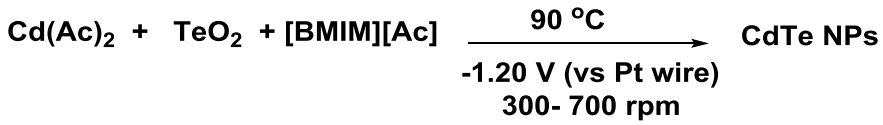

[BMIM][Ac] = 1-butyl-3-methylimidazolium acetate

Scheme 1.26: Synthesis of cadmium teluride nanoparticles

Li et al. reported successful doping of antimony selenide by the electrochemical deposition technique. The doped materials prepared as cracked layers showed superior optical properties and were investigated by cyclic voltammetry to determine their electrochemical behavior [102].

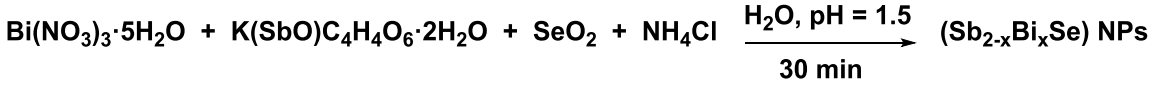

Scheme 1.27: Synthesis of bismuth doped antimony sulphide nanoparticles

Tang et al. reported the successful fabrication of antimony selenide (Sb_2Se_3) on titanium oxide nanotube arrays by utilizing the electrochemical deposition method. The materials were used as catalysts for the 4-nitrophenol reduction with 93.5% conversion [103].

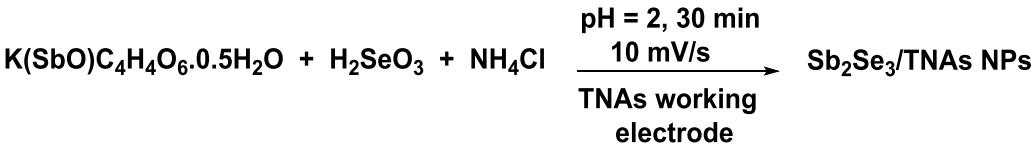

Scheme 1.28: Synthesis of antimony sulphide nanoparticles on titanium oxide

Ngo et al. used electrochemical deposition technique to obtain the thin films of Sb_2Se_3. The thin films of antimony selenide served as an excellent light absorber material for photoconversion cells due to TiO_2/Sb_2Se_3/CuSCN heterostructure formation [104].

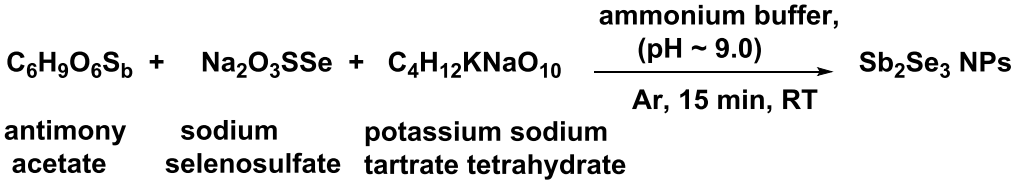

Scheme 1.29: Synthesis of antimony sulphide nanoparticles

Pinaki et al. synthesized tin selenide thin films by electrochemical deposition method. The films were prepared by applying 0.5 V potential with silver-silver chloride as reference electrode. The tin selenide materials were used as photocatalysts in presence of H_2O_2 for the photooxidative decomposition of MB & malachite green [105].

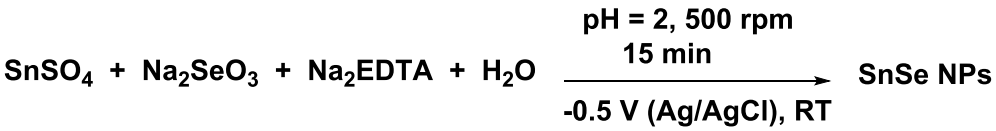

Scheme 1.30: Synthesis of tin sulphide nanoparticles

1.5. Properties of Metal Chalcogenides

Varieties of nanomaterials were prepared with different size, shape, and morphology. The overall physical and chemical properties of nanomaterials depended on their characteristics, like size and shape. Some of the crucial properties of metal chalcogenides are discussed below.

1.5.1. Optical properties

Nanomaterials exhibit unique optical properties compared to bulk counterparts. This uniqueness is because there is a continuum of band levels-conduction and valence bands in bulk counterparts, while in the case of semiconductor nanomaterials, they have intrinsic fundamental levels estranged from each other by ~0.3–3.8 eV [106, 107]. Chalcogenide semiconductor nanomaterials have bandgaps lying in between UV and visible to near IR, e.g., such as ZnS, CdS, and PbS. The cadmium based chalcogenides of the type CdX (X = S, Se, Te) are widely studied because the bandgap can be easily tuned. For example, Covin et al. claimed the production of organic/inorganic composite LEDs using p-paraphenylene vinylene and CdSe. They observed that the emission colour changed from red to yellow at low voltages, which was arising from metal layers only while as at high voltage to green colour predominantly from the polymer matrix. So this hybrid LED shows tunability in colour due to voltage fluctuations [108].

Likewise, Nazzal et al. reported a cadmium selenide composite with polymethylmethaacrylate (PMMA) for gas sensing properties. The nanoparticles immersed in PMMA were irradiated to light both before and while measuring the gas sensing properties. Based on PL intensity, it was observed that while exposing the samples to triethylamine, the intensity increased, and the reverse was observed for benzylamine [109]. Divya et al. claimed the combined synthesis of CdS and ZnS together

in one ternary system as CdZnS by a novel Exploding Wire Technique (EWT). In combination, optical properties got changed with a bandgap value of 2.4–3.6 eV somewhat wider than pure phases. This change is because the optical property depends on the size [110].

1.5.2. Catalytic activity

Noble metal nanomaterials were excessively used as catalysts and got tremendous scientific interests because of their inimitable physio-chemical properties [111, 112–114]. The combination of noble metal and a metal oxide or sulphide as a catalyst has shown portable applicability in different fields. For example, they are used as photocatalyst for toxic chemical degradation, photo energy conversion, water-splitting, carbon dioxide reduction, and electron transfer processes [115,116]. Pt and other noble metals, due to their high stability and proper bandgap, are considered prominent catalysts but costly, less abundance hampers their use for large-scale applications. Therefore, the search for the development of catalysts that can be used as substitutes for noble metal catalysts is in demand [117, 118].

Transition metal chalcogenides (TMCs) have been used as substitutes for noble metal elements for electro- and photocatalytic activities. Transition metal chalcogenides of the general formula MX (where M = Mo, W, Ni, Co, Cd, Cu, Ti; X = S, Se, Te, Po) have received enormous research interests because of their excellent activity like those of Pt [119, 120]. However, TMCs suffer from low conductivity, low absorption coefficients, larger bandgaps, high charge recombinations, photocorrosion at the electrodes [121]. These issues can be overcome by doping, morphological and size changes, forming heterojunctions with other semiconductors having low bandgaps and high surface area [122]. The doping or composite formation will improve the overall catalysis rate due to the synergism between the semiconductor materials. This synergistic effect would reduce the charge recombination rate, improves the absorption coefficient, promotes or extends the absorption in the entire visible spectrum, prevents the photocorrosion at electrodes, and an overall enhancement in the number of active sites [123]. Besides transition metal chalcogenides, the main group metal chalcogenides and their composites have been

prepared for an overall enhancement of the catalytic activity, e.g., SnS_2, C_3N_4/SnS_2, 3D/2D In_2S_3/SnS_2 heterojunction, CdS– SnS_2 [124]. However, they also suffer from similar shortcomings as that of TMCs and also need the same treatment.

1.5.3. Magnetic properties

An atom or a molecule with an unpaired electron will produce a magnetic field due to which it behaves like a tiny bar magnet. Compared to their bulk counterparts, nanomaterials show well-defined magnetic properties that can be easily tuned [125]. The magnetic materials are classified as diamagnetic, paramagnetic, ferromagnetic, ferrimagnetic, and antiferromagnetic based on their response to an external magnetic field [126]. For nanomaterials, the magnetism dates back to 1949 since the revolutionary work by Lious Neel by coming forward with the first representation explaining the magnetic relaxations in magnetic nanoparticles (MNPs). At present, the interest in studying the magnetic nanoparticles aroused enormously because of exceptionally different properties from those of bulk counterparts, which mostly fall in the nano regime [127]. Based on this, MNPs have shown diversified applications in different fields of science.

1.5.4. Dielectric Constant properties

A material is said to be a dielectric material when it behaves like an insulator because of the high value of specific resistance and negative temperature coefficient of resistance. On applying the electric field to a dielectric material, the polarization occurs, which causes the displacement of charges, making the positive charge be placed along the direction of the exterior field while the negative charge is the opposite. The dielectric constant properties of materials can be explained clearly by Maxwell's theory and Koop's theory based on grain boundaries and grains as a function of frequency [128]. According to both theories, the grain boundaries become active in a lower frequency range, which mostly contributes towards polarization. At the high-frequency range, the grains get activated, which mostly contributes to enhancing the conduction of materials.

Dielectric property explains the energy storing capacity of the material like capacitors. Different reports are there about the dielectric constant of nanomaterials. For example, Kamran et al. synthesized $NiCr_xFe_{2-x}O_4$ nanoparticles by varying Cr

concentration following the sol-gel approach. The frequency-dependent dielectric properties of the materials were studied, confirming that the dielectric constant achieved maximum value for $NiCr_2O_4$ [129]. Devmunde et al. synthesized nickel ferrites following the sol-gel approach to study the effect on dielectric properties of materials with different cadmium concentrations. The results claimed that ferrites followed the trend as predicted by the Maxwell Wagner hypothesis [130]. Pankaj et al. claimed the synthesis of manganese ferrite nanoparticles by a PVP-assisted auto combustion method. The dielectric properties of manganese ferrite materials were confirmed within the frequency range of (20 KHz–2 MHz) at a temperature variation of (100 K - 400 K), the dielectric properties were observed to follow the Maxwell-Wagner hypothesis. [131].

1.6. Catalytic Applications of Metal Chalcogenides

As discussed in Section 1.5.2 (Table 1.1), Catalysis is the most potent application of nanomaterials. Nanomaterials as catalysts are classified as homogeneous and heterogeneous catalysts. Homogeneous catalysts are limited because of their non-recoverability from the reaction mixture after catalysis, while heterogeneous catalysts can be recovered easily and environmentally benign [132]. The metal chalcogenides (MCs) are regarded as one of the best catalytic materials in photovoltaic conversion, water oxidation, dye degradation, organic transformations. As quantum dots, MCs show excellent optical absorption properties and absorb easily in the visible region [133]. Different substrates were also used to synthesize metallic or transition metal-based heterogeneous catalysts explicitly to enhance catalytic activities, e.g., carbon [142], nickel foam [134], silica [135], graphene oxide [136], and polymers [137]. Some of the superior catalytic performances of metal chalcogenides are discussed in the following sections.

1.6.1. Photooxidation and Reduction of dyes and Cr(VI)

As discussed above to overcome water pollution different approaches were adopted like adsorption [138], chlorination [139], coagulation [140], ion flotation [141], membrane process [142], and sedimentation [143]. However, these were with the disadvantage that the process was not complete in a one-go. It is needed to be further purified by another

step leading to the complexity of the processes. So the search for the development of new approaches involving oxidation or reduction processes like biodegradation [144], Fenton [145], photofenton [146], photocatalytic [147], ozonation [148]. Among these, the most compatible technique is using photocatalysts.

A nanocatalyst has a higher surface area than bulk materials, which directly influences the photocatalysis by providing an ample amount of active sites. The overall mechanism responsible for the degradation of pollutants involving photocatalysis is shown in scheme 1.31. In general, when a photocatalyst interacts with the light, photogenerated charge carriers like electrons and holes are produced. These charge carriers interact with the dissolved oxygen and H_2O to produce peroxide $O^{2\bullet-}$ and hydroxide $OH^{\bullet}$ radicals, respectively. The active radicals target the pollutants (organic dyes or inorganic chemicals), which finally led to its decomposition [149].

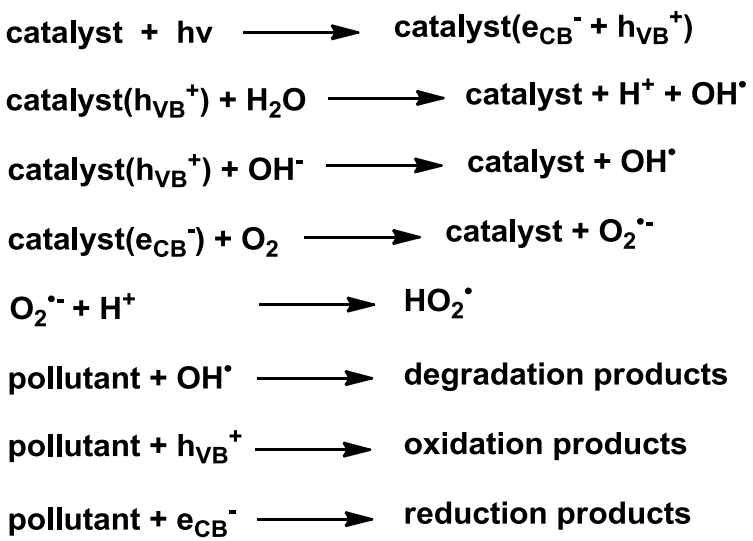

Scheme 1.31. Schematic representation of mechanism involving detoxification of dyes and Cr(VI) reduction.

Yating et al. synthesized heterojunction between WO_3 and CuS as (WO_3@CuS). The composite materials with sheet-like morphology performed well in the detoxification of dyes and inorganic chemicals [150]. Wang et al. claimed the synthesis of a heterojunction between CoS_2/gC_3N_4-rGO by the solvothermal method. The composites served the purpose of a photocatalyst for Cr(VI) reduction reactions [151]. Arif et al. claimed the

heterojunction formation of Ni−Co−S/SDS using the aqueous phase as a solvent. The composites immensely helped in the neutralization of dyes and Cr(VI) [152]. Daljit et al. claimed the synthesis of tin selenide/tin oxide heterojunction using the co-precipitation method. The materials played a better photocatalytic role in the neutralization of toxic dyes like RhB and MB dyes [153].

1.6.2. 4-Nitrophenol Reduction

When present in excess, some of the aromatic compounds are toxic and considered pollutants. For example, 4-nitrophenol (4-NP) has been declared by a US-based ecological safeguard organization as the most common contaminant from the aromatic family [154]. So its conversion to less toxic and useful compounds like aminophenol and the strategies by which this kind of conversion is possible is the demand of time [155]. Various approaches were established time by time for 4-NP reduction, e.g., degradation by microbes [156], electro-fenton method [157], degradation by photocatalysts [158], electrochemical approaches [159]. In these techniques, overall catalysts played a dominant role because of its excellent properties like high surface area and a higher number of active sites. Still, these methods have faults which hamper their further usage like the agglomeration of nanoparticles [160].

The transformation of 4-NP to 4-AP was explained by using the Langmuir-Hinshellwood model. According to this mechanism, at first, sodium borohydride gets activated into borohydride ion by transferring its hydrogen on the catalyst's surface. In this mixture of three components, the catalyst's surface also acts as a base for the 4-NP adsorption and $NaBH_4$. The adsorption of both the sodium borohydride and its activation to borohydride ion and 4-NP adsorption on the catalyst surface is reversible and fast. Hydrogen atoms released by $NaBH_4$ on the catalyst's surface get attracted to the 4-NP resulting in the reduction of 4-NP to 4-AP [161]. This step is fast and hence a rate-determining step. After the completion of the reaction and 4-AP formation, the desired product leaves the catalyst surface (Figure 1.10).

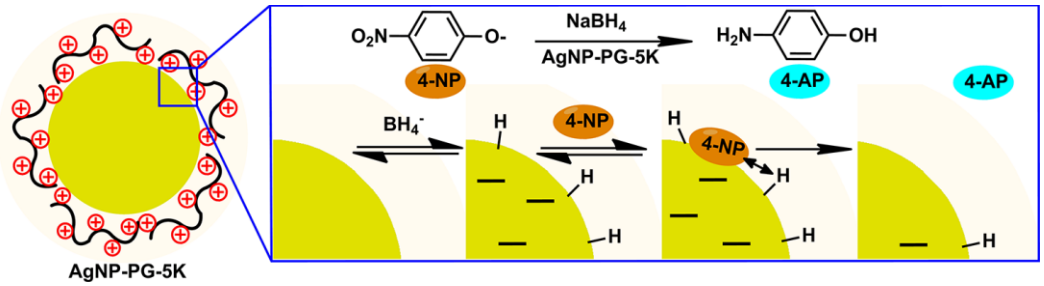

Figure 1.10. Mechanism for 4-NP reduction to 4-AP [162].

Some important reports about the 4-nitrophenol reduction to 4-aminophenol by different literatures is exemplified as follows:

Sukanya et al. successfully synthesized chromium selenide nanomaterials using hydrothermal approach. The chromium selenide nanomaterials electrocatalytically resulted in the reduction of 4-NP to 4-AP [163].

Zhang et al. synthesized cobalt selenide nanomaterials using surfactant assisted solvothermal method. The nanocatalysts having bundle like morphology served as better catalysts for 4-nitrophenol reduction to 4-aminophenol [164].

Azam et al. synthesized cadmium sulphide nanomaterials using a single source precursor. The materials with nanosheet and nanorod like morphology showed better performance for 4-nitrophenol reduction [165].

Yuxiao et al. claimed the synthesis of a biphasic molybdenum sulphide heterostructure consisting of a 1-T and 1-H phase by hydrothermal approach. It is a composite with silicon carbide (MoS_2/SiC) consisting of two phases of molybdenum sulphide resulted in superior photocatalysis of 4-nitrophenol reduction. [166].

1.6.3. Electrochemical Water splitting (oxygen evolution reaction-OER)

Water splitting consists of two main reactions hydrogen evolution reaction (HER) and oxygen evolution reaction (OER). The hydrogen evolved could serve as the efficient and cleanest fuel for energy purposes and as a substitute for renewable energy sources. It involves two important electrode systems-cathode at which HER takes place and anode at which OER finds its route [167]. Mostly noble metals like Pt, Ir, and Ru were designated

to be superior electrocatalysts for water-splitting, but being cost-effective, less in abundance, and lesser stability has put a barrier in their practical applications [168]. An excellent electrocatalyst should be cheaper, abundantly available, stable, working as a bifunctional electrocatalyst in both the acidic and basic mediums [168, 169]. Electrocatalytic OER is typically a complex process because it involves the transfer of four electrons and the creation of O-O linkage, and it requires excess potential than the theoretical potential of 1.23 V relative to normal hydrogen electrode. At the same time, HER is a two-electron transfer process [170]. OER is defined as the oxidation process involving water and hydroxyl moieties as depicted by the following equations:

$$2H_2O \longleftrightarrow O_2 + 4H^+ + 4e^- \quad \text{(acidic medium)}$$

$$4OH^- \longleftrightarrow O_2 + 2H_2O + 4e^- \quad \text{(basic medium)}$$

The mechanistic illustration of 4- electron process involved in OER pathways is shown in Figure 1.11.

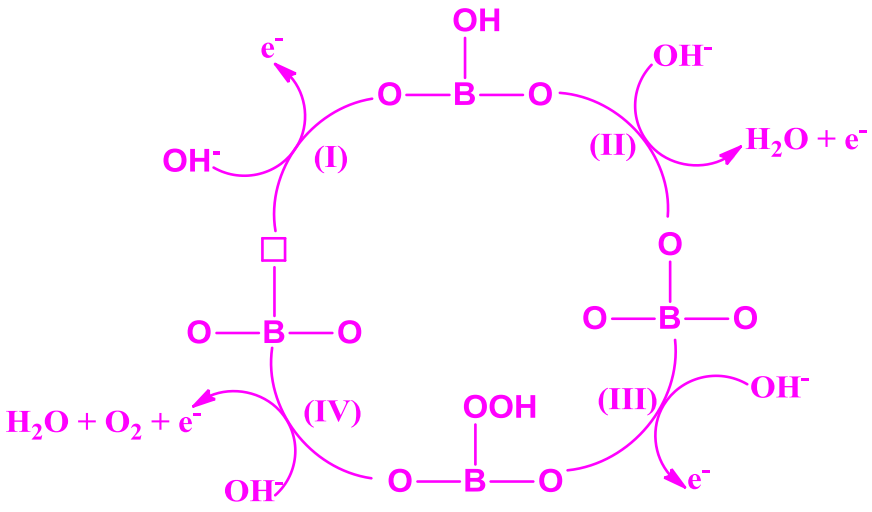

Figure 1.11. Illustration of 4-step electron process involved in OER in an alkaline medium [171].

Some important reports about the electrochemical OER performance by different literatures are exemplified as follows:

Yecan et al. synthesized 3D superstructures of iridium, wherein each structures were built of ultrathin nanosheets of iridium as an excellent electrocatalyst for oxygen evolution reaction with low onset potential [172].

Xuan et al. synthesized NiFeS nanomaterials using precursors of Prussian blue analogues by hydrothermal method with sea urchin morphology and that worked as superior electrocatalysts for OER functioning [173].

Luo et al. successfully produced copper cobalt sulphide using carbon cloth as substrate, which showed good OER performance for water splitting with a minimum overpotential of 276 mV @10 mA cm^{-2} [174]

Zhou et al. successfully synthesized iron doped cobalt sulphide using a hydrothermal method which worked as best electrocatalyst for water oxidation with minimum overpotential of 290 mV [175].

1.7. Scope of Thesis

1.7.1. Definition of problem

Careful scanning of all synthetic procedures reported in section 1.4 reveals that some organic or polymeric molecules are added to control the particle size while synthesizing the nanoparticle. These organic surfactant molecules are known by distinctive names such as stabilizers, passivating agents, and protecting agents. These molecules play a significant role during the synthesis of nanoparticles by way of protecting the surfaces. They also prevent the uncontrollable oxidation of nanomaterials, control the particle size, prevent the particle growth rate, and allow the particle soluble in various solvents. These organic molecules surrounding the particles as capping, and they are not removed entirely after the reaction, or at least some part of it is retained. These residual substances, i.e., the materials other than the active compounds, create an inorganic-organic interface. These intimate interfaces influence the properties of the materials and subsequently, the applications [176]. E.g., they prevent the interfacial electron transfer or reduce the charge mobility, or blocks the active sites present on the surface of materials, hence significantly affects its catalytic properties [177].

1.7.2. Hexamethyldisilazane (HMDS) assisted synthetic method

To circumvent the problem of unwanted organic moieties with active inorganic nanomaterials, our group members earlier developed a surfactant-free scheme to synthesize colloidal nanocrystals. The method involves using hexamethyldisilazne (HMDS) (Figure 1.12), which serves not only the sole purpose of being a reaction medium but also a reductant and a stabilizing agent.

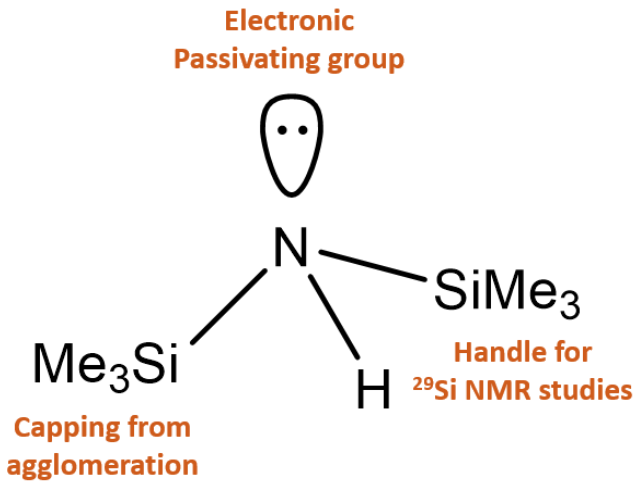

Figure 1.12. The structure of Hexamethyldisilazane (HMDS).

The metal precursors were mostly taken in the form of chlorides because they have better solubility in HMDS, while powder of S, Se, or thiourea was used to form chalcogenides. This reaction was identified to pass through the formation of polymeric $[SN(SiMe_3)]_x$ as an intermediate. These trimethylsilyl groups help in the formation of active metal ions by forming trimethylhalide. It was also observed that the presence of trimethylsilyl helps to prevent the aggregation of nanoparticles during the reaction. The reaction is carried under inert conditions because HMDS is sensitive to moisture (Scheme 1.32).

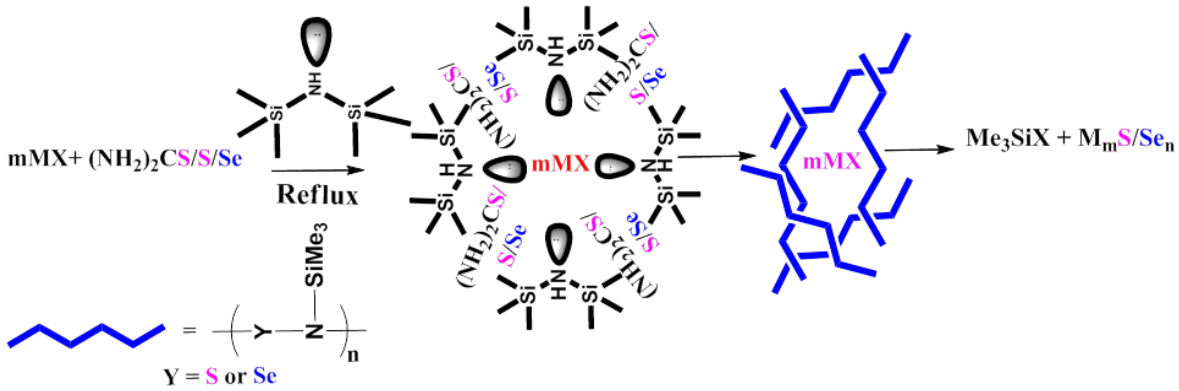

Scheme 1.32. The general reaction sequence of HMDS-assisted synthesis to produce nanomaterials.

Some of the important reactions carried using HMDS–assisted synthetic method produce different kinds of metal chalcogenide nanocrystals are discussed as follows. Our group members have synthesized copper sulphide microflowers without any organic part using the HMDS method (scheme 1.33). The microflowers were formed due to the self-assemblage of copper sulphide nanoflakes. The reaction passes through the S-N transitional formation stage, which leads to the development of copper sulphide microflowers. This intermediate helps in the formation of CuS microflowers by eliminating trimethylsilyl chloride [178].

Similarly, CdS nanoparticles were successfully synthesized (scheme 1.34) without an external surfactant's involvement by the HMDS approach. These nanomaterials worked as photocatalysts to eliminate the toxicity of Cr(VI) by converting it to Cr(III) [179]. Later, the method was extended to synthesize a heterostructure between silver and silver sulphide (scheme 1.35). These heterodimers were formed in a single step reaction [180].

$$CuCl_2 + \text{sulfur} + \text{HMDS} \xrightarrow[6\ h,\ N_2\ atm]{\text{reflux}} \text{CuS NPs}$$

Scheme 1.33: Synthesis of copper sulphide nanoparticles

$$CdCl_2 + (NH_2)_2CS + \text{HMDS} \xrightarrow[3\ h,\ N_2\ atm]{\text{reflux}} \text{CdS NPs}$$

Scheme 1.34: Synthesis of cadmium sulphide nanoparticles

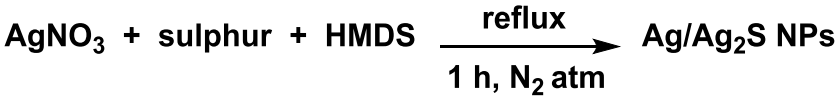

Scheme 1.35: Synthesis of silver-silver sulphide heterodimers

Apart from the binary metal chalcogenides, the HMDS-assisted method was useful for producing different stoichiometric variations. The surfactant-free Ni_3S_4 nanoparticles were prepared through the HMDS synthetic approach (scheme 1.36), and it was evaluated for its catalytic role in the transformation of organic nitroarenes with hydrazine [181]. Bismuth sulphide was also produced by the same approach and studied for its photoresponsive behavior (scheme 1.37) [182].

Scheme 1.36: Synthesis of nickel sulphide nanoparticles

Scheme 1.37: Synthesis of bismuth sulphide nanoparticles

1.7.3. Aim of the present work

Many binary and a few ternary metal chalcogenides have been produced in our lab. Those materials were evaluated for their various applications and performed better as a catalyst or photoresponsive materials. In this present work, using the HMDS-assisted synthetic approach, we have been able to synthesize many binary, ternary metal chalcogenides as well as composites with superior catalytic properties. In all these reactions, HMDS itself played the sole role as a reaction medium, a stabilizing agent, and a reductant, so no external stabilizers are added. By washing the materials with organic solvents and applying vacuum after completing the reaction, we could annihilate the residual impurities of precursors and HMDS from our reaction mixtures.

In this present work, by using one pot HMDS-assisted approach, we are successful in synthesizing various highly crystalline and high purity grade nanomaterials like SnS2 (with and without surfactant polyethylene glycol-PEG), CuS/CdS heterojunctions by

varying the concentration of cadmium precursor, chalcopyrite-$CuFeS_2$, and two novel cobalt-based chalcogenides-$Co_{0.8}Fe_{0.2}S_2$ and $Co_{0.8}Fe_{0.2}Se_2$ as illustrated in Figure 1.13. All these heterojunctions synthesized are evaluated for their role in catalytic processes. The nanomaterials synthesized by the HMDS approach have shown great enhancement in their properties. Herein, we are reporting photocatalytic dye degradation (RhB, MB, and MO), reduction of Cr(VI), 4-nitrophenol reduction, and electrochemical water splitting for oxygen evolution reaction, where the surfactant-free nanomaterials catalyze all these reactions.

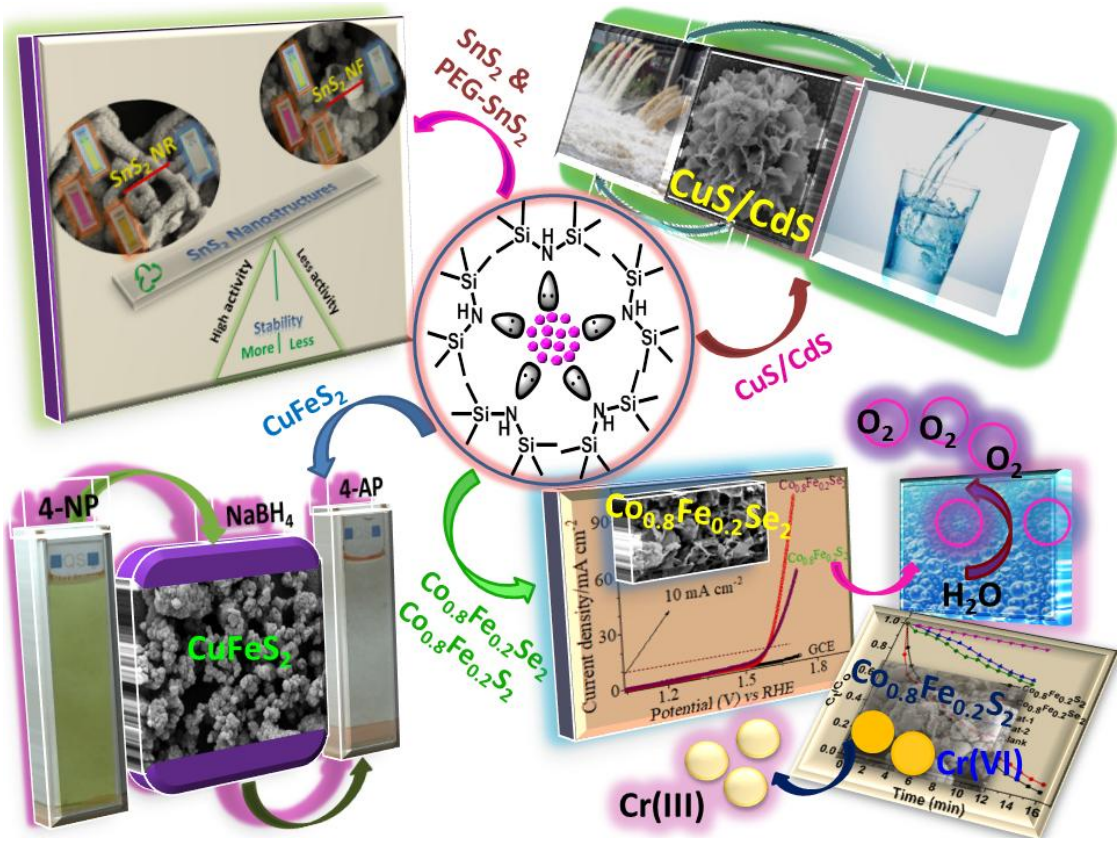

Figure 1.13. Illustration of the synthesis of various nanomaterials synthesized by HMDS-assisted method.

1.8. References

[1] (a) Crooks, R. M.; Zhao, M.; Sun, L.; Chechik, V.; Yeung, L. K. Dendrimer-encapsulated metal nanoparticles: Synthesis, characterization, and applications to

catalysis. *Acc. chem. Res*. **2001**, *34*, 181-190. (b) Murphy, C. J.; Sau, T. K.; Gole, A. M.; Orendorff, C. J.; Gao, J.; Gou, L.; Hunyadi, S. E.; Li, T. Anisotropic metal nanoparticles: synthesis, assembly, and optical applications. *J. Phys. Chem. B* **2005**, *109*, 13857-13870. (c) Chandra, S.; Kumar, A.; Tomar, P. K. Synthesis of Ni nanoparticles and their characterizations. *J. Saudi Chem. Soc.* **2014,** *18*, 437–442. (d) Park, B.; Cho, K.; Yun, J.; Koo, Y. S.; Lee, J. H.; Kim, S. Electrical Characteristics of Floating-Gate Memory Devices with Titanium Nanoparticles Embedded in Gate Oxides. *J. Nanosci. Nanotechnol.* **2009**, *9*, 1904–1908. (e). Figueira, C. E.; Junior, P. F. M.; Giudici, R.; Alves, R. M. B.; Schmal, M. Nanoparticles of Ce, Sr, Co in and out the multi-walled carbon nanotubes applied for dry reforming of methane. *Appl. Catal. A: Gen*. **2018**, *550*, 297-307.

[2] (a) Qi, L.; Colfen, H.; Antonietti, M. Synthesis and Characterization of CdS Nanoparticles Stabilized by Double-Hydrophilic Block Copolymers. *Nano Letters* **2001**, *1*, 61–65. (b) Pathak, C. S.; Mandal, M. K.; Agarwal, V. Synthesis and characterization of zinc sulphide nanoparticles prepared by mechanochemical route. *Superlattices and Microstructures* **2013**, *58*, 135–143. (c) Haram, S. K.; Mahadeshwar, A. R.; Dixit, S. G. Synthesis and characterization of copper sulfide nanoparticles in Triton-X 100 water-in-oil microemulsions. *J. Phys. Chem.* **1996**, *100*, 5868-5873. (d) Dutta, A. K.; Maji, S. K.; Srivastava, D. N.; Mondal, A.; Biswas, P.; Paul, P.; Adhikary, B. Synthesis of FeS and FeSe nanoparticles from a single source precursor: A study of their photocatalytic activity, peroxidase-like behavior, and electrochemical sensing of H_2O_2. *ACS Appl. Mater. Interfaces* **2012**, *4*, 1919-1927. (e) Niasari, M. S.; Monfared, G. B.; Emadi, H.; Enhessari, M. Synthesis and characterization of nickel sulfide nanoparticles via cyclic microwave radiation. *Comptes Rendus Chimie* **2013**, *16*, 929–936.

[3] (a) Uekawa, N.; Kajiwara, J.; Kakegawa, K.; Sasaki, Y. Low temperature synthesis and characterization of porous anatase TiO_2 nanoparticles. *J. Colloid Interface Sci*. **2002**, *250*, 285–290. (b) Retama, J. R.; Zafeiropoulos, N. E.; Serafinelli, C.; Reyna, R. R.; Voit, B.; Cabarcos, E. L.; Stamm, M. Synthesis and characterization of thermosensitive PNIPAM microgels covered with superparamagnetic γ-Fe_2O_3 nanoparticles. *Langmuir*

2007, *23*, 10280-10285. (c) Sahooli, M.; Sabbaghi, S.; Saboori, R. Synthesis and characterization of mono sized CuO nanoparticles. *Mater. Lett.* **2012**, *81*, 169-172.

[4] (a) Xiao, J.; Xie, Y. ; Tang, R.; Qian, Y. Synthesis and characterization of ternary $CuInS_2$ nanorods via a hydrothermal route. *J. Solid State Chem*. **2001**, *161*, 179-183. (b) Bhattacharyya, B.; Pandey, A. $CuFeS_2$ quantum dots and highly luminescent $CuFeS_2$ based core/shell structures: Synthesis, tunability, and photophysics. *J. Am. Chem. Soc*. **2016**, *138*, 10207−10213. (c) Li, Z.; Ji, X.; Han, J.; Hu, Y.; Guo, R. $NiCo_2S_4$ nanoparticles anchored on reduced graphene oxide sheets: In-situ synthesis and enhanced capacitive performance. *J. Colloid Interface Sci.* **2016**, 477, 46–53.

[5] (a) Yu, J.; Zhang, J.; Liu, S. Ion-Exchange synthesis and enhanced visible light photoactivity of Cus/ZnS nanocomposite hollow spheres. *J. Phys. Chem. C* **2010**, *114*, 13642-13649. (b) Zhang, L.; Xie, T.; Wang, D.; Li, S.; Wang, L.; Chen, L.; Lu, Y. Noble-Metal free CuS/CdS composites for photocatalytic H_2 evolution and its photogenerated charge transfer properties. *Int. J. Hydrogen Energy* **2013**, *38*, 11811-11817. (c) Qi, L.; Ma, J.; Cheng, H.; Zhao, Z. Synthesis and characterization of mixed Cd/ZnS nanoparticles in reverse micelles. *Colloids and Surfaces A: Physicochem. Eng. Aspects* **1996**, *111*, 195-202.

[6] (a) Guo, C. X.; Yilmaz, G.; Chen, S.; Chen, S.; Lu, X. Hierarchical nanocomposite composed of layered V_2O_5/PEDOT/MnO_2 nanosheets for high-performance asymmetric supercapacitors. *Nano Energy* **2015**, *12*, 76-87. (b) Moussa, M.; Shi, G.; Wu, H.; Zhao, Z.; Voelcker, N.; Losic, D.; Ma, J. Development of flexible supercapacitors using an inexpensive graphene/PEDOT/MnO_2 sponge composite. *Materials & Design* **2017**, *125*, 1-10. (c) Hu, X.; Shen, Y.; Lu, L.; Xu, J.; Zhen, J. Enhanced electromagnetic interference shielding effectiveness of ternary PANI/CuS/rGO composites. *J. Mater. Sci.: Mater. Electron.* **2017**, *28*, 6865-6872.

[7] (a) Matthews, J.; Boland, E.; Wnek, G.; Simpson, D.; Bowlin, G. Electrospinning of collagen Type II: A feasibility study. *J. Bioactive and Compatible Poly*. **2003**, *18*, 125-134. (b) Huang, Z.; Zhang, Y.; Ramakrishna, S.; Lim, C. Electrospinning and mechanical characterization of gelatin nanofibers. *Polymer* **2004**, *45*, 5361-5368. (c) Zambuzzi, W.;

Ferreira, C.; Granjeiro, J.; Aoyama, H. Biological behavior of pre-osteoblasts on natural hydroxyapatite: A study of signaling molecules from attachment to differentiation. *J. Biomed. Mater. Res. Part A* **2011**, *97A*, 193-200. (d) Terrones, M. Carbon nanotubes: Synthesis and properties, electronic devices and other emerging applications. *Int. Mater. Rev*. 2004, *49*, 325-377. (e). Popov, V. N. Carbon nanotubes: Properties and application. *Mater. Sci. Eng. R* **2004**, *43*, 61–102.

[8] (a) Boyjoo, Y.; Pareek, V.; Liu, J. Synthesis of micro and nano-sized calcium carbonate particles and their applications. *J. Mater. Chem. A* **2014**, *2*, 14270-14288. (b) Koo, A.N.; Min, K.H.; Lee, H.J.; Jegal, J.H.; Lee, J.W.; Lee, S. C. Calcium carbonate mineralized nanoparticles as an intracellular transporter of cytochromec for cancer therapy. *Chem. Asian J.* **2015**, *10*, 2380–2387. (c) Dizaj, S. M.; Jalali, M. B.; Zarrintan, M.; Adibkia, K.; Lotfipour, F. Calcium carbonate nanoparticles as cancer drug delivery system. *Expert Opinion on Drug Delivery* **2015**, *12*, 1649-1660. (d) Hua, K. H.; Wang, H. C.; Chung, R. S.; Hsu, J. C. Calcium carbonate nanoparticles can enhance plant nutrition and insect pest tolerance. *J. Pestic. Sci*. **2015**, *40*, 208–213.

[9] (a) Sun, R.; Yin, L.; Zhang, S. H.; He, L.; Cheng, X. J.; Wang, A. N.; Xia, H. W.; Shi, H. B. Simple light-triggered fluorescent labeling of silica nanoparticles for cellular imaging applications. *Chem. Eur. J*. **2017**, *23*, 13893–13896. (b) Xu, Z. G.; Ma, X. Q.; Gao, Y. E.; Hou, M. L.; Xue, P.; Li, C. M.; Kang, Y. J. Multifunctional silica nanoparticles as a promising theranostic platform for biomedical applications. *Mater. Chem. Front.* **2017**, *1*, 1257–1272. (c) Liu, X. N.; Lu, X. R.; Wen, P.; Shu, X. Y.; Chi, F. T. Synthesis of ultrasmall silica nanoparticles for application as deep-ultraviolet antireflection coatings. *Appl. Surf. Sci*. **2017**, *420*, 180–185. (d) Bergin, I. L.; Witzmann, F. A. Nanoparticle toxicity by the gastrointestinal route: Evidence and knowledge gaps. *Int. J. Biomed. Nanosci. Nanotechnol*. **2013**, *3*, 163–210.

[10] Park, Y.; Mohan, K.; Al-Sanousi, A.; Almaghrabi, B.; Genco, R.; Swihart, M.; Dziak, R. Synthesis and characterization of nanocrystalline calcium sulfate for use in osseous regeneration. *Biomed. Mater*. **2011**, *6*, 055007.

[11] (a) Setiawan, H.; Khairani, R.; Rahman, M. A.; Septawendar, R.; Mukti, R. R.; Dipojono, H. K.; Purwasasmita, B. S. Synthesis of zeolite and gamma-alumina nanoparticles as ceramic membranes for desalination applications. *J. Aus. Ceram. Soc*. **2017**, *53*, 531–538. (b) Singh, I. B.; Gupta, A.; Dubey, S.; Shafeeq, M.; Banerjee, P.; Sinha, A. S. K. Sol-gel synthesis of nanoparticles of gamma alumina and their application in defluoridation of water. *J. Sol-Gel Sci. Technol*. **2016**, *77*, 416–422. (c) Nazari, A.; Sanjayan, J. G. Hybrid effects of alumina and silica nanoparticles on water absorption of geopolymers: Application of Taguchi approach. *Measurement* **2015**, *60*, 240–246.

[12] Won, Y.; Stanciu, L. Cu_2O and Au/Cu_2O Particles: Surface properties and applications in glucose sensing. *Sensors* **2012**, *12*, 13019-13033.

[13] Wang, A.; Kong, X. Review of recent progress of plasmonic materials and nano-structures for surface enhanced Raman scattering. *Materials* **2015**, *8*, 3024-3052.

[14] O'Dwyer, C.; Lavayen, V.; Newcomb, S.; Benavente, E.; Santa Ana, M.; González, G.; Sotomayor Torres, C. Atomic layer structure of vanadium oxide nanotubes grown on nanourchin structures. *Electrochem. Solid-State Lett*. **2007**, *10*, A111.

[15] Wang, C.; Yu, C. Detection of chemical pollutants in water using gold nanoparticles as sensors: A review. *Rev. Analyt. Chem.* **2013**, *32*, 1-14.

[16] Guidelli, E.; Baffa, O.; Clarke, D. R. Enhanced UV emission from silver/ZnO and gold/ZnO core-shell nanoparticles: Photoluminescence, radioluminescence, and optically stimulated luminescence. *Scientific Reports* **2015**, *5*, 14004.

[17] Dac Dien, N. Preparation of various morphologies of ZnO nanostructure through wet chemical methods. *Adv. Mater. Sci.* **2019**, *4*, 1- 5.

[18] Barua, S.; Yoo, J.; Kolhar, P.; Wakankar, A.; Gokarn, Y.; Mitragotri, S. Particle shape enhances specificity of antibody-displaying nanoparticles. *Proceedings of the National Academy of Sciences* **2013**, *110*, 3270-3275.

[19] Gleiter, H. Nanostructured materials: Basic concepts and microstructure. *Acta Mater*. **2000**, *48*, 1-29.

[20] Tiwari, J.; Tiwari, R.; Kim, K. Zero-dimensional, one-dimensional, two-dimensional and three-dimensional nanostructured materials for advanced electrochemical energy devices. *Prog. Mater. Sci*. **2012**, *57*, 724-803.

[21] Pokropivny, V.; Skorokhod, V. Classification of nanostructures by dimensionality and concept of surface forms engineering in nanomaterial science. *Mater. Sci. Eng.: C* **2007**, *27*, 990-993.

[22] Power, A.; Gorey, B.; Chandra, S.; Chapman, J. Carbon nanomaterials and their application to electrochemical sensors: A review. *Nanotechnol. Rev.* **2018**, *7*, 19-41.

[23] (a) Zhang, B.; Zheng, X.; Li, H.; Lin, J. Application of carbon-based nanomaterials in sample preparation: A review. *Analytica Chimica Acta* **2013**, *784*, 1-17. (b) Scida, K.; Stege, P.; Haby, G.; Messina, G.; García, C. Recent applications of carbon-based nanomaterials in analytical chemistry: Critical review. *Analytica Chimica Acta* **2011**, *691*, 6-17.

[24] Dreaden, E.; Alkilany, A.; Huang, X.; Murphy, C.; El-Sayed, M. The golden age: Gold nanoparticles for biomedicine. *Chem. Soc. Rev.* **2012**, *41*, 2740-2779.

[25] Yadav, T. P.; Yadav, R. M.; Singh, D. P. Mechanical milling: A top down approach for the synthesis of nanomaterials and nanocomposites. *Nanoscience and Nanotechnology* **2012**, *2*, 22-48.

[26] Ibanez, M.; Zamani, R.; Gorsse, S.; Fan, J.; Ortega, S.; Cadavid, D.; Morante, J.; Arbiol, J.; Cabot, A. Core–shell nanoparticles as building blocks for the bottom-up production of functional nanocomposites: PbTe–PbS thermoelectric properties. *ACS Nano* **2013**, *7*, 2573-2586.

[27] Eychmüller, A. Aerogels from semiconductor nanomaterials. *Angew. Chem. Int. Ed.* **2005**, *44*, 4839-4841.

[28] Suresh, S. Semiconductor nanomaterials, methods and applications: A review. *Nanoscience and Nanotechnology* **2013**, *3*, 62-74.

[29] (a) Seery, M.; George, R.; Floris, P.; Pillai, S. Silver doped titanium dioxide nanomaterials for enhanced visible light photocatalysis. *J. Photochem. Photobiol. A: Chemistry* **2007**, *189*, 258-263. (b) Wu, W.; Jiang, C. C.; Roy, V. Recent progress in magnetic iron oxide–semiconductor composite nanomaterials as promising photocatalysts. *Nanoscale* **2015**, *7*, 38-58. (c) Wang, W.; Zhu, Y.; Yang, L. ZnO–SnO_2 hollow spheres and hierarchical nanosheets: Hydrothermal preparation, formation mechanism, and photocatalytic properties. *Adv. Funct. Mater*. **2007**, *17*, 59–64. (d) Wang, X.; Liu, G.; Wang, L.; Chen, Z. G.; Lu, G. Q.; Cheng, H. M. ZnO-CdS@Cd heterostructure for effective photocatalytic hydrogen generation. *Adv. Energy Mater.* **2011**, *2*, 42–46.

[30] (a) Harvey, T. B.; Mori, I.; C. Stolle, J.; Bogart, T. D.; Ostrowski, D. P.; Glaz, M. S.; Du, J.; Pernik, D. R.; Akhavan, V. A.; Kesrouani, H.; Vanden Bout, D. A.; Korgel, B. A. Copper indium gallium selenide (CIGS) photovoltaic devices made using multistep selenization of nanocrystal films. *Appl. Mater. Interface* **2013**, *5*, 9134−9140. (b) Bashir, A.; Shukla, S.; Lew, J.; Shukla, S.; Bruno, A.; Gupta, D.; Baikie, T.; Patidar, R.; Akhter, Z.; Priyadarshi, A.; Mathews, N.; Mhaisalkar, S. G. Spinel Co_3O_4 nanomaterials for efficient and stable large area carbon-based printed perovskite solar cells. *Nanoscale* **2018**, *10*, 2341-2350. (c) Kulbak, M.; Cahen, D.; Hodes, G. How important is the organic part of lead halide perovskite photovoltaic cells? Efficient $CsPbBr_3$ cells. *J. Phys. Chem. Lett*. **2015**, *6*, 2452−2456. (d) Zhang, M.; Lyu, M.; Yu, H.; Yun, J.; Wang, Q.; Wang, L. Stable and low-cost mesoscopic $CH_3NH_3PbI_2Br$ perovskite solar cells by using a thin Poly(3-Hexylthiophene) layer as a hole transporter. *Chem. Eur. J*. **2015**, *21*, 434 – 439.

[31] (a) Chen, G.; Wang, W.; Wang, C.; Ding, T.; Yang, Q. Controlled synthesis of ultrathin Sb_2Se_3nanowires and application for flexible photodetectors. *Adv. Sci.* **2015**, *2*, 1500109. (b) Xie, X.; Kwok, S.Y.; Lu, Z.; Liu, Y.; Cao, Y.; Luo, L.; Zapien, J. A.; Bello, I.; Lee, C.S.; Lee, S. T.; Zhang, W. Visible–NIR photodetectors based on CdTe nanoribbons. *Nanoscale* **2012**, *4*, 2914. (c) Wu, J. M.; Kuo, C. H. Ultraviolet photodetectors made from SnO_2 nanowires. *Thin Solid Films* **2009**, *517*, 3870-3873. (d) Lan, C.; Li, C.; Yin, Y.; Guo, H.; Wang, S. Synthesis of single-crystalline GeS nanoribbons for high sensitivity visible-light photodetectors. *J. Mater. Chem. C* **2015**, *3*,

8074—8079. (e) Lan, C.; Zhou, Z.; Zhou, Z.; Li, C.; Shu, L.; Shen, L.; Li, D.; Dong, R.; Yip, S.; Ho, J. Wafer-scale synthesis of monolayer WS_2 for high-performance flexible photodetectors by enhanced chemical vapor deposition. *Nano Res*. **2018**, *11*, 6, 3371–3384. (f) Shao, D.; Yu, M.; Sun, H.; Hu, T.; lian, J.; Sawyer, S. High responsivity, fast ultraviolet photodetector fabricated from ZnO nanoparticle graphene core–shell structures. *Nanoscale* **2013**, *5*, 3664–3667. (g) Yu, S. H.; Lee, X. Y.; Jang, X. S. K.; Kang, X. J.; Jeon, J.; Lee, C.; Lee, J. Y.; Kim, H.; Hwang, E.; Lee, S.; Cho, J. H. Dye-sensitized MoS_2 photodetector with enhanced spectral photoresponse. *ACS Nano* **2014**, *8*, 8285-8291.

[32] (a) Bai, J.; Zhou, B. Titanium dioxide nanomaterials for sensor applications. *Review* **2014**, *114*, 10131−10176. (b) Holt-Hindle, P.; Nigro, S.; Asmussen, M.; Chen, A. Amperometric glucose sensor based on platinum–iridium nanomaterials. *Electrochem. Commun.* **2008**, *10*, 1438-1441. (c) Ding, Y.; Liu, Y.; Parisi, J.; Zhang, L.; Lei, Y. A novel NiO–Au hybrid nanobelts based sensor for sensitive and selective glucose detection. *Biosensors and Bioelectronics* **2011**, *28*, 393-398. (d) Lu, D.; Zhang, Y.; Lin, S.; Wang, L.; Wang, C. Synthesis of PtAu bimetallic nanoparticles on graphene–carbon nanotube hybrid nanomaterials for nonenzymatic hydrogen peroxide sensor. *Talanta* **2013**, *112*, 111-116. (e) Huang, F.; Zhong, Y.; Chen, J.; Li, S.; Li, Y.; Wang, F.; Feng, S. nonenzymatic glucose sensor based on three different CuO nanomaterials. *Analytical Methods* **2013**, *5*, 3050. (f) Lee, T.; Lee, W.; Kim, S.; Kim, J.; Kim, B. Flexible textile strain wireless sensor functionalized with hybrid carbon nanomaterials supported ZnO nanowires with controlled aspect ratio. *Adv. Funct. Mater.* **2016**, *26*, 6206–6214.

[33] (a) Ramadoss, M.; Chen, Y.; Hu, Y.; Li, W.; Wang, B.; Zhang, X.; Wang, X.; Yu, B. Three-Dimensional Ni/Ni_3Fe embedded boron doped carbon nanotubes nanochain frameworks as highly efficient and durable electrocatalyst for oxygen evolution reaction. *J. Pow. Sour.* **2020**, *451*, 227753. (b) Jeyagopal, R.; Chen, Y.; Ramadoss, M.; Marimuthu, K.; Wang, B.; Li, W.; Zhang, X. A three-dimensional porous CoSnS@CNT nanoarchitecture as a highly efficient bifunctional catalyst for boosted oer performance and photocatalytic degradation. *Nanoscale* **2020**, *12*, 3879-3887. (c) Shen, M.; Ruan, C.;

Chen, Y.; Jiang, C.; Ai, K.; Lu, L. Covalent Entrapment of Cobalt–Iron Sulfides in N-Doped Mesoporous Carbon: Extraordinary Bifunctional Electrocatalysts for Oxygen Reduction and Evolution Reactions. *Appl. Mater. Interface* **2015**, *7*, 1207−1218.

[34] (a) Haw, C.; Chiu, W.; Abdul Rahman, S.; Khiew, P.; Radiman, S.; Abdul Shukor, R.; Hamid, M.; Ghazali, N. The design of new magnetic photocatalyst nanocomposites ($CoFe_2O_4$–TiO_2) as smart nanomaterials for recyclable photocatalysis applications. *New J. Chem*. **2016**, *40*, 1124—1136. (b) Bharti, D.; Bharati, A. Photocatalytic Degradation of Alizarin Red Dye Under Visible Light Using ZnO & CdO Nanomaterial. *Optik* **2018**, *160*, 371-379. (c) Senasu, T.; Nanan, S. Photocatalytic Performance of Cds Nanomaterials for Photodegradation of Organic Azo Dyes Under Artificial Visible Light and Natural Solar Light Irradiation. *J. Mater. Sci.: Mater. Electron*. **2017**, *28*, 17421–17441. (d) Kulkarni, A. A.; Bhanage, B. M. Ag@AgCl Nanomaterial Synthesis Using Sugar Cane Juice and its Application in Degradation of azo Dyes. *ACS Sustainable Chem. Eng*. **2014**, *2*, 1007−1013.

[35] (a) Kumar, S.; Prasad, K.; Gil, J.; Sobral, A.; Koh, J. Mesoporous zeolite-chitosan composite for enhanced capture and catalytic activity in chemical fixation of CO_2. *Carbohydrate Polymers* **2018**, *198*, 401-406. (b) Liu, G.; Hoivik, N.; Wang, K.; Jakobsen, H. Engineering TiO_2 Nanomaterials for CO_2 Conversion/Solar Fuels. *Solar Energy Materials and Solar Cells* **2012**, *105*, 53-68. (c) Camarillo, R.; Tostón, S.; Martínez, F.; Jiménez, C.; Rincón, J. Enhancing the Photocatalytic Reduction of CO_2 through Engineering of Catalysts with High Pressure Technology: Pd/TiO_2 Photocatalysts. *J. Supercritical Fluids* **2017**, *123*, 18-27. (d) Hu, J.; Galvita, V.; Poelman, H.; Detavernier, C.; Marin, G. A Core-Shell Structured $Fe_2O_3/ZrO_2@ZrO_2$ Nanomaterial with Enhanced Redox Activity and Stability for CO_2 Conversion. *J. CO_2 Utilization* **2017**, *17*, 20-31. (e) Zeng, Z.; Yan, Y.; Chen, J.; Zan, P.; Tian, Q.; Chen, P. Boosting the Photocatalytic Ability of Cu_2O Nanowires for CO_2 conversion by Mxene Quantum Dots. *Adv. Fun. Mater*. **2018**, *29*, 1806500.

[36] (a) Huang, Z.; Meng, G.; Huang, Q.; Chen, B.; Zhu, C.; Zhang, Z. Large-Area Ag Nanorod Array Substrates for SERS: AAO Template-Assisted Fabrication, Functionalization, and Application in Detection PCBs. *J. Raman Spec.* **2012**, *44*, 240-

246. (b) Sun, L.; Zhao, D.; Ding, M.; Zhao, H.; Zhang, Z.; Li, B.; Shen, D. A White Emitting Zno–Au Nanocomposite and its SERS Applications. *Appl. Surf. Sci.* **2012**, *258*, 7813-7819. (c) Stropp, J.; Trachta, G.; Brehm, G.; Schneider, S. A new version of AgFON substrates for high through put analytical SERS applications. *J. Raman Spec.* **2003**, *34*, 26-32. (d) Chen, L.; Yu, J.; Fujita, T.; Chen, M. Nanoporous Copper with Tunable Nanoporosity for SERS Applications. *Adv. Fun. Mater*. **2009**, *19*, 1221–1226.

[37] (a) Yang, Z.; Cao, Y.; Li, J.; Lu, M.; Jiang, Z.; Hu, X. Smart CuS Nanoparticles as Peroxidase Mimetics for the Design of Novel Label-Free Chemiluminescent Immunoassay. *ACS Appl. Mat. Interfaces* **2016**, *8*, 12031-12038. (b) Zare Khafri, H.; Ghaedi, M.; Asfaram, A.; Javadian, H.; Safarpoor, M. Synthesis of CuS and $ZnO/Zn(OH)_2$ Nanoparticles and their Evaluation for in Vitro Antibacterial and Antifungal Activities. *Appl. Org. Chem.* **2018**, *32*, e4398. (c) Zheng, X.; Mo, G.; He, Y.; Qin, D.; Jiang, X.; Mo, W.; Deng, B. An Electrochemiluminescence Immunosensor Based on ZnSe@ZnS QDs Composite for CEA Detection in Human Serum. *J. Electroanal. Chem.* **2019**, *844*, 132-141. (d) Arjunan, N.; Singaravelu, C.; Kulanthaivel, J.; Kandasamy, J. A Potential Photocatalytic, Antimicrobial and Anticancer Activity of Chitosan-Copper Nanocomposite. *Int. J. Bio. Macro.* **2017**, *104*, 1774-1782.

[38] (a) Yin, Z.; Zhang, X.; Cai, Y.; Chen, J.; Wong, J.; Tay, Y. Y.; Chai, J.; Wu, J.; Zeng, Z.; Zheng, B.; Yang, H. Y.; Zhang, H. Preparation of MoS_2-MoO_3 hybrid nanomaterials for light-emitting diodes. *Angew. Chem. Int. Ed. Engl*. **2014**, *53*, 12560-12565. (b) Thang, B. H; Quang, L. D.; Hong, N. M.; Khoi, P. H.; Minh, P. N. Application of Multiwalled Carbon Nanotube Nanofluid for 450 W LED Floodlight. *J. Nanomater*. **2014**, *2014*, 1-6. (c) Shei, S. SILAR-Based Application of Various Nanopillars on GaN-Based LED to Enhance Light-Extraction Efficiency. *J. Nanomater*. **2013**, *2013*, 1-6.

[39] (a) Shu, D.; Cheng, H.; Lv, C.; Asi, M.; Long, L.; He, C.; Zou, X.; Kang, Z. Soft-template synthesis of vanadium oxynitride-carbon nanomaterials for supercapacitors. *Int. J. Hydrogen Energy* **2014**, *39*, 16139-16150. (b) Wang, C.; Zhou, E.; He, W.; Deng, X.; Huang, J.; Ding, M.; Wei, X.; Liu, X.; Xu, X. $NiCo_2O_4$-based supercapacitor nanomaterials. *Nanomaterials* 2017, *7*, 41. (c) Karthikeyan, K.; Kalpana, D.;

Renganathan, N. Synthesis and Characterization of $ZnCo_2O_4$ Nanomaterial for Symmetric Supercapacitor Applications. *Ionics* **2008**, *15*, 107-110. (d) Kim, B. K.; Chabot, V.; Yu, A. Carbon Nanomaterials Supported $Ni(OH)_2$/NiO Hybrid Flower Structure for Supercapacitor. *Electrochim. Acta* **2013**, *109*, 370-380.

[40] (a) Li, W.; Xu, L.; Chen, J. Co_3O_4 Nanomaterials in Lithium-Ion Batteries and Gas Sensors. *Adv. Fun. Mater.* **2005**, *15*, 851-857. (b) Yuan, Y. F.; Tu, J. P.; Wu, H. M.; Li, Y.; Shi, D. Q.; Zhao, X. B. Effect of ZnO Nanomaterials Associated with $Ca(OH)_2$ as Anode Material for Ni–Zn Batteries. *J. Power Sources* **2006**, *159*, 357-360. (c) Zhang, H.; Zhang, X.; Li, H.; Zhang, Y.; Zeng, Y.; Tong, Y.; Zhang, P.; Lu, X. Flexible Rechargeable Ni//Zn Battery Based on Self-Supported $NiCo_2O_4$ Nanosheets with High Power Density and Good Cycling Stability. *Green Energy & Environment* **2018**, *3*, 56-62.

[41] (a) Sridharan, K.; Tamilselvan, V.; Yuvaraj, D.; Narasimha Rao, K.; Philip, R. Synthesis and nonlinear optical properties of lead telluride nanorods. *Opt. Mater.* **2012**, *34*, 639-645. (b) Irimpan, L.; Krishnan, B.; Nampoori, V.; Radhakrishnan, P. Nonlinear optical characteristics of nanocomposites of ZnO–TiO_2–SiO_2. *Opt. Mater.* **2008**, *31*, 361-365. (c) Dehghani, Z.; Nazerdeylami, S.; Saievar-Iranizad, E.; Majles Ara, M. Synthesis and investigation of nonlinear optical properties of semiconductor ZnS nanoparticles. *J. Phy. Chem. Solids* **2011**, *72*, 1008-1010. (d) Li, L.; Lv, R.; Wang, J.; Chen, Z.; Wang, H.; Liu, S.; Ren, W.; Liu, W.; Wang, Y. Optical Nonlinearity of ZrS_2 and Applications in Fiber Laser. *Nanomaterials* **2019**, *9*, 315.

[42] Cui, Y. Functional nanoscale electronic devices assembled using silicon nanowire building blocks. *Science* **2001**, *291*, 851-853.

[43] Huynh, W. U.; Dittmer, J. J.; Alivisatos, A. P. Hybrid Nanorod-Polymer Solar Cells. *Science* **2002**, *295*, 2425-2427.

[44] Tessler, N.; Medvedev, V.; Kazes, M.; Kan, S. H.; Banin, U. Efficient Near-Infrared Polymer Nanocrystal Light-Emitting Diodes. *Science* **2002**, *295*, 1506-1508.

[45] Sundar, V.; Eisler, H.; Bawendi, M. Room Temperature, Tunable Gain Media from Novel II–VI Nanocrystal–Titania Composite Matrices. *Adv. Mater.* **2002**, *14*, 739.

[46] Johnson, J.; Choi, H.; Knutsen, K.; Schaller, R.; Yang, P.; Saykally, R. Single gallium nitride nanowire lasers. *Nat. Mater.* **2002**, *1*, 106-110.

[47] (a) Gao, X.; Cui, Y.; Levenson, R.; Chung, L.; Nie, S. In-vivo cancer targeting and imaging with semiconductor quantum dots. *Nat. Biotechnol.* **2004**, *22*, 969-976. (b) Hansen, J.; Mukhopadhyay, R.; Hansen, J.; Gothelf, K. Femtomolar Electrochemical Detection of DNA Targets Using Metal Sulfide Nanoparticles. *J. Am. Chem. Soc.* **2006**, *128*, 3860-3861.

[48] Wang, M.; Kaplan-Ashiri, I.; Wei, X.; Rosentsveig, R.; Wagner, H.; Tenne, R.; Peng, L. In-situ TEM measurements of the mechanical properties and behavior of WS_2 nanotubes. *Nano Research* **2008**, *1*, 22-31.

[49] Feng, S.; Xu, R. New Materials in Hydrothermal Synthesis. *Acc. Chem. Res.* **2001**, *34*, 239-247.

[50] Cundy, C.; Cox, P. The Hydrothermal Synthesis of Zeolites: History and Development from the Earliest Days to the Present Time. *Chem. Rev.* **2003**, *103*, 663-702.

[51] Chirayil, T. G.; Zavalij, P. Y.; Whittingham, M. S. $NMe_4V_3O_7$: Critical Role of pH in Hydrothermal Synthesis of Vanadium Oxides. *Chem. Commun*. **1997**, 33-34.

[52] Chirayil, T. G.; Zavalij, P. Y.; Whittingham, M. S. Hydrothermal Synthesis of Vanadium Oxides. *Chem. Mater*. **1998**, *10*, 2629.

[53] Franger, S.; Cras, F. L.; Bourbon, C.; Rouault, H. Comparison between different $LiFePO_4$ synthesis routes and their influence on its physico-chemical properties. *J. Power Sources* **2003**, *119*, 252-257.

[54] Yang, S.; Song, Y.; Zavalij, P. Y.; Whittingham, M. S. Reactivity, Stability and Electrochemical Behavior of Lithium Iron Phosphates. *Electrochem. Commun*. **2002**, *4*, 239-244.

[55] Yang, S.; Zavalij, P.; Whittingham, M. S. Hydrothermal Synthesis of Lithium Iron Phosphate Cathodes. *Electrochem. Commun.* **2001**, *3*, 505-508.

[56] Chen, J. J.; Whittingham, M. S. Hydrothermal Synthesis of Lithium Iron Phosphate. *Electrochem. Commun*. **2006**, *8*, 855-858.

[57] Dokko, K.; Shiraishi, K.; Kanamura, K. Identification of surface impurities on $LiFePO_4$ particles prepared by a hydrothermal process. *J. Electrochem. Soc*. **2005**, *152*, A2199.

[58] Dokko, K.; Koizumi, S.; Kanamura, K. Electrochemical reactivity of $LiFePO_4$ prepared by hydrothermal method. *Chem. Lett.* **2006**, *35*, 338-339.

[59] Dokko, K.; Koizumi, S.; Sharaishi, K.; Kanamura, K. Electrochemical properties of $LiFePO_4$ prepared via hydrothermal route. *J. Power Sources* **2007**, *165*, 656-659.

[60] K. Byrappa, M. K. Devaraju, J. R. Paramesh, B. Basavalingu, A. K. Soga, Hydrothermal Synthesis and Characterization of $LaPO_4$ for Bio-Imaging Phosphors. *J. Mater. Sci*. **2007**, *43*, 2229-2233.

[61] Modeshia, D. R.; Walton, R. I. Solvothermal Synthesis of Perovskites and Pyrochlores: Crystallisation of Functional Oxides under Mild Conditions. *Chem. Soc. Rev*. **2010**, *39*, 4303–4325.

[62] Sobhani, A.; Niasar, M. S. Optimized synthesis of ZnSe nanocrystals by hydrothermal method. *J. Mater. Sci.: Mater. Electron.* **2016**, *27*, 293–303.

[63] Guo, C.; Cao, M.; Hu, C. A novel and low temperature hydrothermal synthesis of SnO_2 nanorods. *Inorg. Chem. Comm.* **2004**, *7*, 929-931.

[64] Liu, X.; Ma, J.; Peng, P.; Zheng, W. One-Pot Hydrothermal Synthesis of ZnSe Hollow Nanospheres from an Ionic Liquid Precursor. *Langmuir* **2010**, *26*, 9968-9973.

[65] Sugarthi, S.; Bakiyaraj, G.; Abinaya, R.; Navaneethan, M.; Archana, J.; Shimomura, M. Effect of different growth temperature on the formation of ternary metal chalcogenides $AgBiS_2$. *Mater. Sci. Semicond. Proc*. **2020**, *107*, 104781.

[66] Hou, K.; Huang, Z.; Liu, S.; Liao, G.; Qiao, H.; Li, H.; Qi, X. A hydrothermally synthesized $MoS_{2(1-x)}Se_{2x}$ alloy with deep-shallow level conversion for enhanced performance of photodetectors. *Nanoscale Advances* **2020**, *2*, 2185–2191.

[67] Subramanian, V.; Zhu, H.; Wei, B. Nanostructured MnO_2: Hydrothermal Synthesis and Electrochemical Properties as a Supercapacitor Electrode Material. *J. Power Sources* **2006**, *159*, 361-364.

[68] Tseng, T.; Lin, Y.; Chen, Y.; Chu, H. A review of photocatalysts prepared by sol-gel method for VOCs removal. *Int. J. Mol. Sci.* **2010**, *11*, 2336-2361.

[69] Klein, L.C. Sol-gel optical-materials. *Annu. Rev. Mater. Sci.* **1993**, *23*, 437–452.

[70] Klein, L.C.; Woodman, R.H. Porous silica by the sol-gel process. *Por. Cer. Mater.* **1996**, *115*, 109–124.

[71] Sheikh, M.; Naikoo, G. A.; Thomas, M.; Bano, M.; Ahirwar, D.; Pandit, U.; Khan. F. Fabrication of hierarchically mesoporous CuO nanostructures and their role as heterogenous catalysts and sensors. *RSC Adv.* **2016**, *6*, 42807–42818.

[72] Kumar, V.; Goswami, Y. C. Synthesis of CdS/CdSe Core/Shell Heterostructures Using Ultrasonic Assisted Sol–Gel Method. *Chemistry Africa* **2020**, *3*, 135–139.

[73] Lemine, O.; Omri, K.; Zhang, B.; El Mir, L.; Sajieddine, M.; Alyamani, A.; Bououdina, M. Sol–Gel Synthesis of 8nm Magnetite (Fe_3O_4) Nanoparticles and their Magnetic Properties. *Superlattices and Microstructures* **2012**, *52*, 793-799.

[74] Wu, J.; Gao, C.; Han, L.; Shen, S.; Jia, M.; Wang, L.; Jiang, L.; Liu, F. The effect of different Cu/Sn ratios on the properties of monoclinic Cu_2SnS_3 thin films and solar cells fabricated by the sol–gel method. *J. Mater. Sci.: Mater. Elect.* **2019**, *30*, 4378–4384.

[75] Lee, M. S.; Hong, S. S.; Mohseni, M. Synthesis of Photocatalytic Nanosized TiO_2–Ag Particles with Sol–Gel Method using Reduction Agent. *J. Mol. Cat. A: Chem.* **2005**, *242*, 135–140.

[76] Prasad, M.; Thyagarajan, K.; Kumar, R. Structural, surface morphological, optical and thermoelectric properties of sol–gel spin coated Zn doped CdS thin flms. *SN Appl. Sci.* **2020**, *2*, 552.

[77] Pejjai, B.; Reddivari, M.; Kotte, T. Phase controllable synthesis of Cus nanoparticles by chemical co-precipitation method: Effect of copper precursors on the properties of Cus. *Mater. Chem. Phy.* **2020**, *239*, 122030.

[78] Neto, N. A.; Nascimento, L.; Correa, M.; Bohn, F.; Bomio, M.; Motta, F. Characterization and Photocatalytic Application of Ce^{4+}, Co^{2+}, Mn^{2+} and Ni^{2+} Doped Fe_3O_4 Magnetic Nanoparticles Obtained by the Co-Precipitation Method. *Mater. Chem. Phy.* **2020**, *242*, 122489.

[79] Iqbal, T.; Ali, F.; Khalid, N. R.; Tahir, M. B.; Ijaz, M. Facile synthesis and antimicrobial activity of CdS-Ag_2S nanocomposites. *Bioorg. Chem.* **2019**, *90*, 103064.

[80] Mirzaee, S.; Kalandaragh, Y. A.; Rahimzadeh, P. Modified Co-Precipitation Process Effects on the Structural and Magnetic Properties of Mn-Doped Nickel Ferrite Nanoparticles. *Solid State Sciences* **2020**, *99*, 106052.

[81] Kappe, C. Controlled Microwave Heating in Modern Organic Synthesis. *Angew. Chem. Int. Ed.* **2004**, *43*, 6250-6284.

[82] Faraji, S.; Ani, F. Microwave-assisted synthesis of metal oxide/hydroxide composite electrodes for high power supercapacitors–A review. *J. Power Sources* **2014**, *263*, 338-360.

[83] Chandrasekaran, S.; Ramanathan, S.; Basak, T. Microwave Food Processing—A Review. *Food Research Int.* **2013**, *52*, 243-261.

[84] Abubakar, Z.; Salema, A.; Ani, F. A New Technique to Pyrolyse Biomass in a Microwave System: Effect of Stirrer Speed. *Biores. Technol.* **2013**, *128*, 578-585.

[85] Motasemi, F.; Ani, F. A Review on Microwave-Assisted Production of Biodiesel. *Renewable and Sustainable Energy Reviews* **2012**, *16*, 4719-4733.

[86] Motasemi, F.; Afzal, M. A Review on the Microwave-Assisted Pyrolysis Technique. *Renewable and Sustainable Energy Reviews* **2013**, *28*, 317-330.

[87] Pan, Q.; Hu, H.; Zou, Y.; Chen, M.; Wu, L.; Yang, D.; Yuan, X.; Fan, J.; Sun, B.; Zhang, Q. Microwave-assisted synthesis of high-quality ‘‘all-inorganic’’ $CsPbX_3$ (X = Cl, Br, I) perovskite nanocrystals and their application in light emitting diodes. *J. Mater. Chem. C* **2017**, *5*, 10947-10954.

[88] Al-Shehri, B.; Shkir, M.; Bawazeer, T.; AlFaify, S.; Hamdy, M. A rapid microwave synthesis of Ag_2S nanoparticles and their photocatalytic performance under UV and visible light illumination for water treatment applications. *Physica E: Low-dimensional Systems and Nanostructures* **2020**, *121*, 114060.

[89] Shkir, M.; Khan, A.; Hamdy, M.; AlFaify, S. A facile microwave synthesis of PbS:Sr nanoparticles and their key structural, morphological, optical, photoluminescence, dielectric and electrical studies for optoelectronics. *Mater. Res. Exp.* **2020**, *6*, 1250e6.

[90] Skoda, D.; Kazda, T.; Munster, L.; Hanulikova, B.; Styskalik, A.; Eloy, P.; Debecker, D.; Vilcakova, J.; Cech, O.; Simonikova, L. Microwave-Assisted Synthesis of Platelet-like Cobalt Metal-Organic Framework, its Transformation to Porous Layered Cobalt-Carbon Nanocomposite Discs and their Utilization as Anode Materials in Sodium-Ion Batteries. *J. Energy Storage* **2020**, *27*, 101113.

[91] Iqbal, M.; Fatima, M.; Javed, T.; Anam, A.; Nazir, A.; Kanwal, Q.; Shehzadi, Z.; Khan, M.; Nisar, J.; Abbas, M.; Naz, S. Microwave Assisted Synthesis of Zinc Vanadate Nanoparticles and Photocatalytic Application. *Mater. Res. Exp.* **2020**, *7*, 015070.

[92] Luoa, W.; Gaumet, J. J.; Magri, P.; Dilibertoc, S.; Li, F.; Franchetti, P.; Ghanbajac, J.; Mai, L. Fast, green microwave-assisted synthesis of single crystalline Sb_2Se_3 nanowires towards promising lithium storage. *J. Energy Chem.* **2018**, *30*, 27-33.

[93] Zhang, Y.; Li, K.; Liao, J.; Wei, X.; Zhang, L. Microwave-Assisted Synthesis of Graphitic Carbon Nitride/CuO Nanocomposites and the Enhancement of Catalytic Activities in the Thermal Decomposition of Ammonium Perchlorate. *Appl. Surf. Sci.* **2020**, *499*, 143875.

[94] Besmann, T.; Stinton, D.; Lowden, R. Chemical Vapor Deposition Techniques. *MRS Bulletin* **1988**, *13*, 45-51.

[95] Wang, S.; Wang, G.; Yang, X.; Yang, H.; Zhu, M.; Zhang, S.; Peng, G.; Li, Z. Synthesis of Monolayer $MoSe_2$ with Controlled Nucleation via Reverse-Flow Chemical Vapor Deposition. *Nanomaterials* **2019**, *10*, 75.

[96] Zhao, S.; Lu, M.; Xue, S.; Tao, L.; Sui, Y.; Wang, Y. Large-area synthesis of continuous two-dimensional $MoTe_xSe_{2-x}$ alloy films by chemical vapor deposition. *Appl. Phys. Lett.* **2019**, *115*, 063105.

[97] Giannazzo, F.; Bosi, M.; Fabbri, F.; Schiliro, E.; Greco, G.; Roccaforte, F. Direct probing of grain boundary resistance in chemical vapor deposition-grown monolayer MoS_2 by conductive atomic force microscopy. *Physica status solidi (RRL)–Rapid Research Letters* **2019**, *14*, 1900393.

[98] Chen, T.; Hao, G.; Wang, G.; Li, B.; Kou, L.; Yang, H.; Zheng, X.; Zhong, J. Controlled growth of atomically thin $MoSe_2$ films and nanoribbons by chemical vapor deposition. *2D Materials* **2019**, *6*, 025002.

[99] Lobaccaro, P.; Raygani, A.; Oriani, A.; Miani, N.; Piotto, A.; Kapadia, R.; Zheng, M.; Yu, Z.; Magagnin, L.; Chrzan, D. C.; Maboudian, R.; Javey. A. Electrodeposition of high purity indium thin films and its application to indium phosphide solar cells. *J. Electrochem. Soc*. **2014**, *161*, D794-D800.

[100] (a) Shaur, A.; Rehman, S.; Kim, H.; Song, R.; Lim, T.; Hong, J.; Park, S.; Lee, S. Hybrid Electrochemical Deposition Route for the Facile Nanofabrication of A Cr-Poisoning-Tolerant $La(Ni,Fe)O_3{-}\Delta$ Cathode for Solid Oxide Fuel Cells. *ACS Appl. Mater. Interfaces* **2020**, *12*, 5730-5738. (b) Shaikh, A.; Mane, R.; Joo, O.; Han, S.; Pathan, H. Electrochemical Deposition of Cadmium Selenide Films and their Properties: A Review. *J. Solid State Electrochem.* **2017**, *21*, 2517-2530.

[101] Waldiya, M.; Bhagat, D.; Mukhopadhyay, I. Photoelectrochemical study of electrochemically synthesized CdTe thin films from acetate-anion based ionic liquid bath. *Electrochim. Acta* **2020**, *331*, 135437.

[102] Li, J.; Wang, B.; Liu, F.; Yang, J.; Li, J.; Liu, J.; Jia, M.; Lai, Y.; Liu, Y. Preparation and characterization of Bi-doped antimony selenide thin films by electrodeposition. *Electrochim. Acta* **2011**, *56*, 8597-8602.

[103] Tang, A.; Long, M.; He, Z. Electrodeposition of Sb_2Se_3 on TiO_2 nanotube arrays for catalytic reduction of p-nitrophenol. *Electrochim. Acta* **2014**, *146*, 346-352.

[104] Ngo, T.; Chavhan, S.; Kosta, I.; Miguel, O.; Grande, H.; Tena-Zaera, R. Electrodeposition of antimony selenide thin films and application in semiconductor sensitized solar cells. *ACS App. Mater. Interfaces* **2014**, *6*, 2836-2841.

[105] Mandal, P.; Show, B.; Ahmed, S.; Banerjee, D.; Mondal, A. Visible-Light Active Electrochemically Deposited Tin Selenide Thin Films: Synthesis, Characterization and Photocatalytic Activity. *J. Mater. Sci.: Mater. Electron.* **2020**, *31*, 4708-4718.

[106] (a) Trindade, T.; O'Brien, P.; Pickett, N. Nanocrystalline Semiconductors: Synthesis, Properties, and Perspectives. *Chem. Mater.* **2001**, *13*, 3843-3858. (b) West, A. R. Basic Solid State Chemistry. *Appl. Organometal. Chem.* **2000**, 14, 227–228.

[107] (a) Klimov, V. I. Semiconductor and Metal Nanocrystals. Marcel Dekker, Inc. New York, **2004**, 1-484. (b) Alivisatos, A. Semiconductor Clusters, Nanocrystals, and Quantum Dots. *Science* **1996**, *271*, 933-937.

[108] Colvin, V. L.; Schlamp, M. C.; Allvlsatos. A. P. Light-Emitting Diodes made from Cadmium Selenide Nanocrystals and a Semiconducting Polymer. *Nature* **1994**, *370*, 354-357.

[109] Nazzal, A.; Qu, L.; Peng, X.; Xiao, M. Photoactivated CdSe Nanocrystals as Nanosensors for Gases. *Nano Letters* **2003**, *3*, 819-822.

[110] Chawla, D.; Goswami, N. Structural and Optical Properties of CdZnS Nanoparticles by Exploding Wire Technique. *Mater. Today: Proceedings* **2020**, *28*, 278-281.

[111] McAllister, J.; Bandeira, N.; McGlynn, J.; Ganin, A.; Song, Y.; Bo, C.; Miras, H. Tuning and Mechanistic Insights of Metal Chalcogenide Molecular Catalysts for the Hydrogen-Evolution Reaction. *Nat. Commun.* **2019**, *10*, 370.

[112] Melchor, M. G.; Braga, A. A. C.; Lledos, A.; Ujaque, G.; Maseras, F. Computational perspective on Pd-catalyzed C-C cross-coupling reaction mechanisms. *Acc. Chem. Res*. **2013**, *46*, 2626–2634.

[113] Zhang, J.; Wang, Y.; Jin, J.; Zhang, J.; Lin, Z.; Huang, F.; Yu, J. Efficient visible-light photocatalytic hydrogen evolution and enhanced photostability of core/shell CdS/g-C_3N_4 nanowires. *ACS Appl. Mater. Int.* **2013**, *5*, 10317–10324.

[114] Zhang, H.; Jin, M.; Xiong, Y.; Lim, B.; Xia, Y. Shape-controlled synthesis of Pd nanocrystals and their catalytic applications. *Acc. Chem. Res.* **2013**, *46*, 1783– 1794.

[115] Ran, J.; Zhang, J.; Yu, J.; Jaroniec, M.; Qiao, S. Z. Earth abundant co-catalysts for semiconductor based photocatalytic water splitting. *Chem. Soc. Rev*. **2014**, *43*, 7787–7812.

[116] Xue, L.; Lin, Z. Theoretical aspects of palladium catalysed carbon-carbon cross coupling reactions. *Chem. Soc. Rev.* **2010**, *39*, 1692–1705.

[117] (a) Zou, J. J.; He, H.; Cui, L.; Du, H. Y. Highly efficient Pt/TiO_2 photocatalyst for hydrogen generation prepared by a cold plasma method. *Int. J. Hydrogen Energy* **2007**, *32*, 1762–1770. (b) Kong, D.; Cha, J.; Wang, H.; Lee, H.; Cui, Y. First-Row Transition Metal Dichalcogenide Catalysts for Hydrogen Evolution Reaction. *Energy & Environ. Sci.* **2013**, *6*, 3553. (c) Yu, W.; Porosoff M. D.; Chen, J. G. Review of Pt-based bimetallic catalysis: from model surfaces to supported catalysts. *Chem. Rev.* **2012**, *112*, 5780–817.

[118] Eftekhari, A. Electrocatalysts for Hydrogen Evolution Reaction. *Int. J. Hydrogen Energy* **2017**, *42*, 11053-11077.

[119] (a) Shi, J. On the synergetic catalytic effect in heterogeneous nanocomposite catalysts. *Chem. Rev.* **2013**, *113*, 2139–81. (b) Bell, A.T. The impact of nanoscience on heterogeneous catalysis. *Science* **2003**, *299*, 1688–91.

[120] (a) Li, Z.; Ma, J.; Zhou, Y.; Yin, Z.; Tang, Y.; Ma, Y.; Wang, D. Synthesis of sulfur-Rich MoS_2 nanoflowers for enhanced hydrogen evolution reaction performance. *Electrochim. Acta* **2018**, *283*, 306-312. (b) Zhu, X.; Mo, L.; Wu, Y.; Lai, F.; Han, X.; Ling, X.; Liu, T.; Miao, Y. Self-Supported MoS_2@NHCF Fiber-In-Tube composites with tunable voids for efficient hydrogen evolution reaction. *Comp. Commun.* **2018**, *9*, 86-91. (c) Shang, X.; Rao, Y.; Lu, S.; Dong, B.; Zhang, L.; Liu, X.; Li, X.; Liu, Y.; Chai, Y.; Liu, C. Novel WS_2/WO_3 heterostructured nanosheets as efficient electrocatalyst for hydrogen evolution reaction. *Materials Chemistry and Physics* **2017**, *197*, 123-128. (d) Yao, Y.; Jin, Z.; Chen, Y.; Gao, Z.; Yan, J.; Liu, H.; Wang, J.; Li, Y.; Liu, S. Graphdiyne-WS_2 2D-Nanohybrid electrocatalysts for high-performance hydrogen evolution reaction. *Carbon* **2018**, *129*, 228-235. (e) Barough, V.; Iranizad, E.; Bayat, A.; Hemmati, K. Synthesis of binder-free $MoSe_2$ nanoflakes as a new electrode for electrocatalytic hydrogen evolution. *J. Electroanal. Chem.* **2018**, *823*, 278-286. (f) He, H. Y.; He, Z.; Shen, Q. TiO_2:Si Nanotube/1T-$MoSe_2$ nanosheet hybrids with highly efficient hydrogen evolution catalytic activity. *J. Colloid and Interface Sci.* **2018**, *522*, 136-143. (g) Adhikari, S.; Sarkar, D.; Madras, G. Hierarchical design of CuS architectures for visible light photocatalysis of 4-Chlorophenol. *ACS Omega* **2017**, *2*, 4009-4021. (h) Eskandari, P.; Kazemi, F.; Zand, Z. Photocatalytic reduction of aromatic nitro compounds using CdS nanostructure under blue LED irradiation. *J. Photochem. Photobiol. A: Chem.* **2014**, *274*, 7-12. (i) Rodriguez, E. M; Rey, A.; Mena, E.; Beltran, F. J. Application of solar photocatalytic ozonation in water treatment using supported TiO_2. *Appl. Catal. B: Environ.* **2019**, *254*, 237-245. (j) Li, H.; Wang, M.; Wei, Y.; Long, F. Noble metal free NiS_2 with rich active sites loaded G-C_3N_4 for highly efficient photocatalytic H_2 evolution under visible light irradiation. *J. Colloid and Interface Sci.* **2019**, *534*, 343-349.

[121] (a) Zhang, L.; Jin, Z.; Ma, X.; Zhang, Y.; Wang, H. Properties of iron vanadate over CdS nanorods for efficient photocatalytic hydrogen production. *New J. Chem.* **2019**, *43*, 3609-3618. (b) Gao, X.; Liu, X.; Zhu, Z.; Gao, Y.; Wang, Q.; Zhu, F.; Xie, Z. Enhanced visible light photocatalytic performance of CdS sensitized TiO_2 nanorod arrays decorated with Au nanoparticles as electron sinks. *Scientific Reports* **2017**, *7*, 973. (c) Keerthana, G. T. B.; Murugakoothan, P. Synthesis and characterization of CdS/TiO_2

nanocomposite: Methylene blue adsorption and enhanced photocatalytic activities. *Vacuum* **2019**, *159*, 476-481. (d) Kudo, A.; Miseki, Y. Heterogeneous photocatalyst materials for water splitting. *Chem. Soc. Rev*. **2009**, *38*, 253–278.

[122] (a) Hamdi, A.; Ferreira, D. P.; Ferraria, A. M.; Conceicao, D. S.; Ferreira, A. P. Carapeto, L. F. V.; Boufi, S.; Bouattour, S.; Rego. A. M. B. TiO_2-CdS nanocomposites: effect of CdS oxidation on the photocatalytic activity. *J. Nanomater.* **2016**, *2016*, 1-11. (b) Feng, J.; Sun, Y.; Mu, J.; Chen, L.; Han, T.; Miao, H.; Liu, E.; Fan, J.; Hu, X. Microwave-assistant synthesis of Au/SnS_2 nanoflowers as improved visible-light responsive photocatalysts. *Mater. Lett.* **2019**, *236*, 534-537. (c) Ayodhya, D.; Veerabhadram, G. Ultrasonic synthesis of G-C_3N_4/CdS composites and their photodegradation, catalytic reduction, antioxidant and antimicrobial studies. *Mater. Res. Inno.* **2019**, *24*, 210-228. (d) Guo, R.; Yan, A.; Xu, J.; Xu, B.; Li, T.; Liu, X.; Yi, T.; Luo, S. Effects of morphology on the visible-light driven photocatalytic and bactericidal properties of $BiVO_4$/CdS heterojunctions: A discussion on photocatalysis mechanism. *J. Alloys and Comp.* **2020**, *817*, 153246.

[123] Guan, H.; Zhang, S.; Cai, X.; Gao, Q.; Yu, X.; Zhou, X.; Peng, F.; Fang, Y.; Yang, S. CdS@Ni_3S_2 core–shell nanorod arrays on nickel foam: A multifunctional catalyst for efficient electrochemical catalytic, photoelectrochemical and photocatalytic H_2 production reaction. *J. Mater. Chem. A* **2019**, *7*, 2560-2574.

[124] (a) Wang, S. Solvothermal synthesis of porous SnS_2 nanotubes with higher adsorption and photocatalytic activity. *Surface Science* **2019**, *690*, 121469. (b) Huo, Y.; Yang, Y.; Dai, K.; Zhang, J. Construction of 2D/2D porous graphitic C_3N_4/SnS_2 composite as a direct Z-scheme system for efficient visible photocatalytic activity. *Appl. Surf. Sci.* **2019**, *481*, 1260-1269. (c) Chen, X.; Zhang, J.; Zeng, J.; Shi, Y.; Huang, G.; Zhang, L.; Wang, H.; Kong, Z.; Xi, J.; Ji, Z. Novel 3D/2D heterojunction photocatalysts constructed by three-dimensional In_2S_3 dandelions and ultrathin hexagonal SnS_2 nanosheets with excellent photocatalytic and photoelectrochemical activities. *Appl. Surf. Sci.* **2019**, *463*, 693-703. (d) Chava, R.; Do, J.; Kang, M. Enhanced photoexcited carrier separation in CdS–SnS_2 heteronanostructures: A new 1D–0D visible-light photocatalytic system for the hydrogen evolution reaction. *J. Mater. Chem. A* **2019**, *7*, 13614-13628.

[125] Dormann, J. L.; Fiorani, D. Magnetic properties of fine particles. North-Holland, Amesterdam, 1992. doi.org/10.1016/C2009-0-13025-8.

[126] Jeong, U.; Teng, X.; Wang, Y.; Yang, H.; Xia, Y. Superparamagnetic colloids: Controlled synthesis and niche applications. *Adv. Mater.* **2007**, *19*, 33-60.

[127] Silva, F.; Depeyrot, J.; Campos, A.; Aquino, R.; Fiorani, D.; Peddis, D. Structural and magnetic properties of spinel ferrite nanoparticles. *J. Nanoscience and Nanotechnology* **2019**, *19*, 4888-4902.

[128] (a) Koops, C. On the dispersion of resistivity and dielectric constant of some semiconductors at audiofrequencies. *Phy. Rev.* **1951**, *83*, 121-124. (b) Kharabe, R.; Devan, R.; Kanamadi, C.; Chougule, B. Dielectric properties of mixed Li–Ni–Cd ferrites. *Smart Materials and Structures* **2006**, *15*, N36-N39.

[129] Kamran, M.; Shoukat, W.; Nadeem, K.; Hussain, S.; Zeb, F.; Hussain, S. Magnetic and dielectric properties of $NiCr_xFe_{2-x}O_4$ nanoparticles. *Mater. Res. Exp.* **2019**, *6*, 076106.

[130] Devmunde, B.; Raut, A.; Birajdar, S.; Shukla, S.; Shengule, D.; Jadhav, K. Structural, electrical, dielectric, and magnetic properties of Cd^{2+} substituted nickel ferrite nanoparticles. *J. Nanoparticles* **2016**, *2016*, 1-8.

[131] Rawat, P. S.; Srivastava, R. C.; Dixit, G.; Joshi, G. C.; Asokan, K. Facile synthesis and temperature dependent dielectric properties of $MnFe_2O_4$ nanoparticles. *AIP Conference Proceedings* **2019**, *2115*, 030104.

[132] Singh, S. B.; Tandon, P. K.; Catalysis: A brief review on nanocatalyst. *J. Energy and Chem. Eng*. **2014**, *2*, 106-115.

[133] (a) Zheng, L.; Zhang, W.; Xiao, X. Preparation of titanium dioxide/tungsten disulfide composite photocatalysts with enhanced photocatalytic activity under visible light. *Kor. J. Chem. Eng*. **2016**, *33*, 107-113. (b) Wang, Q.; Huang, J.; Sun, H.; Ng, Y.; Zhang, K.; Lai, Y. MoS_2 quantum dots@TiO_2 nanotube arrays: An extended spectrum driven photocatalyst for solar hydrogen evolution. *ChemSusChem* **2018**, *11*, 1708-1721.

[134] (a) Liu, Z.; Ling, X.; Su, X.; Lee, J. Carbon-supported Pt and PtRu nanoparticles as catalysts for a direct methanol fuel cell. *J. Phy. Chem. B* **2004**, *108*, 8234-8240. (b) Bulushev, D.; Yuranov, I.; Suvorova, E.; Buffat, P.; Kiwi-Minsker, L. Highly dispersed gold on activated carbon fibers for low temperature CO oxidation. *J. Catal.* **2004**, *224*, 8-17. (c) Chen, S.; Kucernak, A. Electrocatalysis under conditions of high mass transport rate: Oxygen reduction on single submicrometer sized Pt particles supported on carbon. *J. Phy. Chem. B* **2004**, *108*, 3262-3276. (d) Feng, Y. J.; He, T.; Vante, N. A. Carbon-supported $CoSe_2$ nanoparticles for oxygen reduction reaction in acid medium. *Fuel Cells* **2010**, *10*, 77–83. (e) Wu, G.; Cui, G.; Li, D.; Shen, P.; Li, N. Carbon-supported $Co_{1.67}Te_2$ nanoparticles as electrocatalysts for oxygen reduction reaction in alkaline electrolyte. *J. Mater. Chem.* **2009**, *19*, 6581.

[135] (a) Zhang, J.; Chen, Y.; Wang, X. Two-dimensional covalent carbon nitride nanosheets: Synthesis, functionalization, and applications. *Energy & Environmental Science* **2015**, *8*, 3092-3108. (b) Tang, C.; Cheng, N.; Pu, Z.; Xing, W.; Sun, X. Nise Nanowire film supported on nickel Foam: An efficient and stable 3D bifunctional electrode for full water splitting. *Angew. Chem. Int. Ed.* **2015**, *54*, 9351-9355. (c) Zhang, Z.; Wang, Q.; Zhao, C.; Min, S.; Qian, X. One-step hydrothermal synthesis of 3D petal-like Co_9S_8/RGO/Ni_3S_2 composite on nickel foam for high performance supercapacitors. *ACS Appl. Mater. Interface* **2015**, *7*, 4861-4868. (d) Yu, J.; Lv, C.; Zhao, L.; Zhang, L.; Wang, Z.; Liu, Q. Reverse microemulsion-assisted synthesis of $NiCo_2S_4$ nanoflakes supported on nickel foam for electrochemical overall water splitting. *Adv. Mater. Interface* **2018**, *5*, 1701396.

[136] (a) Grill, C. Infrared evidence for the segregation of silica supported Pt-Pd bimetallic clusters in oxidizing atmospheres. *J. Catal.* **1980**, *64*, 487-490. (b) Volkov, S.; Kosmambetova, G.; Kharkova, L.; Shvets, O.; Yanko, O.; Gritsenko, V.; Strizhak, P. Catalytic perfomance of rhodium chalcogen halides and rhodium chalcogenides over silica supports in methane oxidative carbonylation. *J. Nat. Gas Chem.* **2009**, *18*, 399-406. (c) Lamaestre, R. E.; Majimel, J.; Jomard, F.; Bernas, H. Synthesis of lead chalcogenide nanocrystals by sequential ion implantation in silica. *J. Phy. Chem. B* **2005**, *109*, 19148-19155.

[137] (a) Ding, S.; Chen, J.; Luan, D.; Boey, F.; Madhavi, S.; Lou, X. Graphene-supported anatase TiO_2 nanosheets for fast lithium storage. *Chem. Commun.* **2011**, *47*, 5780. (b) Gao, M.; Cao, X.; Gao, Q.; Xu, Y.; Zheng, Y.; Jiang, J.; Yu, S. Nitrogen-doped graphene supported $CoSe_2$ nanobelt composite catalyst for efficient water oxidation. *ACS Nano* **2014**, *8*, 3970-3978. (c) Yuan, W.; Li, J.; Chen, P.; Shen, Y.; Xie, A. A One-pot hydrothermal ssynthesis of 3D nitrogen doped graphene aerogels supported NiS_2 nanoparticles as efficient electrocatalysts for the oxygen-reduction reaction. *J. Nanopart. Res.* **2014**, *16*. (d) Perivoliotisa, D. K.; Tagmatarchisa, N. Recent advancements in metal-based hybrid electrocatalysts supported on graphene and related 2D materials for the oxygen reduction reaction. *Carbon* **2017**, *118*, 493-510.

[138] (a) Zhang, W.; Mu, Y.; He, X.; Chen, P.; Zhao, S.; Huang, C.; Wang, Y.; Chen, J. Robust porous polymers bearing phosphine oxide/chalcogenide ligands for volatile iodine capture. *Chem. Eng. J.* **2020**, *379*, 122365. (b) Selvaraju, K.; babu, G. Assembly of favorable 2D Co-N_4 based polymer nanosheets for proficient oxygen reduction reaction. *Ionics* **2019**, *25*, 5939-5947. (c) Wang, Y.; Fu, D.; Fu, Y.; Yu, Y.; Zhou, J.; Guo, C.; Ma, J.; Li, K.; Zheng, L.; Zuo, X. An 2D polymer used as ingredient of Fe/N/C composite towards oxygen reduction catalyst in acidic medium. *Chem. Select* **2019**, *4*, 884-891. (d) Wang, Z.; Sheng, M.; Qin, S.; Shi, H.; Strømme, M.; Zhang, Q.; Xu, C. Assembly of discrete chalcogenolate clusters into a one-dimensional coordination polymer with enhanced photocatalytic activity and stability. *Inorg. Chem.* **2020**, *59*, 2121-2126.

[139] (a) Nasuha, N.; Hameed, B. H.; Din, A. T. M. Rejected tea as a potential low-cost adsorbent for the removal of methylene blue. *J. Hazard. Mater.* **2010**, *175*, 126-132. (b) Rauf, M. A.; Qadri, S. M.; Ashraf, S.; AlMansoori, K. M. Adsorption studies of toluidine blue from aqueous solutions onto gypsum. *Chem. Eng. J.* **2009**, *150*, 90–95.

[140] (a) Sharma, V. K.; Anquandah, G. A. K.; Yngard, R. A.; Kim, H.; Fekete, J.; Bouzek, K. Nonylphenol, octylphenol, and bisphenol-A in the aquatic environment: A review on occurrence, fate and treatment. *J. Environ. Sci. Health Part A* **2009**, *44*, 423. (b) Ge, F.; Zhu, L.; Wang. J. Distribution of chlorination products of phenols under various pHs in water disinfection. *Desalination* **2008**, *225*, 1.

[141] (a) Riera, T. M.; Bouzán, C. G.; Crespi, M. Combination of coagulation–flocculation and nanofiltration techniques for dye removal and water reuse in textile effluents. *Desalination* **2010**, *252*, 53–59. (b) Ahmad, A. L.; Puasa. S. W. Reactive dyes decolourization from an aqueous solution by combined coagulation/micellar-enhanced ultrafiltration process. *Chem. Eng. J.* **2007**, *132*, 257–265.

[142] Shakir, K.; Elkafrawy, A. F.; Ghoneimy, H. F.; Beheir, S. G. E.; Refaat, M. Removal of rhodamine B (a basic dye) and thoron (an acidic dye) from dilute aqueous solutions and wastewater simulants by ion flotation. *Water Research* **2010**, *44*, 1449.

[143] (a) Lee, M. S.; Huang, C.; Lee, K. R.; Pan, J. R.; Chang, W. K. Factors affecting phenol transfer through polydimethylsiloxane composite membrane. *Desalination* **2008**, *234*, 416. (b) Jirankova, H.; Mrazek, J.; Dolecek, P.; Cak, J. Organic dye removal by combined adsorption–membrane separation process. *Desalination Water Treatment* **2010**, *20*, 96–101.

[144] Zodi, S.; Potier, O.; Lapicque, F.; Leclerc, J. P. Treatment of the industrial wastewaters by electrocoagulation: optimization of coupled electrochemical and sedimentation processes. *Desalination* **2010**, *261*, 186–190.

[145] (a) Ayed, L.; Chaieb, K.; Cheref, A.; Bakhrouf, A. Biodegradation and decolorization of triphenylmethane dyes by Staphylococcus epidermidis. *Desalination* **2010**, *260*, 137–146. (b) CInar, O.; Yasar, S.; Kertmen, M.; Demiroz, K.; Yigit, N.O.; Kitis, M. Effect of cycle time on biodegradation of azo dye in sequencing batch reactor. *Process Safety and Environment Protection* **2008**, *86*, 455–460.

[146] (a) Bouasla, C., Samar, M. E. H.; Ismail, F. Degradation of methyl violet 6B dye by the Fenton process. *Desalination* **2010**, *254*, 35–41. (b) Masarwa, A.; Calis, S. R.; Meyerstein, N.; Meyerstein, D. Oxidation of organic substrates in aerated aqueous solutions by the Fenton reagent. *Coord. Chem. Rev.* **2005**, *249*, 1937–1943.

[147] (a) Monteagudo, J. M.; Duran, A.; Martin, I. S.; Aguirre, M. Catalytic degradation of Orange II in a ferrioxalate-assisted photo-Fenton process using a combined UVA/ C-solar pilot-plant system. *Appl. Catal. B: Environ.* **2010**, *95*, 120–129. (b) Modirshahla,

N.; Behnajady, M. A.; Ghanbary, F. Decolorization and mineralization of C.I. Acid Yellow 23 by Fenton and photo-Fenton processes. *Dyes and Pigments* **2007**, *73*, 305–310.

[148] (a) Rauf, M. A.; Meetani, M. A.; Khaleel, A.; Ahmed, A. Photocatalytic degradation of Methylene Blue using a mixed catalyst and product analysis by LC/MS. *Chem. Eng. J.* **2010**, *157*, 373–378. (b) Xu, R.; Li, J.; Wang, J.; Wang, X.; Liu, B.; Wang, B.; Luan, X.; Zhang, X. Photocatalytic degradation of organic dyes under solar light irradiation combined with Er^{3+}:$YAlO_3$/Fe- and Co-doped TiO_2 coated composites. *Sol. Energy Mater. Sol. Cells* **2010**, *94*, 1157–1165.

[149] Bagha, A. R. T.; Mahmoodi, N. M.; Menger, F. M. Degradation of a persistent organic dye from colored textile wastewater by ozonation. *Desalination* **2010**, *260*, 34–38.

[150] (a) Konstantinou, I. K.; Albanis, T. A. TiO_2- assisted photocatalytic degradation of azo dyes in aqueous solution: kinetic and mechanistic investigations: a review. *Appl. Catal. B: Environ.* **2004**, *49*, 1–14. (b) Mahmoodi, N. M.; Arami, M.; Limaee, N.Y.; Tabrizi, N. S. Kinetics of heterogeneous photocatalytic degradation of reactive dyes in an immobilized TiO_2 photocatalytic reactor. *J. Colloid Interface Sci*. **2006**, *295*,159–164.

[151] Liu, Y.; Li, M.; Zhang, Q.; Qin, P.; Wang, X.; He, G.; Li, L. One-Step synthesis of a WO_3-CuS nanosheet heterojunction with enhanced photocatalytic performance for methylene blue degradation and Cr(VI) reduction. *J. Chem. Tech. Biotechnol.* **2019**, *95*, 665-674.

[152] Wang, Y.; Bao, S.; Liu, Y.; Yang, W.; Yu, Y.; Feng, M.; Li, K. Efficient photocatalytic reduction of Cr(VI) in aqueous solution over CoS_2/G-C_3N_4-rGO nanocomposites under visible light. *Appl. Surf. Sci.* **2020**, *510*, 145495.

[153] Chowdhury, A.; Khan, A.; Kumari, S.; Hussain, S. Superadsorbent Ni–Co–S/SDS nanocomposites for ultrahigh removal of cationic, anionic organic dyes and toxic metal ions: Kinetics, isotherm and adsorption mechanism. *ACS Sustainable Chem. Eng.* **2019**, *7*, 4165-4176.

[154] Kaur, D.; Bagga, V.; Behera, N.; Thakral, B.; Asija, A.; Kaur, J.; Kaur, S. SnSe/SnO_2 nanocomposites: Novel material for photocatalytic degradation of industrial waste dyes. *Adv. Comp. Hyb. Mater.* **2019**, *2*, 763-776.

[155] Shaoqing, Y.; Jun, H.; Jianlong, W. Radiation-induced catalytic degradation of p-nitrophenol (PNP) in the presence of TiO_2 nanoparticles. *Radiat. Phy. Chem.* **2010**, *79*, 1039-1046.

[156] Ma, M.; Yang, Y.; Li, W.; Feng, R.; Li, Z.; Lyu, P.; Ma, Y. Gold nanoparticles supported by amino groups on the surface of magnetite microspheres for the catalytic reduction of 4-nitrophenol. *J. Mater. Sci.* **2018**, *54*, 323-334.

[157] (a) Yarlagadda, V.; Kadali, R.; Sharma, N.; Sekar, R.; Vayalam Purath, V. Rapid Establishment of p-nitrophenol biodegradation in acetate-fed aerobic granular sludge. *Appl. Biochem. Biotechnol.* **2011**, *166*, 1225-1235. (b) Srivastava, S.; Yamada, R.; Ogino, C.; Kondo, A. Biogenic synthesis and characterization of gold nanoparticles by escherichia coli K12 and its heterogeneous catalysis in degradation of 4-nitrophenol. *Nanoscale Research Letters* **2013**, *8*, 70.

[158] (a) Oturan, M. A.; Peiroten, J.; Chartrin, P.; Acher, A. J.; Complete destruction of p-nitrophenol in aqueous medium by electro-fenton method. *Environ. Sci. Technol*. **2000**, *34*, 3474-3479 (b) Angeles, F. D. M.; Emilio, R.; Marıa, F. F.; Marta, P.; Angeles, S. M. Degradation of organic pollutants by heterogeneous electro-fenton process using Mn-alginate composite. *J. Chem. Technol. Biotechnol.* **2015**, *90*, 1439–1447.

[159] Sugiyama, M.; Salehi, Z.; Tokumura, M.; Kawase, Y. Photocatalytic degradation of p-nitrophenol by zinc oxide particles. *Water Sci. Technol.* **2012**, *65*, 1882–1886.

[160] Xue, J.; Xiang, H.; Wang, K.; Zhang, X.; Wang, S.; Wang, X.; Cao, H. The preparation of carbon-encapsulated Fe/Co nanoparticles and their novel applications as bifunctional catalysts to promote the redox reaction for p-nitrophenol. *J. Mater. Sci.* **2012**, *47*, 1737–1744.

[161] (a) Sun, J.; Han, Y.; Fu, H.; Qu, X.; Xu, Z.; Zheng, S. Au@Pd/TiO_2 with atomically dispersed Pd as highly active catalyst for solvent-free aerobic oxidation of

benzyl alcohol. *Chem. Eng. J.* **2017**, *313*, 1–9 (b) Jin, C.; Han, J.; Chu, F.; Wang, X.; Guo, R. Fe_3O_4@PANI hybrid shell as a multifunctional support for Au nanocatalysts with a remarkably improved catalytic performance. *Langmuir* **2017**, *33*, 4520–4527.

[162] (a) Wunder, S.; Polzer, F.; Lu, Y.; Mei, Y.; Ballauff, M. Kinetic analysis of catalytic reduction of 4-nitrophenol by metallic nanoparticles immobilized in spherical polyelectrolyte brushes. *J. Phys. Chem. C* **2010**, *114*, 8814−8820. (b) Guella, G.; Patton, B.; Miotello, A. Kinetic features of the platinum catalyzed hydrolysis of sodium borohydride from 11B NMR measurements. *J. Phys. Chem. C* **2007**, *111*, 18744−18750.

[163] Ramaraj, S.; Mani, S.; Chen, S. M.; Palanisamy, S.; Velusamy, V.; Hall, J. M. Chen, T. W.; Tseng, T. W. Hydrothermal synthesis of Cr_2Se_3 hexagons for sensitive and lowlevel detection of 4-nitrophenol in water. *SCiENTifiC RePOrTS* **2018**, *8*, 4839.

[164] Zhang, Z.; Wang, X.; Wu, K.; Yue, Y.; Zhao, M.; Cheng, J.; Ming, J.; Yu, C.; Wei, X. $Co_{0.85}Se$ bundle-like nanostructure catalysts for hydrogenation of 4-nitrophenol to 4-aminophenol. *New J. Chem.* **2014**, *38*, 6147-6151.

[165] Khan, A.; Rehman, Z.; Khan, A.; Ambareen, H.; Ullah, H.; Abbas, S.; Khan, Y.; Khan, R. Solar-light driven photocatalytic conversion of p-nitrophenol to p-aminophenol on CdS nanosheets and nanorods. *Inorg. Chem. Commun.* **2017**, *79*, 99-103.

[166] Zhang, Y.; Kuwahara, Y.; Mori, K.; Yamashita, H. Construction of hybrid MoS_2 phase coupled with SiC heterojunctions with promoted photocatalytic activity for 4-nitrophenol degradation. *Langmuir* **2020**, *36*, 1174-1182.

[167] Liu, S.; Che, C.; Jing, H.; Zhao, J.; Mu, X.; Zhang, S.; Chen, C.; Mu, S. Phosphorus-triggered synergy of phase transformation and chalcogenide vacancy migration in cobalt sulfide for an efficient oxygen evolution reaction. *Nanoscale* **2020**, *12*, 3129-3134.

[168] (a) Li, F.; Han, G.; Noh, H.; Ahmad, I.; Jeon, I.; Baek, J. Hydrogen evolution reaction: Mechanochemically assisted synthesis of a Ru catalyst for hydrogen evolution with performance superior to Pt in both acidic and alkaline media. *Adv. Mater.* **2018**, *30*, 1803676. (b) Lu, Q.; Wang, A.; Cheng, H.; Gong, Y.; Yun, Q.; Yang, N.; Li, B.; Chen,

B.; Zhang, Q.; Zong, Y.; Gu, L.; Zhang, H. Synthesis of hierarchical 4H/Fcc Ru nanotubes for highly efficient hydrogen evolution in alkaline media. *Small* **2018**, *14*, 1801090.

[169] (a) Zhu, B.; Zou, R.; Xu, Q. Metal-organic framework based catalysts for hydrogen evolution. *Adv. Energy Mater.* **2018**, *8*, 1801193. (b) Zhao, G.; Rui, K.; Dou, S.; Sun, W. Heterostructures for electrochemical hydrogen evolution reaction: A review. *Adv. Fun. Mater.* **2018**, *28*, 1803291. (c) Pi, Y.; Shao, Q.; Zhu, X.; Huang, X. Dynamic structure evolution of composition segregated iridium-nickel rhombic dodecahedra toward efficient oxygen evolution electrocatalysis. *ACS Nano* **2018**, *12*, 7371-7379.

[170] Zhang, T.; Zhu, Y.; Lee, J. Unconventional noble metal-free catalysts for oxygen evolution in aqueous systems. *J. Mater. Chem. A* **2018**, *6*, 8147-8158.

[171] Hong, W.; Risch, M.; Stoerzinger, K.; Grimaud, A.; Suntivich, J.; Shao-Horn, Y. Toward the rational design of non-precious transition metal oxides for oxygen electrocatalysis. *Energy & Environmental Science* **2015**, *8*, 1404-1427.

[172] Pi, Y.; Zhang, N.; Guo, S.; Guo, J.; Huang, X. Ultrathin Laminar Ir Superstructure as Highly Efficient Oxygen Evolution Electrocatalyst in Broad pH Range. *Nano Lett.* **2016**, *16*, 4424−4430.

[173] Xuan, C.; Lei, W.; Wang, J.; Zhao, T.; Lai, C.; Zhu, Y.; Sun, Y.; Wang, D. Sea urchin-like Ni–Fe sulfide architectures as efficient electrocatalysts for the oxygen evolution reaction. *J. Mater. Chem. A* **2019**, *7*, 12350-12357.

[174] Luo, H.; Lei, H.; Yuan, Y.; Liang, Y.; Qiu, Y.; Zhu, Z.; Wang, Z. Engineering ternary copper-cobalt sulfide nanosheets as high-performance electrocatalysts toward oxygen evolution reaction. *Catalysts* **2019**, *9*, 459.

[175] Zhou, Y.; Luo, M.; Zhang, Z.; Li, W.; Shen, X.; Xia, W.; Zhou, M.; Zeng, X. Iron doped cobalt sulfide derived boosted electrocatalyst for water oxidation. *Appl. Surf. Sci.* **2018**, *448*, 9-15.

[176] (a) Cadavid, D.; Ibanez, M.; Shavel, A.; Dura, O.; Torre, M. L.; Cabot, A. Organic Ligand Displacement by Metal Salts to Enhance Nanoparticle Functionality: Thermoelectric Properties of Ag_2Te. *J. Mater. Chem. A* **2013**, *1*, 4864–4870. (b) Kovalenko, M.; Scheele, M.; Talapin, D. colloidal nanocrystals with molecular metal chalcogenide surface ligands. *Science* **2009**, *324*, 1417-1420. (c) Talapin, D.; Lee, J.; Kovalenko, M.; Shevchenko, E. Prospects of Colloidal Nanocrystals for Electronic and Optoelectronic Applications. *Chem. Rev.* **2010**, *110*, 389-458.

[177] (a) Talapin, D.; Lee, J.; Kovalenko, M.; Shevchenko, E. Prospects of Colloidal Nanocrystals for Electronic and Optoelectronic Applications. *Chem. Rev.* **2010**, *110*, 389-458. (b) Sargent, E. H. Colloidal Quantum Dot Solar Cells. *Nat. Photo.* **2012**, *6*, 133-135. (c) Ibanez, M.; Cadavid, D.; Zamani, R.; Garcia-Castello, N.; Izquierdo-Roca, V.; Li, W.; Fairbrother, A.; Prades, J.; Shavel, A.; Arbiol, J.; Perez-Rodríguez, A.; Morante, J. R.; Cabot, A. Composition Control and Thermoelectric Properties of Quaternary Chalcogenide Nanocrystals: The Case of Stannite $Cu_2CdSnSe_4$. *Chem. Mater*. **2012**, *24*, 562–570. (d) Herranz, T.; Deng, X.; Cabot, A.; Guo, J.; Salmeron, M. Influence of the Cobalt Particle Size in the CO Hydrogenation Reaction Studied by in Situ X-Ray Absorption Spectroscopy. *J. Phy. Chem. B* **2009**, *113*, 10721-10727.

[178] Kumar, B.; Muralidharan, K. Organic-free self-assembled copper sulfide microflowers. *Eur. J. Inorg. Chem.* **2013**, *2013*, 2102-2108.

[179] Billakanti, S.; Krishnamurthi, M. Facile preparation of surfactant or support material free CdS nanoparticles with enhanced photocatalytic activity. *J. Environ. Chem. Eng.* **2018**, *6*, 1250-1256.

[180] Kumar, B.; Srinivas, B.; Prasad, M.; Muralidharan, K. Ag/Ag_2S heterodimers: tailoring the metal–semiconductor interface in a single nanoparticle. *J. Nanopart. Res.* **2015**, *17*, 325.

[181] Billakanti, S.; Baskaran, G.; Muralidharan, K. Recyclable Ni_3S_4 nanocatalyst for hydrogenation of nitroarenes. *Chem. Select.* **2017**, *2*, 4753-4758.

[182] Kumar, B.; Srinivas, B.; Muralidharan, K. Photo responsive Bi_2S_3 nanoflakes: synthesis and device fabrication at ambient conditions. *Mater. Res. Bull.* **2017**, *89*, 108-115.

CHAPTER – 2

Importance of Clean Surfaces on the Catalyst: SnS_2 Nanorings for Environmental Remediation

Abstract

The main focus of this chapter is the synthesis of SnS_2 nanomaterials with (peg-SnS_2NF) and without (sf-SnS_2NR) the involvement of the organic template and the comparative study of their catalytic activities. The synthesis of these materials was achieved in a single-step procedure aided by hexamethyldisilazane (HMDS). These nanoparticles were subjected to X-ray diffraction, transmission electron microscopy, scanning electron microscopy, Raman spectroscopy, and UV−vis spectroscopy analyses to investigate their structural, topographical, surface, and optical properties. The present work suggests that the surfactant-free SnS_2 nanoring (sf-SnS_2NR) catalyst has lower surface area compared to the poly(ethylene glycol)-stabilized SnS_2 nanoflower (peg-SnS_2NF) catalyst but shows high activity under visible light for the photoreduction of Cr(VI) and the photocatalytic degradation of organic dyes. The work exposed the importance of the clean surfaces on the catalyst and is expected to have a high impact on the photocatalytic activity of the SnS_2 nanomaterial. The study also endorses the utility of the HMDS-assisted synthetic method for the production of multifunctional semiconductor tin disulfide nanomaterials with multiple potential applications.

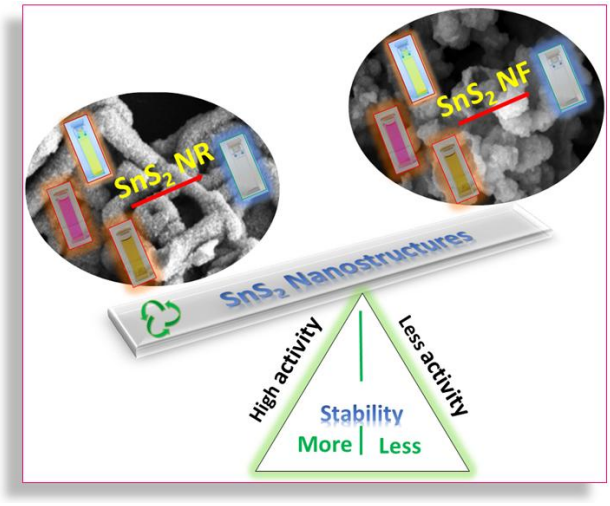

ACS Omega 2019, 4, 14970−14980

2.1. Introduction

The scientific community is always working for the development of an efficient and economical method for the elimination of pollutants such as organic dye molecules and heavy metal ions from aqueous solutions [1]. Among the heavy metal ions, especially, hexavalent chromium compounds Cr(VI) are highly lethal, carcinogenic, and pollutants found recurrently in wastewater from industrial processes [2−4]. The semiconductor-based photocatalytic reduction of Cr(VI) and disintegration of organic pollutants have gained importance due to its remarkable advantages, such as direct use of clean and safe solar energy, reusability, and low cost [5−8]. The multifunctional materials possessing more than one property are more attractive for potent technological applications [9].

Among the semiconducting metal sulphides, tin disulphide (SnS_2) can harvest visible light, which makes them promising sensitizers for wide band gap semiconductors and photocatalysts [10]. Until now, numerous morphologies of SnS_2 nanostructures, such as fullerene-like nanoparticles [11], nanobelts [12], nanosheets [13], and nanoflakes [14], have been produced successfully. Synthesis of these materials was achieved by adopting various methods such as laser ablation [15], template assisted solvothermal processes [12], coevaporation [16], and the sol−gel synthetic route [17]. However, almost all these materials were covered by either organic surfactant molecules or other inorganic materials. Such a covering of the surfaces precludes any interaction that supposed to happen on their surfaces and thus leading to the reduced catalytic activity compared to the potential expected from the materials. There are efforts to increase the activity and performance of the SnS_2 catalyst by modifying their properties with dopants and by making nanocomposites [10b−h]. However, there are no reports on synthesizing and using SnS_2 nanomaterials with unhindered free surfaces.

Here in this chapter, we report the synthesis of surfactant-free SnS_2 nanorings (sf-SnS_2NR) having free surfaces by adopting a modified HMDS-assisted chemical synthetic procedure. The systematic studies on the effect and importance of the clean surface on the catalyst and morphology-controlled synthesis of SnS_2 at nanolevel are also being performed. The unique multifunctional ability of the tin sulfide nanorings as photocatalysts in both removals of organic dyes, rhodamine B (Rh B) and methyl orange

(MO), and the reduction of the polluting inorganic system like Cr(VI) are explored. We have also produced SnS_2 nanoflowers (peg-SnS_2NF) with the poly(ethylene glycol) (PEG) template, carried out a comparative study, and explained the superiority of sf-SnS_2 NR over peg-SnS_2NF toward the reduction of Cr(VI) and degradation of organic dye molecules.

2.2. Experimental Section

2.2.1. Materials

Tin(IV) chloride ($SnCl_4 \cdot 5H_2O$, 99%), hexamethyldisilazane (HMDS, 99%), and thiourea (TU) (99%) were purchased from Sigma-Aldrich, USA. Potassium dichromate ($K_2Cr_2O_7$, 99%), Rh B (99%), and MO (99%) were obtained from Merck, India. All chemicals were used without any further purification.

2.2.2. Synthesis Section

2.2.2.1. Synthesis of Surfactant Free-SnS_2 Nanorings (sf-SnS_2NR)

Surfactant-free tin disulphide (sf-SnS_2) nanomaterials were prepared by a one-pot approach using standard Schlenk line techniques under an inert atmosphere. The typical procedure is as follows. The precursors of tin ($SnCl_4 \cdot 5H_2O$ = 0.200 g, 0.57 mmol) and sulphur (thiourea = 0.086 g, 1.14 mmol) were added in a 1:2 ratio and were mixed with excess hexamethyldisilazane (HMDS) (5 mL, 23.85 mmol) in a 100 mL two-necked flask under a N_2 atmosphere (Table 2.1). The temperature was raised and refluxed for 3 h to complete the reaction. After cooling, the obtained yellow particles were collected by centrifugation and washed with abundant deionized water and methanol to remove unreacted starting materials. Finally, the product was dried under vacuum at 120 °C for 3 h before further analysis.

2.2.2.2. Synthesis of PEG-SnS_2 Nanoflowers (peg-SnS_2NF)

To prepare peg-SnS_2NF, we have followed the same experimental procedure as mentioned above. Additionally, poly(ethylene glycol) (PEG-400) (10 mL) was added to the reaction flask containing other reactants: tin and sulphur sources, (Table 2.1) and

HMDS. After completion of the reaction, the resultant yellow powder was isolated and washed many times with deionized water (3 × 20 mL) followed by methanol (3 × 20 mL) repeatedly, separated by centrifugation, and dried at 120 °C for 3 h for analysis.

Table 2.1. Reaction Conditions for the Synthesis of SnS_2 Diverse Nano architectures.

S.no.	Amount of $SnCl_4.5\ H_2O$ in (g)	Amount of thiourea (TU) (g)	Amount of HMDS (mL)	Amount of surfactant (PEG) (mL)	Morphology
1	0.2	0.16	5 mL	No surfactant	Rings
2	0.2	0.16	5 mL	10 ml	flowers
3	0.2	0.16	0 mL	No surfactant	No reaction

2.2.3. Photocatalytic Activity

2.2.3.1. General Description of Photocatalytic Activity Test

The photocatalytic activities of both sf-SnS_2NR and peg-SnS_2NF were assessed from the experiment of degradation/reduction of different pollutants. All of the photocatalytic tests were performed under standard conditions at room temperature with exposure to natural sunlight, which covered the entire wavelength distribution of the light in the visible region.

The photocatalyst (SnS_2 or peg-SnS_2; 30 mg) was added to 60 mL of either Rh B (5 mg/L), MO (5 mg/L), or Cr(VI) (100 mg/L of pH 3) aqueous solution separately. Then, the reaction mixtures were stirred under dark for 1 h under the open environment at room temperature to ensure the formation of the adsorption−desorption equilibrium between the catalyst and reactants. Then, from the stock solution, 60 mL of suspension was positioned inside a beaker and irradiated with the sunlight. After regular intervals of time, 3 mL of a sample was taken and centrifuged at 3000 rpm to remove the catalyst. The concentrations of the reaction mixture in the supernatant solution were determined by recording absorption spectra. A gradual decrease in the characteristic absorption peak at 550 nm (Rh B), 450 nm (MO), and 350 nm (Cr(VI)) was noted, and each experiment was

repeated twice. The reduction and degradation efficiency was calculated by using the following eq-1:

$$\eta = (C_0 - C)/C_0 \times 100\% \qquad (1)$$

The photocatalytic degradation rate of Cr(VI) and organic dyes followed the Langmuir−Hinshelwood eq-2

$$\ln(C_0/C) = k_{app}t \qquad (2)$$

Where k_{app} is the apparent rate constant of the pseudo-first order, t is the irradiation time, and C_0 and C are the initial and instant residual concentrations of the Cr(VI), Rh B and MO solution. Reduction and degradation experiments were carried out on a recycled SnS_2 sample to study the stability of the SnS_2 photocatalyst.

2.2.3.2. Cr(VI) Reduction Test

The photocatalytic reaction was performed at room temperature. In a beaker, 30 mg of photocatalyst and 60 mL of 100 mg L^{-1} $K_2Cr_2O_7$ aqueous solution (pH = 3) were stirred for a sufficient amount of time to reach the adsorption−desorption equilibrium. Then, it was exposed to sunlight to initiate the reaction. To confirm the photocatalytic reduction of Cr(VI), we have performed few controlled reactions by following our previous article [18, 19]. The Cr(VI) reduction to Cr(III) was confirmed by forming a metal complex with 2,6-pyridine dicarboxylic acid (PDCA).

2.2.3.3. Degradation of Organic Dyes

The photocatalytic dye degradation experiments were performed by measuring the optical absorption of the organic pollutants. By determining the peak intensity of the dye against time in the presence of catalyst under visible light irradiation, the photocatalytic activity was studied. Thirty milligrams of sf-SnS_2 NR or peg- SnS_2 NF was utilized for the degradation of 60 mL of 5 mg L^{-1} solutions of Rh B and MO respectively.

2.2.3.4. Catalyst Reproducibility and Stability

Initially the stability of synthesized SnS_2 nanostructures was checked by execution of XRD studies on the samples stored up to 1 month. All the photocatalytic experiments were repeated several times by varying the amounts of catalyst and concentrations of the substrates. The reduction of Cr(VI) and dye degradation were carried out up to 10 times with the recycled SnS_2 catalyst to check the stability of the catalyst and reproducibility of the obtained results. At the end of each cycle, the photocatalyst was recovered by centrifugation, washed with 1 M nitrite acid solution and deionized water to diminish the amount of Cr(III) and organic dyes deposited on the surface of the catalyst, and dried under vacuum at 60 °C for 4 h.

2.2.4. Instrumentation

XRD patterns of the products were collected at room temperature using a Bruker D8 X-ray diffractometer (XRD) with a scan rate of 1° min^{-1} in a 2θ range from 10° to 80° (Cu Kα = 1.54 Å; operating current = 30 mA; operating voltage = 40 kV). Surface morphology, particle size, and energy-dispersive spectroscopy (EDS) were studied using an Ultra 55 Carl Zeiss instrument (operating voltage = 10 kV). To do TEM measurements, the as synthesized nanomaterials were suspended in isopropanol followed by sonication for 3 min and then dispersed on carbon-coated copper grids (200 mesh). Images were acquired using an FEI Technai G2 20 STEM with a 200 kV acceleration voltage.

The Raman spectra were recorded using a Renishaw microscope at a wavelength of 632 nm. A JASCO 5300 spectrophotometer was used to record the Fourier transform infrared (FT-IR) spectra on the KBr pellet containing the samples. Solid-state UV−vis absorption spectra were recorded with a Shimadzu UV-3600 UV−vis spectrometer. UV−vis diffuse reflectance spectra of the as-synthesized SnS_2 materials were recorded and transformed into the absorption spectra using the Kubelka−Munk function. The direct band gaps of SnS_2 nanostructures were obtained from the Tauc plot (where n = 1/2). Solution-phase UV spectra during photocatalysis reactions were recorded using a JASCO-V770 UV−vis spectrophotometer. Surface area and pore size analyses were

determined from the BET studies, and BET analysis was recorded by the Quantachrome Instruments.

2.3. Results and Discussion

2.3.1. Synthesis, Characterization, and Morphological Analysis

In this chapter we have discussed about the synthesis of SnS_2 nanostructures with two important themes-one without an organic surfactant molecule and other with a good amount of surfactant (PEG) covering the surface of the particles. Simple reactants/reagents were used to synthesize these materials by single-step procedure to minimize residuals and impurities (Scheme 2.1).

The method utilized could successfully evolve two types of morphologies, without any surfactant involvement it yielded sf-SnS_2 NR and with the addition of surfactant PEG it incubated peg-SnS_2NF. In these reactions, the role of HMDS was multiple since it acted as a solvent, reducing agent and also decorated the surroundings like the capping agent during the reaction. In the presence of metal sources and thiourea, HMDS led to the formation of a polymeric network by preventing the aggregation of the nanostructures. After the completion of reaction by applying high vacuum and by washing, HMDS and other residual impurities of precursors were easily removed and stoichiometric SnS_2 nanostructures were obtained. In this reaction setup the HMDS molecules served as medium for the reaction but didn't form a part of either source materials or the product, and so reaction was termed as the HMDS assisted synthesis.

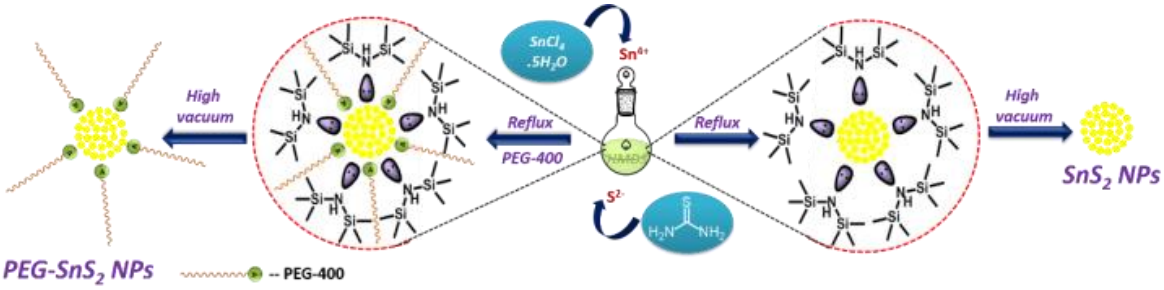

Scheme 2.1. Schematic Illustration of Synthesis of sf-SnS_2NR and peg-SnS_2NF.

The typical X-ray diffraction patterns aided us to explore the structural properties of the as-synthesized SnS_2 nanostructures (Figure 2.1a). The peaks were indexed according to JCPDS data card no. 23-0677, and the corresponding peaks confirmed the formation of the hexagonal structure of SnS_2 [20]. No peaks other than the characteristic peaks of SnS_2 nanostructures were observed, hence confirming the phase purity of the sample. The samples were further investigated by Raman spectra (Figure 2.1b) for the signature of vibrational modes of the SnS_2 material. The spectra of both samples showed the strong characteristic peaks at 313.78 and 313.56 cm^{-1} for the sf-SnS_2NR and peg-SnS_2NF samples respectively, which could be assigned to the A_{1g} mode of SnS_2 [21].

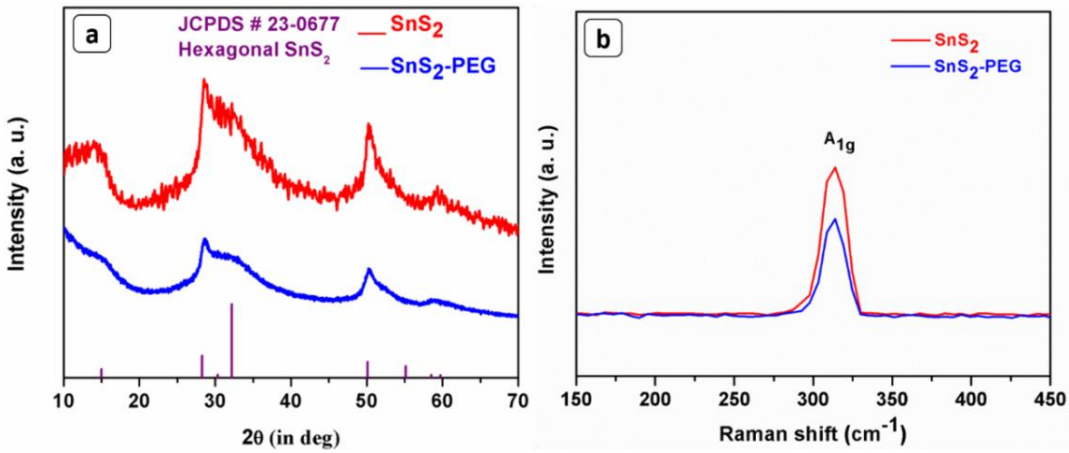

Figure 2.1. Primary characterization of SnS_2 nanocatalyst. (a) XRD pattern of sf-SnS_2NR and peg-SnS_2NF. (Hexagonal SnS_2 (JCPDS no. 23-0677)). (b) Raman spectroscopy of the SnS_2 nanostructures.

Figure 2.2a displays optical absorption by SnS_2 nanostructures within the UV and visible light spectra of wavelength ranging 250−700 nm. The absorption maximum of the materials lays around 385 nm [22]. The broad spectrum of both the nanostructures and the shift in wavelength of peg-SnS_2 in the visible region of could be explained on the basis of quantum confinement. Since the absorption falls in the visible region and the bandgap determined by the Tauc method was found to be around 2.50 eV hence confirming a good photocatalytic nature of the materials. The band gaps determined from DRS spectra recorded for both the nanorings and nanoflowers (Figure 2.2b) were 2.55 and 2.45 eV, respectively [23].

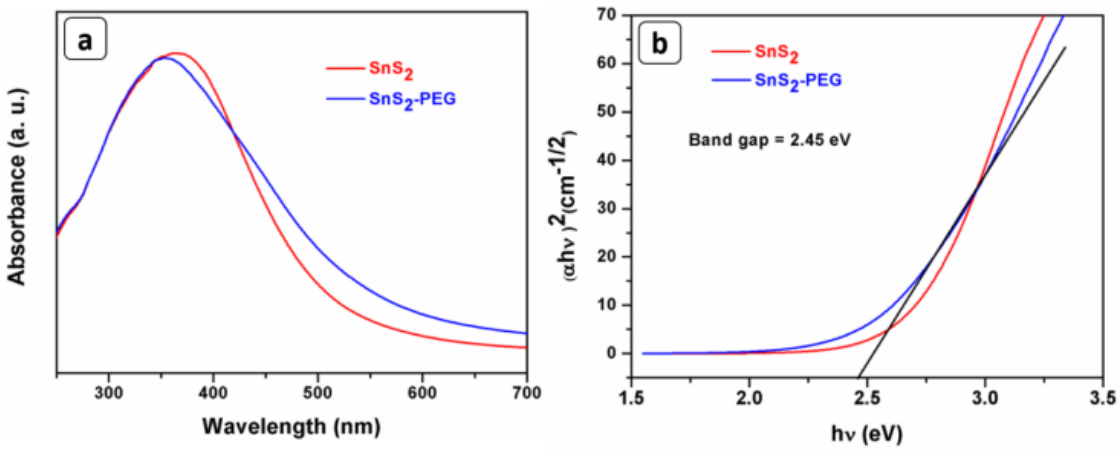

Figure 2.2. Optical study of SnS_2 nanostructures. (a) UV−vis DRS spectra of sf-SnS_2NR and peg-SnS_2NF samples. (b) Band gap calculations of the SnS_2 nanostructures.

The morphology of the resulting powdered sample from the reaction was analyzed by field emission scanning electron microscopy (FESEM) and transmission electron microscopy (TEM). The typical low- and high magnification FE SEM images of the sf-SnS_2 (Figure 2.3a, b) clearly revealed that the sample is built of with nanorings (represented as sf-SnS_2NR) with an average diameter of 50 nm. Similarly the low- and high magnification FESEM images of the as-synthesized peg-SnS_2 nanostructures (Figure 2.3c, d) displayed the nanoflower (represented as peg-SnS_2NF) morphology with an average diameter of 100 nm. Even after the vigorous ultrasonic treatment, the hierarchical structures maintained their integrity showing the structural stability of the products.

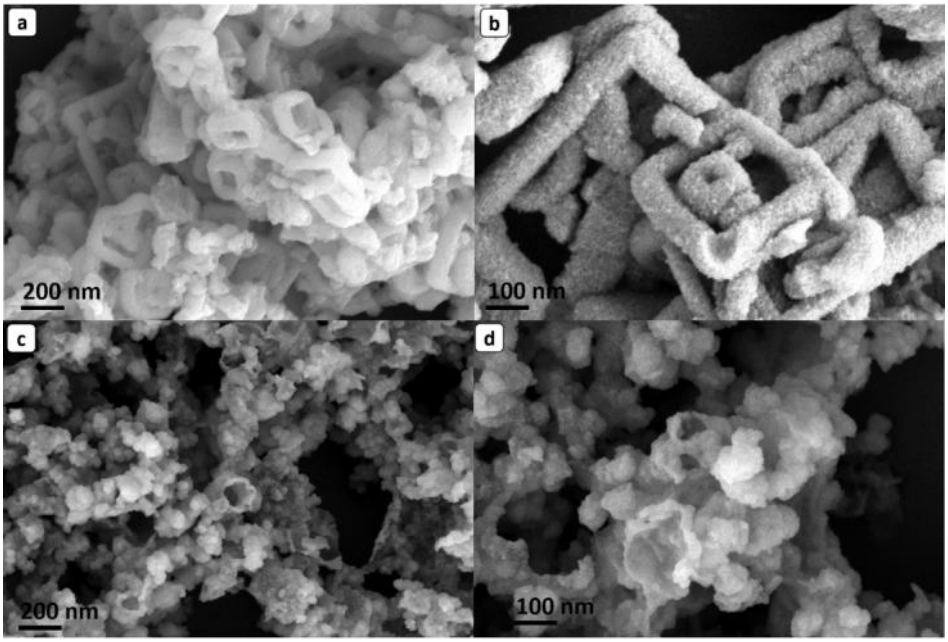

Figure 2.3. Morphological study of SnS_2 nanostructures. (a, b) low and high FESEM micrographs of sf-SnS_2NR. (c, d) low and high FESEM micrographs of peg-SnS_2NF.

Analysis by TEM also confirmed the formation of nanorings of the sf-SnS_2 and nanoflowers of peg-SnS_2 nanostructures (Figure 2.4a, b and d, e).

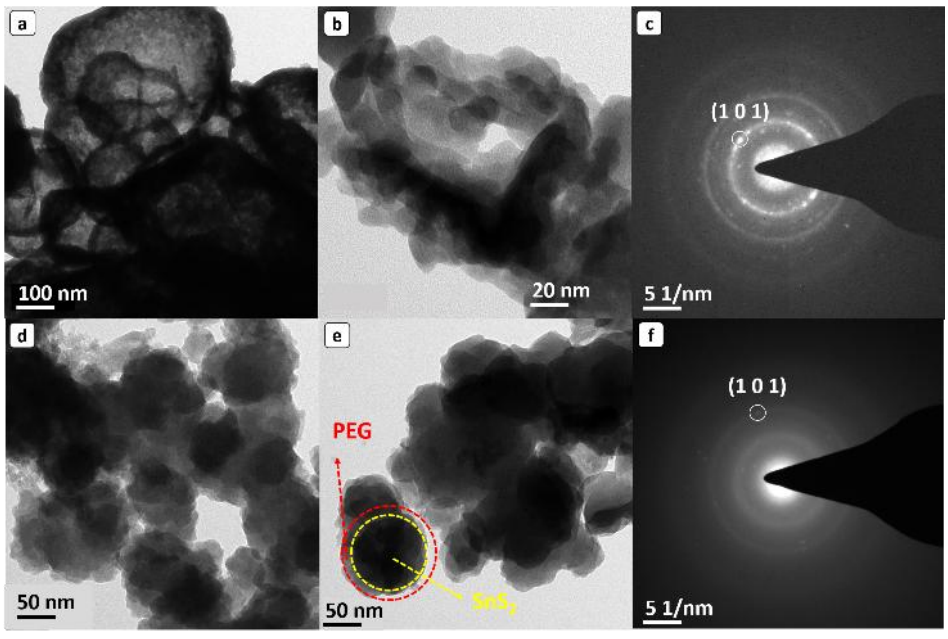

Figure 2.4. TEM data for the SnS_2 nanostructures: (a, b) sf-SnS_2NR, (d, e) peg-SnS_2NF, and (c, f) selected area diffraction pattern for both SnS_2 nanostructures.

The diffraction pattern (Figure 2.4c) consists of polycrystalline rings that can be indexed to the SnS_2 phase (standard diffraction file no. 23-0677). The rings were continuous and devoid of any separate bright spots indicating the crystalline nature of sf-SnS_2NR. A diffraction pattern (Figure 2.4f) for peg-SnS_2NF showed the amorphous ring pattern indicating that the PEG had indeed stabilized the SnS_2NF.

The X-ray photoelectron spectroscopy (XPS) was recorded to conclude the chemical composition and bonding configuration of the as-synthesized materials. The XPS spectrum (Figure 2.5a, survey spectrum sf-SnS_2NR) revealed the presence of Sn and S elements only, and no other elements like N or Si were noticed. These findings clarified that synthesized materials were free from the surfactant on the surfaces of the catalyst. The obtained results were in consistent with the XRD and EDS results.

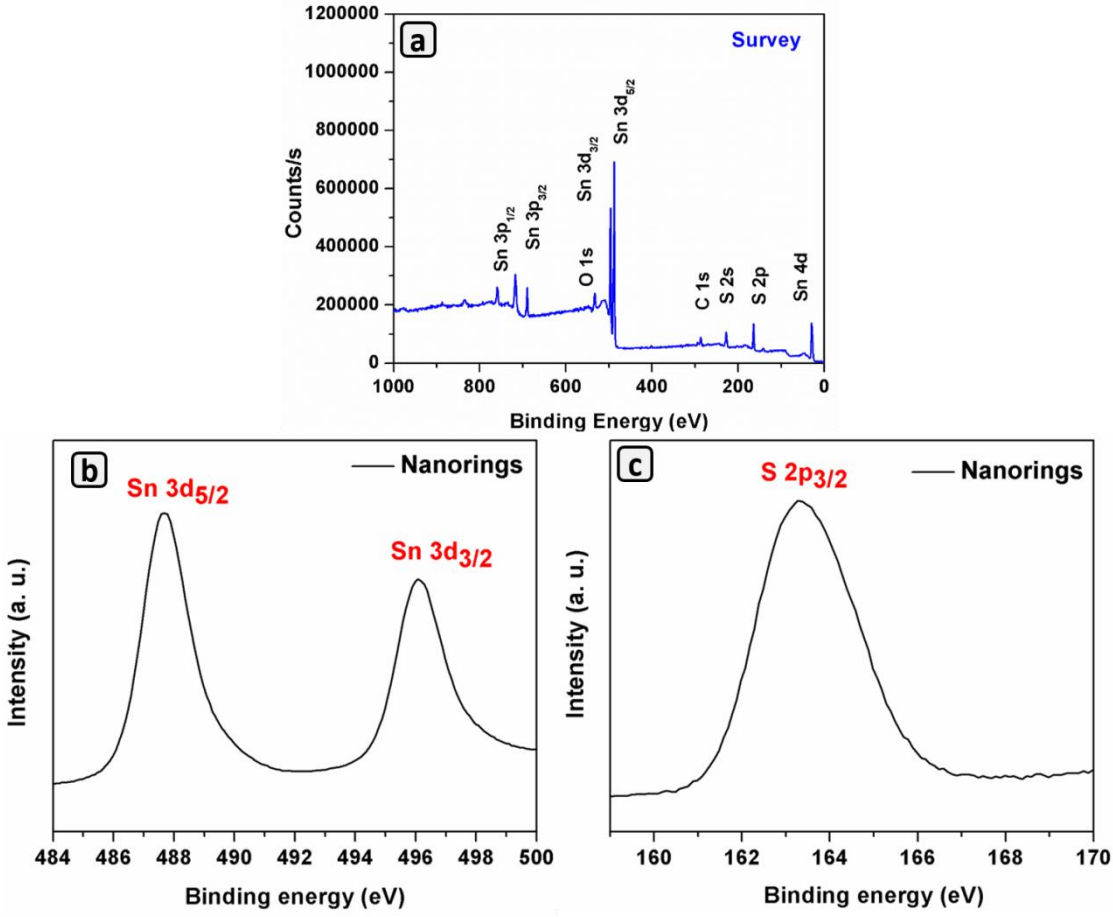

Figure 2.5. XPS spectrum of the as synthesized sf-SnS_2NR for the elements: (a) survey spectrum, (b) Sn 3d, and (c) S 2p.

Characteristic high-resolution XPS spectra of Sn 3d and S 2p are shown in Figure 2.5 b, c. The binding energies of Sn $3d_{5/2}$ (487.66 eV), Sn $3d_{3/2}$ (496.12 eV), and S $2p_{3/2}$ (163.30 eV) in SnS_2 nanostructures were in agreement with the reported characteristic values of Sn^{4+} and S^{2-} in SnS_2 [24].

The broad band peak at 545 cm^{-1} in the FTIR spectrum of sf-SnS_2NR was due to the vibration of Sn−S bands (Figure 2.6). The absence of any peak related to HMDS in the FTIR spectrum of Figure 2.6 b confirmed the complete absence of the capping agent on the surfaces of SnS_2 nanorings [18]. The presence of the signature of PEG (Figure 2.6 d) in the FTIR spectrum confirmed that PEG has effectively worked as a surfactant to stabilize SnS_2 NF.

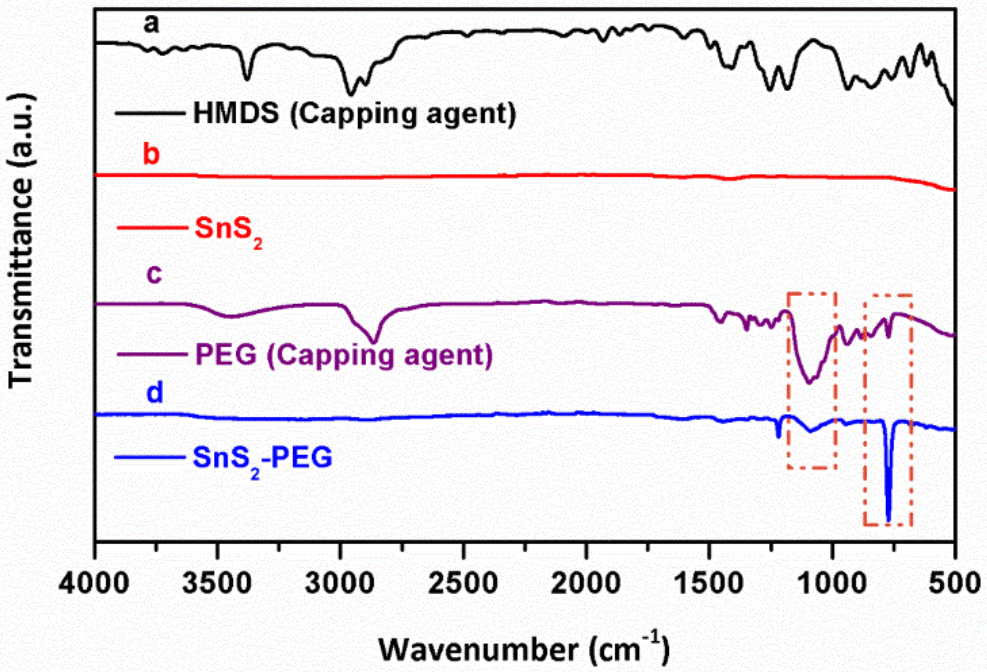

Figure 2.6. FTIR spectra of the as synthesized SnS_2 nanostructures: (a) sf-SnS_2NR and (b) peg-SnS_2NF.

The photocatalytic application is mainly dependent on surface contact, and hence, the surface area of the materials is an essential factor. We have determined the surface area by the nitrogen adsorption−desorption isotherm for both the SnS_2 nanostructures (Figure 2.7). It was observed clearly that both the materials were mesoporous, and the BET surface areas for sf- SnS_2 NR and peg-SnS_2 NF were 26.33 and 33.60 m^2g^{-1}, respectively.

The surface area of the flower-like nanostructures was found to be higher than that of the ring-like nanostructure. This observation was quite the opposite of the catalytic activity performance (vide infra).

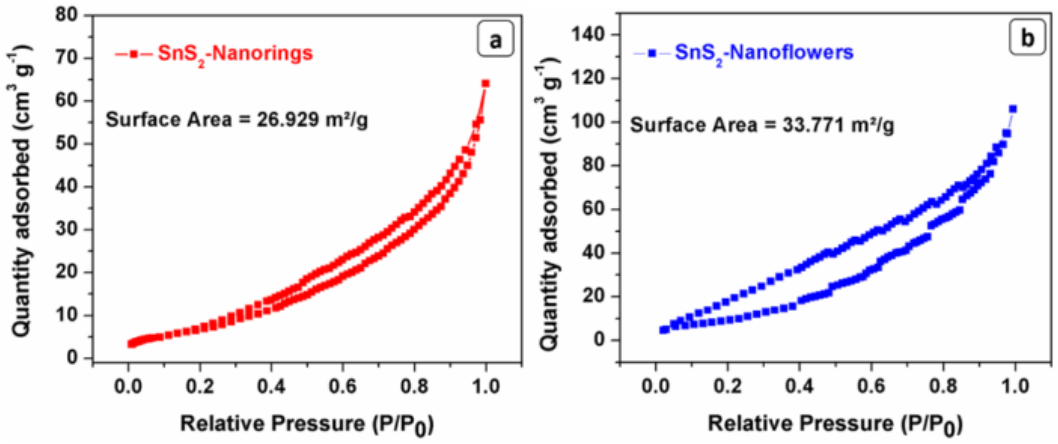

Figure 2.7. Nitrogen adsorption−desorption isotherm of the SnS_2 nanomaterial: (a) sf-SnS_2NR and (b) peg-SnS_2NF.

2.3.2. Photoreduction of Cr(VI) to Cr(III)

The results displayed in Figure 2.8 elucidate the photocatalytic reduction of aqueous Cr(VI) (at pH 3) using sf-SnS_2NR and peg-SnS_2NF as catalysts under visible light irradiation. Few controlled reactions (Figure 2.9) were performed wherein the direct photolysis (in the absence of catalyst) or catalysis (in the absence of light) alone could not drive the reduction of Cr(VI). Therefore, the reduction of aqueous Cr(VI) was the photocatalytically driven reaction completely rather than simple physical adsorption of Cr(VI). The formation of photoreduced product Cr(III) from the toxic Cr(VI) in all these reactions was confirmed by coordinating it with PDCA (Figure 2.10) [18].

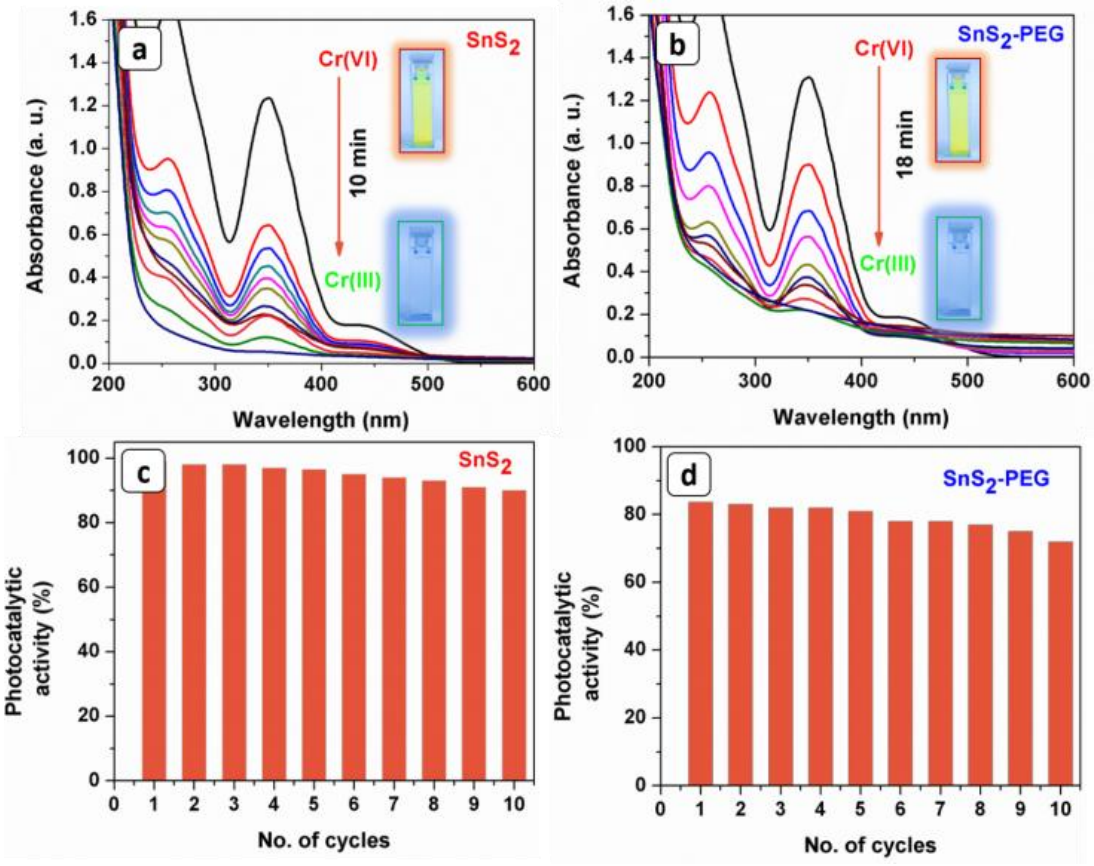

Figure 2.8. Photocatalytic reduction of Cr(VI) to Cr(III) using SnS_2 nanostructures as the photocatalyst. (a, b) The absorption spectra showing a gradual decrease in the typical peak intensity at λmax = 350 nm, by using sf-SnS_2 NR, corroborating 99% reduction of Cr(VI) in 10 min and by using peg-SnS_2 NF, 84% reduction of Cr(VI) in 18 min. (c, d) The recyclability of the SnS_2 nanostructures.

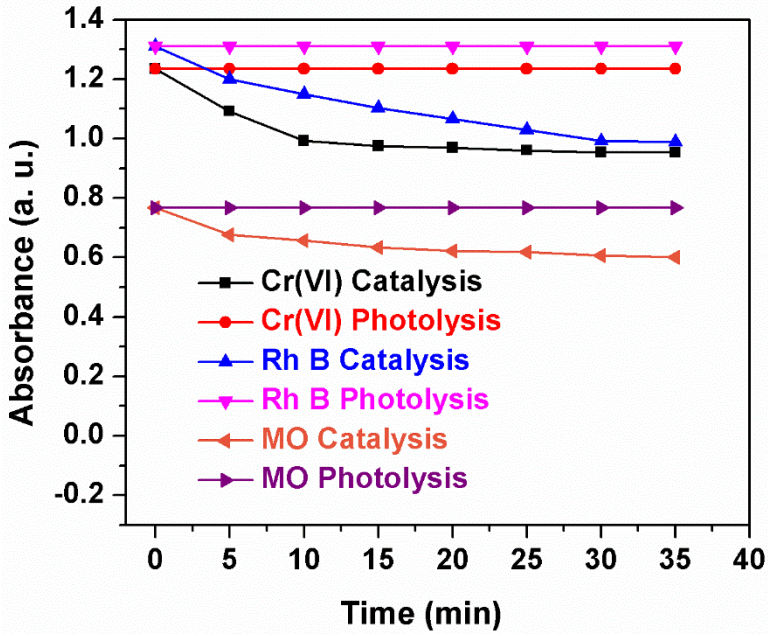

Figure 2.9. Controlled reactions of Cr(VI) reductions, Rh B and MO degradation reactions.

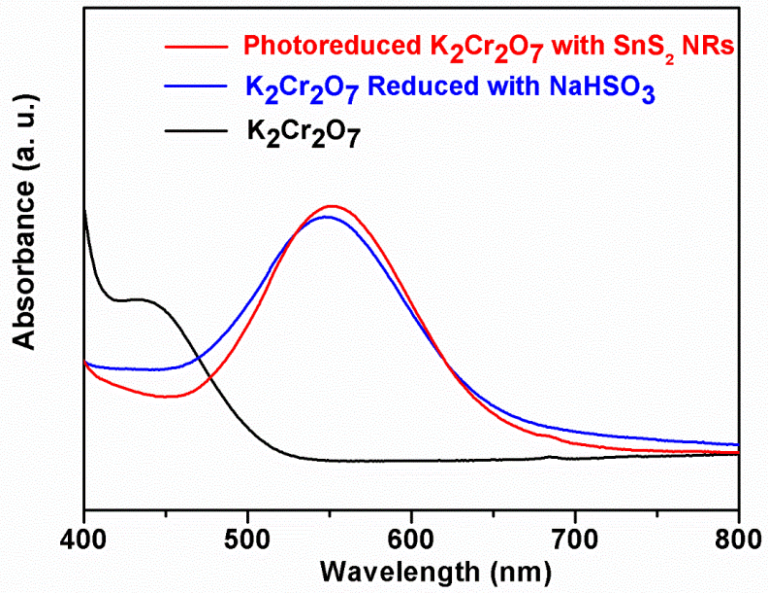

Figure 2.10. UV–vis spectra of PDCA treated solutions of $K_2Cr_2O_7$, $K_2Cr_2O_7$ reduced with $NaHSO_3$, and photoreduced $K_2Cr_2O_7$ with SnS_2 nanoparticles.

In the presence of the sf-SnS_2 NR catalyst, the toxic Cr(VI) reduction happened swiftly with a reaction rate of 0.244 min^{-1}, approached 99% reduction, and reached the equilibrium in 10 min. While in the case of peg-SnS_2 NF, a reaction rate of 0.0982 min^{-1}

was observed and approached only 84% reduction in 18 min. Hence, the sf-SnS_2NR acts as a more active photocatalyst for the reduction of Cr(VI) compared to photocatalysts in earlier reports (Table 2.2). Interestingly, in the case of catalytic decomposition of hydrogen peroxide, Zboril and co-workers also noticed high catalytic activity of iron(III) oxide nanoparticles having relatively lesser surface area [25]. All these results supported our assumption clearly on the importance of clean surfaces on catalysts rather than the larger surface area.

Table 2.2. Comparison table of numerous catalysts with various dopant materials for Cr(VI) reduction.

Catalyst	**Cr(VI) conc.**	**Catalyst**	**Time (min)**	**Ref**
SnS_2	100 ml of 50 mg L^{-1}	100 mg	120	[26]
SnS_2	50 ml of 50 mg L^{-1}	50 mg	90	[27]
RGO-SnS_2	300 ml of 100 mg L^{-1}	200 mg	120	[28]
MOSF-SnS_2	50 ml of 50 mg L^{-1}	50 mg	100	[29]
CNF-SnS_2	50 ml of 50 mgL^{-1}	50 mg	90	[30]
g-C_3N_4/SnS_2	100 ml of 50 mg L^{-1}	40 mg	50	[31]
Ag_2S-SnS_2	70 ml of 50 mg L^{-1}	70 mg	60	[32]
SnO_2- SnS_2	80 ml of 2 x10^{-4} M	20 mg	180	[33]
SnS_2-TiO_2	80 ml of 100 mg L^{-1}	40 mg	100	[34]
*SnS_2	60 ml of 100 mg L^{-1}	30 mg	10	Present work

2.3.2.1. Effect of Amount of Catalyst and Pollutant Cr(VI)

It was necessary to understand the catalyst loading parameters after the results above confirmed about the stability and rapid photocatalytic activity of the sf-SnS_2 NR toward the reduction of toxic Cr(VI). Therefore, the effect of the concentration of Cr(VI) and the amount of catalyst on the rate of the reaction were studied while keeping the other

parameters constant. Figure 2.11 shows the reduction of Cr(VI) when the catalyst (sf-SnS_2NR) quantities were varied. The irradiation time required for the complete reduction of Cr(VI) decreased with increasing initial dosage of the SnS_2 photocatalyst. It was observed that k_{app} depends on the concentration of the Cr(VI) solution and the amount of catalyst added. When the amount (between 0.15 and 0.60 g L^{-1}) of sf-SnS_2 NR catalyst was varied, there was an incremental change in the photocatalytic performance. The rate constant of the reduction reaction had the linear relationship (from 0.01507 to 0.81122 min^{-1}) with the amount of catalyst dosage. The increase of the efficiencies of Cr(VI) reduction with the increase of the initial amount of SnS_2 can be ascribed to the increase in both absorbed light and the numbers of surface active sites. These results suggested that the photocatalytic activity of sf-SnS_2NR could be improved by increasing the amount of catalyst.

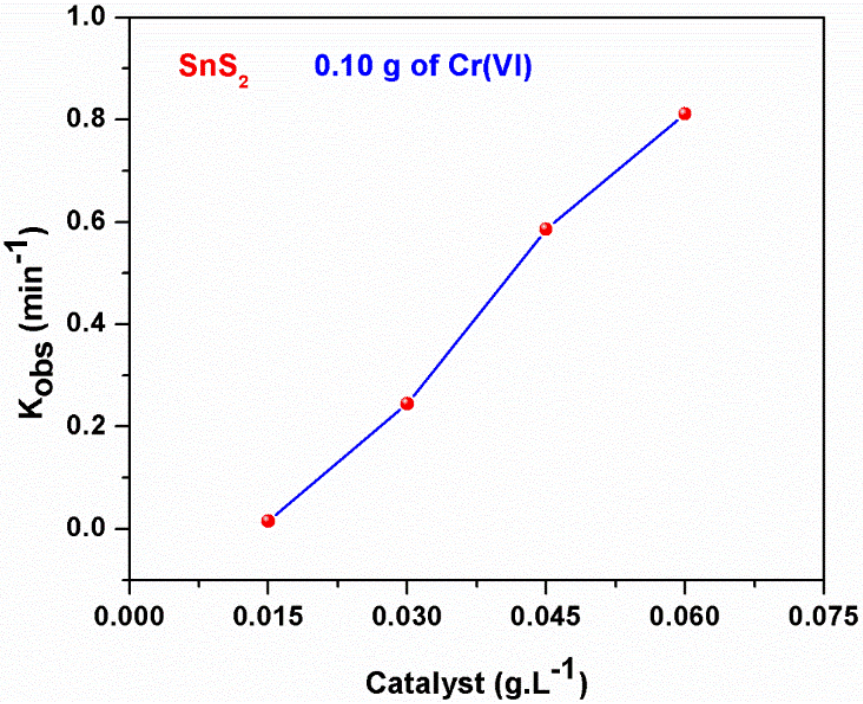

Figure 2.11. Influence of amount of catalyst on the photocatalytic reduction of toxic Cr(VI) to nontoxic Cr(III) using sf-SnS_2NR as the photocatalyst. Catalyst dosage had a linear relationship with the rate constant.

Furthermore, Figure 2.12 depicts the effect of initial concentration of Cr(VI) aqueous solution on the photocatalytic reduction of Cr(VI) while keeping the catalyst dosage (sf-

SnS_2 NR) constant. It was established that the efficiencies of reduction of Cr(VI) in photocatalytic systems consisting of 100 and 200 mg L^{-1} Cr(VI) were observed to be 99 and 81%, respectively (Rate constants were 0.244 and 0.088 min^{-1}). The decrease in the efficiencies of the reduction reaction with the increase of initial Cr(VI) concentration can be attributed to the following two aspects. First, since the reaction occurs on the surface of the photocatalyst, the limited surface active sites of the photocatalyst are not sufficient at higher Cr(VI) concentration. Second, Cr(VI) in a high concentration can absorb the visible light (420−480 nm), thus decreasing the proportion of light received by the SnS_2 photocatalyst.

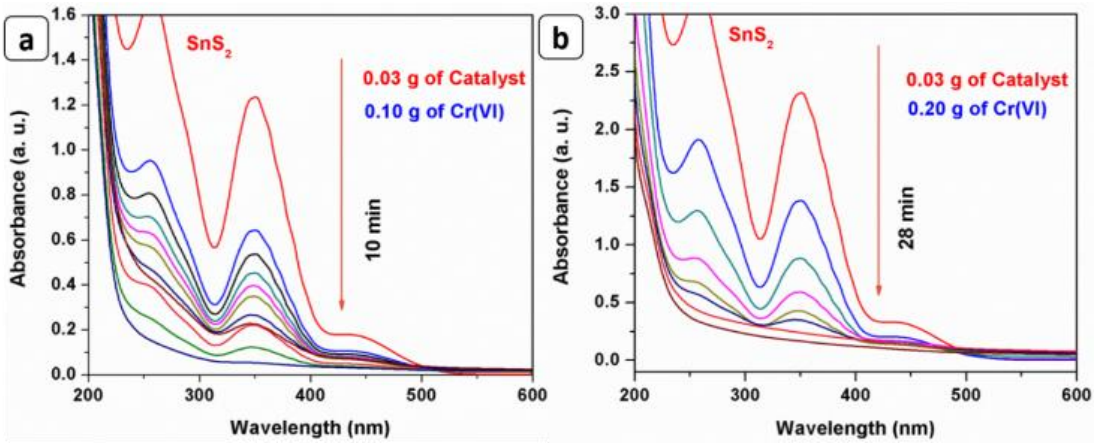

Figure 2.12. Influence of concentration of Cr(VI) (catalyst dosage constant, 0.03 g) on the photocatalytic reduction of toxic Cr(VI) to nontoxic Cr(III) using sf-SnS_2 NR as the photocatalyst. (a) 0.10 g of Cr(VI) and (b) 0.20 g of Cr(VI). Concentration of Cr(VI) had an inverse relationship with the rate constants.

2.3.2.2. Effect of pH on Cr(VI) Reduction

The effect of pH on the photocatalytic reduction of Cr(VI) in the presence of sf-SnS_2 NR was examined by keeping the photocatalyst dosage constant and varying the initial pH from 3 to 5. It was noticed that the photocatalytic reduction of Cr(VI) was retarded with increased pH (Figure 2.13). There was a gradual decrease in the rate constant: 0.24475 min^{-1} at pH 3 and 0.09406 min^{-1} at pH 5. It was witnessed that the Cr(VI) reduction at low pH was much higher than that in a high pH condition. It was assumed that the increased dissolution of sf-SnS_2 NR and along with lower concentration of H^+ in high pH

was responsible for the decreased photocatalytic activity. This is because at low value of pH the $HCrO_4^-$ is the prevailing species, with the result the catalysts surface gets enriched with protonation so accumulation of positive charge takes place which enhances the attraction between catalysts surface and $HCrO_4^-$ [35].

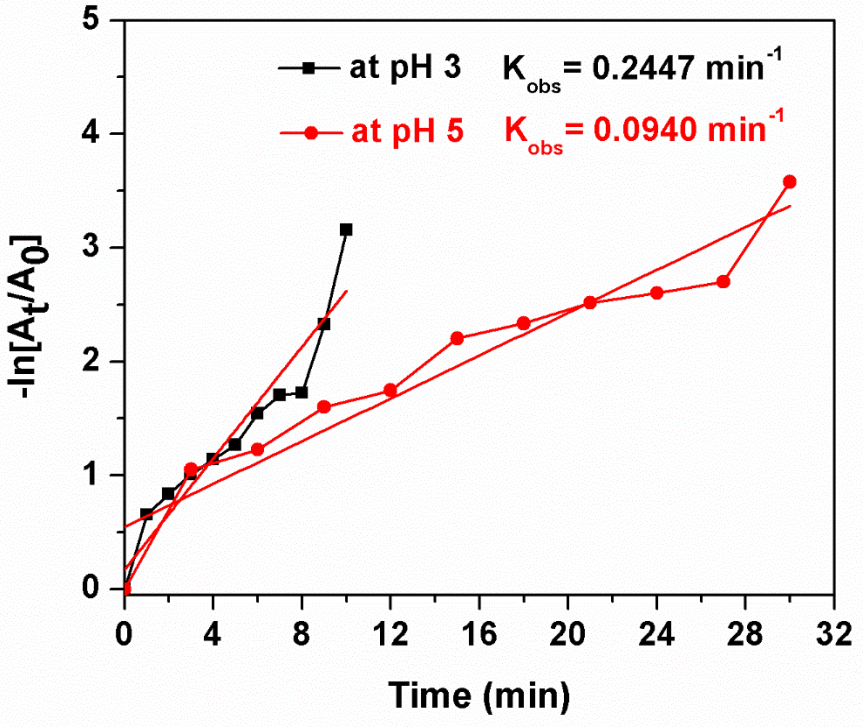

Figure 2.13. pH effect on Cr(VI) reduction by SnS_2 nanorings.

2.3.2.3. Stability and Reusability

The stability and reusability of any photocatalyst during the photocatalytic reaction are critical factors for its industrial usage. Therefore, it is necessary to study the stability of the as-synthesized sf-SnS_2NR in the photocatalytic reduction reactions involving aqueous Cr(VI). The recyclability of the catalyst for photocatalytic reduction of Cr(VI) is illustrated in Figure 2.8c. The performance of the sf- SnS_2NR photocatalyst did not show any significant loss up to 10 cycles. This revealed the durability of sf-SnS_2NR as the photocatalyst in the reduction of aqueous Cr(VI). While checking the reusability of both the SnS_2 nanostructures for 10 cycles, it was observed that there was only 5% efficiency loss for sf-SnS_2 NR, whereas, in the case of peg-SnS_2NF, the efficiency loss was 5−10% (Figure 2.8c, d).

We have analyzed the catalyst after completion of the 10th cycle using SEM and EDAS to identify the accumulation of Cr on the catalyst surface. There are no adsorbed chromium ions found over the catalyst surface (Figures 2.14 and 2.15). The XRD pattern of the materials was recorded after photocatalytic reduction, and no appreciable change in the XRD pattern occurs after the reduction process (Figure 2.16). It implies that the sf-SnS_2 NR had high stability and did not corrode during the photocatalytic reduction of Cr(VI), which showed its potential applications for the treatment of polluted water.

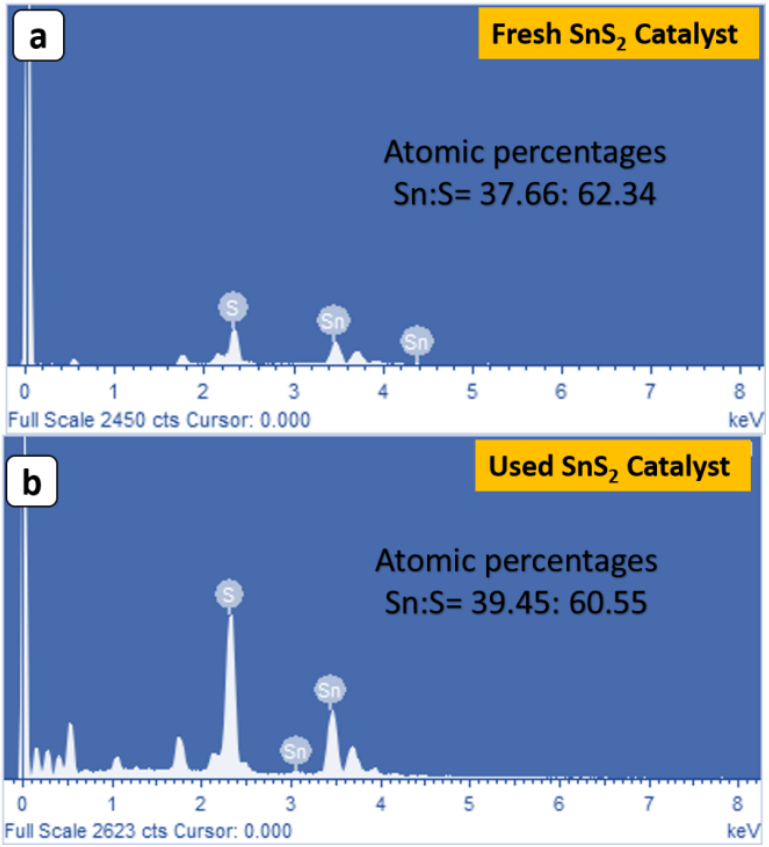

Figure 2.14. Elemental analysis by the energy dispersive X-ray spectroscopy. Atomic ratios were matched with the theoretical values. a) EDAX spectrum of fresh SnS_2 Catalyst. b) EDAX spectrum of reused SnS_2 Catalyst.

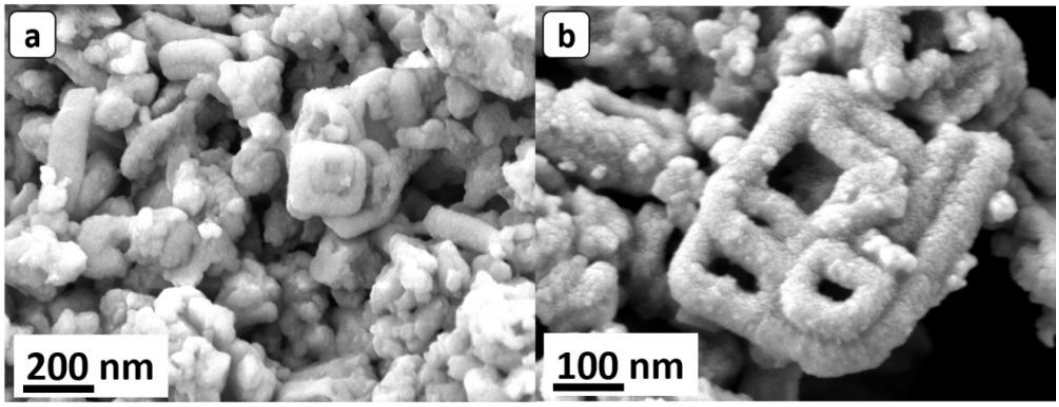

Figure 2.15. Morphological studies for the used catalyst of SnS_2 nanorings.

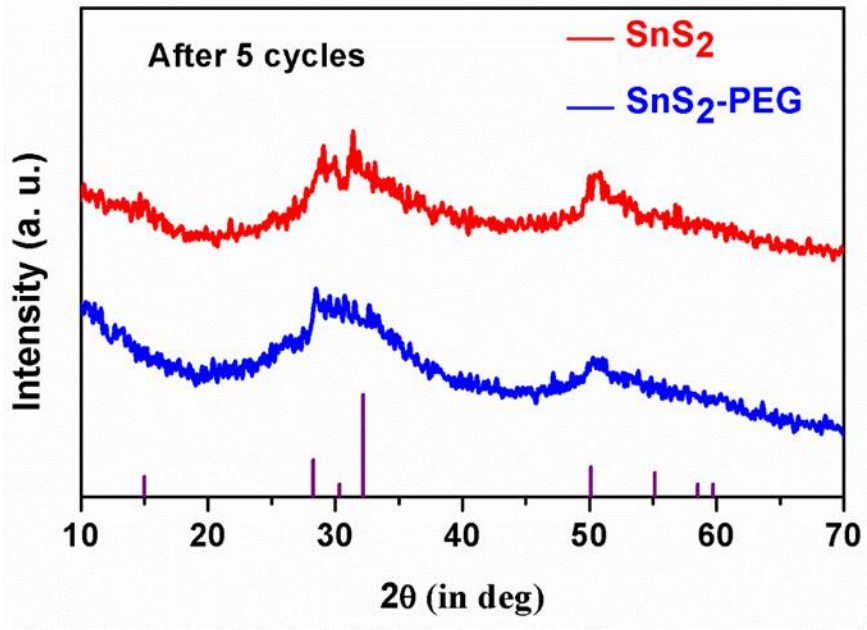

Figure 2.16. PXRD spectra of the reused SnS_2 nanostructures. Since there was no significant changes in the corresponding peaks.

2.3.2.4. Morphology Effect and the Importance of Clean Surface on the Catalyst

As confirmed above in the photocatalytic reduction of Cr(VI), the ring-like nanostructures were more efficient than nanoflower-like morphology (Figure 2.8). The rates of photocatalytic reduction of Cr(VI) by sf-SnS_2NR and peg-SnS_2NF were compared by varying the quantity of the catalysts (Figure 2.11). In every case, the sf-SnS_2NR showed superior photocatalytic activity than the peg-SnS_2NF. The variance in

the photocatalytic activity of both the SnS_2 nanostructures may be explained by the collective action of several factors. Except the specific surface area, almost all the factors were the same as revealed by the various characterization techniques, and it can be said that the difference in photocatalytic activity of SnS_2 nanomaterials was influenced exclusively by a single parameter that is, clean surfaces and morphology.

It is known that the adsorption and desorption of molecules on the surface of catalysts directly affect the photocatalytic process. Thus, the clean and surfactant free surfaces on the catalyst and high surface area of the porous sf-SnS_2NR allowed more number of surface coordination sites exposed to the solution than the peg-SnS_2NF. Moreover, the presence of clean surfaces on the catalyst surface helped more efficient transportation of the reactant molecules to the active sites and, thus, enhances the efficiency of photocatalysis. So overall, the combination of low surface area and surfactant-free surfaces of the sf-SnS_2NR make nanorings a better material for the photocatalytic reduction of Cr(VI) compared to the peg-coated nanoflower-peg-SnS_2NF.

SnS_2 having a central metal ion with the d^{10} configuration favors the separation of photogenerated charges due to the highly dispersive conduction band. Afterward when exposed to light the capture of photoexcited electron at the conduction band takes place. In this process, the separated electron commonly a photogenerated electron is involved in the reduction of Cr(VI) to generate Cr(III) [34]. As an evidence of the photoinduced interfacial charge transfer process, the photoluminescence (PL) and time-resolved photoluminescence (TRPL) of sf-SnS_2NR were recorded and compared with those of peg-SnS_2NF (Figure 2.17). The sf-SnS_2 NR showed a less intense PL peak compared to the peg-SnS_2NF (Figure 2.17a). This observation suggested that the interfacial charge transfer on sf-SnS_2 NR inhibited the recombination of photoinduced charge carriers [36]. For further confirmation time-resolved transient photoluminescence decay (TRPL) spectrum was recorded to understand this process (Figure 2.17b). The average lifetime ($\langle\tau\rangle$) of sf-SnS_2NR (1.30 ns) was found to be less than that of peg-SnS_2NF (2.49 ns). This drop in the lifetime points to the effective separation of charge carriers on sf-SnS_2NR. When the transient photocurrent responses are studied, the sf-SnS_2 NR showed a good response compared to peg-SnS_2NF (Figure 2.18).

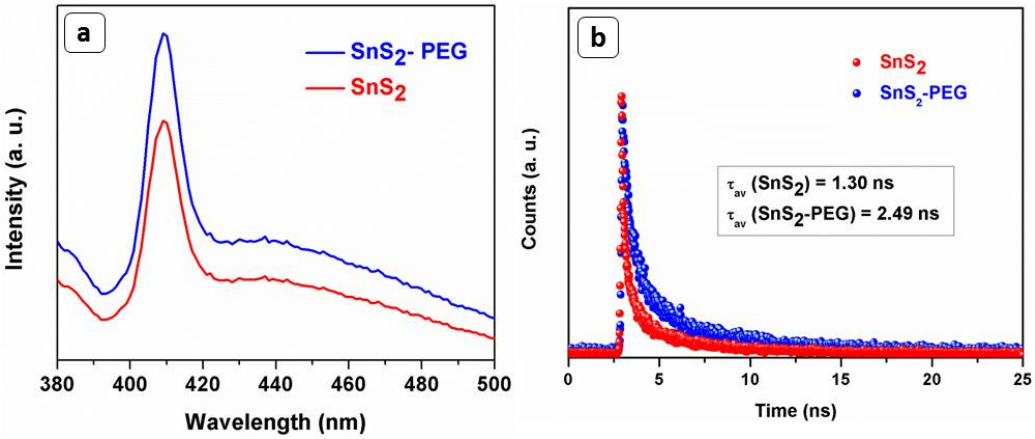

Figure 2.17. (a) Steady-state PL spectra of sf-SnS_2NR and peg-SnS_2NF. (b) Time-resolved transient PL decay of sf-SnS_2NR and peg-SnS_2NF.

This phenomenon occurs because of the smooth transfer of generated electrons from the conduction band (CB) to the valence band (VB) of sf-SnS_2NR, and this assumption was validated with the quenching of emission.

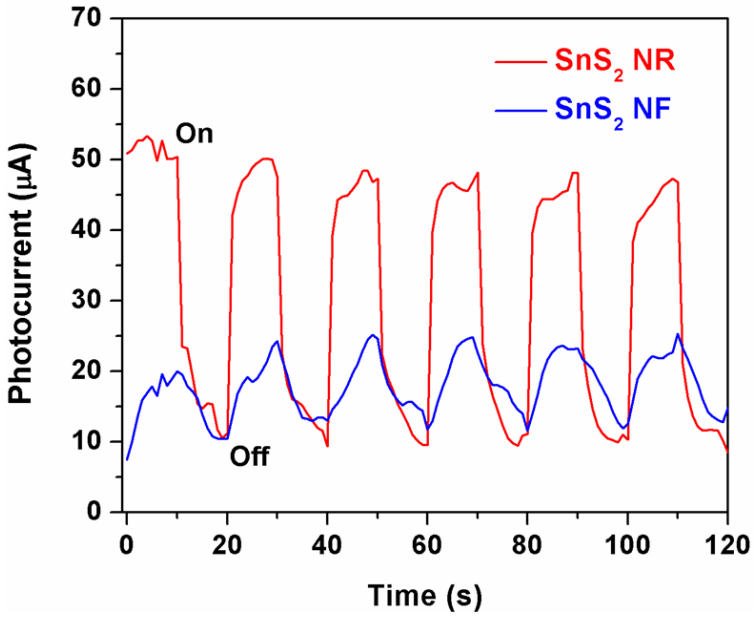

Figure 2.18. Transient photocurrent responses for the sf-SnS_2NR and peg-SnS_2NF.

2.3.7. Photocatalytic Degradation of Dyes

Apart from checking the toxic Cr(VI) reduction reactions, the synthesized sf-SnS_2NR was assessed for the degradation of toxic organic dyes contaminating water like Rh B and

MO. Figure 2.19 illustrates the degradation of Rh B by visible light irradiation (sunlight) in the presence of the sf-SnS_2NR. When the controlled reactions were performed, no reaction took place in the absence of light and SnS_2 catalyst samples, indicating the importance of the photocatalyst for the degradation of the dye (Figure 2.9). After addition of the photocatalyst, a rapid decrease in peak intensity was observed. The complete degradation of 60 mL of 5 mg L^{-1} Rh B with 30 mg of sf-SnS_2NR was observed in only 12 min. The apparent rate constant (k_{app}) calculated from the linear plot of $\ln[A_t]/[A_0]$ versus time was found to be 0.1744 min^{-1}. While in the case of peg-SnS_2 NF, it took nearly 36 min to degrade the dye and the rate constant (k_{app}) was calculated as 0.04695 min^{-1} (Figure 2.19a, b). The decrease in absorption intensity of Rh B at λ_{max} with progression of the reaction time without any shift of the absorption wavelength suggested complete de-functionalization of the Rh B chromophores.

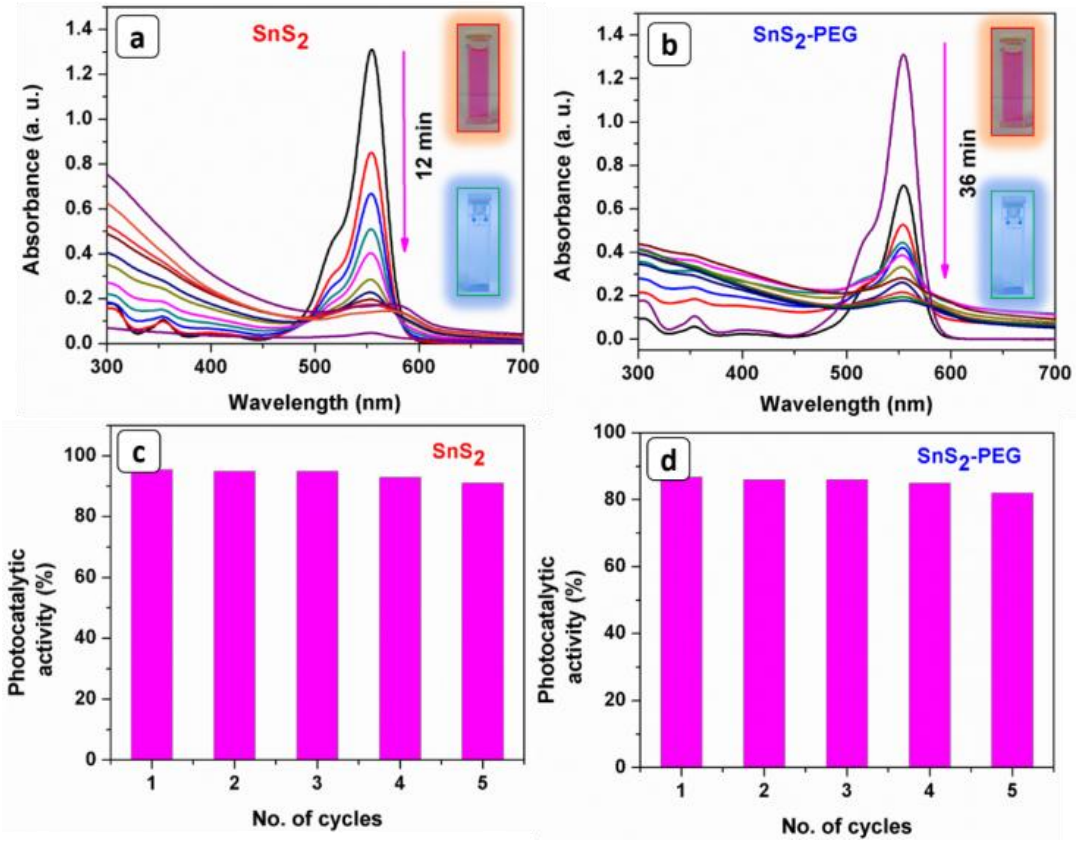

Figure 2.19. Photocatalytic activities of the SnS_2 nanostructures in the degradation of Rh B dye. (a, b) Photocatalytic reduction of Rh B using sf-SnS_2NR and peg-SnS_2NF as the photocatalyst. (c, d) The recyclability of the SnS_2 nanostructures.

The efficiency of the sf-SnS_2 NR photocatalyst for the degradation of the MO dye was also tested (Figure 2.20). Exceptional efficiency was observed in the case of MO with a rate constant (calculated from the linear plot of $\ln[A_t]/[A_0]$ vs time) of 0.06752 min^{-1} and dye degradation time of 30 min for 60 mL of 5 mg L^{-1} MO dye with 30 mg of sf-SnS_2NR (Figure 2.20a, b). While in the case of peg- SnS_2NF, it took nearly 48 min to degrade the dye, and the apparent rate constant (k_{app}) was calculated as 0.03313 min^{-1}. In these cases, no noticeable degradation and no shift in peak positions were observed in the absence of the SnS_2 catalyst under the same experimental conditions. Hence, we found that the sf-SnS_2 NR serves as the best photocatalyst for the photocatalytic reactions.

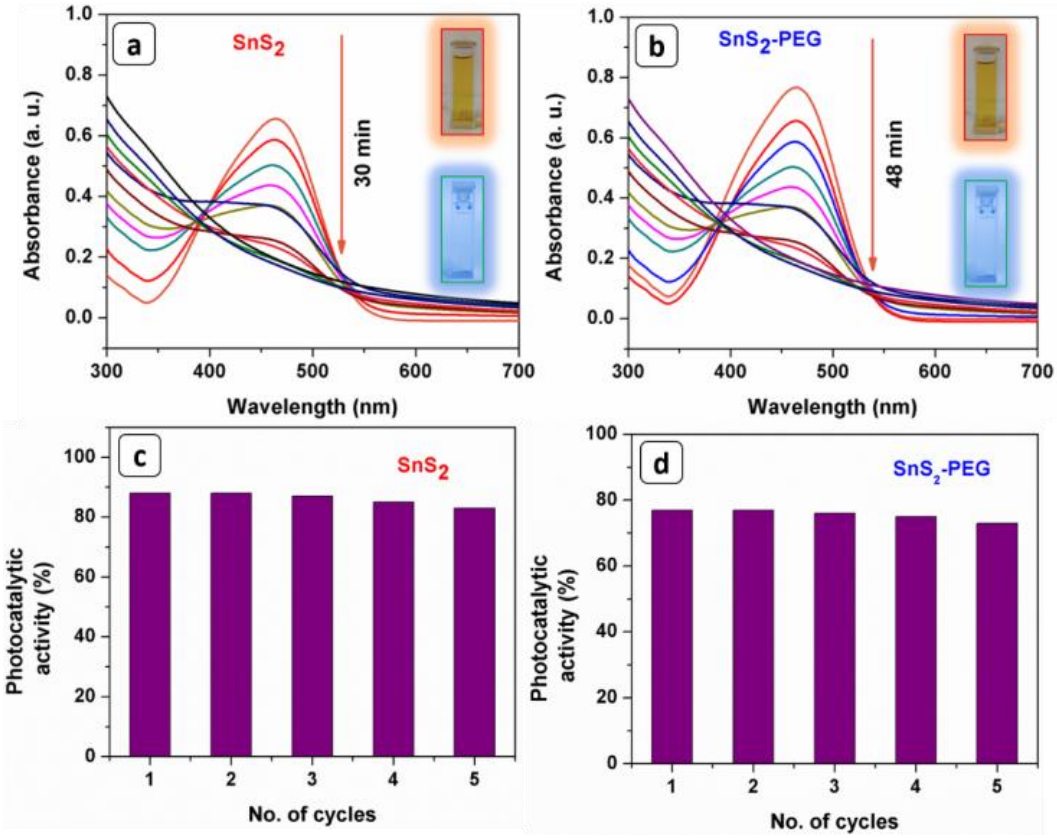

Figure 2.20. Photocatalytic activities of the SnS_2 nanostructures in the degradation of MO dye. (a, b) Photocatalytic reduction of MO using sf-SnS_2NR and peg-SnS_2NF as the photocatalyst. (c, d) The recyclability of the SnS_2 nanostructures.

The catalysts were reused in the water purification to determine the durability of the photocatalyst. For this purpose, the reaction mixture was centrifuged after each run of

the reactions to separate the catalyst. Then, the regenerated catalyst was reused with the fresh reactants in the subsequent cycle of the photocatalytic reaction under the same experimental conditions. The results showed that the sf-SnS_2NR could be used repeatedly for at least 10 times without significant deactivation. However, the peg-SnS_2NF displayed a gradual decrease in dye degradation after five cycles. The peg- SnS_2NF was not robust since it contained big-sized SnS_2 nanoflowers that may perhaps be leached easily in the liquid phase reaction.

The clean surfaces remarkably enhanced the separation efficacy of photoinduced charge carriers on sf-SnS_2 NR through the photoinduced interfacial charge transfer. The mechanism of photoreduction of Cr(VI) and degradation of RhB and MO is illustrated in Figure 2.21. Due to the narrow band gap, the sf-SnS_2NR can be excited by sunlight efficiently to produce electron−hole pairs. Due to the availability of free and clean surfaces on the catalyst, the generated charges will quickly be promoted to the excited state. Simultaneously, the recombination of electron−hole pairs was suppressed owing to the direct reduction and oxidation of pollutants. In the photocatalysis progression, the photogenerated holes were trapped by the hydroxyl groups (or H_2O) on the catalyst surface to yield OH· radicals. Meanwhile, the dissolved oxygen molecules react with electrons and yield superoxide radical anions, $O_2^{\cdot-}$, which on protonation generate the hydroperoxy HO_2, radicals. This radical forms the hydroxyl radical $OH^{\cdot}$, which involves the decomposition of the organic dye. While as the electrons and superoxide radicals cause the reduction of Cr(VI) to Cr(III). Altogether, the efficient charge separation on the clean surfaces affords the enhanced photocatalytic activities. Therefore, all these findings undoubtedly express the importance of clean surfaces on catalysts to achieve high catalytic performance [37].

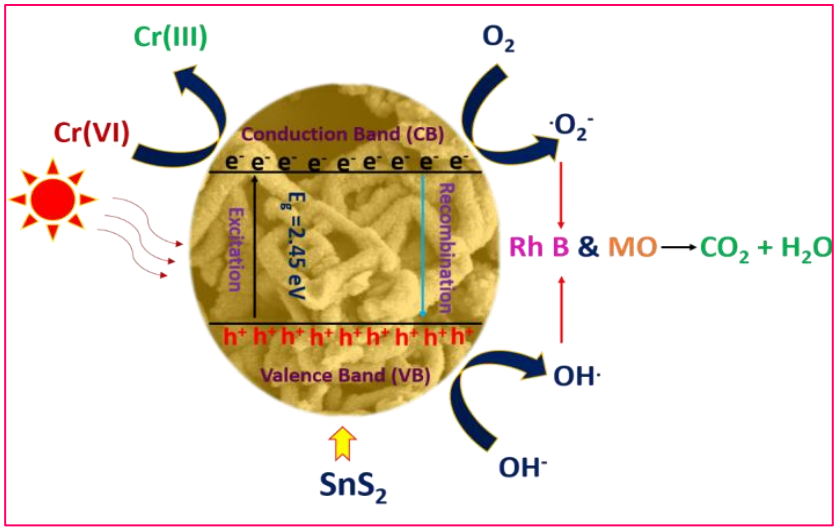

Figure 2.21. Schematic representation of mechanism of the SnS_2 photocatalyst.

2.4. Summary

In this chapter, by utilizing the simple wet chemical approach, surfactant-free SnS_2 nanorings (sf-SnS_2NR) and PEG-stabilized SnS_2 nanoflowers (peg-SnS_2NF) were prepared at gram scale. The developed semiconductor tin disulphide nanomaterials showed multiple potential applications, especially in photoreduction and photodegradation. It was emphasized that as synthesized SnS_2 nanostructures exhibited great photocatalytic activity in the reduction of carcinogenic Cr(VI) to nontoxic Cr(III) under ambient conditions. The SnS_2 nanostructures efficiently degraded mutagenic dyes (MO and Rh B) to nontoxic products in a shorter period. The improved photoactivities are ascribed to the effective charge transfer across the clean surfaces of the catalyst, as evidenced by the electron microscopic analyses and steady-state and time-resolved transient photoluminescence decay studies. In all cases, the reusability of the sf-SnS_2NR photocatalyst was excellent over many cycles.

The excellent photocatalytic behavior of SnS_2 can be credited to the following factors. (i) The clean surfaces on the catalyst enhanced electron mobility in the nanorings. (ii) The specific 2D morphology of the ring structure also contributed to the efficient charge carrier separation in the material. Therefore, the present work provides new

insight into developing photocatalysts with clean surfaces for the effective charge separation and photocatalytic remediation of pollutants from wastewater.

2.5. References

[1] Qu, J.; Fan, M. The current state of water quality and technology development for water pollution control in China. *Crit. Rev. Environ. Sci. Technol*. **2010**, *40*, 519−560.

[2] (a) Chen, C.; Ma, W.; Zhao, J. Semiconductor-mediated photodegradation of pollutants under visible-light irradiation. Chem. Soc. Rev. **2010**, *39*, 4206−4219. (b) Wittbrodt, P.-R.; Palmer, C.-D. Reduction of Cr(VI) in the Presence of Excess Soil Fulvic Acid. *Environ. Sci. Technol*. **1995**, *29*, 255−263.

[3] Wang, W.; Tadé, M. O.; Shao, Z. Research progress of perovskite materials in photocatalysis- and photovoltaics-related energy conversion and environmental treatment. *Chem. Soc. Rev*. **2015**, *44*, 5371−5408.

[4] Wang, Z.; Bush, R. T.; Sullivan, L. A.; Liu, J. Simultaneous Redox Conversion of Chromium(VI) and Arsenic(III) under Acidic Conditions. *Environ. Sci. Technol*. **2013**, *47*, 6486−6492.

[5] (a) Nasrallah, N.; Kebir, M.; Koudri, Z.; Trari, M. Photocatalytic reduction of Cr(VI) on the novel hetero-system $CuFe_{(2)}O_{(4)}$/CdS. *J. Hazard. Mater*. **2011**, *185*, 1398−1404. (b) Hashemzadeh, F.; Gaffarinejad, A.; Rahimi, R. Porous p-NiO/n-Nb_2O_5 nanocomposites prepared by an EISA route with enhanced photocatalytic activity in simultaneous Cr(VI) reduction and methyl orange decolorization under visible light irradiation. *J. Hazard. Mater*. **2015**, *286*, 64–74.

[6] Pawar, R. C.; Lee, C. S. Sensitization of CdS nanoparticles onto reduced graphene oxide (RGO) fabricated by chemical bath deposition method for effective removal of Cr(VI). *Mater. Chem. Phys*. **2013**, *141*, 686−693.

[7] Zhang, N.; Yang, M.-Q.; Tang, Z.-R.; Xu, Y.-J. CdS−graphene nanocomposites as visible light photocatalyst for redox reactions in water: A green route for selective transformation and environmental remediation. *J. Catal*. **2013**, *303*, 60−69.

[8] Liu, S.; Zhang, N.; Tang, Z.-R.; Xu, Y.-J. Synthesis of One- Dimensional CdS@TiO_2 Core−Shell Nanocomposites Photocatalyst for Selective Redox: The Dual Role of TiO_2 Shell. *ACS Appl. Mater. Interfaces* **2012**, *4*, 6378−6385.

[9] (a) Jana, S.; Srivastava, B. B.; Jana, S.; Bose, R.; Pradhan, N. Multifunctional Doped Semiconductor Nanocrystals. *J. Phys. Chem. Lett*. **2012**, *3*, 2535. (b) Xia, Q. N.; Cuan, Q.; Liu, X.-H.; Gong, X.-Q.; Lu, G.-Z.; Wang, Y.-Q. Pd/$NbOPO_4$ Multifunctional Catalyst for the Direct Production of Liquid Alkanes from Aldol Adducts of Furans. *Angew. Chem., Int. Ed*. **2014**, *53*, 9755. (c) Kumar, M.; Deka, S. Multiply Twinned AgNi Alloy Nanoparticles as Highly Active Catalyst for Multiple Reduction and Degradation Reactions. *ACS Appl. Mater. Interfaces* **2014**, *6*, 16071.

[10] (a) Lai, C. H.; Lu, M. Y.; Chen, L. J. Metal sulfide nanostructures: synthesis, properties and applications in energy conversion and storage. *J. Mater. Chem*. **2012**, *22*, 19−30. (b) Zhang, Y. C.; Du, Z. N.; Li, K. W.; Zhang, M. Size-controlled hydrothermal synthesis of SnS_2 nanoparticles with high performance in visible light-driven photocatalytic degradation of aqueous methyl orange. *Sep. Purif. Technol*. **2011**, *81*, 101−107. (c) Wei, H.; Hou, C.; Zhang, Y.; Nan, Z. Scalable low temperature in air solid phase synthesis of porous flower-like hierarchical nanostructure SnS_2 with superior performance in the adsorption and photocatalytic reduction of aqueous Cr(VI). *Sep. Purif. Technol*. **2017**, *189*, 153−161. (d) Wang, S.; Peng, T.; Zhang, Y. NH_4Cl-assisted in air, low temperature synthesis of SnS_2 nanoflakes with high visible-lightactivated photocatalytic activity. *Mater. Lett*. **2019**, *234*, 361−363. (e) Zhang, Y. C.; Yao, L.; Zhang, G.; Dionysiou, D. D.; Li, J.; Du, X. One-step hydrothermal synthesis of high-performance visible-lightdriven SnS_2/SnO_2 nanoheterojunction photocatalyst for the reduction of aqueous Cr(VI). *Appl. Catal. B* **2014**, *144*, 730−738. (f) Zhang, Y. C.; Li, J.; Xu, H. Y. One-step in situ solvothermal synthesis of SnS_2/TiO_2 nanocomposites with high performance in visible light-driven photocatalytic reduction of aqueous Cr(VI). *Appl. Catal. B* **2012**, *123*, 18−26. (g) Zhang, Y.; Zhang, F.; Yang, Z.; Xue, H.; Dionysiou, D. D. Development of a new efficient visible-light-driven photocatalyst from SnS_2 and polyvinyl chloride. *J. Catal*. **2016**, *344*, 692−700. (h) Zhang, F.; Zhang, Y.; Zhang, G.; Yang, Z.; Dionysiou, D. D.; Zhu, A. Exceptional synergistic enhancement of

the photocatalytic activity of SnS_2 by coupling with polyaniline and N doped reduced graphene oxide. *Appl. Catal. B* **2018**, *236*, 53−63.

[11] Hong, S. Y.; Popovitz-Biro, R.; Prior, Y.; Tenne, R. Synthesis of SnS_2/SnS fullerene-like nanoparticles: A superlattice with polyhedral shape. *J. Am. Chem. Soc.* **2003**, *125*, 10470−10474.

[12] Ji, Y.; Zhang, H.; Ma, X.; Xu, J.; Yang, D. Single-crystalline SnS_2 nano-belts fabricated by a novel hydrothermal method. *J. Phys. Condens. Matter* **2003**, *15*, L661−L665.

[13] Chen, X.; Hou, Y.; Zhang, B.; Yang, X. H.; Yang, H. G. Low cost SnS_x counter electrodes for dye-sensitized solar cells. *Chem. Commun*. **2013**, *49*, 5793.

[14] Chen, D.; Shen, G.; Tang, K.; Lei, S.; Zheng, H.; Qian, Y. Microwave-assisted polyol synthesis of nanoscale SnS_x (x=1, 2) flakes. *J. Cryst. Growth* **2004**, *260*, 469−474.

[15] Johny, J.; Sepulveda-Guzman, S.; Krishnan, B.; Avellaneda, D.; Shaji, S. Facile and fast synthesis of SnS_2 nanoparticles by pulsed laser ablation in liquid. *Appl. Surf. Sci*. **2018**, *435*, 1285−1295.

[16] Yang, Y.-B.; Dash, J. K.; Littlejohn, A. J.; Xiang, Y.; Wang, Y.; Shi, J.; Zhang, L. H.; Kisslinger, K.; Lu, T.-M.; Wang, G.-C. Large Single Crystal SnS_2 Flakes Synthesized from Coevaporation of Sn and S. *Cryst. Growth Des.* **2016**, *16*, 961−973.

[17] Ludi, B.; Olliges-Stadler, I.; Rossell, M. D.; Niederberger, M. Extension of the benzyl alcohol route to metal sulfides: "nonhydrolytic" thio sol-gel synthesis of ZnS and SnS_2. *Chem. Commun.* **2011**, *47*, 5280−5282.

[18] (a) Zhang, Z.; Shao, C.; Li, X.; Sun, Y.; Zhang, M.; Mu, J.; Zhang, P.; Guo, Z.; Liu, Y. Hierarchical assembly of ultrathin hexagonal SnS_2 nanosheets onto electrospun TiO_2 nanofibers: enhanced photocatalytic activity based on photoinduced interfacial charge transfer. *Nanoscale* **2013**, *5*, 606−618. (b) Kumar, B. G.; Srinivas, B.; Prasad, M. D.; Muralidharan, K. Ag/Ag_2S heterodimers: tailoring the metal−semiconductor interface in a single nanoparticle. *J. Nanopart. Res*. **2015**, *17*, 325−336. (c) Srinivas, B.; Kumar, B.

G.; Muralidharan, K. Stabilizer free copper sulphide nanostructures for rapid photocatalytic decomposition of rhodamine B. *J. Mol. Catal. A: Chem*. **2015**, *410*, 8−18. (d) Billakanti, S.; Baskaran, G. K.; Muralidharan, K. Recyclable Ni_3S_4 Nanocatalyst for Hydrogenation of Nitroarenes. *ChemistrySelect* **2017**, *2*, 4753−4758. (e) Billakanti, S.; Krishnamurthi, M. Facile preparation of surfactant or support material free CdS nanoparticles with enhanced photocatalytic activity. *J. Environ. Chem. Eng.* **2018**, *6*, 1250−1256.

[19] Chen, Z.; Naidu, R.; Subramanian, A. Separation of chromium (III) and chromium (VI) by capillary electrophoresis using 2,6-pyridinedicarboxylic acid as a pre-column complexation agent. *J. Chromatogr. A* **2001**, *927*, 219−227.

[20] Lakshmi, V.; Chen, Y.; Mikhaylov, A. A.; Medvedev, A. G.; Sultana, I.; Rahman, M. M.; Lev, O.; Prikhodchenko, P. V.; Glushenkov, A. M. Nanocrystalline SnS_2 coated onto reduced graphene oxide: demonstrating the feasibility of a non-graphitic anode with sulfide chemistry for potassium-ion batteries. *Chem. Commun*. **2017**, *53*, 8272−8275.

[21] Bharatula, L. D.; Erande, M. B.; Mulla, I. S.; Rout, C. S.; Late, D. J. SnS_2 nanoflakes for efficient humidity and alcohol sensing at room temperature. *RSC Adv*. **2016**, *6*, 105421−105427.

[22] (a) Lin, C.; Zhu, M.; Zhang, T.; Liu, Y.; Lv, Y.; Li, X.; Liu, M. Cellulose/SnS_2 composite with enhanced visible-light photocatalytic activity prepared by microwave-assisted ionic liquid method. *RSC Adv*. **2017**, *7*, 12255−12264. (b) Liu, Y.; Chen, P.; Chen, Y.; Lu, H.; Wang, J.; Yang, Z.; Lu, Z.; Li, M.; Fang, L. In situ ion-exchange synthesis of SnS_2/g-C_3N_4 nanosheets heterojunction for enhancing photocatalytic activity. *RSC Adv*. **2016**, *6*, 10802−10809.

[23] (a) Xia, J.; Zhu, D.; Wang, L.; Huang, B.; Huang, X.; Meng, X.- M. Large-Scale Growth of Two-Dimensional SnS_2 Crystals Driven by Screw Dislocations and Application to Photodetectors. *Adv. Funct. Mater*. **2015**, *25*, 4255−4261. (b) Li, X.; Zhu, J.; Li, H. Comparative study on the mechanism in photocatalytic degradation of differenttype organic dyes on SnS_2 and CdS. *Appl. Catal. B* **2012**, *123-124*, 174−181. (c) Zhang, Y. C.; Du, Z. N.; Li, S. Y.; Zhang, M. Novel synthesis and high visible light

photocatalytic activity of SnS_2 nanoflakes from $SnCl_2.2H_2O$ and S powders. *Appl. Catal*. B **2010**, *95*, 153−159. (d) Wu, Z.; Xue, Y.; Zhang, Y.; Li, J.; Chen, T. SnS_2 nanosheet-based microstructures with high adsorption capabilities and visible light photocatalytic activities. *RSC Adv*. **2015**, *5*, 24640−24648. (e) Wei, R.; Zhou, T.; Hu, J.; Li, J. Glutatione modified ultrathin SnS_2 nanosheets with highly photocatalytic activity for wastewater treatment. *Mater. Res. Express* **2014**, *1*, No. 025018.

[24] Lei, Y.; Song, S.; Fan, W.; Xing, Y.; Zhang, H. Facile synthesis and assemblies of flowerlike SnS_2 and In^{3+}-doped SnS_2: Hierarchical structures and their enhanced photocatalytic property. *J. Phys. Chem. C* **2009**, *113*, 1280−1285.

[25] Gregor, C.; Hermanek, M.; Jancik, D.; Pechousek, J.; Filip, J.; Hrbac, J.; Zboril, R. The Effect of Surface Area and Crystal Structure on the Catalytic Efficiency of Iron(III) Oxide Nanoparticles in Hydrogen Peroxide Decomposition. *Eur. J. Inorg. Chem*. **2010**, 2343−2351.

[26] Zhang, Y. C.; Li, J.; Zhang, M.; Dionysiou, D. D. Size-Tunable Hydrothermal Synthesis of SnS_2 Nanocrystals with High Performance in Visible Light-Driven Photocatalytic Reduction of Aqueous Cr(VI). *Environ. Sci. Technol*. **2011**, *45*, 9324−9331.

[27] Mondal, C.; Ganguly, M.; Pal, J.; Roy, A.; Jana, J.; Pal, T. Morphology Controlled Synthesis of SnS_2 Nanomaterial for Promoting Photocatalytic Reduction of Aqueous Cr(VI) under Visible Light. *Langmuir* **2014**, *30*, 4157−4164.

[28] Yuan, Y.-J.; Chen, D.-Q.; Shi, X.-F.; Tu, J.-R.; Hu, B.; Yang, L.-X.; Yu, Z.-T.; Zou, Z.-G. Facile fabrication of "green" SnS_2 quantum dots/reduced graphene oxide composites with enhanced photocatalytic performance. *Chem. Eng. J*. **2017**, *313*, 1438−1446.

[29] Qu, J.; Chen, D.; Li, N.; Xu, Q.; Li, H.; He, J.; Lu, J. Coral-Inspired Nanoscale Design of Porous SnS_2 for Photocatalytic Reduction and Removal of Aqueous Cr(VI). *Appl. Catal. B* **2017**, *207*, 404−411.

[30] Zhong, Y.; Qiu, X.; Chen, D.; Li, N.; Xu, Q.; Li, H.; He, J.; Lu, J. Flexible Electrospun Carbon Nanofiber/Tin(IV) Sulfide Core/Sheath Membranes for Photocatalytically Treating Chromium(VI)-Containing Wastewater. *ACS Appl. Mater. Interfaces* **2016**, *8*, 28671−28677.

[31] Sun, M.; Yan, Q.; Yan, T.; Li, M.; Wei, D.; Wang, Z.; Wei, Q.; Du, B. Facile fabrication of 3D flower-like heterostructured g-C_3N_4/SnS_2 composite with efficient photocatalytic activity under visible light. *RSC Adv*. **2014**, *4*, 31019−31027.

[32] Liu, J.; Jing, L.; Gao, G.; Xu, Y.; Xie, M.; Huang, L.; Ji, H.; Xie, J.; Li, H. Ag_2S quantum dots in situ coupled to hexagonal SnS_2 with enhanced photocatalytic activity for MO and Cr(VI) removal. *RSC Adv.* **2017**, *7*, 46823−46831.

[33] Zhang, X.; Zhang, P.; Wang, L.; Gao, H.; Zhao, J.; Liang, C.; Hu, J.; Shao, G. Template-oriented Synthesis of Monodispersed SnS_2@SnO_2 hetero-nanoflowers for Cr(VI) photoreduction. *Appl. Catal. B* **2016**, *192*, 17−25.

[34] Wang, J.; Li, X.; Li, X.; Zhu, J.; Li, H. Mesoporous yolk−shell SnS_2−TiO_2 visible photocatalysts with enhanced activity and durability in Cr(VI) reduction. *Nanoscale* **2013**, *5*, 1876−1881.

[35] Padhi, D. K.; Parida, K. Facile fabrication of a-FeOOH nanorod/RGO composite: a robust photocatalyst for reduction of Cr(VI) under visible light irradiation. *J. Mater. Chem. A*, **2014**, *2*, 10300–10312.

[36] (a) Ye, S.; Qiu, L.-G.; Yuan, Y.-P.; Zhu, Y.-J.; Xia, J.; Zhu, J.-F. Facile fabrication of magnetically separable graphitic carbon nitride photocatalysts with enhanced photocatalytic activity under visible light. *J. Mater. Chem. A* **2013**, *1*, 3008−3015. (b) Yang, C.; Wang, W.; Shan, Z.; Huang, F. Preparation and photocatalytic activity of highefficiency visible-light-responsive photocatalyst SnS_x/TiO_2. *J. Solid State Chem.* **2009**, *182*, 807−812.

[37] Zhang, Z.; Huang, J.; Zhang, M.; Yuan, Q.; Dong, B. Ultrathin hexagonal SnS_2 nanosheets coupled with g-C_3N_4 nanosheets as 2D/2D heterojunction photocatalysts toward high photocatalytic activity. *Appl. Catal. B* **2015**, *163*, 298−305.

CHAPTER-3

A simplistic approach for the synthesis of CuS-CdS heterostructure: A novel photo catalyst for oxidative dye degradation

Abstract

In this chapter, we have discussed improving the catalytic activities of nanostructures by forming a heterojunction besides surfactant-free synthesis. Direct synthesis of CuS-CdS based mesoporous composite materials and their photocatalytic activity is delineated. In this study, a series of CuS micro flowers (mf) decorated with varying amounts of CdS nanoparticles (NP) have been synthesized successfully in a controlled manner. Relatively easy synthesis of material along with its surfactant-free clean surfaced heterojunction accentuates the reliability of the protocol described here. Full characterization of these semiconducting materials was accomplished with a series of analytical techniques, which include powder x-ray diffraction (PXRD), scanning electron microscopy (SEM), tunnelling electron microscopy (TEM), x-ray photoelectron spectroscopy (XPS), UV–vis, IR, BET and lifetime studies. Upon varying the concentration of precursor of Cd in the reactions, the resulting materials exhibited a well-demarcated change in morphologies ranging from undifferentiated mass to well-differentiated flower-like architectures. The thoroughly characterized composite was accessed finally for its potential photocatalytic activity for the degradation of organic dyes. The results showed 96.0% degradation of rhodamine B (RhB) over 10 min and 94.7% degradation of methylene blue (MB) over 9 min. This observed rate of degradation was much higher compared to that observed in the case of pure CuS (62.0% of Rh B and 50.2% of MB).

Journal of Environmental Chemical Engineering 8, (2020), 103542

3.1. Introduction

Nefarious chemical by-products from various small as well as large industrial units have created menace of environmental pollution, and the problem is aggravating at an alarming rate. For instance, the contamination of water by various industrial sewages, including the organic dyes, poses a difficult task to handle [1–4]. Towards a viable solution, many biological, as well as physical treatment procedures, including adsorption, ultrafiltration, and coagulation, was developed. Unfortunately, all strategies were limited either by their complicacy or expensiveness [5, 6], and therefore, for a practical solution to these hazards, there is a need to develop more specific and environmentally benign strategies.

Among the many treatment protocols developed over the years for the treatment of contaminated water, the semiconductor-based catalytic treatment materials picked up full acceptance. In this context, metal chalcogenides, especially CuS and CdS, which exhibited peculiar properties including suitable band gap and required electronic band position, makes them ideal visible light active semiconducting photocatalysts for wastewater treatment [6–8]. Although, CuS, a p-type semiconductor having a narrow bandgap (E_g = 2.0–2.2 eV) is an efficient visible-light photo catalyst for wastewater treatment [9–11]. Nevertheless, the immediate recombination of charge carriers that are generated on exposure to visible light limits the efficiency as a photocatalyst. Therefore, many modified CuS based composite nanostructures were synthesized with different synthetic modifications, including heterojunction formation, doping with some other active metals.

The materials obtained by various modifications exhibited better photocatalytic activity applications compared to the parent compounds. For instance, Liu et al. reported the synthesis of CuS-modified Bi_2S_3, which showed enhanced visible-light photocatalytic performance towards rhodamine B (RhB) degradation [12]. Similarly, Lee et al. Carried a successful fabrication of CuS (p-type) and ZnO (n-type) nanoarrays using stainless steel mesh as support. This material exhibited the ability to function as a photo catalyst for the decomposition of acid orange under visible light irradiation [7, 13]. Soltani et al. produced ZnS and CdS nanoparticles with absorption spanning into the visible region that

showed better durability towards photo-erosion [14]. Sunita et al. synthesized TiO_2/CuS core-shell nanostructure that was useful to degrade methylene blue in a time of 60 min of exposure to radiations [15]. Basu et al. synthesized ZnO/CuS heterojunction, which worked as an excellent catalyst for the photodecomposition of methylene blue (MB) at room temperature [16]. These composite materials eased the charge transfer through heterojunctions by means of increasing the separation of electron-hole pairs [17].

Zhu et al. performed efficient photocatalytic degradation of the tetracycline hydrochloride on the α-Fe_2O_3@CN composite under the visible light [18]. Wei et al. synthesized a series of different nanostructures like SiO_2 nanoparticles, MoS_2 based polymer composites, and magnetic graphene oxide composites via mussel inspired chemistry and were used successfully for the removal of toxic organic dyes like Congo red, methylene blue respectively [19]. Similarly Jorfi et al claimed the synthesis of a series of diverse nanomaterials comprising of Fe-TiO_2/rGO, ZnO/TiO_2 on r-GO substrate and Fe_3O_4–TiO_2–Ag. They used these materials as the catalysts for photocatalytic degradation of rhodamine B, photocatalytic decontamination of phenol and petrochemical wastewater, and photocatalytic degradation of 4-chlorophenol (4-CP) respectively [20]. The observations described above explain that the creation of heterostructure between semiconductors leads to the improved catalytic activities in photo catalysis.

It is propounded that a heterostructure between CuS and CdS would establish better contact between these two materials through the formation of heterojunction. CuS and CdS are active individually, under visible light irradiation. Further, the synthetic procedure with better control over tuning the bandgap of these individual materials has been well established in the literature. However, the faster recombination rate of photo generated excitons reduces their catalytic activity. The presence of heterojunction can lead to an enhanced charge separation by transferring charge carriers. This process could induce an increase in the mobility of charge carriers and the stability of the material, and so finally, its photocatalytic activity [21–26]. Moreover, the availability of free and unprotected surfaces is critical to enhance the catalytic activity of nanoparticles further. Therefore, a method that can deliver the nanocomposites devoid of stabilizing molecules like surfactants, which otherwise hamper their photocatalytic activity is worth to look for [27].

This chapter describes a novel approach for the synthesis of well-constructed micro/nano composite materials of CuS micro flowers (mf) decorated with CdS nanoparticles (NP). The work includes the preparation of a series of CuS-CdS composites (CSD-0, CSD-0.5, CSD-1, CSD-2, and CSD-3) and investigation of their potential catalytic activity towards the degradation of organic dyes like rhodamine B and methylene blue. We observed that the catalytic performance shown by assynthesized composites towards the reduction of organic dyes is far better as compared to pure CuS nanomaterials. Further, enhancement in the catalytic activity of nanocomposites has also been verified by studying the lifetime of photo generated charge carriers using the FLTM technique. The presence of a clean-surface path for photo generated charges in these highly stable CSD composites extended the recyclability of the catalyst in the degradation reactions [27]. Therefore, this work is expected to sensitize newer ways for the improvement of a lowcost and competent photo catalysts for wastewater treatment.

3.2. Experimental Section

3.2.1. Materials

Copper nitrate ($Cu(NO_3)_2 \cdot 3H_2O$), cadmium chloride ($CdCl_2$, anhydrous), thiourea [$H_2NC(S)NH_2$] and hexamethyldisilazane [$(Me_3Si)_2NH$] (HMDS) were procured from Sigma Aldrich. The chemicals of analytical grade were used as such without further purification.

3.2.2. Synthesis of CuS decorated with CdS micro/nano composite materials

In a typical reaction, cadmium chloride ($CdCl_2$, anhydrous), (n mmol; where n = 0, 0.5, 1, 2, and 3) copper (II) nitrate trihydrate ($Cu(NO_3)_2 \cdot 3H_2O$) (4 mmol) and thiourea [$H_2NC(S)NH_2$] (3 mmol) were added into 7 mL of HMDS in a reaction vessel. The reagents in the vessel were stirred continuously for 6 h at 140 °C using a magnetic stirrer under continuous supply of nitrogen gas using Schleck lines. Subsequently, the assimilated precipitate was separated by centrifugation, filtered, and then washed using deionized water and ethanol for 3–4 times each. At final, the products were dried by applying vacuum. The products, CuS mf decorated with CdS NP (CuS-CdS micro/nano

composites) were named as CSD-0, CSD-0.5, CSD-1, CSD-2, and CSD-3 respectively for the products obtained from the reactions wherein the amounts of $CdCl_2$ used in these reactions were 0, 0.5, 1, 2 and 3 mmol.

3.2.3. Photocatalytic activity

The aqueous solutions of rhodamine B (Rh B) and methylene blue (MB) were separately prepared by adding each 10 mg L^{-1} in deionized water. From this stock solution of dyes, 60 mL was placed in a beaker for the experiment, which was then supplemented with 30 mg of CuS-CdS micro/nano composites [CSD-0, CSD-0.5, CSD-1, CSD-2, and CSD-3]. Afterwards, the solution was stirred in dark for about 30 min to ensure the establishment of an adsorption–desorption equilibrium before being illuminated to sunlight. Then the dispersion was exposed to sunlight while being continuously stirred. At a regular time interval, about 3 mL of the suspension was removed, centrifuged for catalyst separation and the liquid then placed in cuvette to study absorption properties. The UV–vis absorption spectra were recorded by continuously repeating the above procedure, the characteristic absorption peaks at 553 nm for Rh B and 660 nm for MB were monitored to follow the catalytic degradation process. The decrease in the intensity of colour of toxic organic dyes while carrying photo catalysis reaction was noticed. This reaction was found to follow a first order reaction kinetics and the rate of degradation was calculated by the following formula;

$$\text{Degradation (\%)} = (1- C_t/C_0) \times 100\% \quad (1)$$

Here, C_0 is the initial concentration and C_t the concentration of the dye at time t. To highlight the stability and reusability of the catalyst, the same materials used one time were centrifuged from the solution and washed to be reused as in aforementioned steps.

3.2.4. Instrumentation

XRD patterns of the synthesized products were collected at room temperature using Bruker D8 X-ray diffractometer (XRD) at a scan rate of $1°min^{-1}$ (CuKα=1.54 Å; operating voltage =40 kV; operating current = 30 mA) in a 2θ range from 10° to 80°. The morphological texture (FESEM), energy dispersive spectroscopy (EDS) were studied

using an Ultra 55 Carl Zeiss instrument at an operating voltage of 10 kV. The synthesized materials were made into suspension in isopropanol by sonicating for 2−3 min. It was drop cast on carbon-coated copper grids (200 mesh) for the TEM analyses. FEI Technai G2 20 STEM with a 200 kV acceleration voltage was used to capture TEM images. JASCO 5300 spectrophotometer was used to analyse the Fourier transform infrared (FT-IR) spectra (KBr pellet). The optical properties were confirmed by studying the UV/Vis absorption spectra of samples in the solid and liquid states (for photo catalysis) using JASCO-V770 UV/Vis spectrometer, wherein barium sulphate was used as the filler. BET studies were carried to determine surface area and pore size analysis, which were conducted on the Quantachrome instruments. The X-ray photoelectron spectra (XPS) were obtained using a Thermo scientific Escalab 250Xi spectrometer with Al−Kα radiation. The lifetime studies were performed by using MicroTime 200 resolved confocal fluorescence setup from PicoQuant equipped with an inverted microscope, a 485 nm pulsed laser source used for excitation.

3.3. Results and Discussion

3.3.1. Synthesis and characterization

Using HMDS-assisted synthetic method, we have synthesized (Scheme 3.1) five different CuS mf decorated by CdS NP by varying the amount of cadmium source (anhydrous $CdCl_2$) and fixing the amounts of copper and sulphur sources [$Cu(NO_3)_2 \cdot 3H_2O$, 4 mmoL and $H_2NC(S)NH_2$, 3 mmol] in the synthesis. Accordingly, for the amounts of $CdCl_2$ of 0, 0.5, 1, 2 and 3 mmol, the products (CuS mf decorated by CdS NP) obtained were named as CSD-0, CSD-0.5, CSD-1, CSD-2, and CSD-3 respectively. In this synthetic process, HMDS was proven to react with sulphur in presence of metal salts to form [S-N($SiMe_3$)]n polymer as an intermediate, which would release S^{2-} ion. Also, this intermediate controls the growth of the particles during the reaction. Formation of stable Si-Cl bond drives this reaction and yields Me_3SiCl as a side product. Although HMDS played manifold roles; as a solvent, a reducing agent, as the stabilizing agent since it behaves like surfactant and halts the growth of the particles during the synthesis, yet no atom of HMDS forms the composition of the product materials. Therefore, the reaction is termed as the HMDS–assisted synthesis.

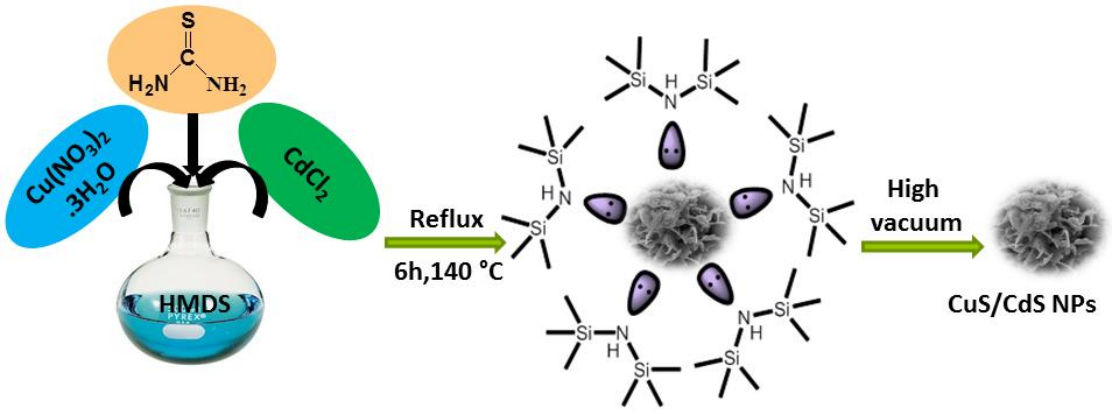

Scheme 3.1. Schematic illustration of surfactant free CdS decorated CuS nanostructures.

Powder X-ray diffraction (XRD) data confirmed the formation of the CuS-CdS micro/nano composite materials in the HMDS-assisted synthesis. Figure 3.1 portrays the XRD patterns of the samples of nanocomposites with different Cd concentrations.

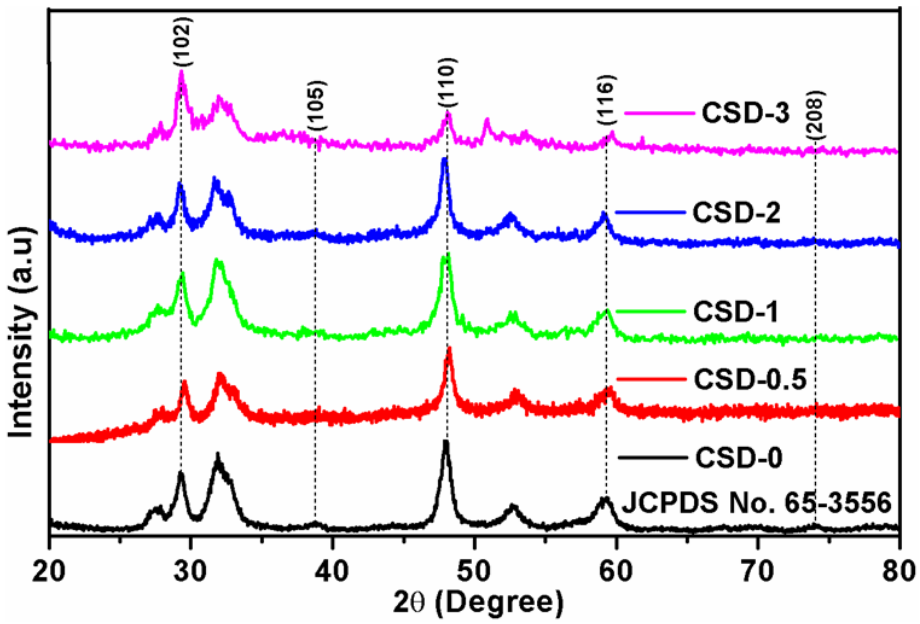

Figure 3.1. PXRD patterns of CSD-0, CSD-0.5, CSD-1, CSD-2, and CSD-3 with varying amounts of $CdCl_2$ in the reaction while keeping all other reaction conditions same.

All the peaks in the figure correspond to the hexagonal CuS phase (JCPDS No. 65–3556). The XRD patterns of synthesized composites did not specify the characteristic peaks related to other materials, hence confirming high phase purity embedded with lesser

loadings of CdS on CuS. However, XRD analysis provided subtle proof for the presence of detached CdS in the materials even for the samples obtained in presence of 1−3 mol% Cd source. Nevertheless, the presence of cadmium was confirmed by X-ray photoelectron spectroscopy (XPS) and energy-dispersive X-ray spectroscopy (EDS) analysis (vide infra). Only the difference observed in the PXRD patterns was the increase of intensity of (102) peak and the decrease in the intensity of (110) and (116) peaks. This change in the peak intensity can be attributed to the addition of Cd^{+} and Cl^{-} ions while synthesizing the composite materials that resulted in a subtle change in the stoichiometry of copper sulphides. No change in phase as well as in the composition of synthesized composites was observed [28]. Based on Scherer equation, the peak-width analysis of PXRD spectra showed an average crystallite size of ~30−40 nm.

The elemental distribution of the synthesized composites was analysed by energy dispersive X-ray spectroscopy (EDS) analysis, which revealed that Cu, Cd and S elements were homogeneously distributed throughout the composite (Figure 3.2). The atomic weight ratios of Cu, Cd and S were found 45.6, 25.3 and 29.12 for CSD-1 respectively.

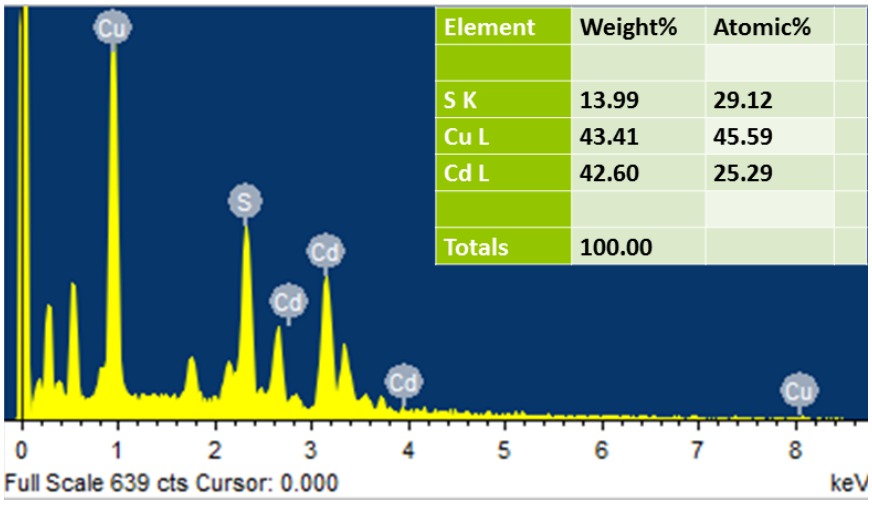

Figure 3.2. EDS spectrum of fresh CuS/CdS materials (CSD-1).

The valence states of Cu and Cd atoms in the composite were investigated with X-ray photoelectron spectroscopy (XPS) (Figure 3.3).

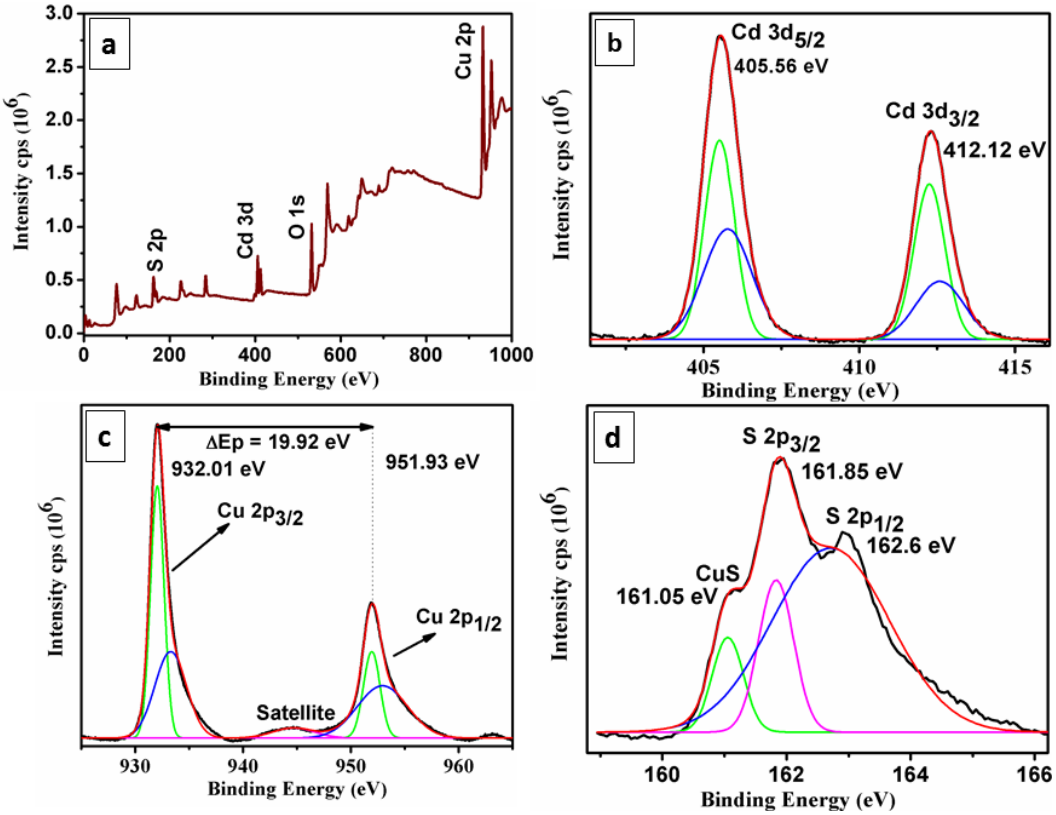

Figure 3.3. XPS analysis of CSD-1 in the Cu 2p, Cd 3d and S 2p regions. (a) Survey spectrum of the composite material. (b–d) showing the binding energies of Cd, Cu and S respectively for CSD-1.

The survey (Figure 3.3a) scans show that all main peaks, though the intensities were different, could be indexed to Cu, Cd and S of CSD-1 sample, which was the most active catalyst examined in this work. The XPS spectrum of Cd 3d shown in Figure 3.3b revealed a doublet at 404.6 and 411.4 eV corresponding to Cd^{2+} $3d_{5/2}$ and $3d_{3/2}$ core-levels in CdS confirming the presence of Cd^{2+} in CdS. Similarly, figure 3.3c displays XPS spectrum of Cu 2p for CSD-1 mf, showing the binding energies of Cu $2p_{3/2}$ and Cu $2p_{1/2}$ core-level signals at 932.6 and 952.4 eV respectively. These peaks are being characteristic for Cu^{2+} in CuS compound, existence as Cu(II) was confirmed. For Cu 2p, the symmetrical shape of peaks confirms the existence of copper in the catalyst as CuS. Besides two main peaks, a weak satellite peak approximately at 943.2 eV further confirmed the paramagnetic nature of Cu^{2+}. The core-level XPS spectrum of S 2p is shown in Figure 3.3d. For the sample of CSD-1 obtained with the addition of $CdCl_2$, two

foremost peaks located at 161.85 eV (S $2p_{3/2}$) and 162.6 eV (S $2p_{1/2}$) were observed. These peaks were ascribed to S^{2-}, specifying the presence of two different metal sulphides (CuS and CdS) in the composite. For Cu $2p_{1/2}$ and S 2p the peaks observed at 951.9 eV for former and 161.8 eV for latter were found to be slightly shifted to lower binding energy region due to $CdCl_2$ addition, confirming the presence of more Cu^+ on the surface in CSD-1 [29, 30].

3.3.2. Structural and morphological analysis

From the FESEM (Figure 3.4) images of CSD-0 (where there was no Cd) showed nanofiber like particles and developing of mf (Figure 3.4a-b). Interestingly, after the addition of Cd precursor to the reaction, the morphology transformed into flower-like structure for the sample of CSD-0.5 but with inhomogeneous sizes and thin petals (Figure 3.4c). Further increase in the amount of $CdCl_2$ to the reaction (for CSD-1, Figure 3.4d-e) resulted in the formation of well-developed microflower-like structure with highly thin porous petals. With another increment in CdS content, the mf developed to somewhat relaxed structure with its petals seeming to expand in space but associated with the decrease in density of pores (sample CSD-2, Figure 3.4f and g). After the addition of final increment of CdS, the mf grew to highly dense and thick sheet like diverse flowers accompanied with reduction in the density of pores of CSD-3 (Figure 3.4h and i). These stepwise incremental changes in the CdS addition clearly highlighted the change in morphology from messy to thin porous like microflowers. These changes finally ended up by completely transforming morphology to well-developed thick sheet and high particle density flowers confirming the regular deposition of CdS particles on flowers.

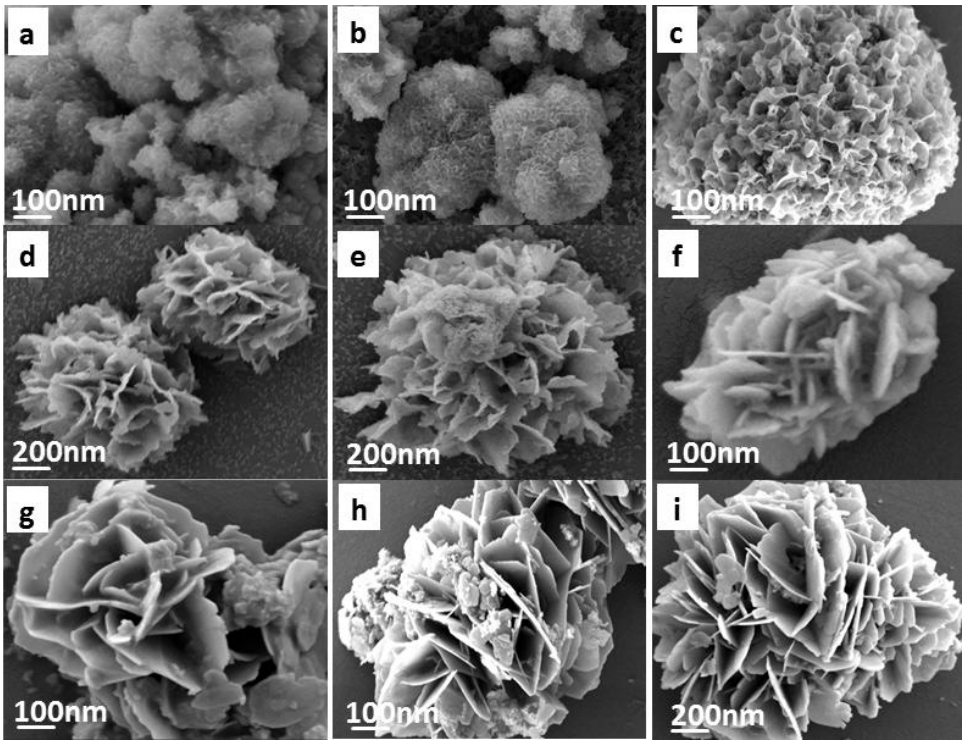

Figure 3.4. SEM images of different CSD composites: (a–b) CSD-0, (c) CSD-0.5, (d–e) CSD-1, (f–g) CSD-2 and (h–i) CSD-3.

Further evaluations about morphological transformation were confirmed from studying TEM measurements (Figure 3.5). Figure (3.5a, for CSD-1 and Figure 3.6a, c, e and g for CSD-0, CSD-0.5, CSD-2, and CSD-3) shows the TEM images of CSD composite materials. From the figure, it is clear that all the TEM images are almost in close confirmation with their corresponding SEM images with flowers becoming more porous and thin up to CSD-1 and after that with further enhancement in CdS concentration the overall thickness increases but with the decrease in porosity. The elemental mapping (Figure 3.5c, d, e, and f, for CSD-1) further confirms the distribution of elements (Cu, Cd, and S) present in the composite materials. To understand the crystalline nature of the mesoporous network, the synthesized composites were subjected to selected-area electron diffraction (SAED), which presented (Figure 3.5b for CSD-1 and Figure 3.6b, d, f, and h for CSD-0, CSD-0.5, CSD-2 and CSD-3) a sequence of diffused Debye-Scherer rings corresponding to the zinc blende structure of CdS, agreeing well with XRD results. These results confirmed the successful deposition of CdS particles on the CuS surface.

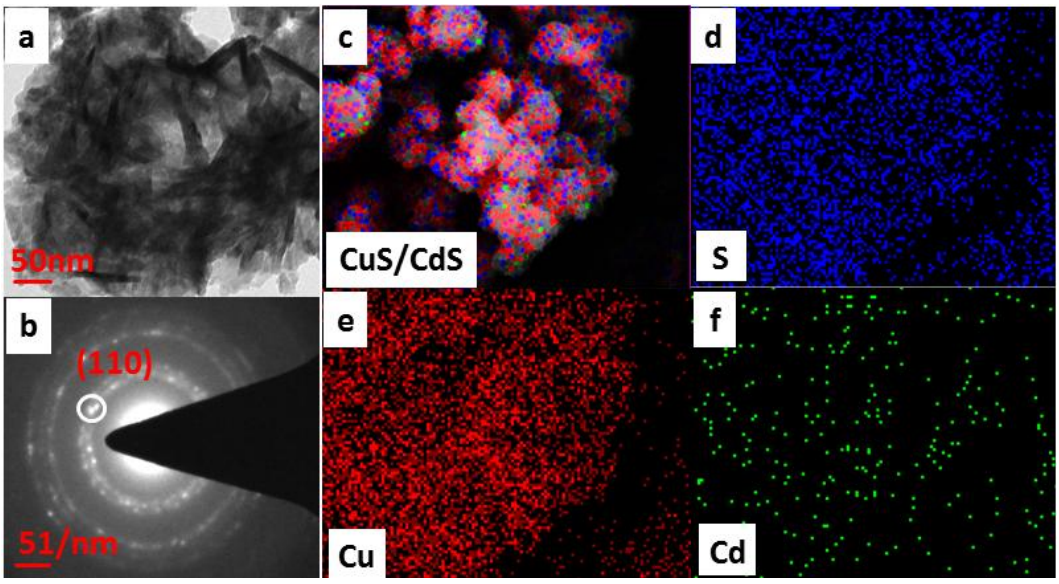

Figure 3.5. TEM image, SAED patterns and Elemental mapping from SEM of CSD-1composite: (a, b) TEM images and SAED patterns of CSD-1. (c, d, e and f) elemental mapping of CSD-1.

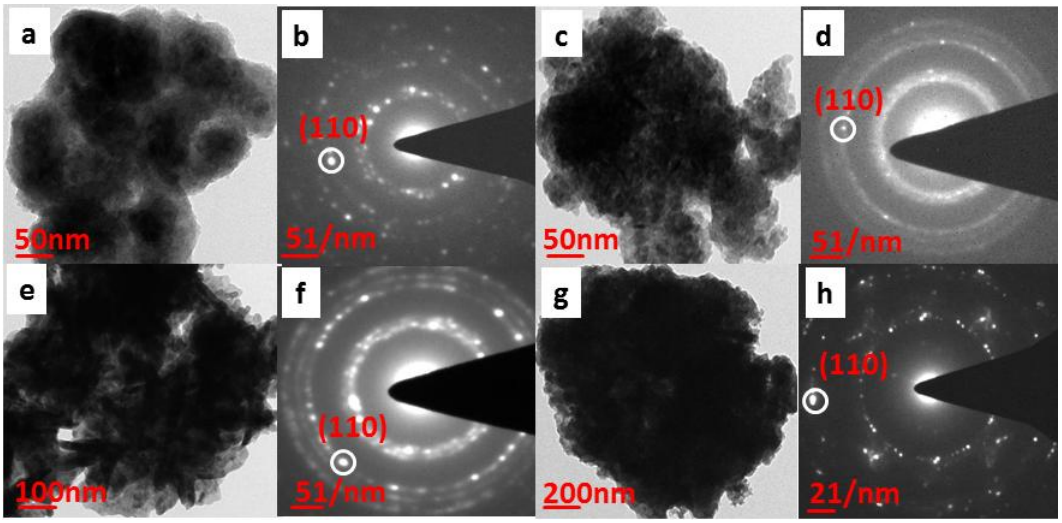

Figure 3.6. TEM images and SAED patterns of CSD-0, CSD-0.5, CSD-2 and CSD-3: (a, c, e and f) TEM images and (b, d, f and h) SAED patterns.

Consistency in all, data from XRD, XPS, SEM and TEM confirmed the well-defined synthesis of mesoporous composite materials compromising of covellite (CuS) and cubic CdS nanostructures [29].

3.3.3. Clean surface area and optical properties

As discussed earlier in the chapter 2, the availability of free surface of the micro and nanoparticles for the catalytic activity is the key for their success in catalysis. The main side product in the synthesis described here is Me_3SiCl and it can be removed from the reaction mixture by vacuum along with HMDS used in the reactions. Since no other surfactant molecules are used in the synthesis, and starting materials [thiourea, $Cu(NO_3)_2.3H_2O$ and $CdCl_2$] are removed by washing with water and ethanol, the product is supposed to have clean surfaces. EDAS analysis did not show any signature of silicon in the products. As exemplified in different works of literature that an external surfactant hinders the catalytic activity of a catalyst by decreasing the generation of electron-hole pairs, their mobility and puts a barrier for access towards the active sites on catalysts surface. For better catalytic activity, to circumvent the problem of surfactant molecules, it is necessary to develop surfactant free nanostructures. In this regard, the FTIR spectrum of CSD-1 material (Figure 3.7) showed that there are no significant signals for the materials. For visual comparison, the FTIR spectrum (Figure 3.7a) of the HMDS is presented as well. These observations explain clearly that CSD materials discussed here have clean surfaces and can be suitable materials for catalysis.

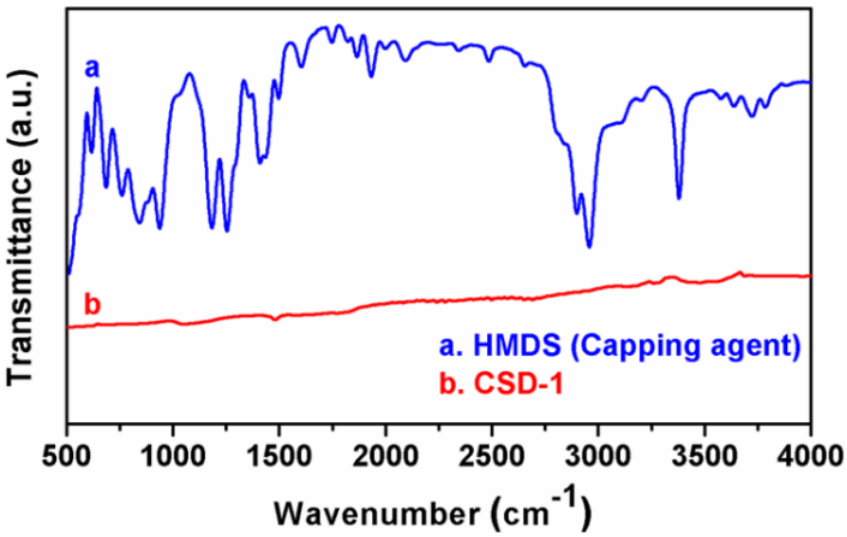

Figure 3.7. FTIR spectrum of CdS decorated CuS nanostructures (CSD-1 sample) (b). For visual comparison FTIR spectrum of HMDS presented (a).

In order to evaluate the specific surface area and corresponding pore structure, we have carried out the nitrogen adsorption-desorption isotherms (BET) for the CSD materials (Figure 3.8). A sample of CSD-1 exhibited type IV isotherms and its specific surface area was calculated to be 18.1m^2g^{-1}. The obtained surface area is not so much higher but still CSD-1 showed the best photocatalytic activity among all these composite catalysts. This is due to the existence of special hierarchical structure and highly porous nature of petals, providing a good number of active sites for catalytic activities, together. These results are in good agreement with the FTIR analysis which states that the as synthesized catalysts are having clean and free (free from surfactants) surfaces.

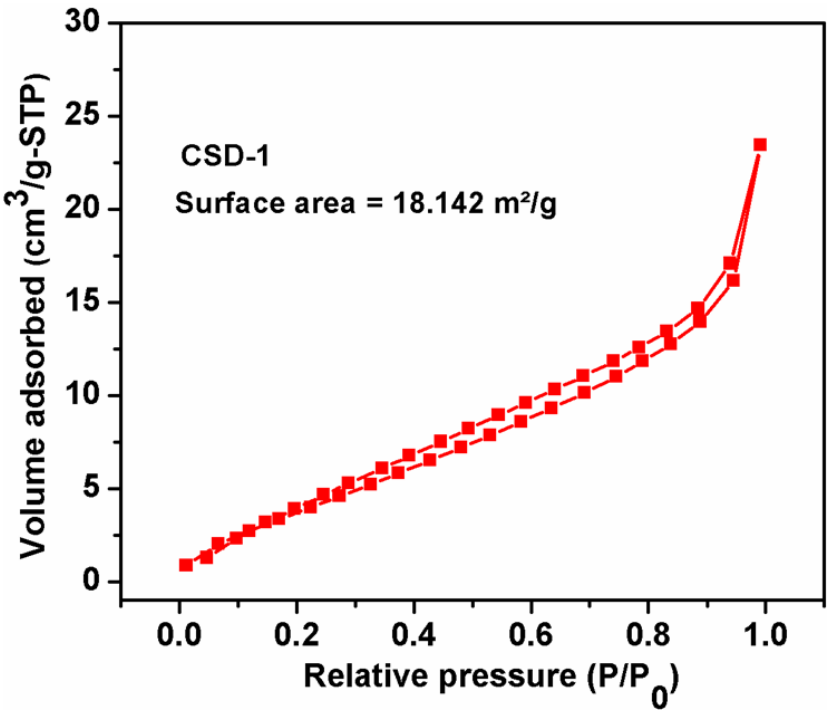

Figure 3.8. BET surface area analysis of CuS/CdS nanostructures (CSD-1). Nitrogen adsorption-desorption isotherm.

The optical properties of composite catalysts were confirmed from UV–vis absorption spectra (Figure 3.9). It is observed that all the catalysts show similar absorption, mostly in the visible region with broad peak absorption in the 500-700 nm range. Still, CSD-1 shows superior photocatalytic activity as compared to other samples. This increased activity might be due to some morphological changes giving CSD-1 a particular hierarchical type structure which might cause some slight changes in the

absorption spectra, but overall the absorption spectra of all the samples remain unaffected [31]. The average band gap values calculated from the absorption data was 2.29 eV for CSD materials.

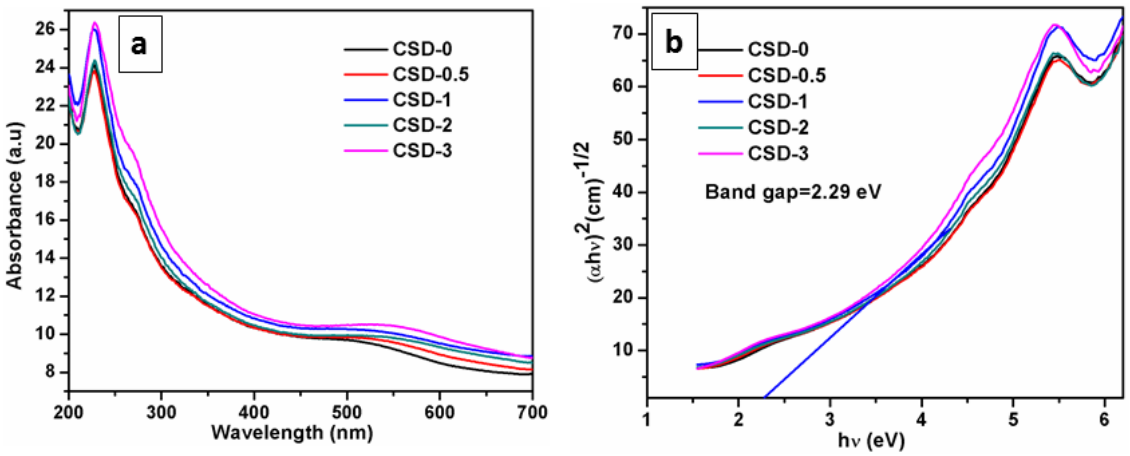

Figure 3.9. UV-visible spectrum of all catalysts (CSD-0, CSD-0.5, CSD-1, CSD-2, CSD-3) (a) and band gap (b) for different concentrations of Cd.

3.3.4. Photocatalytic properties

Rh B and MB represent the most commonly used organic dyes at industrial scale and therefore are used as probe molecules predominantly while studying the heterogeneous catalysis. Therefore, to evaluate the photocatalytic potential of CSD materials, the time dependent photo degradation of Rh B and MB dyes was studied. A set of control experiments for CSD-1 material (Figure 3.10) which include one without catalyst (photolysis) and another one without the visible light intervention but in the presence of a catalyst (catalysis). These reactions revealed the photocatalytic potential of CSD materials in the presence of visible light, divulging the importance of both catalyst and light to impact the dye degradation.

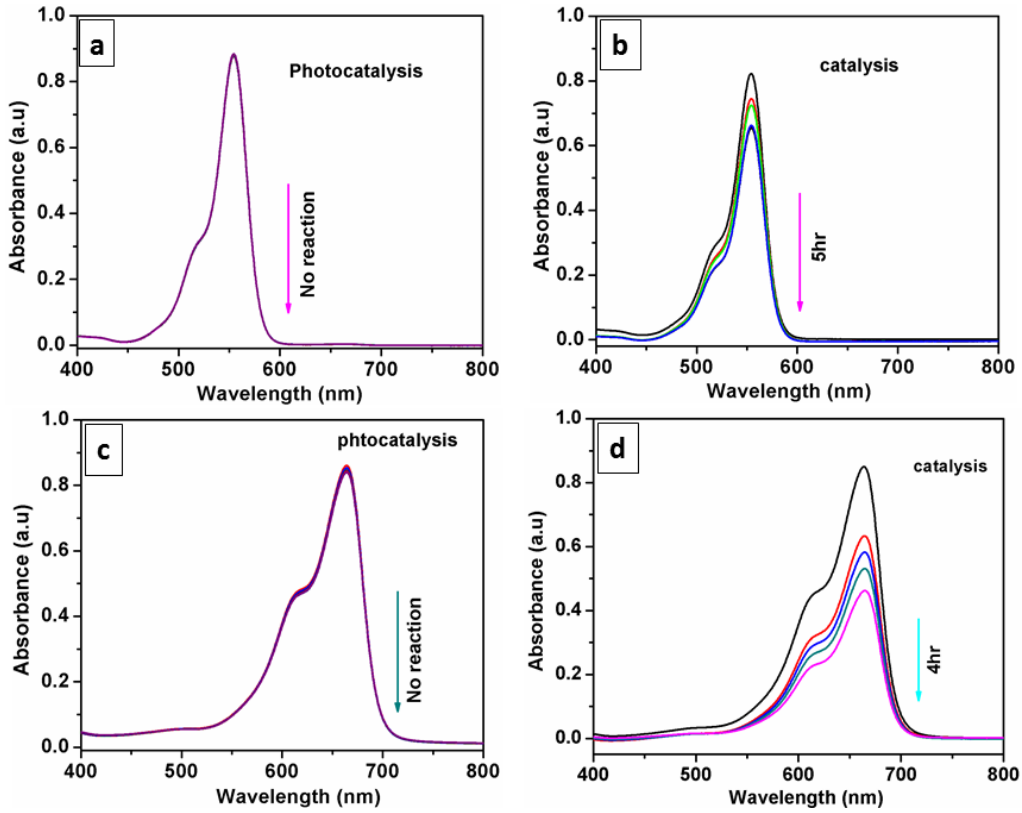

Figure 3.10. Controlled reactions of Rh B and MB dyes using CSD-1. (a, c) Photocatalysis (b, d) catalysis.

The photocatalytic ability of CSD composite materials (CSD-0, CSD-0.5, CSD-1, CSD-2, CSD-3) were tested individually. All the composite materials showed varying photocatalytic activity towards the degradation of toxic organic dyes Rh B and MB. The lowest photo degradation efficiency was observed for CSD-0 sample compared to the other CSD materials that are having definite amounts of CdS, which could be attributed to the effect of morphology. From above analysis, it is clear that the photocatalytic activities were enhanced obviously by loading CdS on to CuS surfaces. However the trend was not followed regularly with a series of CSD materials. Among these composite materials, the sample CSD-1 showed the highest photocatalytic activity towards Rh B and MB dyes which is matching well with the photocatalytic degradation kinetics. With CSD-1 catalyst, there was a rapid decrease in the intensity of absorption peak with increasing time of exposure. The degradation of Rh B and MB dye solutions was

observed to be 96.04% after 10 min for former and 94.69% after 9 min for latter respectively (Figure 3.11a, c) and remained at a relatively stable level after this time.

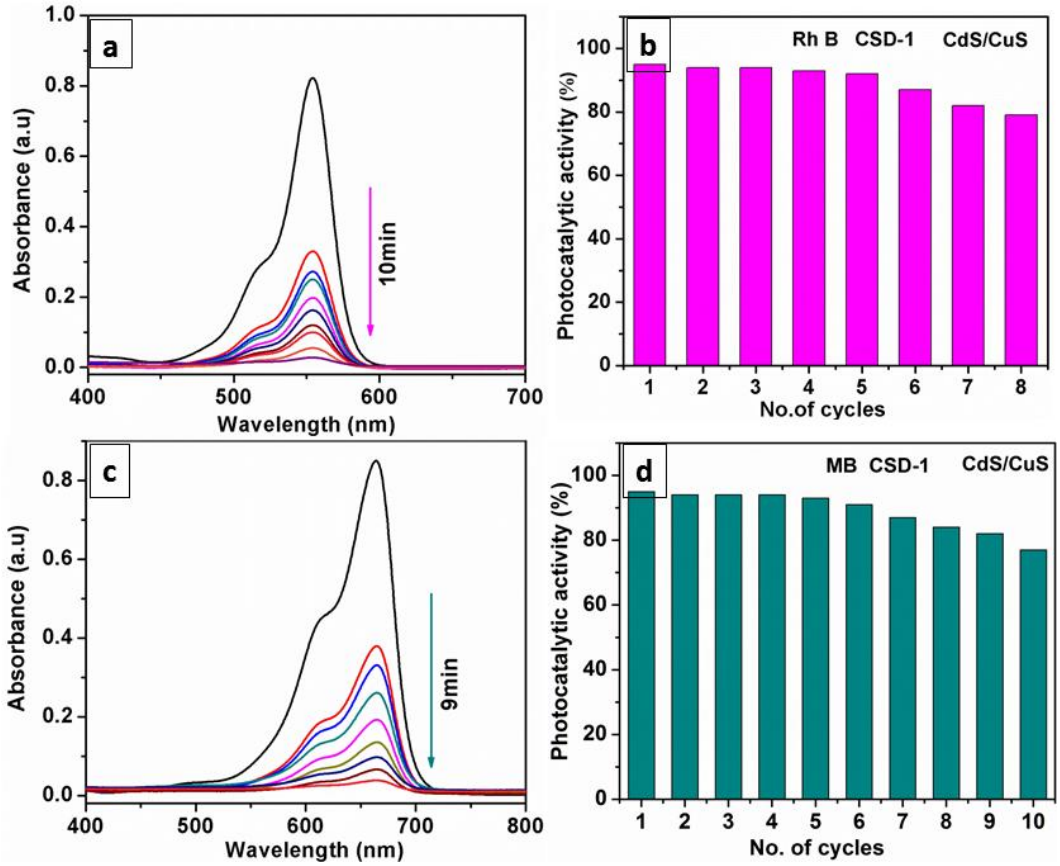

Figure 3.11. (a and c) are the optical absorption profiles for the RhB and MB dyes under visible light irradiation using the CSD-1 sample. (b and d) are the recyclability studies for the composite material [CSD-1] in the photodecomposition of RhB and MB respectively.

The photocatalytic activity of other composite materials (CSD-0, CSD-0.5, CSD-2, CSD-3) towards the degradation of Rh B and MB shown by their UV–vis absorption spectrum are represented in Figure 3.12 and 3.13 respectively.

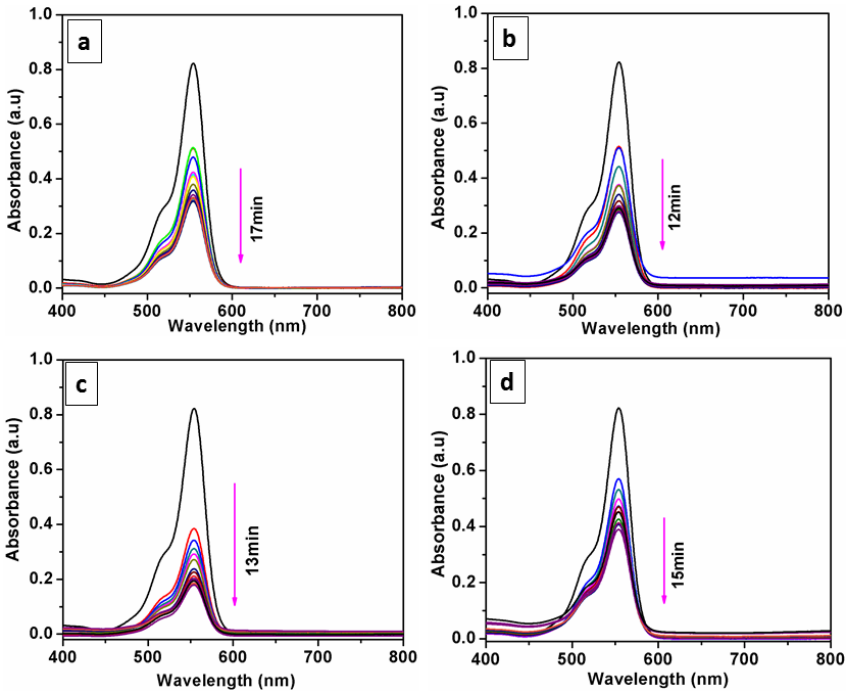

Figure 3.12. Controlled reactions of Rh B degradation experiments for (a) CSD-0, (b) CSD-0.5, (c) CSD-2, (d) CSD-3.

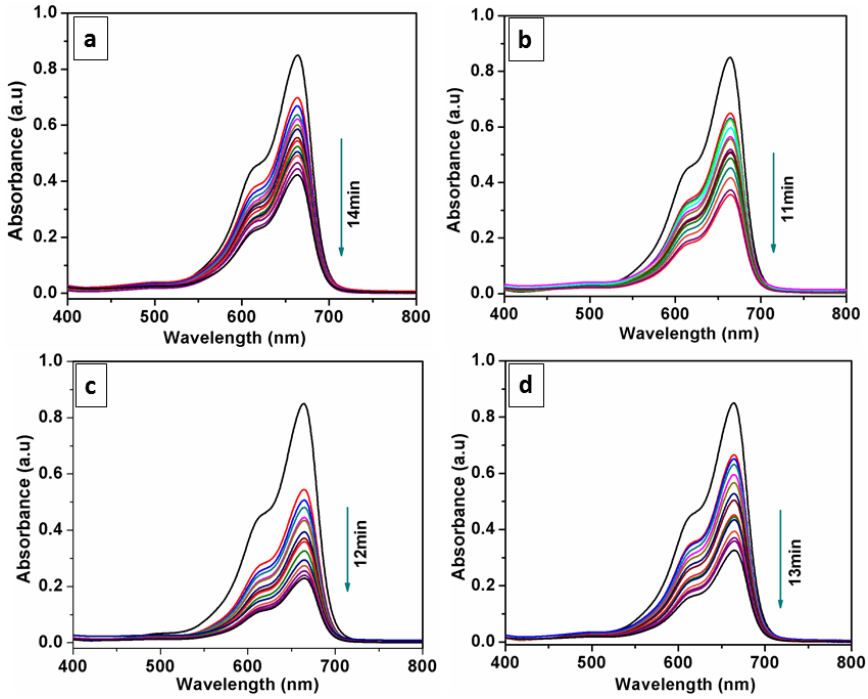

Figure 3.13. Controlled reactions of MB degradation experiments for (a) CSD-0, (b) CSD-0.5, (c) CSD-2, (d) CSD-3.

The photocatalytic degradation of Rh B and MB using CSD composite materials were found to follow the first order kinetics. The first-order rate constant is calculated by the following equation-2 [32].

$$\ln(C/C_0) = -kt \qquad (2)$$

Where C_0 is the initial concentration of organic dyes, C is the concentration at time t, and k is the first-order rate constant (min^{-1}), and t is the irradiation time (min). From Figure 3.14a c, it is observed that the samples prepared by adding different amounts of Cd, have different photocatalytic abilities. The rate constant of photodecomposition when plotted against time as per Eq. 2 gave a straight line for all the CSD materials (Figure 3.14b and d) confirming the first order kinetics of the degradation of organic dyes. The correlation between the reaction rate constant and the amount of CdS in the composite materials was also plotted (Figure 3.15).

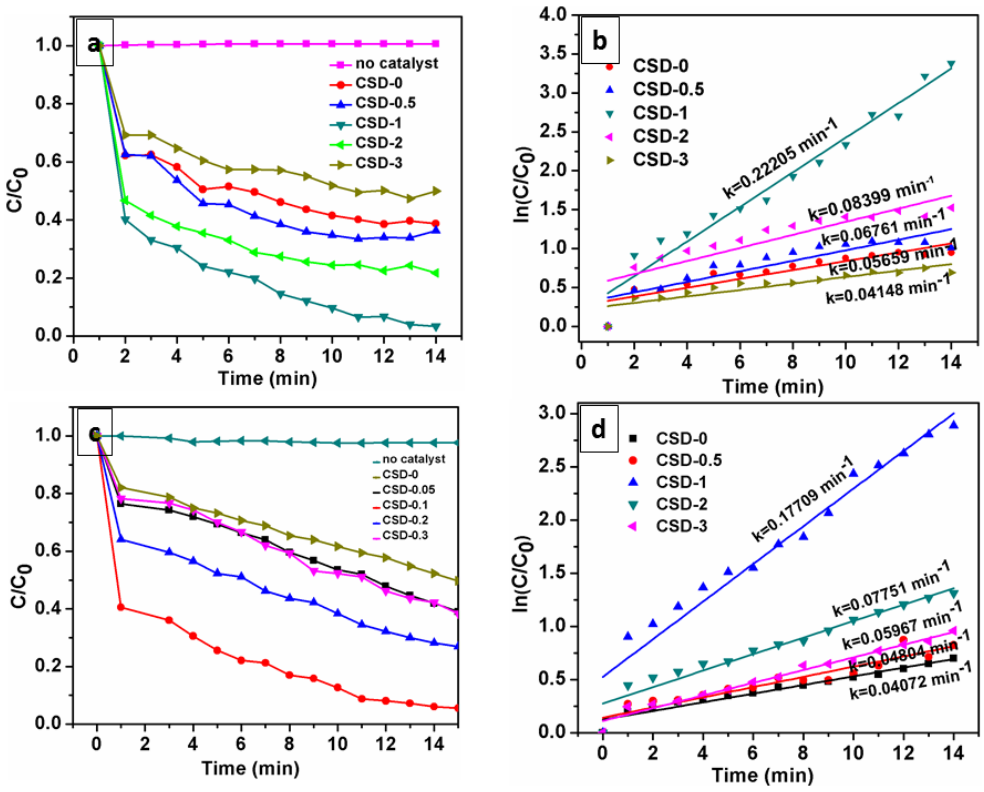

Figure 3.14. (a, c) Relative concentration (C/C_0) of Rh B and MB using as prepared composite materials by varying $CdCl_2$ concentrations under visible light. (b, d) The linear fit plots of $\ln(C/C_0)$ vs. time of the data in (a, c) for CSD heterojunctions.

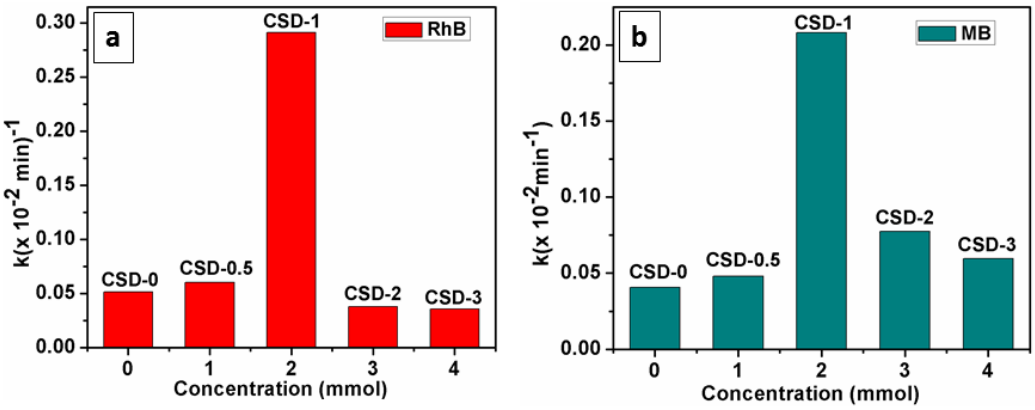

Figure 3.15. Showing the relationship between the reaction rate constant and CdS content for all the five samples (CSD-0, CSD-0.5, CSD-1, CSD-2, CSD-3) (a) Rhodamine b. (b) Methylene blue.

Data in Table 3.1 and plots (Figure 3.14) explain that CSD-1 with the appropriate CdS amount can achieve the optimal photo degradation efficiency. The first-order rate constant (K/min) of CSD-1 mf for the degradation of Rh B (0.22205/min) is much higher than that of CSD-0 (0.05659/min) and CSD-0.5(0.0676/min). A similar trend was observed for MB degradation, were the rate constant for CSD-1 mf (0.17709/min) was much higher than that of CSD-0 (0.04072/min).

Table 3.1. The first order rate constants, R^2 values, maximum degradation (%) and time required for maximum degradation for the Rh B and MB by CSD mf.

Sample	K_{app} (CuS/CdS)		R^2		Maximum Degradation (%)		Time taken for maximum degradation (min)	
	RhB	MB	RhB	MB	RhB	MB	RhB	MB
CSD-0	0.0566	0.0407	0.76371	0.95213	62.04	50.21	17	14
CSD-0.5	0.0676	0.0480	0.73335	0.89161	66.99	58.57	12	11
CSD-1	0.2221	0.1771	0.96082	0.94981	96.04	94.69	10	9
CSD-2	0.0839	0.0775	0.70341	0.93671	78.76	73.18	13	12
CSD-3	0.0415	0.0597	0.68105	0.97541	53.03	62.13	15	13

The durability of the catalyst was evaluated by recycling the catalyst in the photo degradation reactions of Rh B and MB in aqueous solutions. Again CSD-1 holds the best durability than others (Figure 3.11b and d). Table 3.2 compares the catalytic efficiencies of many catalysts with CSD composite materials and shows increased catalytic activity of CSD-1 compared to other reported systems [12-16, 33–37]. The data clearly explains that the heterostructures between two binary metal chalcogenides will increase the catalytic activity towards organic dye degradation experiments and the importance of clean surfaces on the catalyst surfaces.

Table 3.2. Comparison table for the various heterostructure catalysts for the photocatalytic degradation of organic dyes.

Catalyst	Pollutant Conc.	Catalyst amount	Time (min)	ref
CuS/Bi_2S_3	10 mg/L	0.1g/L	300	[12]
CuS/ZnO	2×10^{-5} M	20 mg/50 mL	40	[13]
CdS/ZnS	10 mg/L	100 mg/L	360	[14]
TiO_2/CuS	10^{-5} M	30 mg/L	60	[15]
ZnO/CuS	(1.0×10^{-5} M)	2cm x 2cm/50 mL	300	[16]
CuS/Bi_2S_3	2×10^{-5} 10mg/L	0.050 g/L	150	[33]
CuS/ZnS	10^{-5} 10mg/L	0.050 g/L	60	[34]
CuS/TiO_2	10 mg/L	0.100 g /L	180	[35]
CuS-rgo	4 mg/L	0.1 g/L	120	[36]
CdS-rGo	10 mg/L	0.160 g/L	150	[37]
CuS/CdS	5 mg/L	0.030 g/L	10	This work

3.3.5. Structural influence of the degradation reactions.

The mechanism for the performed photo degradation of organic dyes by using CSD composite materials is presented in Figure 3.16 [38]. According to this mechanism, irradiation of CSD composite materials with natural light resulted in the generation of electron and hole pairs. Owing to the driving force attained from the heterostructures with reduced potential energy, the electrons were transferred easily to the conduction band of

CdS. This whole process, in turn, resulted in the formation of super oxygen radicals ($\cdot O_2$) because of the combining of these electrons with absorbed O_2 on the surface. At the same time, the photo generated holes were transferred to CuS from CdS and generated hydroxyl radicals (·OH). At the end, the organic dyes (Rh B and MB) could be degraded efficiently into smaller molecules such as CO_2 and H_2O by these strongly oxidizing species generated in the process.

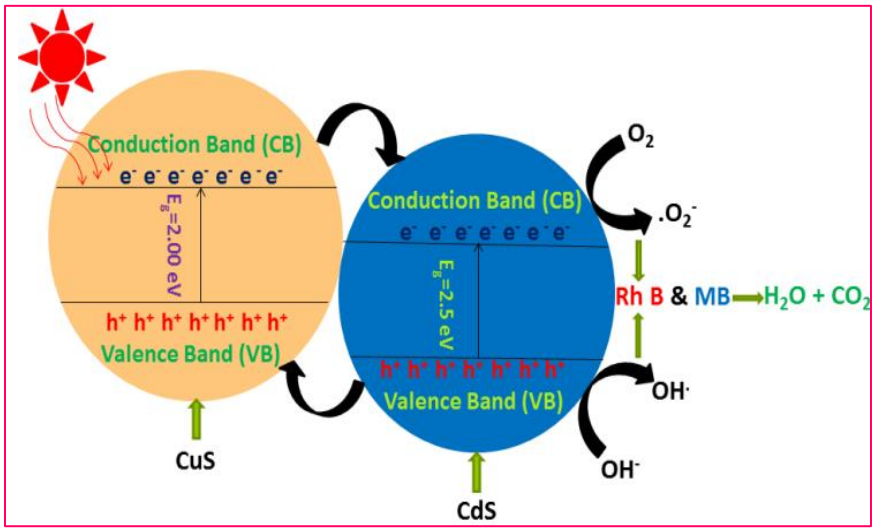

Figure 3.16. The sketch of the band energy level and charge transfers involved in CSD photo catalysts.

The photocatalytic activity of any synthesized catalyst has both the synergistic as well as antagonistic contributions from many underlying factors. Concerning the catalyst described here, there is also scope for both types of factors to operate. For instance, (1) If individual CuS or CdS generate photo-induced charges, those charges can recombine easily resulting in the decreased photocatalytic activity; (2) specific surface area of the catalyst is the main influencing factor of the efficiency of photo degradation; (3) The formation of heterostructure due to its synergistic effect plays a pivotal role in facilitating the parting away of photo induced charges, thus resulting in the enhancement of mobility of charge carriers, hence an overall increase in photocatalytic activity [39].

In the newly created CuS-CdS heterojunction described here, there was an increase in sizes of flower petals with the addition of CdS loadings and a simultaneous increase in

porosity from CSD-0 to CSD-1. Further, there was a decrease (CSD-2 to CSD-3) in the porous cavities of the petals with a further increase in CdS loading. This decrease in the porosity reflected as the lowest adsorption and catalytic activities in relation with their less surface area. Even though CSD-1 has relatively low BET surface area, the adsorption capability of CSD-1 was slightly higher than others. This increased activity was due to highly porous nature and clean surfaces on the catalyst, which provided more catalytic active sites. The availability of surfactant free-surface of photo catalyst facilitates efficient contact with organic contaminants and enhanced charge carrier transfer and thereby presenting the highest photocatalytic decomposition of organic dyes (Rh B and MB) [40]. The enhanced photocatalytic activity was further authenticated from the lifetime studies, as shown in Figure 3.17. The lifetime studies supported our activity performance; the average lifetime for the CSD-1 is less (2.78 ns) compared to other materials [CSD-0, 3.22 ns; CSD-0.5, 3.08 ns; CSD-2, 3.12 ns, and CSD-3, 2.82 ns] [40, 41] which shows its better photocatalytic potential.

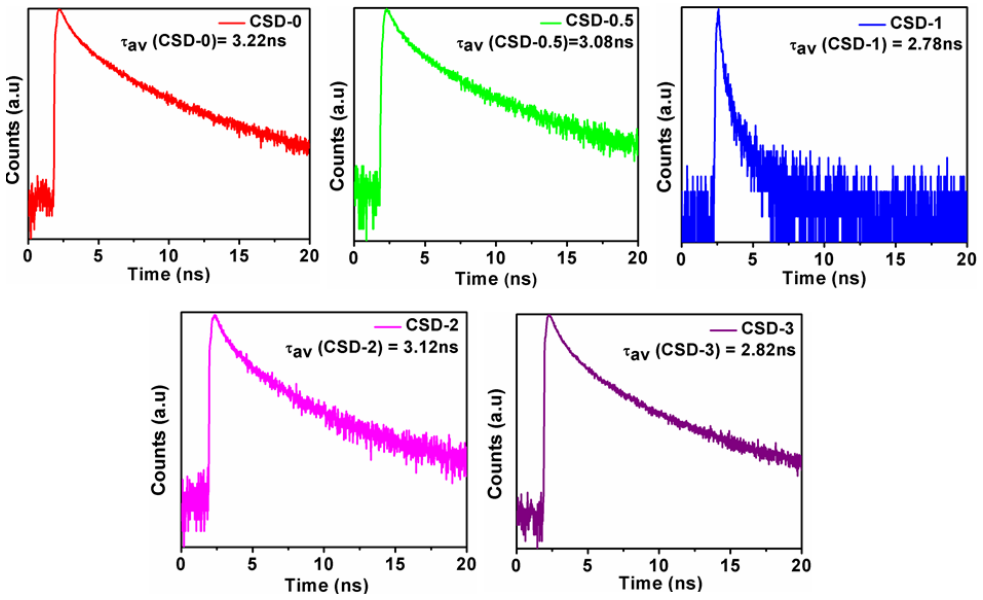

Figure 3.17. Life time studies for composite materials. (a) CSD-0, (b) CSD-0.5, (c) CSD-1, (d) CSD-2 and (e) CSD-3.

For broad spectrum applicability, the recyclability of catalyst is decisive and in this regard, we have tested the reusability of our CSD heterostructure material by repeating the photocatalytic decomposition of organic dyes using the recovered catalyst

under the same experimental procedure. For this purpose, after the experiment, the catalyst was separated by centrifugation (3000 rpm), sequentially washed with distilled water and acetone and then finally dried over vacuum for 2 h at 60 °C. The well-dried catalyst was reused in the procedure, as mentioned above. Interestingly, the heterostructure showed higher stability with no decrease in the activity until the 5th cycle, as can be seen from (Figure 3.11). Although a slight decrease in activity was noticed after 5th catalytic cycle, the photo catalyst was stable until 8 cycles in the case of Rh B and 10 cycles for MB. Further, we have performed morphological (Figure 3.18) studies and obtained XRD spectrum (Figure 3.19) of the reused catalyst (CSD-1). From FESEM images and XRD plots, it was clear that the catalyst was stable with no appreciable changes in the morphology and peak intensities were observed even after 10 cycles. These studies highlight the importance of the heterostructures and clean surfaces on the catalyst for the secure promotion of charges, which directly affects the activity and durability of the photo catalyst.

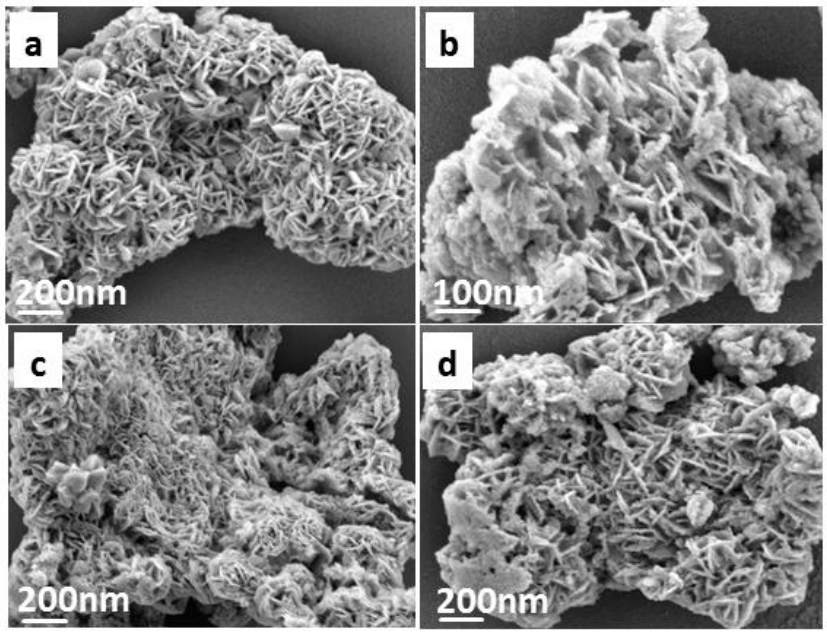

Figure 3.18. Morphological studies for the used catalyst of CuS/CdS nanostructures (CSD-1), (a-b) for MB and (c-d) for Rh B.

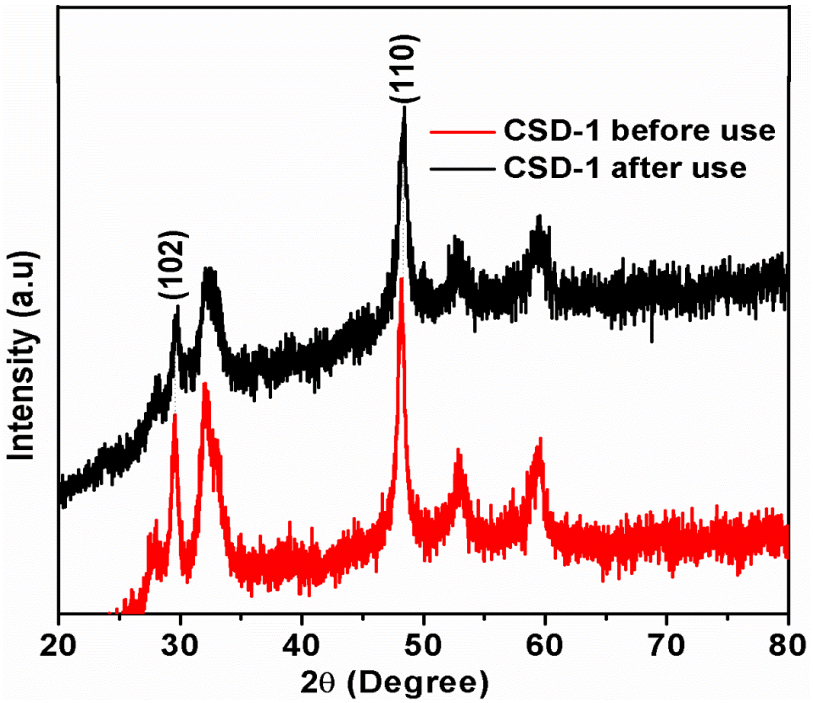

Figure 3.19. Showing the XRD of CSD-1 before (red) and after (black) 10th cycle.

3.4. Summary

In summary, in this chapter, we have demonstrated the formation of a simple CuS-CdS heterojunction resulting from decorating CuS micro flowers (mf) with CdS nanoparticles (NP). These heterojunctions helped to substantially enhance their photocatalytic activity compared to individual binary CuS and CdS nanostructures. These materials, which resulted from a one-pot HMDS-assisted synthesis, were unambiguously characterized by a series of analytical techniques which include PXRD, SEM, EDX, TEM, XPS, and BET. Their incisive structural and morphological investigations revealed that $CdCl_2$ loading decisively affects the composition and morphological transformation from irregular to petals through micro flowers, probably because of the induction of Cl^- ions and the formation of CuS-CdS heterojunction. Investigation of photocatalytic activity interpreted that these nanocomposites possess better photocatalytic efficiency compared to pure CuS and CdS nanostructures, with sample CSD-1 having 1 mmoL $CdCl_2$ loading being the best hit for the degradation of RhB and MB dyes. Moreover, the post-experimental analysis points to that as-prepared catalysts were highly stable (10 cycles) for the photo

degradation of organic dyes, which provided it with excellent potential for further photocatalytic applications.

3.5. References

[1] (a) Eltzov, E.; Pavluchkov, V.; Burstin, M.; Marks, R. S. Creation of a fiber optic based biosensor for air toxicity monitoring. *Sens. Actuators B Chem*. **2011,** *155*, 859–867; (b) Chen, C.; Ma, W.; Zhao, J. Semiconductor-mediated photodegradation of pollutants under visible-light irradiation. *Chem. Soc. Rev*. **2010**, *39*, 4206–4219.

[2] Zhou, L. J.; Zou, Y. C.; Zhao, J.; Wang, P. P.; Feng, L. L.; Sun, L. W.; Wang, D. J.; Li, G. D. Facile synthesis of highly stable and porous Cu_2O/CuO cubes with enhanced gas sensing properties. *Sens. Actuators B Chem*. **2013**, *188*, 533–539.

[3] Kumar, B.; Saha, S.; Ganguly, A.; Ganguli, A. K. A facile low temperature (350 °C) synthesis of Cu_2O nanoparticles and their electrocatalytic and photocatalytic properties. *RSC Adv.* **2014**, *4*, 12043–12049.

[4] Basnet, P.; Larsen, G. K.; Jadeja, R. P.; Hung, Y. C.; Zhao, Y. P. α-Fe_2O_3 nanocolumns and nanorods fabricated by Electron beam evaporation for visible light photocatalytic and antimicrobial applications. *ACS Appl. Mater. Interfaces* **2013**, *5* 2085–2095.

[5] Ma, L. L.; Li, J. L.; Sun, H. Z.; Qiu, M. Q.; Wang, J. B.; Chen, J. Y.; Yu, Y. Self-assembled Cu_2O flowerlike architecture: polyol synthesis, photocatalytic activity and stability under simulated solar light. *Mater. Res. Bull*. **2010**, *45*, 961–968.

[6] Basnet, P.; Zhao, Y.P. Tuning the Cu_xO nanorod composition for efficient visible light induced photocatalysis. *Catal. Sci. Technol*. **2016**, *6*, 2228–2238.

[7] Kudo, A.; Miseki, Y. Heterogeneous photo catalyst materials for water splitting. *Chem. Soc. Rev*. **2009**, *38*, 253–278.

[8] (a) Wang, L. L.; Ge, J.; Wang, A. L.; Deng, M. S.; Wang, X. J.; Bai, S.; Li, R.; Jiang, J.; Zhang, Q.; Luo, Y.; Xiong, Y. J. Designing p-Type semiconductor–Metal hybrid structures for improved photocatalysis. *Angew. Chem. Int. Ed*. **2014**, *53*, 5107–5111 (b)

Zhu, C.; Lu, B.; Su, Q.; Xi, E.; Lan, W. A simple method for the preparation of hollow ZnO nanospheres for use as a high performance photo catalyst. *Nanoscale* **2012**, *4*, 3060–3064. (c) Zhang, G.; Duan, H.; Lu, B.; Xu, Z. Electrospinning directly synthesized metal nanoparticles decorated on both sidewalls of TiO_2 nanotubes and their applications. *Nanoscale* **2013**, *5*, 5801–5808. (d) Zhang, M.; Shao, C.; Mu, J.; Zhang, Z.; Guo, Z.; Zhang, P.; Liu, Y. One-dimensional Bi_2MoO_6/TiO_2 hierarchical heterostructures with enhanced photocatalytic activity. *Cryst. Eng. Commun.* **2012**, *14*, 605–612. (e) Zhang, L.; Jing, D.; She, X.; Liu, H.; Yang, D.; Lu, Y.; Li, J.; Zheng, Z.; Guo, L. Heterojunctions in g-C_3N_4/TiO_2(B) nanofibres with exposed (001) plane and enhanced visible-light photoactivity. *J. Mater. Chem. A* **2014**, *2*, 2071–2078. (f) Chen, X.; Li, C.; Gratzel, M.; Kostecki, R.; Mao, S. S. Nanomaterials for renewable energy production and storage. *Chem. Soc. Rev*. **2012**, *41*, 7909–7937.

[9] Basu, M.; Sinha, A. K.; Pradhan, M.; Sarkar, S.; Negishi, Y.; Govind.; Pal, T. Evolution of hierarchical hexagonal stacked plates of CuS from liquid-Liquid interface and its photocatalytic application for oxidative degradation of different dyes under indoor lighting. *Environ. Sci. Technol.* **2010**, *44*, 6313–6318.

[10] Liu, X.; Mayer, M. T.; Wang, D. Negative differential resistance and resistive switching behaviors in Cu_2S nanowire devices. *Appl. Phys. Lett*. **2010**, *96*, 223103.

[11] Meng, X.; Tian, G.; Chen, Y.; Zhai, R.; Zhou, J.; Y. Shi.; Cao, X.; Zhou, W.; Fu, H. Hierarchical CuS hollow nanospheres and their structure-enhanced visible light photocatalytic properties. *Cryst. Eng. Commun*. **2013**, *15*, 5144–5149.

[12] Liu, Z. Q.; Huang, W. Y.; Zhang, Y. M.; Tong, Y. X. Facile hydrothermal synthesis of Bi_2S_3 spheres and CuS/Bi_2S_3 composites nanostructures with enhanced visible-light photocatalytic performances. *Cryst. Eng. Commun*. **2012**, *14*, 8261–8267.

[13] Lee, M.; Yong, K. Highly efficient visible light photocatalysis of novel CuS/ZnO heterostructure nanowire arrays. *Nanotechnology* **2012**, *23*, 194014.

[14] Soltani, N.; Saiona, E.; Yunus, W. M. M.; Erfani, M.; Navasery, M.; Bahmanrokh, G.; Rezaee, K. Enhancement of visible light photocatalytic activity of ZnS and CdS

nanoparticles based on organic and inorganic coating. *Appl. Surf. Sci.* **2014**, *290*, 440–447.

[15] Khanchandani, S.; Kumar, S.; Ganguli, A. K. Comparative study of TiO_2/CuS Core/Shell and composite nanostructures for efficient visible light photocatalysis. *ACS Sustainable Chem. Eng*. **2016**, *4*, 3, 1487–1499.

[16] Basu, M.; Garg, N.; Ganguli, A. K. A type-II semiconductor (ZnO/CuS heterostructure) for visible light photocatalysis. *J. Mater. Chem. A* **2014**, *2*, 7517–7525.

[17] Thangavel, S.; Krishnamoorthy, K.; kim, S. J.; Venugopal, G. Designing ZnS decorated reduced graphene-oxide nanohybrid via microwave route and their application in photocatalysis. *J. Alloys. Compd.* **2016**, *683*, 456–462.

[18] Rasheed, H. U.; Lv, X.; Wei, W.; Sam, D. K.; Ullah, N.; Xie, J.; Zhu, W. Highly efficient photocatalytic degradation of the Tetracycline hydrochloride on the α-Fe_2O_3@CN composite under the visible light. *J. Environ. Chem. Eng.* **2019**, *7*, 103322.

[19] (a) Huang, Q.; Liu, M.; Mao, L.; Xu, D.; Zeng, G.; Huang, H.; Jiang, R.; Deng, F.; Zhang, X.; Wei, Y. Surface functionalized SiO_2 nanoparticles with cationic polymers via the combination of mussel inspired chemistry and surface initiated atom transfer radical polymerization: characterization and enhanced removal of organic dye. *J. Colloid Interface Sci*. **2017**, *499*, 170–179. (b) Huang, Q.; Liu, M.; Chen, J.; Wan, Q.; Tian, J.; Huang, L.; Jiang, R.; Wen, Y.; Zhang, X.; Wei, Y. Facile preparation of MoS_2 based polymer composites via mussel inspired chemistry and their high efficiency for removal of organic dyes. *Appl. Surf. Sci*. **2017**, *419*, 35–44. (c) Liu, Y.; Huang, H.; Gan, D.; Guo, L.; Liu, M.; Chen, J.; Deng, F.; Zhou, N.; Zhang, X.; Wei, Y. A facile strategy for preparation of magnetic graphene oxide composites and their potential for environmental adsorption. *Ceram. Int*. **2018**, *44*, 18571–18577.

[20] (a) Isari, A. A.; Payan, A.; Fattahi, M.; Jorfi, S.; Kakavandi, B. Photocatalytic degradation of rhodamine B and real textile wastewater using Fe-doped TiO_2 anchored on reduced graphene oxide (Fe-TiO_2/rGO): Characterization and feasibility, mechanism and pathway studies. *Appl. Surf. Sci*. **2018**, *462*, 549–564. (b) Hayati, F.; Isari, A. A.; Fattahi,

M.; Anvaripour, B.; Jorfi, S. Photocatalytic decontamination of phenol and petrochemical wastewater through ZnO/TiO_2 decorated on reduced graphene oxide nanocomposite: influential operating factors, mechanism, and electrical energy consumption. *RSC Adv*. **2018**, *8*, 40035–40053. (c) Shojaie, A.; Fattahi, M.; Jorfi, S.; Ghasemi, B. Synthesis and evaluations of Fe_3O_4–TiO_2–Ag nanocomposites for photocatalytic degradation of 4‑chlorophenol (4‑CP): effect of Ag and Fe compositions. *Int. J. Ind. Chem*. **2018**, *9*, 141–151.

[21] Wan, X.; Liang, X. Y.; Zhang, C. R.; Li, X. X.; Liang, W. W.; Xu, H. S.; Lan, S.; Tie, S. L. Morphology controlled syntheses of Cu-doped ZnO, tubular Zn(Cu)O and Ag decorated tubular Zn(Cu)O microcrystals for photocatalysis. *Chem. Eng. J*. **2015** *272*, 58–68.

[22] Xu, X.; Gao, Z. H.; Cui, Z. D.; Liang, Y. Q.; Li, Z. Y.; Zhu, S. L.; Yang, X. J.; Ma, J. M. Synthesis of Cu_2O Octadecahedron/TiO_2 quantum dot heterojunctions with high visible light photocatalytic activity and high stability. *ACS Appl. Mater. Interfaces* **2016**, *8*, 91–101.

[23] (a) Chen, L.; Yin, S. F.; Luo, S. L.; Huang, R.; Zhang, Q.; Hong, T.; Au, P. C. T.; $Bi_2O_2CO_3$/BiOI photocatalysts with heterojunctions highly efficient for visible-light treatment of dye-containing wastewater. *Ind. Eng. Chem. Res*. **2012**, *51*, 6760. (b) Chen, L.; Zhang, Q.; Huang, R.; Yin, S. F.; Luo, S. L.; Au, C. T. Porous peanut-like Bi_2O_3–$BiVO_4$ composites with heterojunctions: one-step synthesis and their photocatalytic properties. *Dalton Trans*. **2012**, *41*, 9513. (c) Xiong, M.; Chen, L.; Yuan, Q.; He, J.; Luo, S. L.; Au, C. T.; Yin, S. F. Facile fabrication and enhanced photosensitized degradation performance of the g-C_3N_4–$Bi_2O_2CO_3$ composite. *Dalton Trans*. **2014**, *43*, 8331. (d) Chen, L.; Huang, R.; Ma, Y. J.; Luo, S. L.; Au, C. T. Controllable synthesis of hollow and porous Ag/$BiVO_4$ composites with enhanced visible-light photocatalytic performance. *RSC Adv*. **2013**, *3*, 24354. (e) Kumar, S. G.; Rao, K. S. R. K. Zinc oxide based photocatalysis: tailoring surface bulk structure and related interfacial charge carrier dynamics for better environmental applications. *RSC Adv*. **2015**, *5*, 3306-3351.

[24] Wang, Q.; Yun, G.; Bai, Y.; An, N.; Chen, Y.; Wang, R.; Lei, Z.; Guan, W. S. CuS, NiS as cocatalyst for enhanced photocatalytic hydrogen evolution over TiO_2. *Int. J. Hydrogen Energy* **2014**, *39*, 13421–13428.

[25] Guan, X. H.; Yang, L.; Guan, X.; Wang, G. S. Synthesis of a Flower-Like CuS/ZnS Nanocomposite Decorated on Reduced Graphene Oxide and Its Photocatalytic Performance. *RSC Adv.* **2015**, *5*, 36185-36191.

[26] (a) Mondal, C.; Singh, A.; Sahoo, R.; Sasmal, A.K.; Negishi, Y.; Pal, T. Preformed ZnS nanoflower prompted evolution of CuS/ZnS p–n heterojunctions for exceptional visible-light driven photocatalytic activity. *New J. Chem*. **2015**, *39*, 5628–5635; (b) Dzhagana, V.; Kempken, B.; Valakh, M.; Parisi, J.; Kolny- Olesiak, J.; Zahn, D.R.T. Probing the structure of $CuInS_2$-ZnS core-shell and similar nanocrystals by Raman spectroscopy. *Appl. Surf. Sci*. **2017**, *395*, 24–28.

[27] (a) Kumar, B. G.; Muralidharan, K. Hexamethyldisilazane-assisted synthesis of indium sulphide nanoparticles. *J. Mater. Chem*. **2011**, *21*, 11271–11275. (b) Kumar, B. G.; Muralidharan, K. Organic-free self-assembled copper sulfide microflowers. *Eur. J. Inorg. Chem*. **2013**, 2102–2108. (c) Kumar, B. G.; Muralidharan, K. S_4N_4 as an intermediate in Ag_2S nanoparticle synthesis. *RSC Adv*. **2014**, *4*, 28219–28224. (d) Kumar, B. G.; Srinivas, B.; Prasad, M. D.; Muralidharan, K. Ag/Ag_2S heterodimers: tailoring the metal–semiconductor interface in a single nanoparticle. *J. Nanopart. Res*. **2015**, *17*, 325–336. (e) Srinivas, B.; Kumar, B. G.; Muralidharan, K. Stabilizer free copper sulphide nanostructures for rapid photocatalytic decomposition of rhodamine, B. *J. Mol. Catal. A*: *Chem*. **2015**, *410*, 8–18. (f) Billakanti, S.; Baskaran, G. K.; Muralidharan, K. Recyclable Ni_3S_4 nanocatalyst for hydrogenation of nitroarenes. *Chem. Select* **2017**, *2*, 4753–4758. (g) Billakanti, S.; Muralidharan, K. Facile preparation of surfactant or support material free CdS nanoparticles with enhanced photocatalytic activity. *J. Environ. Chem. Eng*. **2018**, *6*, 1250–1256. (h) Billakanti, S.; Pandit, M. A.; Muralidharan, K. Importance of clean surfaces on the catalyst: SnS_2 nanorings for environmental remediation. *ACS Omega* **2019**, *4*, 14970–14980.

[28] Kumar, P.; Gusain, M.; Nagarajan, R. Synthesis of $Cu_{1.8}S$ and CuS from copperthiourea containing precursors; Anionic (Cl^{-}, NO^{3-}, SO_4^{2-}) influence on the product stoichiometry. *Inorg. Chem*. **2011**, *50*, 3065–3070.

[29] Zhang, L. J.; Xie, T. F.; Wang, D. J.; Li, S.; Wang, L. L.; Chen, L. P.; Lu, Y.C. Noble-metal free CuS/CdS composites for photocatalytic H_2 evolution and its photogenerated charge transfer properties. *Int. J. Hydrogen Energy* **2013**, *38*, 11811–11817.

[30] (a) Zong, X.; Han, J. F.; Ma, G. J.; Yan, H. J.; Wu, G. P.; Li, C. Photocatalytic H_2 evolution on CdS loaded with WS_2 as cocatalyst under visible light irradiation. *J. Phys. Chem. C* **2011**, *115*, 12202–12208. (b) Kar, P.; Farsinezhad, S.; Zhang, X.; Shankar, K. Anodic Cu_2S and CuS nanorod and nanowall arrays: preparation, properties and application in CO_2 photoreduction. *Nanoscale* **2014**, *6*, 14305–14318.

[31] (a) Saranya, M.; Ramachandran, R.; Jeong, S. K.; Grace, A. N. Enhanced visible light photocatalytic reduction of organic pollutant and electrochemical properties of CuS catalyst. *Powder Technol*. **2015**, 209–220. (b) Hosseinpour, Z.; Hosseinpour, S.; Maaza, M.; Scarpellini, A. Co^{2+} and Ho^{3+} doped CuS nanocrystals with improved photocatalytic activity under visible light irradiation. *RSC Adv*. **2016**, *6*, 42581–42588.

[32] (a) Xiong, S.; Xi, B.; Qian, Y. CdS hierarchical nanostructures with tunable morphologies: preparation and photocatalytic properties. *J. Phys. Chem. C* **2010**, *114*, 14029–14035. (b) Tian, Q. Y.; Wu, W.; Sun, L. G.; Yang, S.; Lei, M.; Zhou, J.; Liu, Y.; Xiao, X. G.; Ren, F.; Jiang, C. Z.; Roy, V. A. L. Tube-like ternary α-Fe_2O_3@SnO_2@Cu_2O sandwich heterostructures: synthesis and enhanced photocatalytic properties. *ACS Appl. Mater. Interfaces* **2014**, *6*, 13088–13097.

[33] Chen, L.; He, J.; Yuan, Q.; Zhang, Y. W.; Wang, F.; Au, C. T.; Yin, S. F. CuS–Bi_2S_3 hierarchical architectures: controlled synthesis and enhanced visible-light photocatalytic performance for dye degradation. *RSC Adv*. **2015**, *5*, 33747–33754.

[34] Yu, J.; Zhang, J.; Liu, S. Ion-exchange synthesis and enhanced visible-light photoactivity of CuS/ZnS nanocomposite hollow spheres. *J. Phys. Chem. C* **2010**, *114*, 13642–13649.

[35] Hou, G.; Cheng, Z.; Kang, L.; Xu, X. J.; Zhang, F.; Yang, H. Controllable synthesis of CuS decorated TiO_2 nanofibers for enhanced photocatalysis. *Cryst. Eng. Comm*. **2015**, *17*, 5496–5501.

[36] Zhang, Y.; Tian, J.; Li, H.; Wang, L.; Qin, X.; Asiri, A. M.; Youbi, A. O. Al.; Sun, X. Biomolecule-Assisted, Environmentally Friendly, One-Pot Synthesis of CuS/ Reduced Graphene Oxide Nanocomposites with Enhanced Photocatalytic Performance. *Langmuir* **2012**, *28*, 12893–12900.

[37] Wang, X.; Tian, H.; Yang, Y.; Wang, H.; Wang, S.; Zheng, W.; Liu, Y. Reduced graphene oxide/CdS for efficiently photocatalystic degradation of methylene blue. *J. Alloys Compd*. **2012**, *524*, 5–12.

[38] (a) Tanveer, M.; Cao, C. B.; Aslam, I.; Ali, Z.; Idrees, F.; Tahir, M.; Khan, W. S.; Butt, F. K.; Mahmood, A. Effect of the morphology of CuS upon the photocatalytic degradation of organic dyes. *RSC Adv*. **2014**, 4, 63447–63456. (b) Kundu, J.; Pradhan, D. Controlled synthesis and catalytic activity of copper sulfide nanostructured assemblies with different morphologies. *ACS Appl. Mater. Interfaces* **2014**, *6*, 1823–1834.

[39] Khan, Z.; Chetia, T. R.; Vardhaman, A. K.; Barpuzary, D.; Sastri, C. V.; Qureshi, M. Visible light assisted photocatalytic hydrogen generation and organic dye degradation by CdS–metal oxide hybrids in presence of graphene oxide. *RSC Adv*. **2012**, *2*, 12122–12128.

[40] Shen, R. C.; Xie, J.; Guo, P.; Chen, L.; Chen, X.; Li, X. Bridging the g-C_3N_4 nanosheets and robust CuS cocatalysts by metallic acetylene black interface mediators for active and durable photocatalytic H_2 production. *ACS Appl. Energy Mater*. **2018**, *1*, 5, 2232–2241.

[41] Chauhan, H.; Soni, K.; Kumar, M.; Deka, S. Tandem photocatalysis of graphenestacked SnS_2 nanodiscs and nanosheets with efficient carrier separation. *ACS Omega* **2016**, *1*, 127–137.

CHAPTER-4

Chalcopyrite with Magnetic and Dielectric Properties: An Introductory Catalyst for 4-Nitrophenol Reduction

Abstract

The progress for the development of active, stable, and economic catalysts for the chemical transformation of noxious chemicals to benign is of primary importance. The synthesis of surfactant-free chalcopyrite, sf-$CuFeS_2$, by a wet-chemical one-pot hexamethyldisilazane-assisted synthetic method was accomplished. Various analytical and spectroscopic techniques were used for the physical characterization of the material produced. From the observation of magnetic properties, the material chalcopyrite was found to be paramagnetic. The dielectric constant and dielectric loss were also determined and were found to be decreasing with an increase in frequency. The dielectric behavior of the material was explained by the Maxwell−Wagner theory of polarization, and the dielectric constant of the as-synthesized sample was found to be 3.176 at 100 °C and 500 kHz. The potential catalytic activity was confirmed by performing the reduction of 4-nitrophenol (4-NP) to 4-amino phenol (4-AP) in the presence of sodium borohydride (NaBH4) in aqueous medium at room temperature. The catalyst showed about 90% yield in the reduction reactions, which can be attributed to easy access to active sites invigorated by the absence of surfactant molecules. The reusability of the catalyst was checked to find out the stability, and excellent retention of activity up to five cycles was observed.

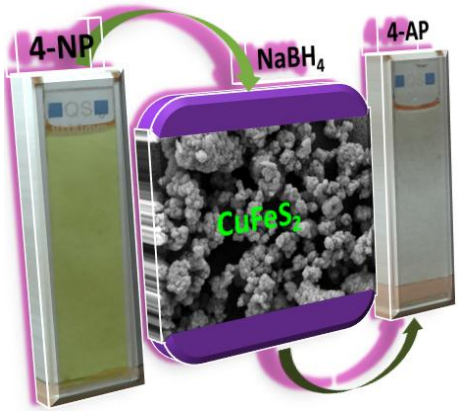

J. Phys. Chem. C 2020, 124, 18010−18019

4.1. Introduction

Ternary chalcogenides of a transition metals of type $CuMX_2$ (where M = Al, In, Ga and Fe, X = S, Se) that are behaving as semiconductors have attracted immense research interest because of their characteristic physical and chemical properties. These materials have shown potential applications in spintronics and photo conversion in solar cells [1–8]. Among these transition metal chalcogenides, the chalcopyrite has been studied widely. Chalcopyrite with an elemental composition of earth-abundant elements like Cu and Fe, besides S, lags in the race of literature of semiconductors of Cu-based nanocrystals (NCs) [9, 10]. Chalcopyrite has a zinc blende-type structure with a coordination number of four for both cations and anions forming distinct corner-sharing tetrahedral [11].

The chalcopyrite mineral ($CuFeS_2$) having the dazzling golden surface is considered the most capable semiconductor material with unfamiliar optical, electrical, and magnetic properties [12, 13]. It also possesses high values of thermoelectric power [14] and rectification [15] with an optical band gap [16, 17] of (0.5–0.6 eV) behaving as an n-type semiconductor. Chalcopyrite exhibits magnetic property changing from antiferromagnetic behavior to paramagnetic depending on temperature. It displays antiferro-magnetic property achievable at a Neel temperature of 823 K, while a paramagnetic arrangement at around 50 K. The probable reason for this complicated magnetic behavior is as follows. Neutron diffraction studies of $CuFeS_2$ showed an effective magnetic moment of 3.85 μB for Fe, which is lower compared to the expected value for Fe^{3+} ions (~5.0 μB) [12]. The lesser magnetic moment was attributed to the significant Fe−S covalent interactions [18-20]. The magnetic moment of Cu in chalcopyrite could not be calculated accurately in the vicinity of a large moment of the iron ion [21, 22].

For many nanostructured materials, the exciting variation in properties is observed based on the crystal structure and morphology of materials, which in turn depends on the synthetic procedures. $CuFeS_2$ nanostructures have received tremendous research interest. Silvester et al. synthesized colloidal sols of $CuFeS_2$ nanocrystals by a hydrothermal method under the controlled conversion of iron (III) oxide. These materials were optically transparent and their properties were closely matching to that of bulk

material [23, 24]. Wang et al. [25] and Liang et al. [26] independently developed prominent colloidal methods to synthesize $CuFeS_2$ nanocrystals. Various types of nanostructures of $CuFeS_2$, including thin films [27], (nanowires, nanorods, spherical particles) [16, 17], and nanocrystals [25, 26, 28] have been synthesized for probable applications in photovoltaics [29], thermoelectric [26], and spintronic devices, dye degradation [30].

One of the biggest challenges and concerns in front of researchers is to make the environment pollutant-free. Large quantities of toxic and carcinogenic chemical by-products like organic dyes [31-33], nitro-based aromatic compounds [34], and heavy metal ions [35-37], are continuously being released into water bodies from industrial units. These pollutants contaminate water as well as create environmental menace at an alarming rate and are becoming a difficult task to handle [38-46]. Nitrophenols (NP) are considered to be the most common pollutants in both industrial and agricultural wastewaters, particularly among them 4-NP which is highly soluble and stable in water. It is a most tarnished pollutant and has made life vulnerable on exposure, causing severe health problems [47-50].

Various treatments were designed for the removal of 4-NP from water like adsorption [51, 52] catalytic reduction [53, 54]. Adsorption is considered a best remedy for waste water treatment from nitro-compounds. Adsorption involves the use of an adsorbent which can adsorb the adsorbate mostly contaminate on its surface. Adsorption is also economical, efficient and an easy approach for 4-NP reduction. Nevertheless, the adsorption process mostly depends on the nature of the adsorbent, like its morphology, surface area, and size [49]. Besides these temperatures, pH and time are the important factors going to decide the fate of adsorption process [55]. Whereas on the other hand the catalytic approach is considered a very simple, versatile and cost effective process, involving the use of a reducing agent like $NaBH_4$ in presence of nanomaterials as catalysts for the reduction of 4-NP [56].

The primary purpose of the work in this chapter is to produce chalcopyrite nanoparticles in a simplified method and determine their unique magnetic and dielectric properties compared to the same materials known in the literature. Also, it is of interest to

test the hitherto unknown catalytic ability of $CuFeS_2$ in organic functional group transformation reactions. We are able to synthesize surfactant-free $CuFeS_2$ nanoparticles (sf-$CuFeS_2$) using a realistic HMDS-assisted synthetic approach. The synthesized nanostructures were characterized by powder X-ray diffraction, scanning electron microscopy (SEM), and high resolution transmission electron microscopy (HRTEM). The magnetic property measurement (at room temperature and 100 K) confirms the paramagnetic nature of the chalcopyrite material. Dielectric studies showed a substantial decrease in the value of both dielectric constant and dielectric loss at low frequency, but at a higher frequency, it remains unchanged. After confirming the properties of sf-$CuFeS_2$ nanoparticles without any organic molecules in their surroundings, the synthesized chalcopyrite was assessed for its potential catalytic ability in the reduction of 4-NP to 4-aminophenol (4-AP). It is important to mention here that there is no report yet on the catalytic reduction of 4-NP to 4-AP using $CuFeS_2$ nanoparticles. The catalyst developed consists of naturally abundant and low-cost non-noble elements that make the easy availability of the catalyst on a large scale.

4.2. Experimental Section

4.2.1. Materials

Copper chloride ($CuCl_2$ anhydrous), ferric chloride ($FeCl_3$ anhydrous), thiourea [$H_2NC(S)NH_2$] and hexamethyldisilazane [$(Me_3Si)_2NH$] (HMDS) were purchased from Sigma Aldrich. All the above reagents were of analytical grade and used without further purification.

4.2.2. Synthesis of $CuFeS_2$ chalcopyrites

For the synthesis of sf-$CuFeS_2$ nanoparticles, hexamethyldisilazane (HMDS)-assisted wet chemical method was employed. In a typical reaction 1.48 mmol $CuCl_2$, 1.48 mmol $FeCl_3$ and 2.56 mmol thiourea were added one by one to RB flask connected to the Schlenk lines to maintain the inert conditions. Then, 6 ml HMDS (26 mmol) were injected by syringe under the continuous supply of nitrogen gas. The reaction mixture was set to reflux at 160 °C for 3 hours with continuous stirring. After the completion of reaction the

precipitates were separated by centrifugation at 2500 rpm, decanted and then washed by deionized water and ethanol each 3-4 times. The material collected was subjected to high vacuum for the complete removal of any residual solvents. The product was dried at 70 °C for overnight in a vacuum oven.

4.2.3. Catalytic reduction of 4-Nitrophenol

In order to perform the catalytic reduction of 4-nitrophenol, a general procedure was applied. A 0.5 ml of $NaBH_4$ (0.1 M) aqueous solution was added to 2.5 ml of 4-nitrophenol (0.1 mM) aqueous solution. To this mixture was added 0.8 ml of sf-$CuFeS_2$ suspension (8 mg/100 ml) to perform the catalysis. The reduction of 4-nitophenol to 4-aminophenol was regularly monitored using UV-Vis absorption spectrum within a range of 200 nm to 600 nm. The conversion percentage of the $CuFeS_2$ catalyst is given by the equation-1.

$$\% \text{ Conversion} = (C_o - C_t/C_o) * 100 \qquad (1)$$

Here C_o is the initial concentration (corresponding to absorbance) of 4-nitrophenol at λ_{max}, and C_t is the concentration at time (t).

4.2.4. Instrumentation

Various analytical techniques used for the characterization of $CuFeS_2$ are described as follows. The X-ray diffraction measurements for determining crystal structure and phase purity were performed using Bruker D8 X-ray diffractometer equipped with CuKa radiation (λ = 1.54056 Å, 2θ range from 20° to 70°).The Surface morphology, particle size, and elemental analysis were carried by FESEM, and EDAS studies using an Ultra 55 Carl Zeiss instrument with an operating voltage of 10 kV. The TEM images were acquired using an FEI Technai G2 20 STEM with a 200 kV acceleration voltage. The samples were prepared by drop casting of a colloidal suspension of chalcopyrite on carbon-coated copper grids (200 meshes). Optical properties and catalysis were recorded with a JASCO-V770 UV/Vis spectrometer; Barium sulphate was used as standard. The specific surface area and the pore size of the material were estimated by Nova 2000e, Quantachrome Instruments Limited, USA using liquid nitrogen (77 K). The Specific surface area and the average pore size distribution were determined by using Multipoint BET equation and

from BJH plots, respectively. The oxidation state and elemental compositions were determined by X-ray photoelectron spectra (XPS) using a Thermo scientific Escalab 250Xi spectrometer with Al−Kα radiation. Magnetic properties were studied by the VSM instrument at two different temperatures. For studying dielectric properties, the principle of parallel plate capacitor was applied, and the measurements were carried on HF-LCR meter (6505 P, Wayne Kerr Electronics, UK) instrument. An 8 mm, thick disk-shaped pellet of 0.5 mm thickness was prepared under a uniaxial pressure of 5 tons and 5% of polyvinyl alcohol (PVA) as a binder. The prepared pellet was sintered at 500 °C for the removal of binder. A thin paste of silver acting as a conducting layer was applied on the pellet to function as an electrode.

4.3. Results and Discussion

4.3.1. Synthesis and characterization

The chalcopyrite material (sf-$CuFeS_2$) was synthesized (Scheme 4.1) by one-pot HMDS assisted wet chemical approach supplemented with Schlenk lines to maintain the continuous inert atmosphere.

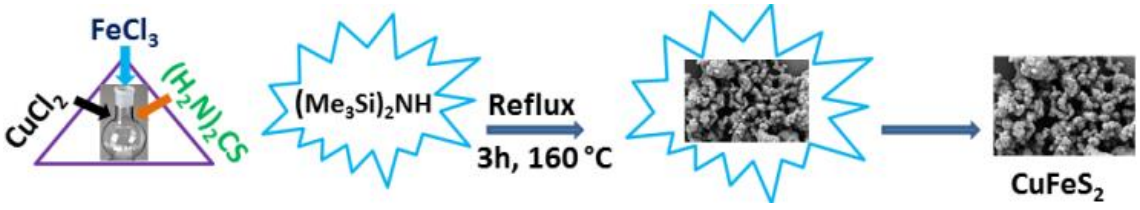

Scheme 4.1. Schematic illustration of the reaction showing chalcopyrite formation.

PXRD pattern confirmed the crystalline nature and phase purity of the prepared sample. As shown in Figure 4.1, all the peaks can be indexed to the tetragonal structure of chalcopyrites with JCPDS No. 37-0471 [57]. The peaks at 2θ of 29.4, 49.01, and 57.8 can be indexed to planes of (112), (220), and (312), respectively. No other characteristics peaks was found in the PXRD pattern that can indexed to either pure CuS or FeS_2 phases or any other stoichiometry of both, hence confirming the single-phase and high purity of the material.

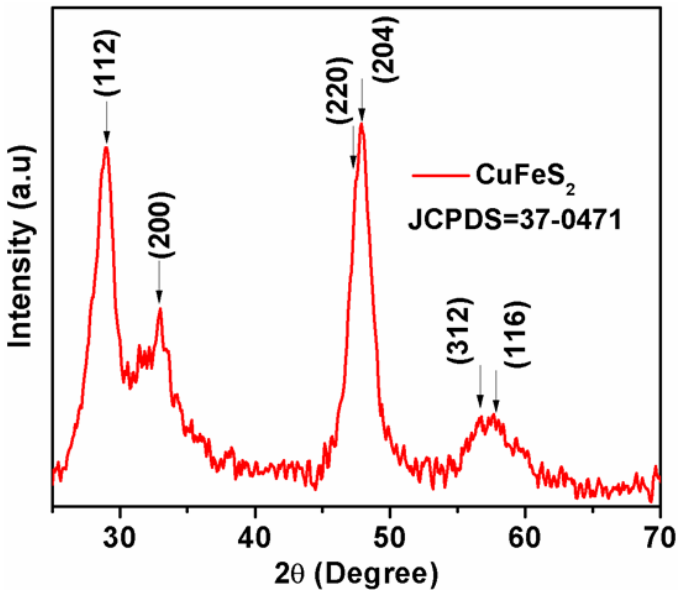

Figure 4.1. The PXRD pattern of $CuFeS_2$ showing high crystalline nature with high intensity peaks. All the peaks correspond to JCPDS = 37-0471.

SEM and EDAS images revealed the morphology and elemental distribution. As shown in Figure 4.2a, scanning electron microscopy (SEM) confirms that the nanostructures have particle type morphology with almost all the particles of similar size. The particles formed clusters probably because of surfactant-free synthesis.

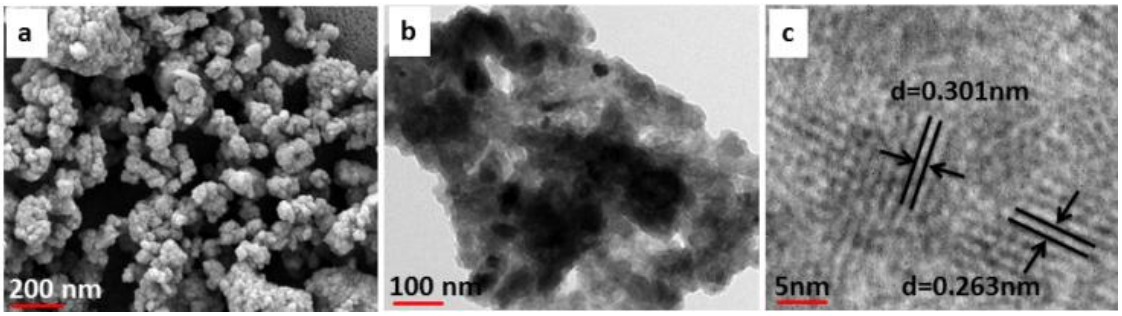

Figure 4.2. The morphological analysis of sf-$CuFeS_2$. (a) FE SEM images (b) TEM and (c) HRTEM images.

The high magnification SEM image also depicts the particle size formation; the aggregation might be because of surfactant free synthesis (Figure 4.4a). The study aims to develop surfactant-free materials in order to exhibit excellent properties. The elemental distribution analysis spectra (EDAS) (Figure 4.3) reveal that all three elements (Cu, Fe, and S) are distributed well in the stoichiometric ratios.

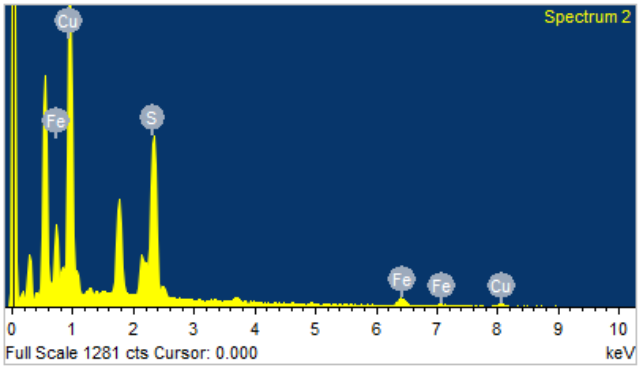

Element	Weight%	Atomic%
S K	21.52	34.28
Fe L	23.77	21.74
Cu L	54.71	43.98
Totals	100.00	

Figure 4.3. The elemental distribution analysis of $CuFeS_2$ nanomaterial showing by EDAS.

Further confirmation about the particle morphology of synthesized materials was performed by TEM analysis. Figure 4.2b represents the distinctive TEM images of sf-$CuFeS_2$ nanoparticles. From the figure, it is clear that the particles are of nano dimensions with the average particle size approximately equals to ~65 nm. The High-resolution TEM images (HRTEM) is shown in Figure 4.2c. It shows that the distance between two crystal facet planes is 0.301 nm and 0.263 nm, which correspond well to planes (112) and (200) respectively of the synthesized material. The dark field TEM images (Figure 4.4b) shows bright spots corresponding to the particle nature of synthesized materials, hence agreeing well with the SEM. The SAED patterns (Figure 4.4c) shows some diffraction rings corresponding to (112), (220) and (204) crystal planes, which matches well with the PXRD patterns, so confirming the well crystalline nature of sf-$CuFeS_2$ nanoparticles.

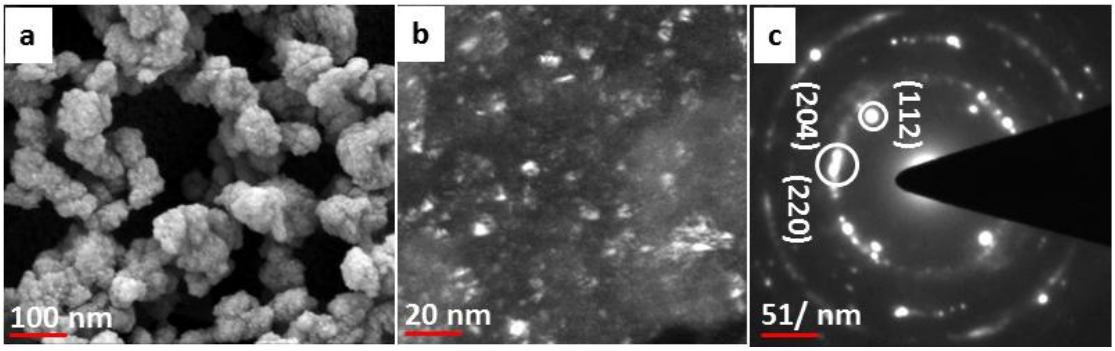

Figure 4.4. (a).high magnification SEM images (b). Dark field TEM images (c). SAED patterns of $CuFeS_2$.

The further validity of chalcopyrite formation and the elemental composition with valance states was confirmed by performing XPS analysis (Figure 4.5). The survey

spectrum (Figure 4.5a) shows that all the elements Cu, Fe, and S are well present in the chalcopyrite. The spectrum shows Cu 2p split to two dominant peaks, Cu $2p_{1/2}$ and Cu $2p_{3/2}$ at a binding energy of 955.15 eV and 935.20 eV, indicating the presence of Cu as Cu^{+} ion (Figure 4.5b). Besides this two weak satellite peaks located at 944.93 eV and 963.8 eV are observed clearly in the Cu 2p spectrum which is reliable with the presence of Cu^{2+} rather than as Cu (0) [58]. Similarly, Fe peak (Figure 4.5c) got split to two peaks, Fe $2p_{1/2}$ and Fe $2p_{3/2}$ at 726.03 eV and 712.05 eV respectively, revealing the existence of Fe as Fe^{3+} [59]. The S 2p spectrum (Figure 4.5d) shows two peaks one at 164.9 for S $2p_{3/2}$ and other peak at 169.5 eV assigned for S-O bond showing oxidized Sulphur related species but since there is no proof for the oxidation of S in the $CuFeS_2$ happening, so indicating the presence of S as S^{2-} [60, 61].

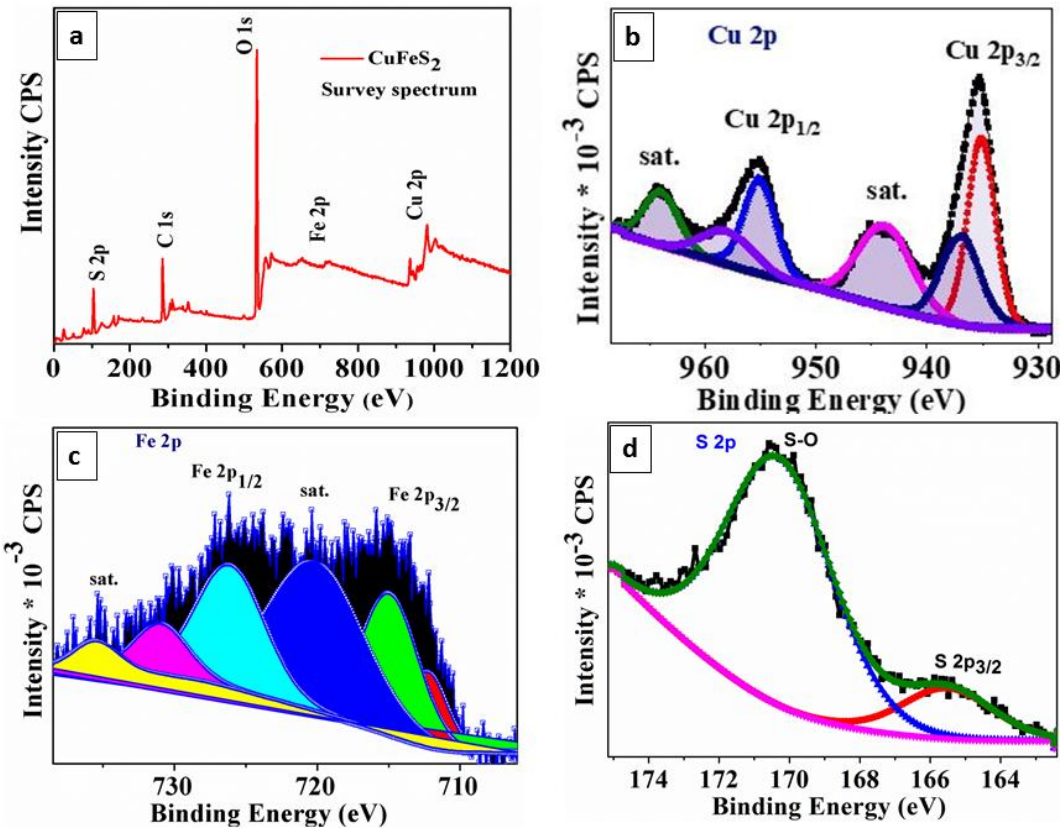

Figure 4.5. XPS spectrum of sf-$CuFeS_2$. (a) the survey spectrum showing the presence of all requisite elements Cu, Fe and S. (b-d) representing the Binding energy values of Cu, Fe and S respectively.

4.3.2. Magnetic Property

The chalcopyrite, $CuFeS_2$ is known for its magnetic properties and related applications. Therefore, it is required to study the sf-$CuFeS_2$ prepared in this study. Figure 4.6a shows Magnetization vs. applied magnetic field ($M(H)$) plots for the samples of sf-$CuFeS_2$ at 300 and 100 K, respectively. Almost straight line behaviour of M(H) curve indicates the paramagnetic behavior of the sample. Magnetization values at 1.5 Tesla are 148 and 17 milli emu/gm at 300 and 100 K respectively. Coercivity values are 23 and 48 milli tesla at 300 and 100 K, respectively. A decrease in magnetization is noticed at 100 K while coercivity values are increased at lower temperature. Even though coercivity and remanant magnetization values are very small but the existence of these parameters indicates the presence of small ferromagnetism in sf-$CuFeS_2$. But the ferromagnetism in the samples is suppressed with the dominating paramagnetic nature of the samples.

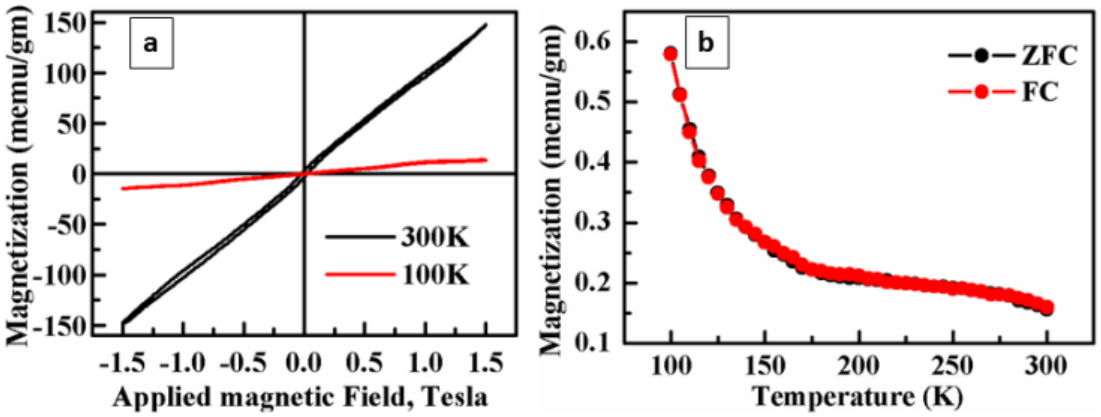

Figure 4.6. (a) Magnetization vs. applied magnetic field plots for the samples at 300 and 100 K, respectively. (b) Magnetization vs. temperature plots for the samples.

Figure 4.6b shows the magnetization vs. temperature (M(T)) plots in the temperature range 100 to 300 K in zero field-cooled (ZFC) and field cooled (FC) mode at applied field of 500 Oe. Bifurcation between ZFC and FC curve is very narrow indicates that paramagnetism is dominating in the synthesized sf-$CuFeS_2$ material [62].

4.3.3. Dielectric constant properties

For many minerals finding out dielectric properties has become a topic of discussion. Since the dielectric property depends on the conductivity, it is of curiosity to understand

the frequency-dependent variation in the dielectric constant of sf-$CuFeS_2$. The following formula is used to determine the dielectric constant of a mineral,

$$\varepsilon' = Cd/A\varepsilon_0 \quad (1) \text{ and}$$

$$\varepsilon' = \acute{\varepsilon} \tan\delta \quad (2)$$

Here d represents the thickness, A area of the sample and C is capacitance.

The dielectric properties of sf-$CuFeS_2$ pellet sintered at 500 °C were studied by varying frequency from 20 Hz to 1 MHz within a temperature range of 100 °C to 400 °C (Figure 4.7). From Figure 4.7a, it is clear that the dielectric constant values decrease continuously with the increase in frequency [63]. Upto 100 kHz there is regular decrease, but after then, with the further increase in frequency, it remains constant. Also, it is seen that the dielectric loss of the material shows similar behavior like dielectric constant (Figure 4.7b). This behavior of the synthesized sample could be explained based on the Maxwell-Wagner polarization theory of dielectrics. Space charge polarization is a factor responsible for the decrease in values of dielectric properties, which is associated with the charge concentrated at the grain boundaries or grain deficiencies of the sample particles of various dielectric properties [64]. The contribution from grain sizes mostly controls the low-frequency values of ε. From the figure, we see that the values of both dielectric constant and dielectric loss drop with the increase of frequency for this sf-$CuFeS_2$ material.

According to Maxwell-Wagner theory at lower frequencies, different polarization mechanisms, including space charge, dipolar, and ionic polarization contribute to the dielectric properties of the material [65]. However, with an increase in frequency, the space charge polarization does not get enough time to follow the applied external frequency, therefore are relaxed out, leading to the reduction of dielectric properties of the material with an increase in the frequency. It was found that the dielectric constant determined at different temperatures remains unchanged at higher frequencies indicating that dielectric property does not vary with the change in temperature. The dielectric loss at higher frequencies was found to be relatively low because the electric wave frequency was not found to be in proper comparison to the natural frequency of the bounded charge, so the reason for weak radiation. The dielectric constant of sf-$CuFeS_2$ at 100 °C and 500

kHz is 3.176 the low value might be presumably because of the particle type morphology as compared to bulk or sheet morphology as reported previously [66].

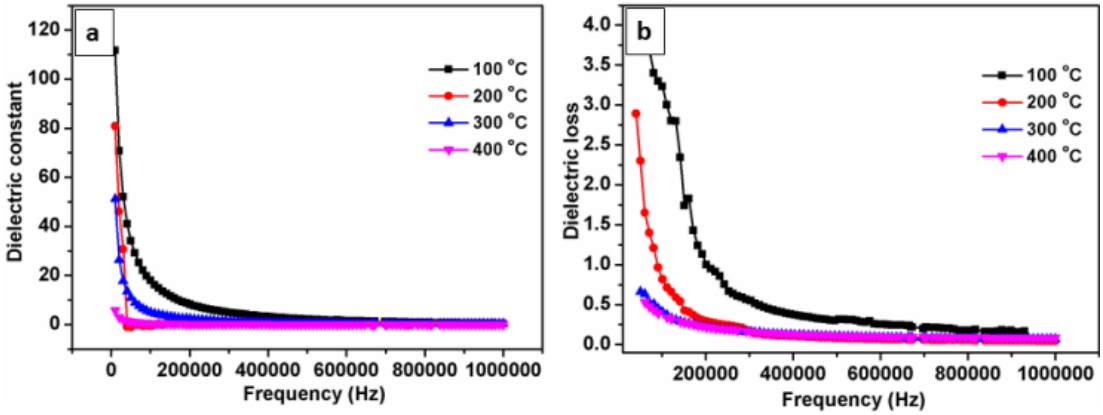

Figure 4.7. Plot showing variation of (a) dielectric constant and (b) dielectric loss with frequency at different temperatures.

4.3.4. Surface area and photo physical properties

The active surface area and photophysical properties of catalysts are the most critical parameter to determine the catalytic activity. A general sense is prevailing in the catalysts related to the surface area that is- large the surface area, higher will be the catalytic activity. The reason is that a material with a large surface area will be having a sufficient amount of active sites that will undergo maximum adsorption, hence higher catalytic activity (Figure 4.8). From Figure 4.8a, it is evident that the N_2 adsorption-desorption curves of chalcopyrite follow the type III isotherm. The isotherm shows an excellent interface that is formed between the adsorbent and the adsorbed layer, suggesting a strong interaction between these two, showing multilayer adsorption taken place [67].

The specific surface area of sf-$CuFeS_2$was found to be 36 m^2/g. The average pore size of chalcopyrite, as calculated from BJH plots (Figure 4.8b), was found to be ca. 17 Å. From the observations (high surface area and average pore size), it is clear that the nature of the sample is mesoporous, and the enhancement in the porosity is because of the surfactant-free synthesis. Since there is no other organic surfactant molecules are surrounding the sf-$CuFeS_2$, the whole surface area is available for catalytic activity.

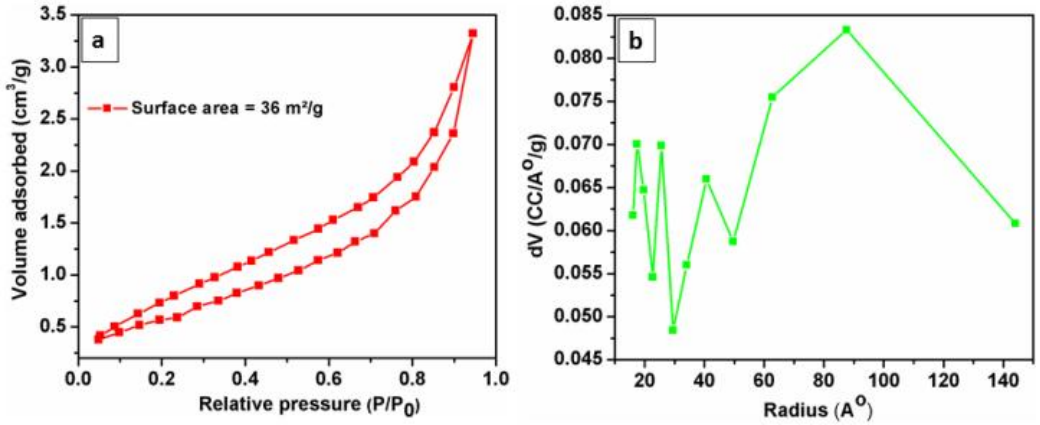

Figure 4.8. The active surface area of $CuFeS_2$ (a) Nitrogen adsorption/desorption isotherm, (b) BJH average pore size distribution plot of chalcopyrite.

The photophysical properties of the material were determined from the UV-Visible absorption spectrum. As is clear from Figure 4.9a, the chalcopyrite shows absorption mostly in the range of 300 nm to 800 nm, and the maximum absorption onset is at 480 nm. As discussed above the $CuFeS_2$ band gap mostly varies in the range from (0.5–0.6 eV). The energy bandgap (E_g) can be determined by extrapolating the linear region of the plot $(\alpha h\nu)^2$ vs. $h\nu$ to zero absorption as shown in the equation – 2 [41-43].

$$\alpha h\nu = A(h\nu - Eg)^2 \qquad (2)$$

Where α is the optical adsorption coefficient, h is the Planck constant; ν is the frequency of light; E_g is the band gap energy. The bandgap corresponding to the absorption onset calculated for sf-$CuFeS_2$ by the Tauc plot given in equation-2 was found to be 0.81 eV (Figure 4.9b).

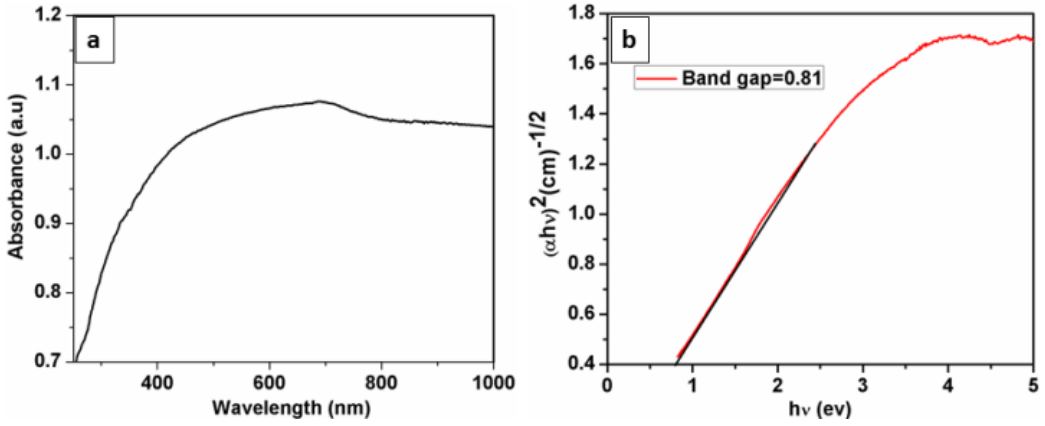

Figure 4.9. UV-Visible Diffuse Reflectance Spectra of $CuFeS_2$ (a). Absorption spectrum (b). Band gap.

Since the band gap is of high value as depicted for chalcopyrites, the possible reason maybe the quantum confinement [68]. This result showed that the removal of surfactant is not affecting the bandgap sf-$CuFeS_2$ nanoparticles significantly compared to $CuFeS_2$ nanoparticles reported earlier.

4.3.5. Catalytic reduction of 4-NP

The potential of catalytic application of sf-$CuFeS_2$ was confirmed by the reduction of toxic 4- nitrophenol (4-NP) using $NaBH_4$. The schematic representation of 4- nitrophenol (4-NP) reduction is shown in Scheme 4.2.

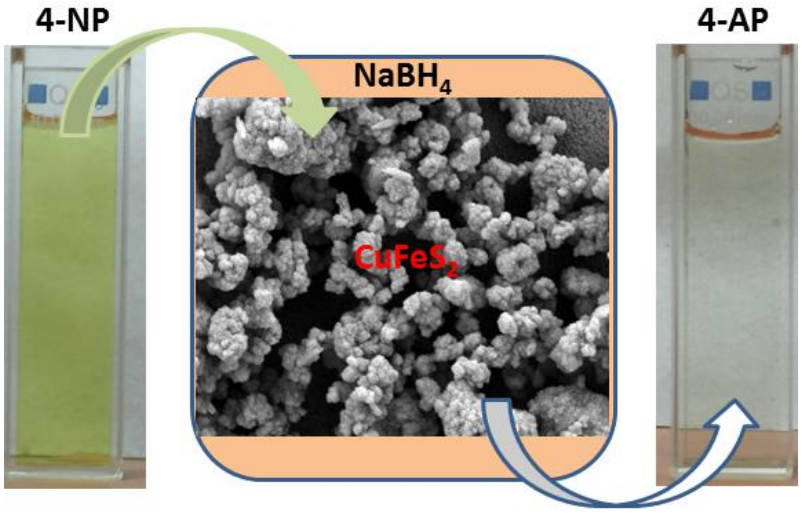

Scheme 4.2. The reduction of 4-NP on the surface of $CuFeS_2$ catalyst.

The water treatment contaminated with 4-NP by this catalytic reduction way is the realistic approach to deal with it. The reduction reaction is confirmed by the changes in the absorption spectrum of 4- NP to 4-AP. The UV-Vis spectrum of 4-NP has strong absorption in the 317 nm range with light yellow. By the addition of $NaBH_4$, the light yellow color changed to bright yellow with the concomitant shift in absorption peak to 400 nm region (Figure 4.10a). This change in color is due to the transformation of 4-nitrophenol to its corresponding phenoxide ion- 4-nitrophenolate ion by the subsequent addition of $NaBH_4$. When the solution with $NaBH_4$ was kept for a long time, it was observed that on checking UV there was no further decrease in intensity of peak obtained at 400 nm (Figure 4.10a) for phenolate ion, which indicates that without the addition of a

catalyst (sf-$CuFeS_2$) no further reaction is possible. By the addition of a proper amount of sf-$CuFeS_2$ to the solution the intensity of peak at 400 nm was found to decrease swiftly, whereas another peak at 318 nm region was found to increase in intensity with time progresses (Figure 4.10b) [69]. The new peak at 318 nm region gives an indication of the reduction of 4-NP, the new peak corresponds to amine thereby suggesting the formation of 4-aminophenol (4-AP). On the other hand, the complete change of color from yellow to colorless also indicates the formation of 4-AP by the reduction of 4-NP.

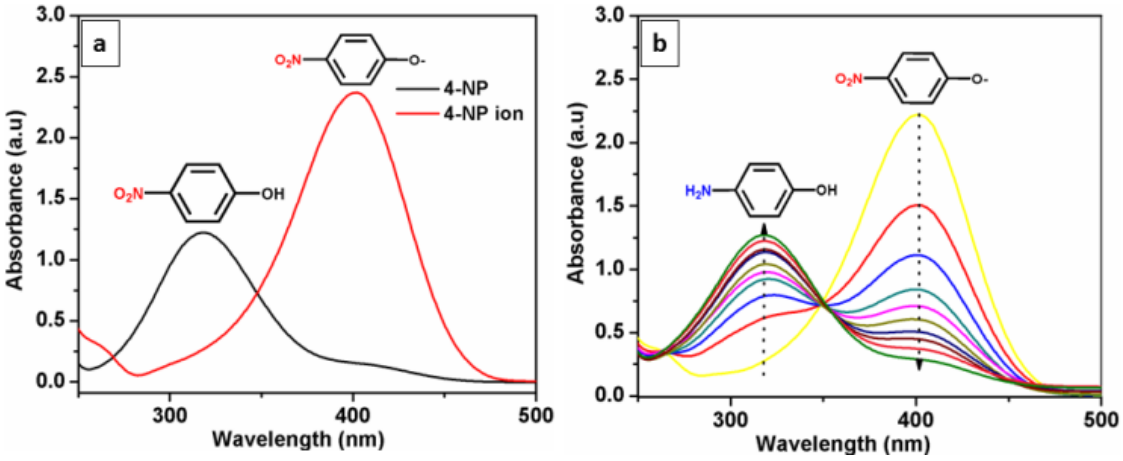

Figure 4.10. Representing the effective role of catalyst for 4-NP reduction to 4-AP with $NaBH_4$. (a) UV–Vis spectra of 4-NP before and after adding $NaBH_4$ solution. (b) The continuous reduction of 4-NP to 4-AP in presence of $CuFeS_2$ catalyst.

For studying the reaction kinetics of the reduction reaction, the change in concentration is determined from C_t/C_0 (Figure 4.11a), which in turn are measured from (A_t/A_0) in terms of the change in relative intensity in absorption spectrum at 400 nm. Here C_t and C_0 is the 4-NP concentration at time t and the initial concentration.

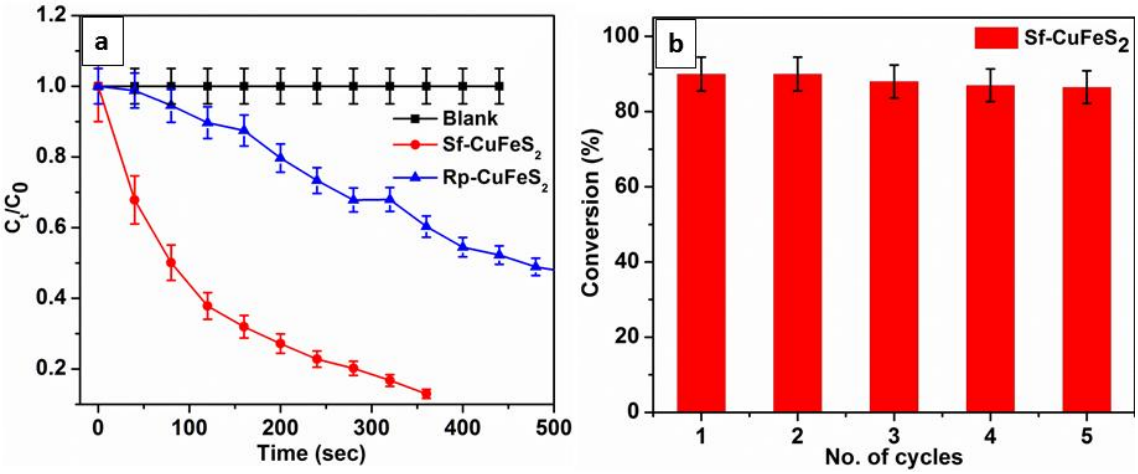

Figure 4.11. The Plots showing the kinetics and stability of the synthesized **sf-$CuFeS_2$** for the reduction of **4-NP** with $NaBH_4$ and its comparison with Rp-$CuFeS_2$. C_t/C_0 (a) and (b) Reusability of catalyst.

The linear correlation between $\ln(C_t/C_0)$ and the reaction time shows that it is first order kinetics as given by the equation-3 [70].

$$\ln(C_t/C_0) = -kt \qquad (3)$$

Here k indicates first order rate constant (s^{-1}) and t is the reaction time. The calculated value of k (Figure 4.12b) is found to be 5.21 $x10^{-3}$ s^{-1} and the total time taken for the completion of reduction reaction is 6 minutes. Since this type of catalysis by $CuFeS_2$ is the first time reported by our group in this manuscript, so a comparison of the catalytic activity of sf-$CuFeS_2$ with the other materials reported literature is given in Table 4.1. The data in the table clearly shows the superior catalytic activity of sf-$CuFeS_2$ in the reduction of 4-NP to 4-AP. For explaining the role of catalyst, a controlled reaction (Figure 4.12a) was performed in the presence of an excess of $NaBH_4$, where there was no influence on the reaction by $NaBH_4$ besides serving as an electron donor.

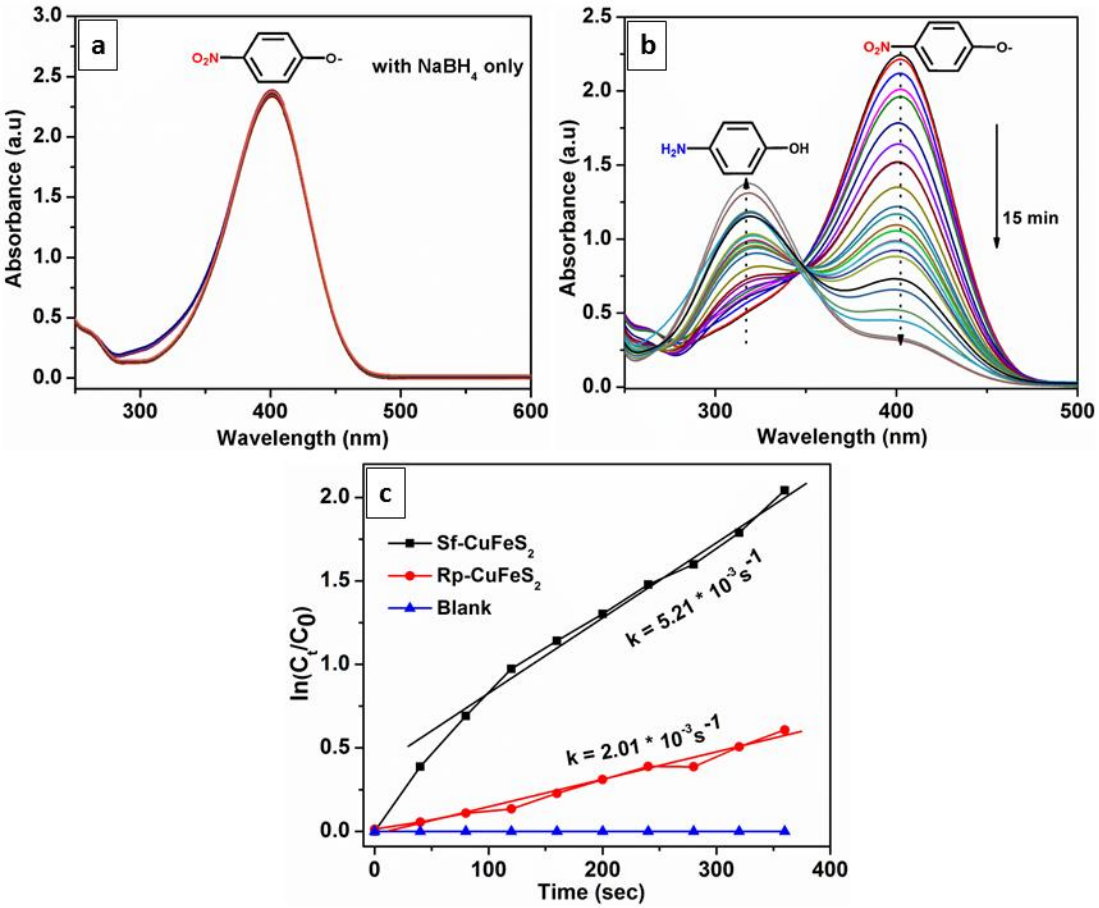

Figure 4.12. The Plots showing the absorption spectra and kinetics of 4-NP reduction. (a) Controlled reaction with $NaBH_4$ only (b) 4-NP reduction by Rp-$CuFeS_2$ in presence of $NaBH_4$ and (c) $\ln(C_t/C_0)$ Vs time, showing rate constant with Sf-$CuFeS_2$ and Rp-$CuFeS_2$.

The attractiveness of the HMDS-assisted synthetic approach is that the reaction yields materials without any surfactant molecules post synthesis. Since the surface of the catalyst is free from any capping, sf-$CuFeS_2$ showed better catalytic activity compared to the same materials prepared using a method reported in literature. For comparison purpose, we have prepared $CuFeS_2$ (named as Rp-$CuFeS_2$) by a known method and tested its catalytic activity in the reduction of 4-NP (Figure 4.11a and Figure 4.12b) [71]. The calculated value of k (Figure 4.12c) is found to be 2.01 x 10^{-3} s^{-1}, which is much lower compared with k observed for sf-$CuFeS_2$. This result highlights the advantages of both the preparation of $CuFeS_2$ without surfactant as well as the supremacy of HMDS-assisted synthesis.

The mechanism of reduction of 4-NP in the presence of $CuFeS_2$ using $NaBH_4$ can be explained as follows. When the catalyst is added to the reaction medium, both $NaBH_4$ and 4-NP adsorb on the surface of the catalyst. The catalyst initiates the reduction process by the electron accepted from BH_4^- to 4-NP. The adsorbed borohydride ion transfer surface hydrogen to the catalyst surface. Once the hydride gets adsorbed on the catalyst surface, it transfers its electron to catalyst-$CuFeS_2$. In this electron transfer process, a hydrogen atom is generated, which attacks the nitro group of the 4-NP molecule adsorbed on the catalyst surface. Through this electron transfer process from catalyst to 4-NP, reduction of 4-NP to 4-AP takes place. The mechanistic pathway proposed here for the catalytic reduction of 4-NP is similar to previously stated mechanisms including Langmuir–Hinshelwood mechanisms [72, 73].

Table 4.1. Comparison list of 4-NP reduction with catalysts reported in literatures.

Catalyst	Amount of catalyst used	Time of completion (min)	References
Ag/Fe_3O_4	0.20 g/l	40	[48]
Au/AC	0.20 g/l	30	[74]
Au	0.15 g/l	30	[75]
Ag/PAN	10 mg	70	[76]
S-Ag	6 mg/5 ml	15	[77]
$g\text{-}C_3N_4/CuS$	10 mg	50	[78]
Cu catalyst	12.5 mg	50	[79]
$CuFe_2O_4$–G	20 mg	9	[80]
$Ag@CeO_2$	0.25 mg	2.1	[81]
$CuFeS_2$	8 mg	6	This work

The stability of the catalyst is the paramount factor for its application on a large scale. Therefore, to determine stability, the reusability of the catalyst was checked by repeating the catalytic reduction of 4-NP using the recuperated catalyst. While performing the reusability test, the catalyst was separated by centrifugation (3000 rpm)

and repeatedly washed with water and acetone and dried in a vacuum. Attractively, the chalcopyrite presented excellent stability with no appreciable reduction in activity until the 5th cycle (Figure 4.11b). It's only after 5th catalytic cycle a slight reduction in activity is observed. The structural analysis and morphological observations of the used catalyst revealed after catalysis are shown in Figure 4.13. So the good stability, working of catalyst for larger number of cycles is the important advantages of using $CuFeS_2$ as a catalyst for 4-NP reduction [82].

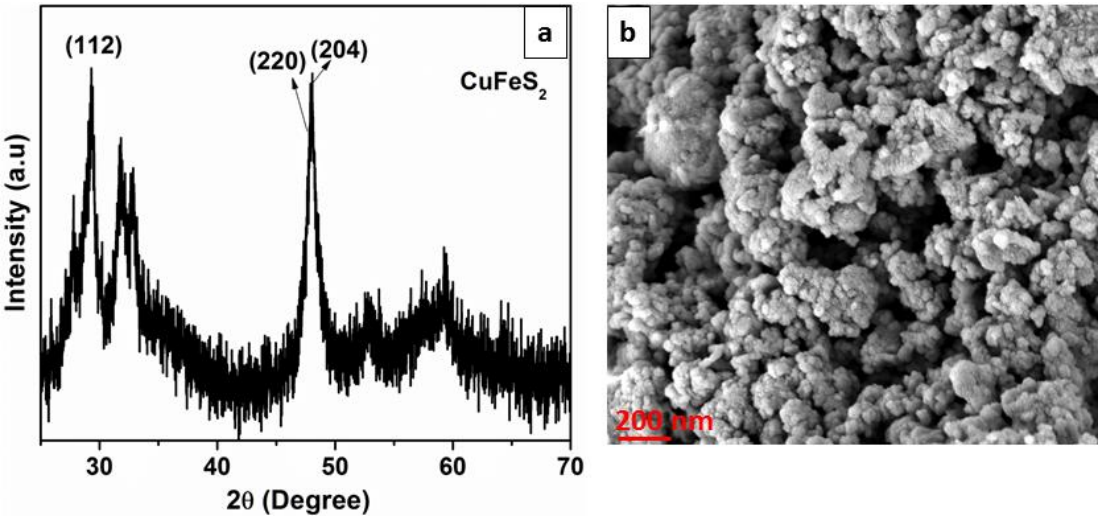

Figure 4.13. The effects on catalyst structure after catalysis. (a) PXRD after 5 cycles of catalysis and (b) SEM images after 5 cycles.

The effect of the amount of catalyst on the conversion efficiency was performed. The catalyst amounts were increased from 4 to 8 mg by keeping other parameters constant. As shown in Figure 4.14 with the increase in the catalyst dosage, the rate of conversion efficiency also increased. The efficiency was found to increase from 58% to 89%. The increase in the efficiency with catalyst dosage is possibly because of the increase in the number of active sites.

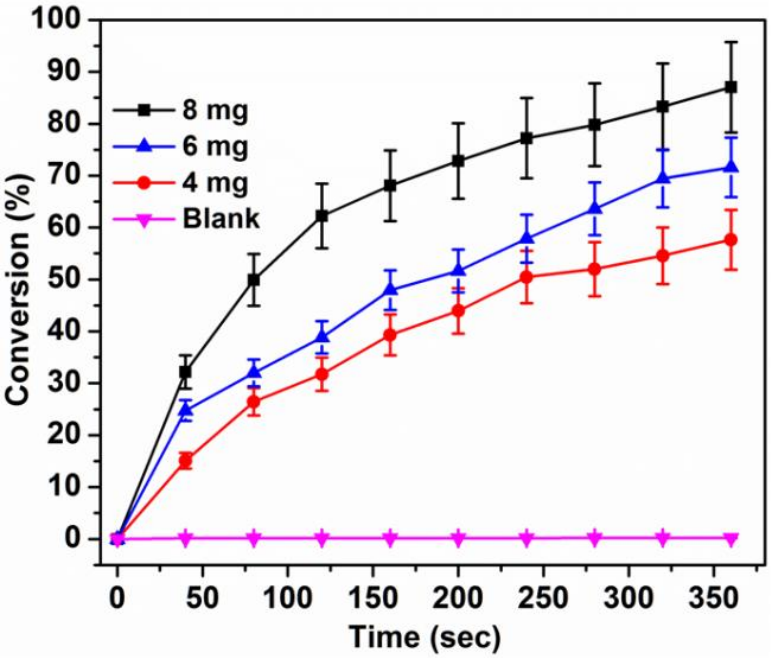

Figure 4.14. Effect of the catalyst–$CuFeS_2$ dosage on the conversion efficiency of 4-NP.

Besides this, the effect of initial concentrations of 4-NP on the conversion efficiency of the catalytic process was performed keeping the amount of catalyst constant at 8 mg/100 ml as well as 0.1 M of $NaBH_4$. As shown in Figure 4.15, with the increase in

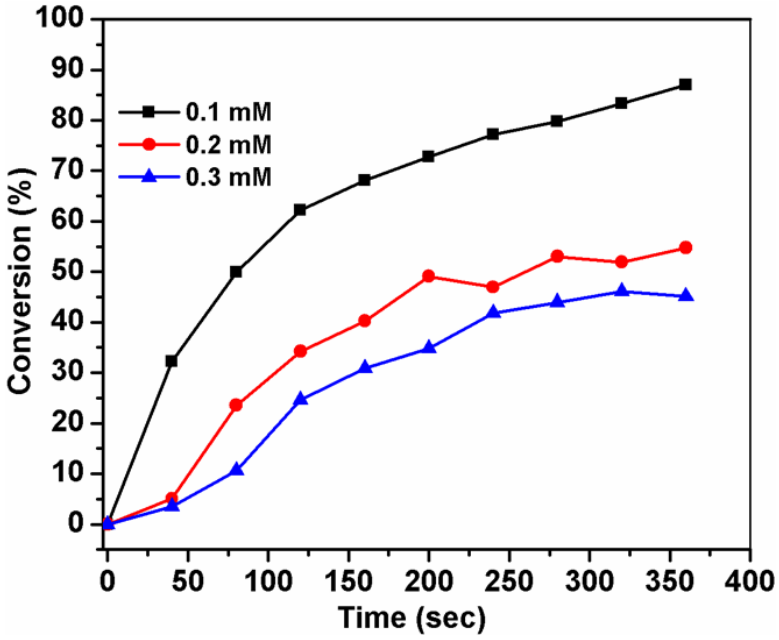

Figure 4.15. The effects of the initial concentration of the 4-NP on the conversion efficiency keeping the other parameters constant.

substrate concentration from 0.1 mM to 0.3 mM, the conversion efficiency decreased from 89% to 46%, showing that initial concentration of the substrate has great influence on the conversion efficiency of the catalyst. The figure shows that conversion efficiency directly depends on both the amount of catalyst and pollutant concentration used. The decrease in the efficiency might be due to decrease in the number of active sites on the catalyst as the concentration of 4-NP is increased. Because with the increase in substrate concentration due to easy access more of the active sites on catalyst are occupied thereby leaving lesser number of active sites for the new entrant on the catalyst.

4.4. Summary

In summary, chalcopyrite with a high surface area was synthesized by an HMDS-assisted wet-chemical method. After a successful synthesis, the materials were subjected to various analytical characterizations. The sf-$CuFeS_2$ is of a highly crystalline nature with no other phase impurities, as confirmed by PXRD. Both SEM and TEM determined and confirmed the particle morphology of nanostructures. The study of magnetic properties of sf-CuFeS2 revealed its paramagnetic nature. Measurement of dielectric properties showed a reduction in the values initially at low frequencies, which then remains unchanged at higher frequencies. The chalcopyrite exhibited superior catalytic activity on the reduction of 4-NP most likely because of clean surfaces on the catalyst and high surface area. This work corroborates new ways for the designing of materials with multiple roles like in catalysis and energy storing devices.

4.5. References

[1] Berends, A.C.; Mangnus, M. J. J.; Xia, C.; Rabouw, F. T.; Donega, C. M. Optoelectronic Properties of Ternary I−III−VI2 Semi-conductor Nanocrystals: Bright Prospects with Elusive Origins. *J. Phys. Chem. Lett*. **2019**, *10*, 1600-1616.

[2] Zhang, Y.; Yang, Y.; Hou, Z.; Jiang, X.; Zhang, L.; Yang, Y.; Wang, Y. The Effect of Reaction Temperature and Time on $CuInSe_2$ Quantum Dots by Solvothermal Method. *AIP Adv*. **2020**, *10*, 035313.

[3] Matthews, P. D.; McNaughter, P. D.; Lewis, D. J.; O'Brien, P. Shining a Light on Transition Metal Chalcogenides for Sustainable Photovoltaics. *Chem. Sci*. **2017**, *8*, 4177-4187.

[4] Marron, D. F.; Marti, A.; Luque, A. Thin-Film Intermediate Band Photovoltaics: Advanced Concepts for Chalcopyrite Solar Cells. *Phys. Status Solidi A* **2009**, *206*, 1021-1025.

[5] Tu, X.; Li, M.; Su, Y.; Yin, G.; Lu, J.; He, D. Self-Templated Growth of $CuInS_2$ Nanosheet Arrays for Photoelectrochemical Water Splitting. *J. Alloy. Comp*. **2019**, *809*, 151794.

[6] Kolny-Olesiak, J.; Weller, H. Synthesis and Application of Colloidal $CuInS_2$ Semiconductor Nanocrystals. *ACS Appl. Mater. Interfaces* **2013**, *5*, 12221−12237.

[7] Yarema, O.; Yarema, M.; Wood, V. Tuning the Composition of Multicomponent Semiconductor Nanocrystals: The Case of I−III−VI Materials. *Chem. Mater*. **2018**, *30*, 1446-1461.

[8] van der Stam, W.; Berends, A. C.; de Mello Donega, C. Prospects of Colloidal Copper Chalcogenide Nanocrystals. *ChemPhysChem* **2016**, *17*, 559−581.

[9] Aldakov, D.; Lefrancois, A.; Reiss, P. Ternary and Quaternary Metal Chalcogenide Nanocrystals: Synthesis, Properties and Applications. *J. Mater. Chem. C* **2013**, *1*, 3756-3776.

[10] Gabka, G.; Bujak, P.; Zukrowski, J.; Zabost, D.; Kotwica, K.; Malinowska, K.; Ostrowski, A.; Wielgus, I.; Lisowski, W.; Sobczak, J. W.; Przybylski, M.; Pron, A. Non-Injection Synthesis of Monodisperse Cu-Fe-S Nanocrystals and Their Size Dependent Properties. *Phys. Chem. Chem. Phys*. **2016**, *18*, 15091-15101.

[11] Nasluzov, V.; Shor, A.; Romanchenko, A.; Tomashevich, Y.; Mikhlin, Y. DFT + U and Low-Temperature XPS Studies of Fe-Depleted Chalcopyrite ($CuFeS_2$) Surfaces: A Focus on Polysulfide Species. *J. Phys. Chem. C*. **2019**, *123*, 21031-21041.

[12] Zhang, Z.; Xu, B.; Zhang, L.; Ren, S. Hybrid Chalcopyrite−Polymer Magnetoconducting Materials. *ACS Appl. Mater. Interfaces* **2016**, *8*, 11215-11220.

[13] Conejeros, S.; Alemany, P.; Llunell, M.; Moreira, I. P. R.; Sanchez, V.; Llanos, J. Electronic Structure and Magnetic Properties of $CuFeS_2$. *Inorg. Chem*. **2015**, *54*, 4840-4849.

[14] Zhang, P.; Zhang, Y. X.; Lai, H.; Deng, J.; Feng, J.; Ge, Z. H. Enhanced Thermoelectric Properties of Natural Chalcopyrite by Vacuum Annealing. *Mater. Lett.* **2019**, *253*, 430-433.

[15] Sherbini, M. A. E.; Yousef, Y. L. The Effect of Cooling and of Magnetic Fields on Crystal Rectification. *Proc. Phys. Soc*. **1939**, *51*, 449-455.

[16] Wang, M. X.; Wang, L.S.; Yue, G.H.; Wang, X.; Yan, P.X.; Peng, D.L. Single Crystal of $CuFeS_2$ Nanowires Synthesized Through Solventothermal Process. *Mater. Chem. Phys*. **2009**, *115*, 147-150.

[17] Disale, S. D.; Garje, S. S. A Convenient Synthesis of Nano-crystalline Chalcopyrite, $CuFeS_2$ using Single-Source Precursors. *Appl. Organometal. Chem*. **2009**, *23*, 492-497.

[18] Boekema, C.; Krupski, A. M.; Varasteh, M.; Parvin, K.; Til, F. V.; Van Der Woude, F.; Sawatzky, G. A. Cu and Fe Valence States in $CuFeS_2$. *J. Magn. Magn. Mater*. **2004**, *272*, 559-561.

[19] Sato, K.; Harada, Y.; Taguchi, M.; Shin, S.; Fujimori, A. Characterization of Fe 3d States in $CuFeS_2$ by Resonant X-ray Emission Spectroscopy. *Phys. Status Solidi A* **2009**, *206*, 1096-1100.

[20] Engin, T. E.; Powell, A. V.; Hull. S. A High Temperature Diffraction-Resistance Study of Chalcopyrite, $CuFeS_2$. *J. Solid State Chem*. **2011**, *184*, 2272-2277.

[21] Woolley, J. C.; Lamarche, A. M.; Lamarche, G.; Quintero, M.; Swainson, I. P.; Holden, T. M. Low Temperature Magnetic Behaviour of $CuFeS_2$ from Neutron Diffraction Data. *J. Magnetism and Magnetic Materials* **1996**, *162*, 347-354.

[22] Knight, K. S.; Marshall, W. G.; Zochowski, S. W. The Low-Temperature and High-Pressure Thermoelastic and Structural Properties of Chalcopyrite, $CuFeS_2$. *Can. Mineral.* **2011**, *49*, 1015-1034.

[23] Silvester, E. J.; Healy, T. W.; Grieser, F.; Sexton, B. A. Hydrothermal Preparation and Characterization of Optically Transparent Colloidal Chalcopyrite ($CuFeS_2$). *Langmuir* **1991**, *7*, 19-22.

[24] Oguchi, T.; Sato, K.; Teranishi, T. Optical Reflectivity Spec-trum of a $CuFeS_2$ Single Crystal. *J. Phys. Soc. Jpn*. **1980**, *48*, 123-128.

[25] Wang, Y.-H. A.; Bao, N.; Gupta, A. Shape-Controlled Synthesis of Semiconducting $CuFeS_2$ Nanocrystals. *Solid State Sci*. **2010**, *12*, 387−390.

[26] Liang, D.; Ma, R.; Jiao, S.; Pang, G.; Feng, S. A Facile Synthetic Approach for Copper Iron Sulfide Nanocrystals with Enhanced Thermoelectric Performance. *Nanoscale* **2012**, *4*, 6265-6268.

[27] Barkat, L.; Hamdadou, N.; Morsli, M.; Khelil, A.; Bernede. J. C.; Growth and Characterization of $CuFeS_2$ Thin Films. *J. Cryst. Growth* **2006**, *297*, 426-431.

[28] Wang, C.; Xue, S.; Hu, J.; Tang, K. Raman, Far Infrared, and Mossbauer Spectroscopy of $CuFeS_2$ Nanocrystallites. *Jpn. J. Appl. Phys*. **2009**, *48*, 023003.

[29] Wu, Y.; Zhou, B.; Yang, C.; Liao, S.; Zhang, W. H.; Li, C.;$CuFeS_2$ Colloidal Nanocrystals as an Efficient Electrocatalyst for Dye Sensitized Solar Cells. *Chem. Commun*. **2016**, *52*, 11488-11491.

[30] Dalui, A.; Pradhan, B.; Thupakula, U.; Khan, A. H.; Kumar, G. S.; Ghosh, T.; Satpati, B.; Acharya, S. Insight into the Mechanism Revealing the Peroxidase Mimetic Catalytic Activity of Quaternary CuZnFeS Nanocrystals: Colorimetric Biosensing of Hydrogen Peroxide and Glucose. *Nanoscale* **2015**, *7*, 9062-9074.

[31] Gan, D.; Liu, M.; Huang, H.; Chen, J.; Dou, J.; Wen, Y.; Huang, Q.; Yang, Z.; Zhang, X.; Wei, Y. Facile Preparation of Functionalized Carbon Nanotubes with Tannins

Through Mussel-Inspired Chemistry and their Application in Removal of Methylene Blue. *J. Mol. Liq*. **2018**, *271*, 246-253.

[32] Huang, Q.; Liu, M.; Mao, L.; Xu, D.; Zeng, G.; Huang, H.; Jiang, R.; Deng, F.; Zhang, X.; Wei, Y. Surface Functionalized SiO_2 Nanoparticles with Cationic Polymers Via the Combination of Mussel Inspired Chemistry and Surface Initiated Atom Transfer Radical Polymerization: Characterization and Enhanced Removal of Organic Dye. *J. Colloid Interface Sci*. **2017**, *499*, 170-179.

[33] Huang, Q.; Liu, M.; Chen, J.; Wan, Q.; Tian, J.; Huang, L.; Jiang, R.; Wen, Y.; Zhang, X.; Wei. Y. Facile Preparation of MoS_2 Based Polymer Composites Via mussel Inspired Chemistry and their High Efficiency for Removal of Organic Dyes. *Appl. Surf. Sci*. **2017**, *419*, 35-44.

[34] Zeng, G.; Huang, L.; Huang, Q.; Liu, M.; Xu, D.; Huang, H.; Yang, Z.; Deng, F.; Zhang, X.; Wei. Y. Rapid Synthesis of MoS_2-PDA-Ag Nanocomposites as Heterogeneous Catalysts and Antimicrobial Agents via Microwave Irradiation. *Appl. Surf. Sci*. **2018**, *459*, 588-595.

[35] Dou, J.; Gan, D.; Huang, Q.; Liu, M.; Chen, J.; Deng, F.; Zhu, X.; Wen, Y.; Zhang, X.; Wei. Y. Functionalization of Carbon Nano-tubes With Chitosan Based on MALI Multicomponent Reaction for Cu^{2+} Removal. *Int. J. Biol. Macromol*. **2019**, *136*, 476-485.

[36] Gan, D.; Huang, Q.; Dou, J.; Huang, H.; Chen, J.; Liu, M.; Wen, Y.; Yang, Z.; Zhang, X.; Wei, Y. Bioinspired Functionalization of MXenes (Ti_3C_2TX) with Amino Acids for Efficient Removal of Heavy Metal Ions. *Appl. Surf. Sci*. **2020**, *504*, 144603.

[37] Huang, Q.; Liu, M.; Zhao, J.; Chen, J.; Zeng, G.; Huang, H.; Tian, J.; Wen, Y.; Zhang, X.; Wei, Y. Facile Preparation of Polyethylenimine-Tannins Coated SiO_2 Hybrid Materials for Cu^{2+} Removal. *Appl. Surf. Sci*. **2018**, *427*, 535-544.

[38] Pandit, M. A.; Billakanti, S.; Muralidharan, K. A Simplistic Approach for the Synthesis of CuS-CdS Heterostructure: A Novel Photocatalyst for Oxidative Dye Degradation. *J. Environ. Chem. Eng*. **2020**, *8*, 103542.

[39] Srinivas, B.; Pandit, M. A.; Muralidharan, K. Importance of Clean Surfaces on the Catalyst: SnS_2 Nanorings for Environmental Remediation. *ACS Omega* **2019**, *4*, 14970-14980.

[40] Lei, Y.; Cui, Y.; Huang, Q.; Dou, J.; Gan, D.; Deng, F.; Liu, M.; Li, X.; Zhang, X.; Wei, Y. Facile Preparation of Sulfonic Groups Functionalized Mxenes for Efficient Removal of Methylene Blue. *Ceram. Int*. **2019**, *45*, 17653-17661.

[41] Manigandan, R.; Dhanasekaran, T.; Padmanaban, A.; Giribabu, K.; Suresh, R.; Narayanan,V. Bifunctional Hexagonal Ni/NiO Nanostructures: Influence of the Core–Shell Phase on Magnetism, Electrochemical Sensing of Serotonin, and Catalytic Reduction of 4-Nitrophenol. *Nanoscale Adv*. **2019**, *1*, 1531-1540.

[42] Zhang, X.; Huang, Q.; Liu, M.; Tian, J.; Zeng, G.; Li, Z.; Wang, K.; Zhang, Q.; Wan, Q.; Deng, F.; Wei, Y. Preparation of Amine Functionalized Carbon Nanotubes via a Bioinspired Strategy and their Application in Cu^{2+} Removal. *Appl. Surf. Sci*. **2015**, *343*, 19-27.

[43] Huang, Q.; Zhao, J.; Liu, M.; Li, Y.; Ruan, J.; Li, Q.; Tian, J.; Zhub, X.; Zhang, X.; Wei, Y. Synthesis of Polyacrylamide Immobilized Molybdenum DiSulfide (MoS_2@PDA@PAM) Composites via Mussel-Inspired Chemistry and Surface-Initiated Atom Transfer Radical Polymerization for Removal of Copper (II) Ions. *J. Taiwan Inst. Chem. Eng*. **2018**, *86*, 174-184.

[44] Liu, Y.; Huang, H.; Gan, D.; Guo, L.; Liu, M.; Chen, J.; Deng, F.; Zhou, N.; Zhang, X.; Wei, Y. A Facile Strategy for Preparation of Magnetic Graphene Oxide Composites and their Potential for Environmental Adsorption. *Ceram. Int*. **2018**, *44*, 18571-18577.

[45] Zeng, G.; Liu, X.; Liu, M.; Huang, Q.; Xu, D.; Wan, Q.; Huang, H.; Deng, F.; Zhang, X.; Wei, Y. Facile Preparation of Carbon Nanotubes Based Carboxymethyl Chitosan Nanocomposites Through Combination of Mussel Inspired Chemistry and Michael Addition Reaction: Characterization and Improved Cu^{2+} Removal Capability. *J. Taiwan Inst. Chem. Eng*. **2016**, *68*, 446-454.

[46] Huang, Q.; Zhao, J.; Liu, M.; Chen, J.; Zhu, X.; Wu, T.; Tian, J.; Wen, Y.; Zhang, X.; Wei. Y. Preparation of Polyethylene Polyamine@Tannic Acid Encapsulated MgAl-Layered Double Hydroxide for the Efficient Removal of Copper (II) Ions from Aqueous solution. *J. Taiwan Inst. Chem. Eng*. **2018**, *82*, 92-101.

[47] Chang, Y.C.; Chen, D.H. Catalytic Reduction of 4-Nitrophenol by Magnetically Recoverable Au Nanocatalyst. *J. Hazard. Mater*. **2009**, *165*, 664-669.

[48] Chiou, J. R.; Lai, B. H.; Hsu, K. C.; Chen, D. H. One-Pot Green Synthesis of Silver/Iron Oxide Composite Nanoparticles for 4-Nitrophenol Reduction. *J. Hazard. Mater*. **2013**, *248*, 394-400.

[49] Yao, Y. X.; Li, H. B.; Liu, J.Y.; Tan, X. L.; Yu, J. G.; Peng, Z. G. Removal and Adsorption of p-Nitrophenol from Aqueous Solutions Using Carbon Nanotubes and Their Composites. *J. Nanomater*. **2014**, *1*, 1-9.

[50] Hamidouche, S.; Bouras, O.; Zermane, F.; Cheknane, B.; Houari, M.; Debord, J.; Harel, M.; Bollinger, J. C.; Baudu, M. Simultaneous Sorption of 4-Nitrophenol and 2-Nitrophenol on a Hybrid geocomposite Based on Surfactant Modified Pillared-Clay and Activated Carbon. *Chem. Eng. J*. **2015**, *279*, 964-972.

[51] Tumbas, I. I.; Hobby, R.; Kuchle, B.; Panglisch, S.; Gimbel, R. p-Nitrophenol Removal by Combination of Powdered Activated Carbon Adsorption and Ultrafiltration-Comparison of Different Operational Modes. *Water research* **2008**, *42*, 4117-4124.

[52] Mehrizad, A.; Zare, K.; Aghaie, H.; Dastmalchi, S. Removal of 4-Chloro-2-Nitrophenol Occurring in Drug and Pesticide Waste by Adsorption onto Nano-Titanium Dioxide. *Int. J. Environ. Sci. Technol*. **2012**, *9*, 355-360.

[53] Das, S. K.; Khan, Md. M. R.; Guha, A. K.; Naskar, N. Bio-Inspired Fabrication of Silver Nanoparticles on Nanostructured Silica: Characterization and Application as a Highly Efficient Hydrogenation Catalyst. *Green Chem.* **2013**, *15*, 2548-2557.

[54] Holden, M. S.; Nick, K. E.; Hall, M.; Milligan, J. R.; Chen, Q.; Perry, C. C. Synthesis and Catalytic Activity of Pluronic Stabilized Silver–Gold Bimetallic Nanoparticles. *RSC Adv*. **2014**, *4*, 52279-52288.

[55] Magdy, Y. M.; Altaher, H.; ElQada, E. Removal of Three Ni-trophenols from Aqueous Solutions by Adsorption onto Char Ash: Equilibrium and Kinetic Modeling. *Appl. Water Sci*. **2018**, *8*, 26.

[56] Veisi, H.; Kazemi, S.; Mohammadi, P.; Safarimehr, P.; Hem-mati, S. Catalytic reduction of 4-nitrophenol Over Ag nanoparticles Immobilized on Stachys Lavandulifolia Extract-Modified Multi Walled Carbon Nanotubes. *Polyhedron* **2019**, *157*, 232-240.

[57] Gabka, G.; Bujak, P.; Ostrowski, A.; Tomaszewski, W.; Lisowski, W.; Sobczak, J. W.; Pron, A. Cu−Fe−S Nanocrystals Exhibiting Tunable Localized Surface Plasmon Resonance in the Visible to NIR Spectral Ranges. *Inorg. Chem*. **2016**, *55*, 6660-6669.

[58] Yu, J.; Ran, J. Facile Preparation and Enhanced Photocatalytic H_2-Production Activity of $Cu(OH)_2$ Cluster Modified TiO_2. *Energy Environ. Sci.* **2011**, *4*, 1364-1371.

[59] Naik, S. R.; Salker, A. V. Change in the Magnetostructural Properties of Rare Earth Doped Cobalt Ferrites Relative to the Magnetic Anisotropy. *J. Mater. Chem*. **2012**, *22*, 2740-2750.

[60] Girma, W. M.; Tzing, S. H.; Tseng, P. J.; Huang, C. C.; Ling, Y. C.; Chang, J. Y. Synthesis of Cisplatin(IV) Prodrug-Tethered $CuFeS_2$ Nanoparticles in Tumor-Targeted Chemotherapy and Photothermal Therapy. *ACS Appl. Mater. Interfaces* **2018**, *10*, 4590-4602.

[61] Jeyagopal, R.; Chen, Y.; Ramadoss, M.; Marimuthu, K.; Wang, B.; Li, W.; Zhang, X. A Three-Dimensional Porous CoSnS@CNT Nanoarchitecture as a Highly Efficient Bifunctional Catalyst for Boosted OER Performance and Photocatalytic Degradation. *Nanoscale* **2020**, *12*, 3879–3887.

[62] Kobayashi, K.; Azuma, Y.; Kawashima, K.; Horigane, K.; Akaki, M.; Tokunaga, M.; Akimitsu, J. Magnetic Properties of Chalcopyrite $Cu_{1-x}FeS_2$ at Low Temperatures. *JPS Conf. Proc*. **2014**, *3*, 017020.

[63] Farooq, U.; Phul, R.; Alshehri, S. M.; Ahmed, J.; Ahmad, T. Electrocatalytic and Enhanced Photocatalytic Applications of Sodium Niobate Nanoparticles Developed by Citrate Precursor Route. *Scientific Reports* **2019**, *9*, 4488.

[64] Lesmes, D.P.; Morgan, F.D. Dielectric Spectroscopy of Sedi-mentary Rocks. *J. Geophys. Res*. **2001**, *106*, 13329-13346.

[65] Ahmad, T.; Lone, I. H. Citrate Precursor Synthesis and Multifunctional Properties of $YCrO_3$ Nanoparticles. *New J. Chem*. **2016**, *40*, 3216-3224.

[66] Prameena, B.; Anbalagan, G.; Gunasekaran, S.; Ramkumaar, G. R.; Gowtham, B. Structural, Optical, Electron Paramagnetic, Thermal and Dielectric Characterization of Chalcopyrite. *Spectro-chimica Acta Part A: Molecular and Biomolecular Spectroscopy* **2014**, *122*, 348-355.

[67] Thommes, M.; Kaneko, K.; Neimark, A. V.; Olivier, J. P.; Reinoso, F. R.; Rouquerol, J.; Sing, K. S. W. Physisorption of Gases, with Special Reference to the Evaluation of Surface Area and Pore Size Distribution (IUPAC Technical Report). *Pure Appl. Chem.* **2015**, *87*, 1051-1069.

[68] Tonpe, D.; Gattu, K.; More, G.; Upadhye, D.; Mahajan, S.; Sharma, R. Synthesis of $CuFeS_2$ Thin Films From Acidic Chemical Baths. *Am. Inst. Phys*. **2016**, *1728*, 020676.

[69] Yuan, M.; Yang, R.; Wei, S.; Hu, X.; Xu, D.; Yang, J.; Dong, Z. Ultra-Fine Pd Nanoparticles Confined in a Porous Organic Polymer: A Leaching-and-Aggregation-Resistant Catalyst for the Efficient Reduction of Nitroarenes by $NaBH_4$. *J. Colloid Interface Sci*. **2019**, *538*, 720-730.

[70] Dong, Z.; Le, X.; Li, X.; Zhang, W.; Dong, C.; Ma, J. Silver Nanoparticles Immobilized on Fibrous Nano-Silica as Highly Efficient and Recyclable Heterogeneous

Catalyst for Reduction of 4-Nitrophenol and 2-Nitroaniline. *Appl. Catal. B: Environ*. **2014**, *158*, 129-135.

[71] Hu, J.; Lu, Q.; Tang, K.; Qian, Y.; Zhou, G.; Liu, X. A Sol-vothermal Reaction Route for the Synthesis of $CuFeS_2$ Ultrafine Powder. *J. Mater. Res*. **1999**, *14*, 3870-3971.

[72] Baruah, B.; Gabriel, G. J.; Akbashev, M. J.; Booher, M. E. Facile Synthesis of Silver Nanoparticles Stabilized by Cationic Poly-norbornenes and Their Catalytic Activity in 4‑Nitrophenol Reduction. *Langmuir* **2013**, *29*, 4225-4234.

[73] Wunder, S.; Polzer, F.; Lu, Y.; Mei, Y.; Ballauff, M. Kinetic Analysis of Catalytic Reduction of 4-Nitrophenol by Metallic Nano-particles Immobilized in Spherical Polyelectrolyte Brushes. *J. Phys. Chem. C* **2010**, *114*, 8814-8820.

[74] Kumar, A.; Belwal, M.; Maurya, R. R.; Mohan, V.; Vishwanathan, V. Heterogeneous Catalytic Reduction of Anthropogenic Pollutant, 4-Nitrophenol by Au/AC Nanocatalysts. *Materials Science for Energy Technologies* **2019**, *2*, 526-531.

[75] Guo, P.; Tang, L.; Tang, J.; Zeng, G.; Huang, B.; Dong, H.; Zhang, Y.; Zhou, Y.; Deng, Y.; Ma, L.; Tan, S. Catalytic Reduction–Adsorption for Removal of p-Nitrophenol and its Conversion p-Aminophenol from Water by Gold Nanoparticles Supported on Oxidized Mesoporous Carbon. *J. Colloid Interface Sci*. **2016**, *469*, 78-85.

[76] Gao, S.; Zhang, Z.; Liu, K.; Dong, B. Direct Evidence of Plasmonic Enhancement on Catalytic Reduction of 4-Nitrophenol Over Silver Nanoparticles Supported on Flexible Fibrous Networks. *Appl. Catal. B: Environ*. **2016**, *188*, 245-252.

[77] Kalantari, K.; Afifi, A. B. M.; Bayat, S.; Shameli, K.; Yousefi, S.; Mokhtar, N.; Kalantari, A. Heterogeneous Catalysis in 4-Nitrophenol Degradation and Antioxidant Activities of Silver NanoParticles Embedded in Tapioca Starch. *Ar. J. Chem*. **2019**, *12*, 5246-5252.

[78] Ayodhya, D.; Veerabhadram, G. Influence of g-C_3N_4 and g-C_3N_4 Nano Sheets Supported CuS Coupled System with Effect of pH on the Catalytic Activity of 4-NP Reduction Using $NaBH_4$. *FlatChem* **2019**, *14*, 100088.

[79] Deka, P.; Deka, R. C.; Bharali, P. In Situ Generated Copper Nanoparticle Catalyzed Reduction of 4-Nitrophenol. *New J. Chem*. **2014**, *38*, 1789-1793.

[80] Zhang, H.; Gao, S.; Shang, N.; Wang, C.; Wang, Z. Copper Ferrite–Graphene Hybrid: A Highly Efficient Magnetic Catalyst for Chemoselective Reduction of Nitroarenes. *RSC Adv*. **2014**, *4*, 31328-31332.

[81] Shi, Y.; Zhang, X.; Zhu, Y.; Tan, H.; Chen, X.; Lu, Z-H. Core–Shell Structured Nanocomposites Ag@CeO_2 as Catalysts for Hydrogenation of 4-Nitrophenol and 2-Nitroaniline. *RSC Adv*. **2016**, *6*, 47966-47973.

[82] Lu, Z-H.; Li, J; Zhu, A; Yao, Q.; Huang, W.; Zhou, R.; Zhou, R.; Chen, X. Catalytic Hydrolysis of Ammonia Borane via Magnetically Recyclable Copper Iron Nanoparticles for Chemical Hydrogen Storage. *Int. J. Hydrogen Energy* **2013**, *38*, 5330-5337.

CHAPTER-5

Boosting the Bifunctional Catalytic Role of Cobalt Iron Chalcogenide-$Co_{0.8}Fe_{0.2}L_2$ (L = S and Se) as an Electrochemical OER Performer and a Photocatalyst for Cr(VI) Reduction

Abstract

The progress for the development of active, stable, and economic catalysts for the chemical transformation of noxious chemicals to benign is of primary importance. In this scenario, for the first time, we used the hexamethyldisilazane (HMDS)-assisted method constructively to synthesize a novel ternary cobalt and iron based metal chalcogenide $Co_{0.8}Fe_{0.2}L_2$ (L=S, Se) [$Co_{0.8}Fe_{0.2}S_2$ and $Co_{0.8}Fe_{0.2}Se_2$]. These materials behaved as a bifunctional catalyst for both electrochemical OER and photocatalysis for the reduction of Cr(VI). The materials showed good electrochemical water splitting properties for OER performance (345 and 350 mV @η_{10}, 52.4, and 84.5 mV/dec respectively for the Tafel values of $Co_{0.8}Fe_{0.2}Se_2$ and $Co_{0.8}Fe_{0.2}S_2$). Besides electrochemical water splitting, these materials were tested for the photocatalytic reduction of toxic Cr(VI) to Cr(III) on exposure to sunlight irradiations. As photocatalysts, $Co_{0.8}Fe_{0.2}S_2$ and $Co_{0.8}Fe_{0.2}Se_2$ could convert about 96% and 91% of Cr(IV) to Cr(III). While with their recyclability tests, both the catalysts presented balanced electrocatalysis activities for 1500 CV cycles and photocatalysis of 5 cycles. This observation is an important criterion governing their usage for large scale applications.

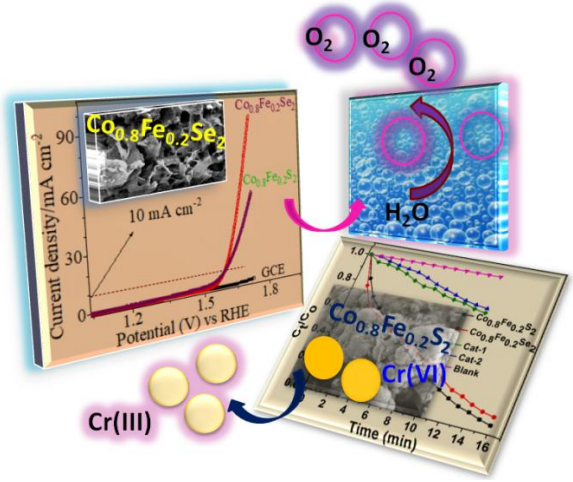

Manuscript submitted

5.1. Introduction

Global energy consumption is rising at an alarming rate with the unprecedented rise in population and progressive improvement in science and technology. Since the deposits of non-renewable resources of energy are finishing at an increasing rate, there is a need to switch over towards the alternative sources. The most useful way to mitigate the issue of energy sources is splitting water by either photo- or electro- catalytically. Therefore, over the years, scientists have geared up the research interests to a considerable extent involving water splitting using nanomaterials. The two most critical half-reactions involved in electrocatalysis of water include hydrogen evolution reaction (HER) and oxygen evolution reaction (OER). Among these two half-reactions, OER through electrocatalysis is considered the most promising way for green and cheap energy creation [1-4].

Mostly, noble metal-based catalysts like Pt, RuO_2, or IrO_2 perform well in OER catalysis, but the high cost and less abundant naturally are hindrances to their usage as electrocatalyst on large scale [5, 6]. Therefore, the focus is on transition metal [7, 8] based catalysts because of their easy access, less cost, less toxicity, and abundant availability with efficiency almost matching to those of Pt or other noble metal catalysts [9]. Various transition metal compounds like sulphides, oxides, and phosphides were tested for electrocatalytic OER performance and as bifunctional catalysts [10-15]. Besides these, materials such as alloys [16], phosphides [17], carbides [18], selenides [19], borates [20], nitrides [21], carbon-based materials [22], and hydroxides [23], were used as the OER catalysts effectively. Among these transition metal compounds, chalcogenides (mostly sulphides and selenides) have emerged as an elegant class of electrocatalysts for OER. Moreover, the ternary chalcogenides have shown superior properties like high electrical conductance value compared to monometallic owing to the low activation energy for electron transfer between cations [5].

The active transition elements like Ni, Co, Fe, Cu, and Mo and their combinations with sulfur are investigated continuously because of their excellent properties. Some combinations include Co-Ni-S [24-27], Cu-Co-S and Cu-Mo-S [28-30], Co-Fe-S [31-35], Co-Mo-S [36], and Zn-Co-S [37]. Apart from the stoichiometric combinations, different

features such as crystalline phase, morphology and particle size are influencing the electrocatalytic activity of transition metal sulphides [14, 15, 38-40]. Shen et al. reported a composite formation between cobalt iron sulfide and nitrogen-doped mesoporous graphitic carbon ($Co_{0.5}Fe_{0.5}S$@N-MC) using a simple soft template scheme. In this material, the nanostructures are covalently bonded on a mesoporous graphitic layer and played the catalytic role for water oxidation reactions [41].

Metal selenides, belonging to chalcogenides family, also received tremendous research interests owing to their outstanding physical and electrochemical properties [42-44]. The superior performance of selenides than sulphides is rationalized as they possess more metallic character than sulphide [45]. Many transition metal selenides of the type MSe_2 (here M = Fe, Co, Mo, Ni, Cu, and Mn) were used as an electrode in energy conversion or storage devices such as solar cells, battery, supercapacitor, fuel cells, sensors, and in water-splitting reactions (HER and OER) [46-51]. Xiao et al. succeeded in depositing lamellar structured nanosheets of $CoSe_2$ on Ti plate ($CoSe_2$NS@Ti) by an in-situ method and used it directly as a cathode for superior hydrogen evolution activity [52]. Zhao et al. reported the synthesis of ultrasmall $FeSe_2$ nanoparticle by a high-temperature solution-based method that acted as an excellent material for sodium-ion storage [53]. Sakthivel et al. claimed hydrothermal synthesis of $CoFeSe_2$/f-CNF and its use to detect caffeic acid electrochemically [54]. Yiqing et al. reported sulphidation and selenation of cobalt iron by the hydrothermal method as the precursors to produce the Prussian-blue-analog (PBA) nanocubes and used it as excellent electrodes for dye-sensitized solar cells [55].

The bright side of the rise in technology is that it made life comfortable. On the other side, the continuous elimination of toxic and harmful chemicals created environmental havoc. Many toxic and carcinogenic chemicals significantly affect both aquatic as well as terrestrial life. The water bodies contaminated with such carcinogenic and toxic chemicals including organic dyes (e.g., rhodamine (Rh B), methylene blue (MB) dyes, nitro compounds) [56-58] and toxic inorganic chemicals (e.g., Cr(VI)) [59] are unfit to drink or use for other purposes. So the challenging task is to develop such photocatalysts that are easily accessible, cheap, and have abundantly available precursors.

Thus the need is to develop highly efficient and stable catalysts that can perform multirole in OER or detoxification of toxic organic/inorganic chemicals.

Although many reports documented sulphides and selenides as catalysts, there are seldom reports on their role as bifunctional catalysts. In this chapter, we report a study on transition metal chalcogenides ($Co_{0.8}Fe_{0.2}S_2$ and $Co_{0.8}Fe_{0.2}Se_2$) as bifunctional catalysts. These materials were produced via hexamethyldisilazane (HMDS) – assisted synthesis and characterized using different analytical and spectroscopic techniques. We have determined their chemical composition, the oxidation state of elements, crystalline structure, morphology, surface area, and optical properties. The activity of nanomaterials as a photo or electrocatalyst is a crucial requirement to produce green and carbon-free energy sources. Therefore, we have established the unexplored bifunctional roles of $Co_{0.8}Fe_{0.2}S_2$ and $Co_{0.8}Fe_{0.2}Se_2$ as dual catalysts. Their catalytic activities for electrochemical water splitting (OER) and photocatalytic Cr(VI) reduction were assessed. The present work establishes a newer way to develop such kind of catalysts with multiple roles.

5.2. Experimental Section

5.2.1. Materials

Cobalt chloride ($CoCl_2$ anhydrous), ferric chloride ($FeCl_3$ anhydrous), thiourea [$H_2NC(S)NH_2$], selenium powder, hexamethyldisilazane [$(Me_3Si)_2NH$] (HMDS), $K_2Cr_2O_7$ were purchased from Sigma Aldrich. Distilled water used for photocatalysis. All the above reagents were of analytical grade and used without further purification.

5.2.2. Synthesis of $Co_{0.8}Fe_{0.2}S_2$ and $Co_{0.8}Fe_{0.2}Se_2$ chalcogenides

Likewise as discussed in previous chapters, for the synthesis of $Co_{0.8}Fe_{0.2}S_2$ nanoparticles, hexamethyldisilazane (HMDS)-assisted wet chemical method with slight modification was a promising method. In a typical reaction 1.54 mmol $CoCl_2$, 0.31 mmol $FeCl_3$ were added one by one to a two neck RB, then 6ml HMDS were injected by syringe under the continuous supply of nitrogen gas, by connecting the RB to Schlenk lines to maintain the inert conditions. The reaction mixture was stirred for 30 minutes to

allow dissolution of precursor salts in the medium at 40 °C, then after 30 minutes 3.08 mmol thiourea was added. The reaction was set to reflux at 160 °C for 3 hours with continuous stirring. After the completion of reaction the precipitates were separated by centrifugation (set) at 2500 rpm, washed by deionized water and ethanol each 3-4 times to get the desired product. The material collected was subjected to high vacuum for the complete removal of any residual solvents. The product was dried at 70 °C for overnight in a vacuum oven.

Similar procedure was applied for the synthesis of $Co_{0.8}Fe_{0.2}Se_2$. Se (3.08 mmol) powder was used instead of thiourea to produce ternary metal selenide.

5.2.3. Preparation of Electrocatalyst for OER

5.2.3.1 Fabrication of working electrodes and electrochemical measurements

OER were carried using the electrochemical CHI 660D, workstation at room temperature (298 K). A home-made set-up with three electrode system was used (working electrode as glassy carbon ($Co_{0.8}Fe_{0.2}S_2$ and $Co_{0.8}Fe_{0.2}Se_2$ modified and bare GCE), Pt ring as counter electrode, and silver electrode reference electrode in 1 M KOH. Electrocatalyst on GCE was loaded (~ 0.3 mg/cm^2) with Nafion binder via drop-cast method with the micropipette assistance and then dried at oven. All the electrochemical measurements were repeated again to ensure consistency and reproductive performance. Throughout this all electrochemical performance, potentials of Linear sweep voltammetry (LSV) and cyclic voltammogram (CV) were calibrated vs. reversible electrode (RHE as follows, $E_{RHE} = E_{obt} + E_{Ag/AgCl} + 0.059*pH$ V). LSV measurements (0.005 V/s, 1 to 1.8 V potential windows) were done to calculate onset overpotentials at current densities (j_{10},10 mA/cm^2) and Tafel plots (log (j) vs. V_{RHE}). Double-layer capacitances (C_{dl}) were done using CV measurements in between the V_{dl} windows 1.203 V to 1.302 V. The EIS measurements were also opted with 10^5 to 0.01 Hz frequency ranges at 1.6 V vs. RHE.

5.2.4. Photocatalytic reduction of Cr(VI)

An aqueous solution of 0.34 mM (50 mg/500 mL) $K_2Cr_2O_7$ was prepared. To find out photocatalytic reduction of Cr(IV), from this stock solution 60 mL were taken. A

required amount (20 mg) of photocatalyst was added to this solution. The photocatalysis of Cr(IV) to Cr(III) was regularly monitored on UV-Vis absorption spectrum within a range of 200 nm to 600 nm. The percentage reduction of Cr(IV) to Cr(III) using $Co_{0.8}Fe_{0.2}S_2$ and $Co_{0.8}Fe_{0.2}Se_2$ as photocatalyst is given by the equation-1.

$$\% \text{ Reduction} = (C_0 - C_t/C_0) * 100 \qquad (1)$$

Here C_o is the initial concentration (corresponding to absorbance) of Cr (IV) at λ_{max}, and C_t is the concentration at time (t).

5.2.5. Instrumentation

The synthesized materials were subjected to different analytical techniques for their characterization. The crystal structure and phase purity were confirmed by using Bruker D8 X-ray diffractometer equipped with CuKa radiation (λ = 1.54056 Å, 2θ range from 20° to 70°). The morphological structure, surface analysis and elemental distribution were performed by FESEM (Ultra 55 Carl Zeiss instrument with an operating voltage of 10 kV), TEM (FEI Technai G2 F20 STEM with a 200 kV) and EDAS studies. Optical properties and catalysis were recorded with a JASCO-V770 UV/Vis spectrophotometer containing $BaSO_4$ as standard. The nitrogen adsorption-desorption isotherms and the pore distribution of materials were estimated by Brunauer-Emmett-Teller instrument (BET) (Nova 2000e, Quantachrome Instruments Limited, USA using liquid nitrogen (77 K)). The oxidation state of elements and chemical composition were determined by X-ray photoelectron spectra (XPS) using a Thermo scientific Escalab 250Xi spectrometer with Al−Kα radiation.

5.3. Results and Discussion

5.3.1. Synthesis and characterization

As already discussed in our previous reports, for the synthesis of $Co_{0.8}Fe_{0.2}S_2$ nanoparticles, hexamethyldisilazane (HMDS)-assisted wet chemical method with slight modification was a promising method. The $Co_{0.8}Fe_{0.2}S_2$ and $Co_{0.8}Fe_{0.2}Se_2$ materials were synthesized by our previously reported work with some modifications (Scheme 5.1) using

HMDS as an asset accompanied with Schlenk lines to maintain the continuous inert atmosphere using nitrogen gas.

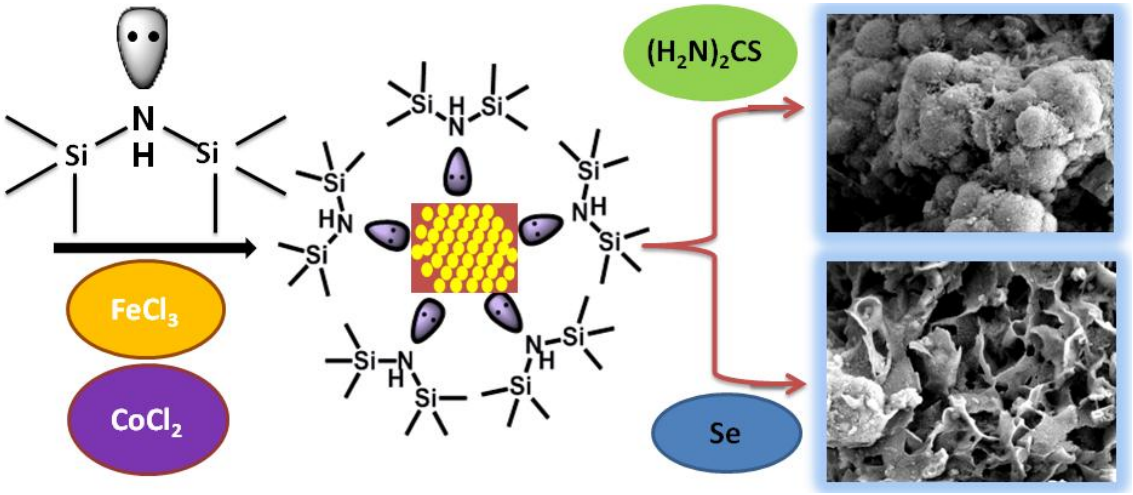

Scheme 5.1. Illustration of the reaction scheme carried for the synthesis of $Co_{0.8}Fe_{0.2}S_2$ and $Co_{0.8}Fe_{0.2}Se_2$ desired materials.

The crystal structure determination together with phase purity begins with powder x-ray diffraction studies (PXRD). Figure 5.1 show the crystal structure information of $Co_{0.8}Fe_{0.2}S_2$ and $Co_{0.8}Fe_{0.2}Se_2$ chalcogenide materials. As shown in Figure 5.1a, all the peaks correspond to the hexagonal structure of $Co_{0.8}Fe_{0.2}S_2$ with JCPDS. No. 75-0607. The peaks at 2θ of 30.80, 33.21, 35.38, 46.72 and 54.64 can be indexed to planes of (100), (022), (101), (102) and (110) respectively. Likewise Figure 5.1b representing the diffraction spectra of $Co_{0.8}Fe_{0.2}Se_2$ has various intense peaks at 2θ values of 23.4˚, 29.67˚, 35.77˚, 41.28˚, 43.72˚, 45.25˚ and 52.3˚ designated to crystal planes of (110), (011), (111), (210), (102), (221) and (311) respectively [54]. Besides this the high intense peaks shows the high crystalline nature of $Co_{0.8}Fe_{0.2}Se_2$. From the PXRD spectra, its visible no other characteristics peaks can be found indexed to either pure CoS_2, $CoSe_2$ and FeS_2 phases or any other stoichiometry's of these trio, hence confirming the single phase and high purity of the material.

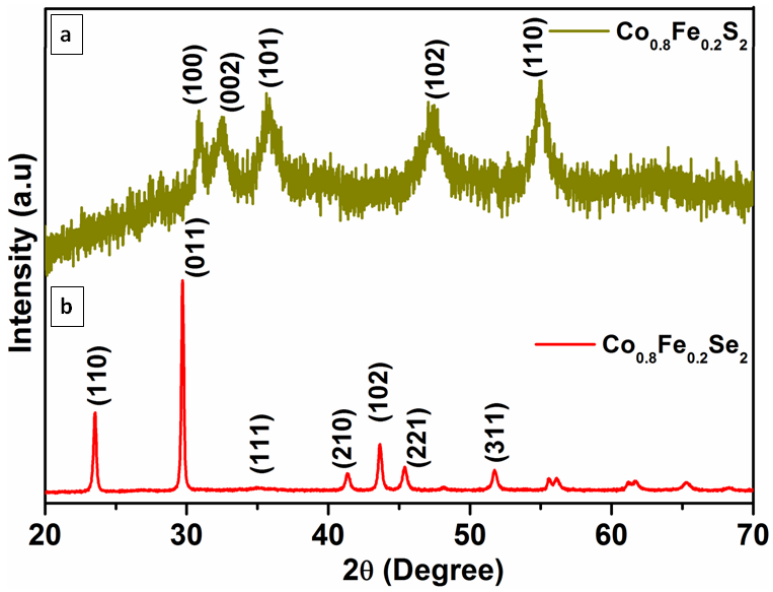

Figure 5.1. PXRD of $Co_{0.8}Fe_{0.2}S_2$ and $Co_{0.8}Fe_{0.2}Se_2$ materials elucidating the high crystallinity.

The morphological metaphors of as synthesized materials were determined from scanning electron microscopy (SEM) (Figure 5.2) and EDAS (Figure 5.3) used to chalk out elemental analysis. From Figure 5.2a, b it shows that $Co_{0.8}Fe_{0.2}S_2$ has got spherical morphology. The outlook of spheres seems loose texture type. Since here no external surfactant is used during the synthesis process, so the spheres look aggregated or fused. As shown in both low and high magnification SEM images the spheres are fused involving incomplete growth of spheres. The average particle size determined for $Co_{0.8}Fe_{0.2}S_2$ calculated comes up to ~112 nm. The reason for bigger size must be because of aggregation of particles. Similarly Figure 5.2c, d shows flower or flakes type morphology for $Co_{0.8}Fe_{0.2}Se_2$. Both low and high magnifications reveal flower like morphology delineated with thin flakes of loose textural for $Co_{0.8}Fe_{0.2}Se_2$. A good amount of spaces and porous textural is visible from the flowers showing they can act as good materials for electrochemical OER purposes, which can be further confirmed from BET surface area analysis. The elemental analysis documented from EDAS (Figure 5.3) for both the materials certified the well dispersal of elements Co, Fe, S and Se. Further analysis about the morphological features of the materials was ascertained from TEM measurements. From the Figure 5.2e and f, the TEM images clearly indicate that the materials show similar type of morphology as in SEM.

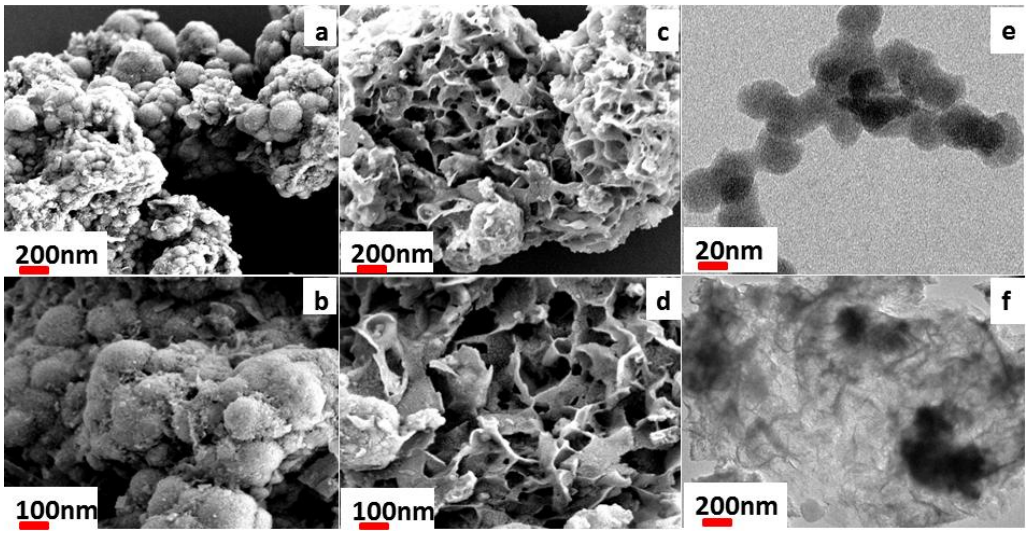

Figure 5.2. The morphological analysis of $Co_{0.8}Fe_{0.2}S_2$ and $Co_{0.8}Fe_{0.2}Se_2$ materials. (a, b) showing low and high magnification FE SEM images of $Co_{0.8}Fe_{0.2}S_2$ displaying sphere type morphology (c, d) low and high magnification FE SEM images of $Co_{0.8}Fe_{0.2}Se_2$ presenting flower type morphology respectively. (e, f) Representing the TEM images of $Co_{0.8}Fe_{0.2}S_2$ and $Co_{0.8}Fe_{0.2}Se_2$ respectively.

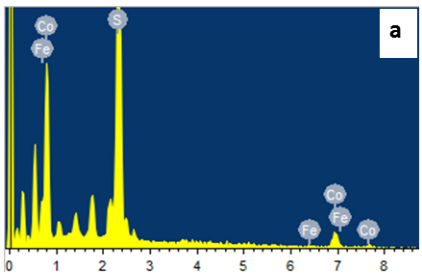

Element	Weight%	Atomic%
S K	43.88	58.93
Fe L	1.82	1.40
Co L	54.30	39.67
Totals	100.00	

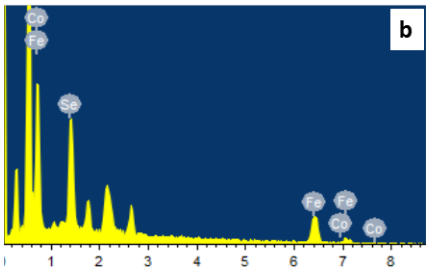

Element	Weight%	Atomic%
Se L	72.50	78.52
Fe L	1.59	1.63
Co L	25.91	19.85
Totals	100.00	

Figure 5.3. Elemental distribution by EDAS of $Co_{0.8}Fe_{0.2}S_2$ and $Co_{0.8}Fe_{0.2}Se_2$ respectively.

The aim of the study is to develop surfactant free materials in order to exhibit excellent catalytic properties.

The chemical composition and the valence oxidation states of $Co_{0.8}Fe_{0.2}Se_2$ material were studied by x-ray photoelectron (XPS) analysis as shown in Figure 5.4.

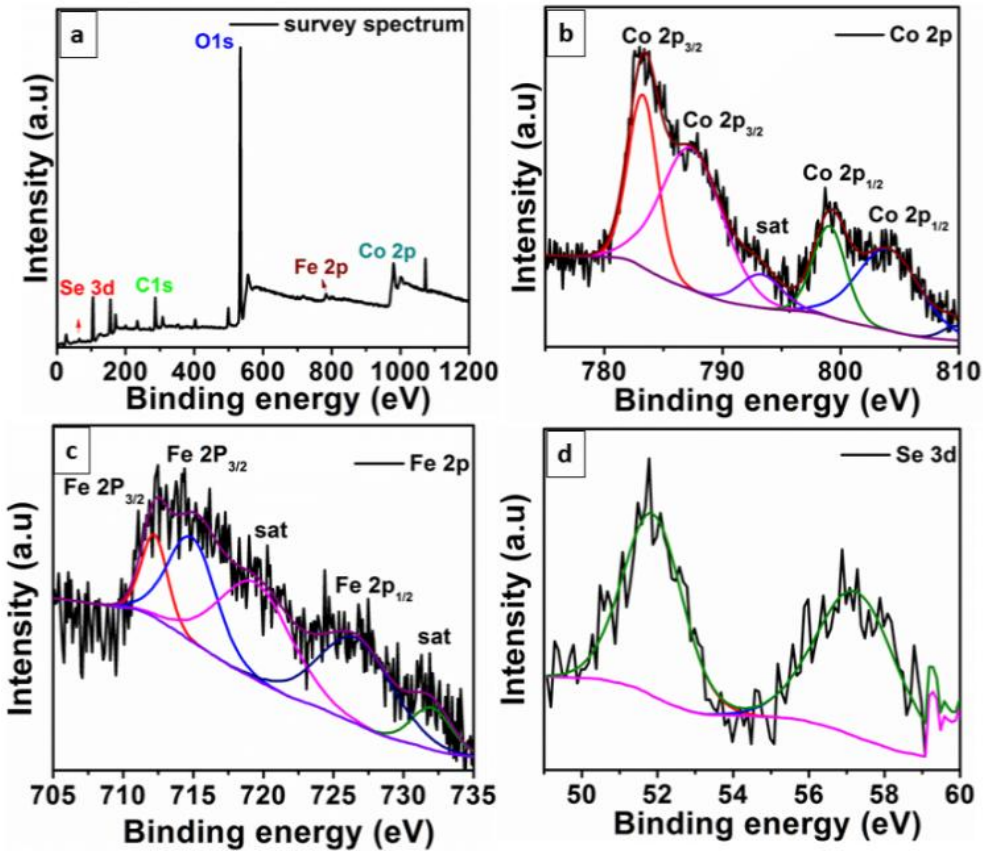

Figure 5.4. The XPS spectrum of $Co_{0.8}Fe_{0.2}Se_2$ (a) survey spectrum showing the presence of requisite elements. (b – d) showing the binding energy values for Co 2p, Fe 2p and Se 3d energy levels.

The survey spectrum (Figure 5.4a) shows the presence of Co, Fe and Se, besides the presence of C and O is also indicative. As shown in Figure 5.4b, Co $2p_{1/2}$ has got peaks at 798.12 eV and 802.79 eV and the two other peaks for Co $2p_{3/2}$ at 782.90 eV and 786.31 eV, which are the characteristic peaks of Co^{3+} and Co^{2+} [55]. The XPS spectrum of Fe (Figure 5.4c) shows peaks at 711.96 eV and 714.56 eV which are delineated with Fe^{2+} $2p_{3/2}$ and Fe^{3+} $2p_{3/2}$ respectively, besides these two peaks one more peak is obtained at 726.10 eV characteristic for Fe $2p_{1/2}$ [54]. The two satellite peaks which are obtained at the binding energies of 719.08 eV and 732.12 eV are an excellent proof for the existence of bivalency for Fe in $Co_{0.8}Fe_{0.2}Se_2$. The XPS spectrum of selenide (Figure 5.4d) assigns

two peaks at 52.06 eV for $3d_{5/2}$ and 57.30 eV for $3d_{3/2}$ respectively indicating the existence of metal- selenide bond.

The surface area analysis for any material is the most crucial factor explaining its catalytic activities. The surface area and pore size distribution analysis were determined by studying BET surface area isotherms. The N_2 adsorption–desorption isotherm of $Co_{0.8}Fe_{0.2}S_2$ and $Co_{0.8}Fe_{0.2}Se_2$ materials representing the surface area of materials is shown in Figure 4a, b. The hysteresis curves depict the surface of area of 10.69 m^2/g and 21.41 m^2/g for $Co_{0.8}Fe_{0.2}S_2$ and $Co_{0.8}Fe_{0.2}Se_2$ materials. Besides the surface area, the pore size distribution as determined by BJH plots (Figure 4c, d) was found to be 18.753 A° and 17.147 A° for $Co_{0.8}Fe_{0.2}S_2$ and $Co_{0.8}Fe_{0.2}Se_2$ materials confirming the mesoporous nature of synthesized materials. The high surface of $Co_{0.8}Fe_{0.2}Se_2$ materials show that more number of the active sites will be available and hence more diffusion of electrolytic solution into pores providing better catalytic performance mostly for OER activities.

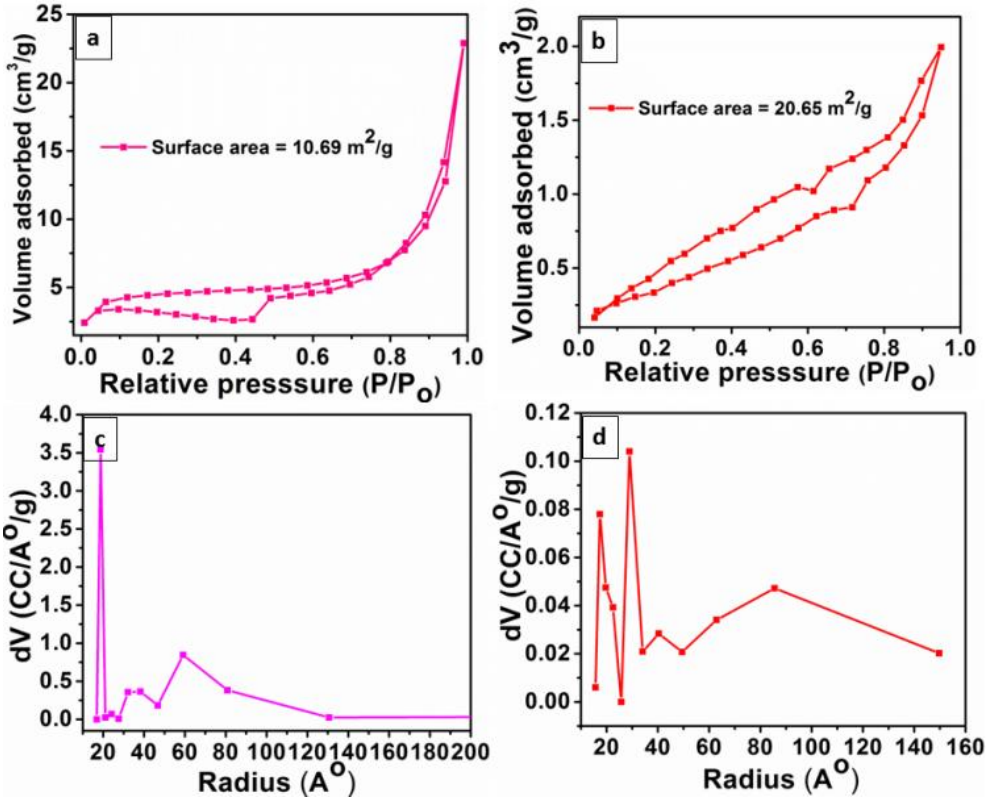

Figure 5.5. Surface area analysis of (a) $Co_{0.8}Fe_{0.2}S_2$ and (b) $Co_{0.8}Fe_{0.2}Se_2$ materials. The pore radius of $Co_{0.8}Fe_{0.2}S_2$ (c) and $Co_{0.8}Fe_{0.2}Se_2$ (d).

The optical properties of $Co_{0.8}Fe_{0.2}S_2$ and $Co_{0.8}Fe_{0.2}Se_2$ materials were evaluated from UV-visible DRS spectra (Figure 5.6). The absorption spectrum shows the materials absorbing mostly in the visible region with onset absorption at 260 nm. The absorption shows a broad band located mostly in the region extending from 400 to 700 nm with a maximum absorption at 650 nm.

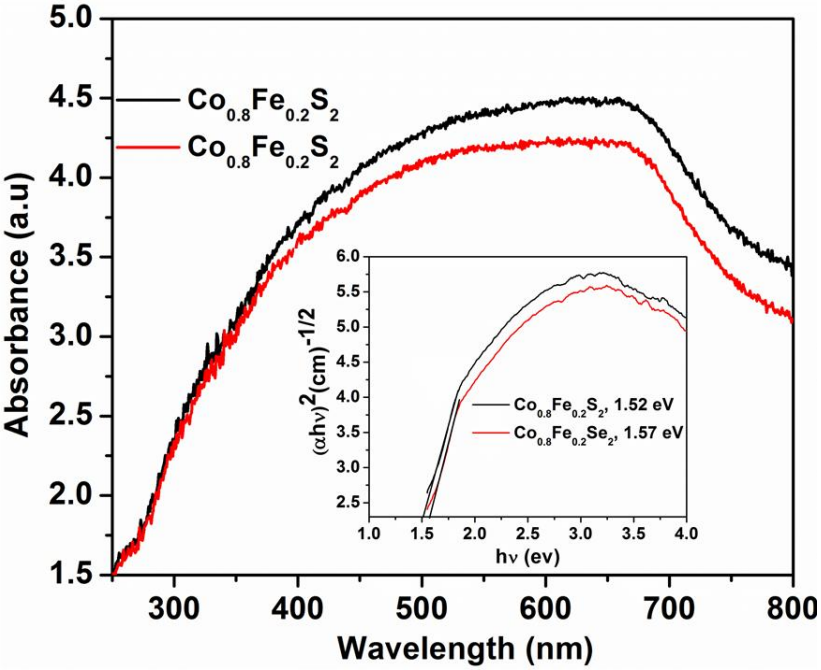

Figure 5.6. Showing solid UV-visible DRS spectra of $Co_{0.8}Fe_{0.2}S_2$ and $Co_{0.8}Fe_{0.2}Se_2$ materials. The inset representing the band gap of the materials.

The broadness of the absorption peak might be because of the morphological differences as we experience an inherent property shown by all the nanomaterials based on their size and shape. From the DRS spectrum of these materials the band gap calculated were found to be 1.52 eV for $Co_{0.8}Fe_{0.2}S_2$ and 1.57 eV for $Co_{0.8}Fe_{0.2}Se_2$. The low band gap of spheres is because of quantum confinement which results in blue shift. The energy band gap (E_g) can be estimated from $(\alpha h\nu)^2$ vs. $h\nu$ plot by projecting the straight line to $h\nu$ axis were the point of intersection confirms the band value as shown in equation –2 [60].

$$\alpha h\nu = A(h\nu - Eg)^2 \qquad (2)$$

In this equation α represents optical adsorption constant, h is the Planck constant; ν is the frequency of light; E_g directs the band edge value.

5.3.2. Electrocatalytic excellence of $Co_{0.8}Fe_{0.2}S_2$ and $Co_{0.8}Fe_{0.2}Se_2$

The strong electroactive sites $Co_{0.8}Fe_{0.2}S_2$ and $Co_{0.8}Fe_{0.2}Se_2$ preelectrocatalyst is modified on GCE to achieve excellent oxygen evolution reaction (OER), which is resulting low overpotential and Tafel values, thus identifies $Co_{0.8}Fe_{0.2}S_2$ and $Co_{0.8}Fe_{0.2}Se_2$ preelectrocatalyst as unique type of bifunctional electrocatalysts. The capable OER behaviours of $Co_{0.8}Fe_{0.2}S_2$ and $Co_{0.8}Fe_{0.2}Se_2$ materials are evaluated by the CV, EIS and LSV polarization measurements using typical home-made three-electrode system. The achieved less overpotential via LSV measurements is calculated as follows, $E_{(RHE)}$-1.23 V. As displayed in Figure 5.7a, $Co_{0.8}Fe_{0.2}Se_2$ materials (345 mV @η_{10} and 425 mV @η_{50}) results relatively less overpotential than $Co_{0.8}Fe_{0.2}S_2$ (350 mV@η_{10} and 475 mV@η_{50}) whereas GCE results negligible OER current, indicating $Co_{0.8}Fe_{0.2}Se_2$ and $Co_{0.8}Fe_{0.2}S_2$

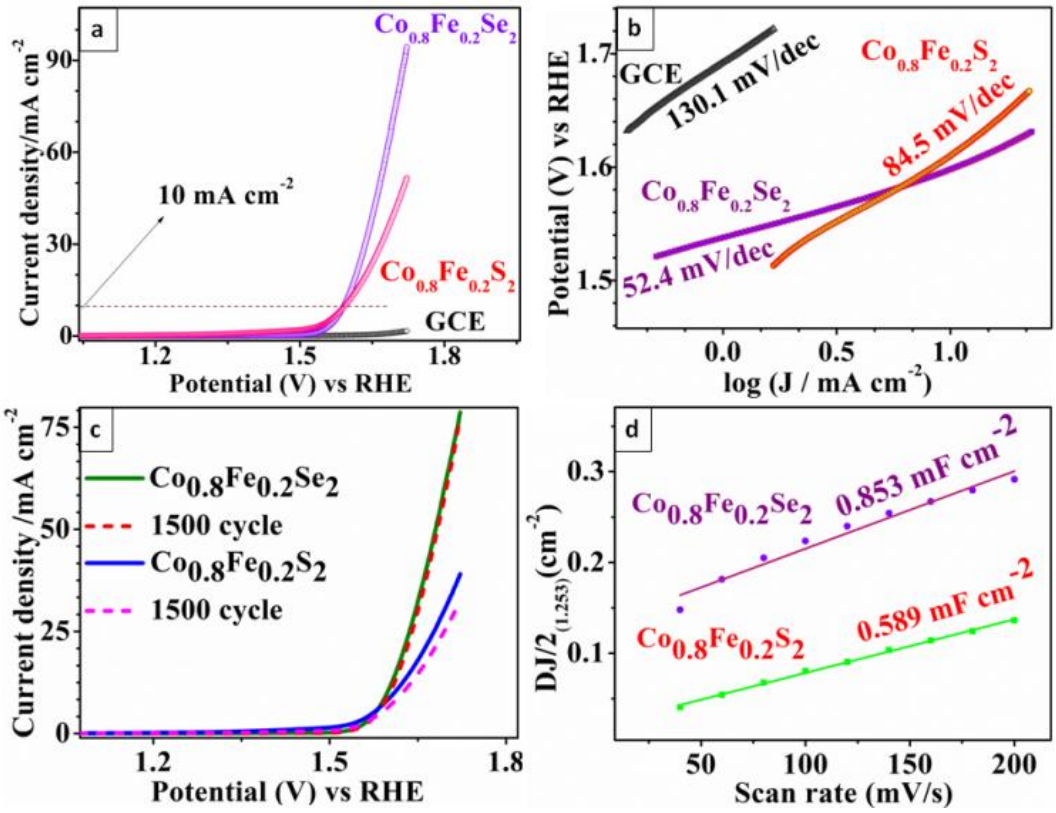

Figure 5.7. Electrochemical measurements (OER performances) by $Co_{0.8}Fe_{0.2}Se_2$ and $Co_{0.8}Fe_{0.2}S_2$. **(**a) LSV curves, (b) Tafel plots (c) stability of electrocatalysts and (d) C_{dl} measurements in 1 M KOH.

have robust OER ability. Furthermore, $Co_{0.8}Fe_{0.2}Se_2$ precatalysts OER kinetics (Tafel plots) are also favorable toward OER and consistent with reports, which is derived from Tafel equation as follows, $\eta=a+b \log |J|$ [33]. Tafel plots of $Co_{0.8}Fe_{0.2}Se_2$ (52.4 mV/dec) and $Co_{0.8}Fe_{0.2}S_2$ (84.5 mV/dec) are very smaller than bare GCE (73 mV/dec). In general, this robust OER could be resulted from unique surface behaviors, multicomponent synergistic environments and unique morphology of electro-active sites, which leads to improved electron transport and enhanced current densities [14,15, 38-40, 32]. Moreover, the electrocatalytic durability of both $Co_{0.8}Fe_{0.2}Se_2$ and $Co_{0.8}Fe_{0.2}Se_2$ hybrid electrocatalysts are evaluated through continuous 1500 CV cycling measurements, which shows $Co_{0.8}Fe_{0.2}Se_2$ has negligible current density loss than $Co_{0.8}Fe_{0.2}S_2$ is at after 1500 CV cycles measurements, which indicates the electrocatalytic stability of $Co_{0.8}Fe_{0.2}Se_2$.

In addition, the insight into electrode kinetics of modified electrodes is evaluated using double-layer capacitance (C_{dl}) and electrochemical surface area (ECSA). Generally, ECSA is directly proportional to the C_{dl} values. The C_{dl} measurements of $Co_{0.8}Fe_{0.2}Se_2$ and $Co_{0.8}Fe_{0.2}S_2$ (Figure 5.8) using cyclic voltammetry are carried with various scan rates from 0.02 to 0.002 Vs^{-1} in 1 M KOH solution. $Co_{0.8}Fe_{0.2}Se_2$ possesses an excellent C_{dl} value (0.853 mF/cm^2) than $Co_{0.8}Fe_{0.2}S$ (0.589 mF/cm^2).

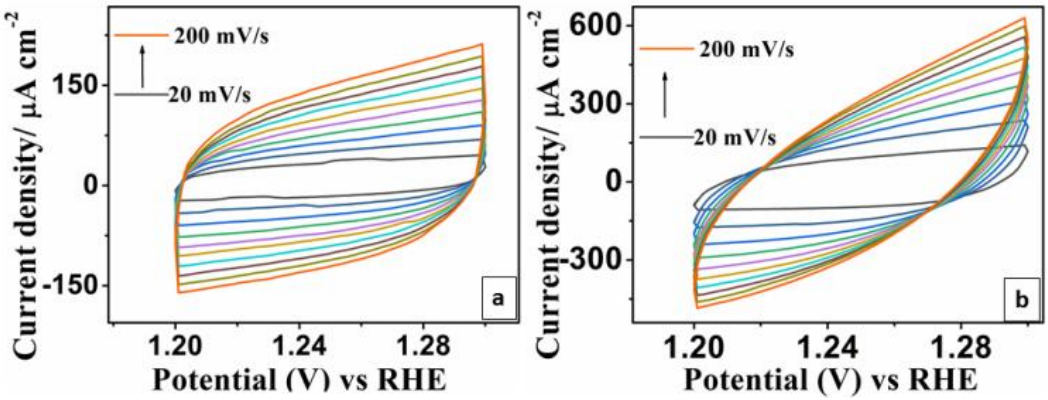

Figure 5.8. C_{dl} measurements of $Co_{0.8}Fe_{0.2}S_2$ and $Co_{0.8}Fe_{0.2}Se_2$ materials

Remarkably, these outcomes emphasize that $Co_{0.8}Fe_{0.2}Se_2$ and $Co_{0.8}Fe_{0.2}S$ catalyst achieved through our HMDS assisted one-pot approach can perform as a class of efficient catalyst for alkaline OER electrocatalysis. Consequently, exceptional high surface area properties and mesoporous behaviors resulted through our novel approach on

$Co_{0.8}Fe_{0.2}Se_2$ and $Co_{0.8}Fe_{0.2}S$ materials have made them as a suitable candidate to achieve effective redox kinetics and also with decreased charge transport barriers, thus leads to favorable OER performance.

5.3.3. Photocatalytic Excellence of $Co_{0.8}Fe_{0.2}S_2$ and $Co_{0.8}Fe_{0.2}Se_2$

As already discussed, the number of pollutants, including organic/inorganic chemicals [e.g., dyes, nitro compounds, Cr(VI)], are highly toxic and noxious. The environmental pollution rose at an alarming rate, which poses a serious threat to life, whether aquatic or terrestrial. Therefore, the need is to develop such materials that can play multiple roles. In this concern, the synthesized materials have been tested as photocatalysts. Here for the first time, we have tested the dual catalytic performance by the as-synthesized materials. First, as a catalyst in electrochemical water splitting for OER reactions and second as photocatalyst in decreasing the toxicity of Cr(VI) by reducing it to less toxic Cr(III). Figure 5.9a, b shows the decreasing intensity in the absorption spectrum of Cr(VI) in an acidic medium (pH = 3) while using $Co_{0.8}Fe_{0.2}S_2$ and $Co_{0.8}Fe_{0.2}Se_2$ as photocatalysts in the daylight. The results clearly show that reduction takes place feasibly in less time.

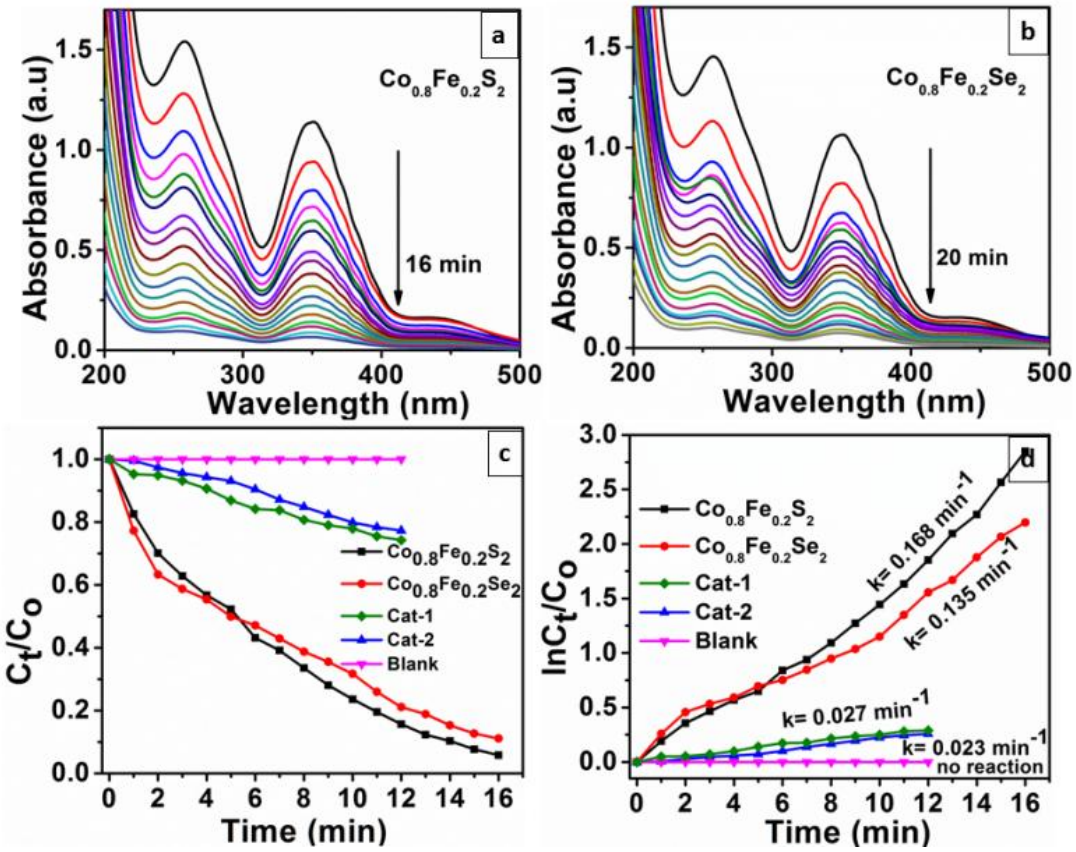

Figure 5.9. The absorption spectrum of Cr(VI) photoreduction using (a) $Co_{0.8}Fe_{0.2}S_2$ and (b) $Co_{0.8}Fe_{0.2}Se_2$ as photocatalysts. (c, d) Showing the kinetics measurements of Cr(VI) photoreduction.

The photocatalytic experiments were tested by performing the following control experiments. (i) A reaction, where only the catalyst was present (catalysis) [Either $Co_{0.8}Fe_{0.2}S_2$ (Cat-1) or $Co_{0.8}Fe_{0.2}Se_2$ (Cat-2)]. (ii) The second reaction with sunlight alone (photolysis) (Figure 5.10a, b, c, d).

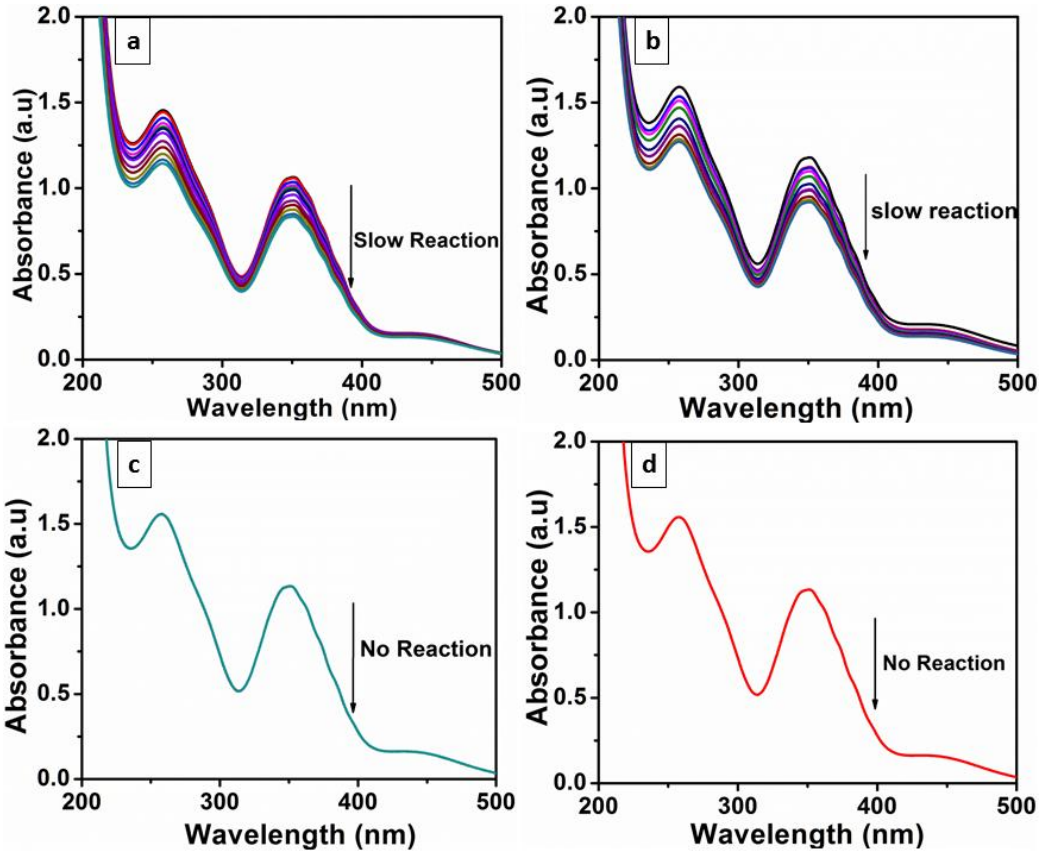

Figure 5.10. The controlled reactions for Cr(VI) reduction (a, b) catalysis-when only catalyst $Co_{0.8}Fe_{0.2}S_2$ (Cat-1) and $Co_{0.8}Fe_{0.2}Se_2$ (Cat-2) is present (c, d) photolysis-when only light is present (Blank).

Under both conditions, no appreciable change in the intensity of Cr(VI) absorption spectrum was noticed indicating slow reduction during catalysis and almost no reaction in photolysis. These experiments clarified that both catalysts and light are necessary for the reduction to occur.

The overall photocatalytic reduction was well explained by pseudo first order kinetics (Figure 5.9c, d) given by equation-3.

$$\ln(C_t/C_0) = -kt \qquad (1)$$

The C_o and C_t representing the initial and final concentration were determined corresponding to change in absorbance values (A_o and A_t) and k is the rate constant. The rate constant values observed for two photocatalysts were found to 0.168 min^{-1} and 0.135 min^{-1} respectively. The values show that $Co_{0.8}Fe_{0.2}S_2$ has higher photoreduction ability

than $Co_{0.8}Fe_{0.2}Se_2$. A 96% reduction of Cr(VI) was observed using $Co_{0.8}Fe_{0.2}S_2$ as photocatalyst while as 91% reduction was obtained under the influence of $Co_{0.8}Fe_{0.2}Se_2$ as photocatalyst (Figure 5.11).

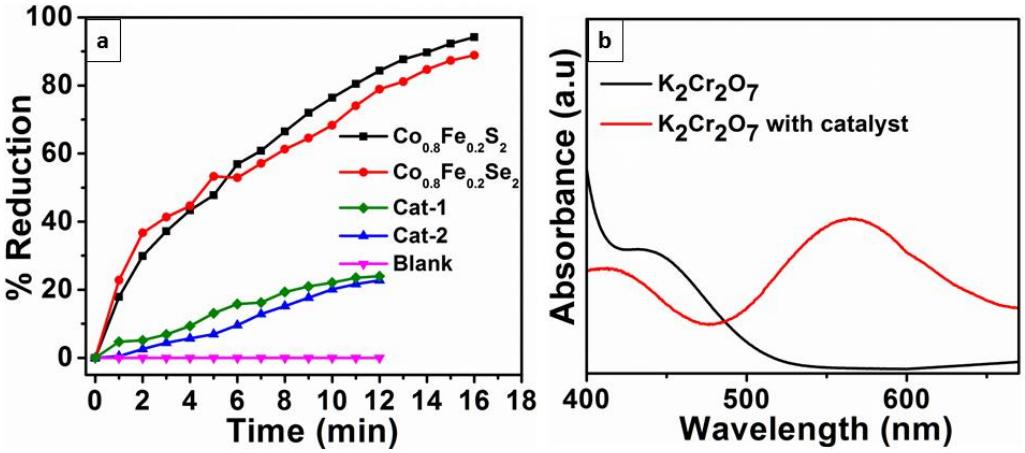

Figure 5.11. The graphs representing (a) % degradation of $Co_{0.8}Fe_{0.2}S_2$ and $Co_{0.8}Fe_{0.2}Se_2$ materials (b) controlled reactions for confirming the Cr(VI) reduction to Cr(III).

For any catalyst on large scale applications, stability is the most crucial parameter, and hence we tested their reusability. In these experiments, both the catalysts retained superior catalytic activities up to 5 cycles with an overall 90% retention Figure 5.12.

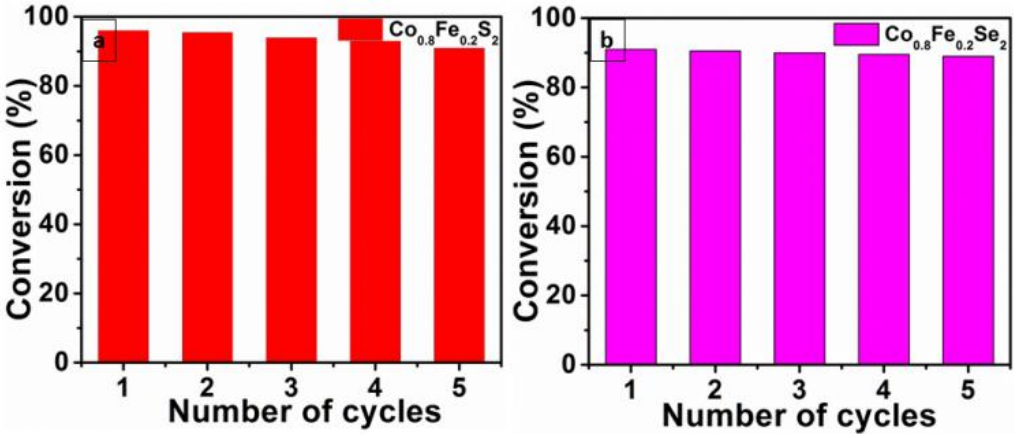

Figure 5.12. Reusability of photocatalysts (a) $Co_{0.8}Fe_{0.2}S_2$ and (b) $Co_{0.8}Fe_{0.2}Se_2$.

Further, a few controlled experiments were performed to confirm whether Cr(VI) was reduced by photocatalysts or by simple adsorption on the catalyst surface. The reduction product Cr(III) yielded a pink color complex on treating with 2, 6-pyridine dicarboxylic acid (PDCA), confirming that the reduced product indeed Cr(III). The

reaction was followed from the absorption spectrum wherein the peak in the region between 550 to 570 nm corresponds to Cr(III) absorption (Figure 5.11b) [59, 61, 62].

The mechanism by which the Cr(VI) reduction takes place using $Co_{0.8}Fe_{0.2}S_2$ and $Co_{0.8}Fe_{0.2}Se_2$ as photocatalysts is shown schematically in Scheme 5.2.

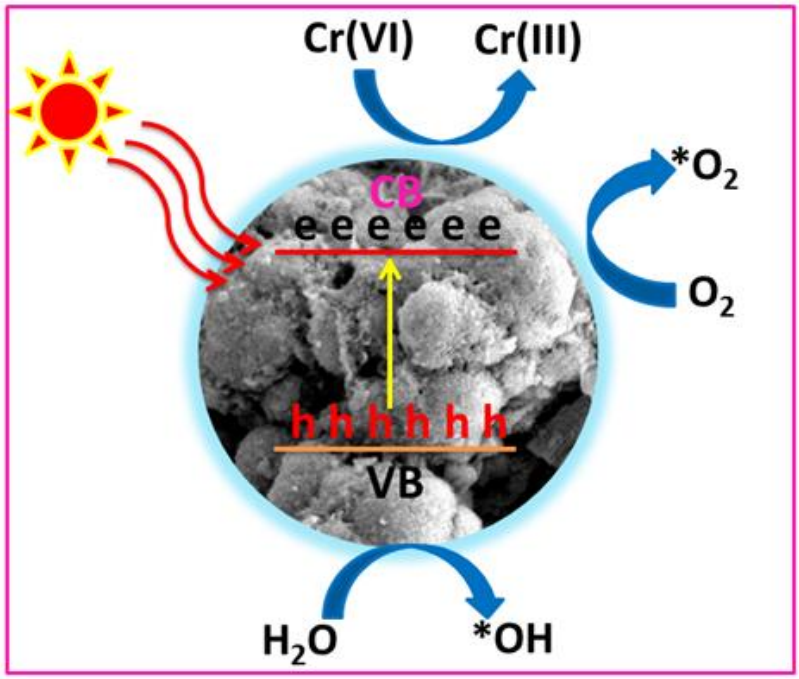

Scheme 5.2. Mechanism of Cr(VI) reduction involving $Co_{0.8}Fe_{0.2}S_2$ and $Co_{0.8}Fe_{0.2}Se_2$ as a photocatalysts.

The photocatalytic reduction of Cr(VI) was performed in an acidic medium with a pH value of 3. At this low value of pH the $HCrO_4^-$ is the prevailing species, with the result the catalysts surface gets enriched with protonation so accumulation of positive charge takes place which enhances the attraction between catalysts surface and $HCrO_4^-$. The photocatalysts when exposed to electromagnetic spectrum absorbs light as per its bandwidth, with the result generation of electrons and holes occurs. These photogenerated electrons jump from valence band to conduction band leaving behind a positive hole. These charge carriers then recombine with the water and dissolved oxygen resulting in the generation of active oxidizing species- hydroxide radical and superoxide radicals. These active radicals then cause the reduction of Cr(VI) to Cr(III), with the side wise formation of water and CO_2 as byproducts [63].

5.4. Summary

In this chapter, a pair of cobalt iron based transition metal chalcogenides comprising of sulpher and selenium were synthesized with a newly developed HMDS- assisted one-pot synthesis method. The main purpose of this report is to develop bifunctional materials. The materials were successfully characterized by various sophisticated techniques. The electrocatalytic role of water splitting for OER performances shows that the synthesized materials could better serve as electrocatalysts with $Co_{0.8}Fe_{0.2}Se_2$ showing superior activity than $Co_{0.8}Fe_{0.2}S_2$ as indicated by the low overpotential and Tofel values (345 and 350 mV @η_{10}, 52.4 and 84.5 mV/dec Tofel values for $Co_{0.8}Fe_{0.2}Se_2$ and $Co_{0.8}Fe_{0.2}S_2$, respectively). The bifunctional catalytic activity was determined by performing photocatalysis of toxic chemical Cr(VI). The materials show about 96% Cr(VI) reduction by $Co_{0.8}Fe_{0.2}S_2$ and 91% reduction by $Co_{0.8}Fe_{0.2}Se_2$ with superior activity retained after more than 5 cycles. This work provides a platform for the development of catalysts with multiple roles in catalysis.

5.5. References

[1] Ramadoss, M.; Chen, Y.; Hu, Y.; Li, W.; Wang, B.; Zhang, X.; Wang, X.; Yu, B. Three-dimensional Ni/Ni_3Fe embedded boron-doped carbon nanotubes nanochain frameworks as highly efficient and durable electrocatalyst for oxygen evolution reaction. *J. Power Sources* **2020**, *451*, 227753.

[2] Hu, X.; Huang, T.; Tang, Y.; Fu, G.; Lee, J. M. Three-dimensional graphene-supported Ni_3Fe/Co_9S_8 composites: rational design and active for oxygen reversible electrocatalysis. *ACS Appl. Mater. Interfaces* **2019**, *11*, 4028–4036.

[3] S. Jiang Yang, Y. Zhao, L. Zhu, S. Chen, X. Wang, Q. Wu, J. Ma, Y. Ma, Z. Hu, Boron-doped carbon nanotubes as metal-free electrocatalysts for the oxygen reduction reaction. *Angew. Chem.* **2011**, *123*, 7270–7273.

[4] Yang, Y.; Zhang, W.; Xiao, Y.; Shi, Z.; Cao, X.; Tang, Y.; Gao, Q. $CoNiSe_2$ heteronanorods decorated with layered-double-hydroxides for efficient hydrogen evolution. *Appl. Catal. B: Environ.* **2019**, *242*, 132–139.

[5] Jeyagopal, R.; Chena, Y.; Ramadoss, M.; Marimuthu, K.; Wang, B.; Li, W.; Zhanga, X. A Three-Dimensional Porous CoSnS@CNT Nanoarchitecture as Highly Efficient Bifunctional Catalyst for Boosted OER Performance and Photocatalytic Degradation. *Nanoscale* **2020**, *12*, 3879-3887.

[6] Farooq, U.; Phul, R.; Alshehri, S. M.; Ahmed, J.; Ahmad, T. Electrocatalytic and Enhanced Photocatalytic Applications of Sodium Niobate Nanoparticles Developed by Citrate Precursor Route. *Scientific Reports* **2019**, *9*, 4488.

[7] Huan, Y.; Shi, J.; Zhao, G.; Yan, X.; Zhang, Y. 2D Metallic Tran-sitional Metal Dichalcogenides for Electrochemical Hydrogen Evolution. *Energy Technology* **2019**, *7*, 1801025.

[8] Yao, M.; Sun, B.; He, L.; Wang, N.; Hu, W.; Komarneni, S. Self-Assembled Ni_3S_2 Nanosheets with Mesoporous Structure Tightly Held on Ni Foam as a Highly Efficient and Long-Term Electrocatalyst for Water Oxidation. *ACS Sustainable Chem. Eng*. **2019**, *7*, 5430-5439.

[9] Gratzel, M. Recent Advances in Sensitized Mesoscopic Solar Cells. *Acc. Chem. Res*. **2009**, *42*, 1788-1798.

[10] Li, Z-y.; Ye, K-h.; Zhong, Q-s.; Zhang, C-j.; Shi, S-t.; Xu, C. Au–Co_3O_4/C as an Efficient Electrocatalyst for the Oxygen Evolution Reaction. *ChemPlusChem*. **2014**, *79*, 1569–1572.

[11] Ghosh, S.; Kar, P.; Bhandary, N.; Basu, S.; Sardar, S.; Mai-yalagan, T.; Majumdar, D.; Bhattacharya, S. K. Bhaumik, A.; Lemmens, P.; Pal, S. K. Microwave-assisted synthesis of porous Mn_2O_3 nanoballs as bifunctional electrocatalyst for oxygen reduction and evolution reaction. *Catal. Sci. Technol*. **2016**, *6*, 1417–1429.

[12] Jiang, Y.; Li, X.; Wang, T.; Wang, C. Enhanced electrocatalytic oxygen evolution of α-$Co(OH)_2$ nanosheets on carbon nano-tube/polyimide films. *Nanoscale* **2016**, *8*, 9667–9675.

[13] Feng, J-X.; Xu, H.; Dong, Y-T.; Ye, S-H.; Tong, Y-X.; Li, G-R. FeOOH/Co/FeOOH Hybrid Nanotube Arrays as High-Performance Electrocatalysts for the Oxygen Evolution Reaction. *Angew. Chem*. **2016**, *128*, 3758–3762.

[14] Bockris, J. O.; Otagawa, T. The Electrocatalysis of Oxygen Evolution on Perovskites. J. *Electrochem. Soc*. **1984**, *131*, 290–302.

[15] Gao, M. R., Xu, Y. F., Jiang, J.; Yu, S. H. Nanostructured metal chalcogenides: synthesis, modification, and applications in energy conversion and storage devices. *Chem. Soc. Rev*. **2013**, *42*, 2986–3017.

[16] Zhang, X.; Chen, Y.; Wang, B.; Chen, M.; Yu, B.; Wang, X.; Zhang, W.; Yang, D. FeNi nanoparticles embedded porous nitrogen-doped nanocarbon as efficient electrocatalyst for oxygen evolution reaction. *Electrochim. Acta* **2019**, *321*, 134720–134729.

[17] Yang, D.; Hou, W.; Lu, Y.; Wang, X.; Zhang, W.; Chen, Y. Scalable synthesis of bimetallic phosphide decorated in carbon nanotube network as multifunctional electrocatalyst for water splitting. *ACS Sustainable Chem. Eng*. **2019**, *7*, 13031–13040.

[18] Hu, Y.; Yu, B.; Ramadoss, M.; Li, W.; Yang, D.; Wang, B.; Chen, Y. Scalable synthesis of heterogeneous W-W_2C nanoparticle-embedded CNT networks for boosted hydrogen evolution reaction in both acidic and alkaline media. *ACS Sustainable Chem. Eng*. **2019**, *7*, 10016–10024.

[19] Zheng, B.; Chen, Y.; Qi, F.; Wang, X.; Zhang, W.; Li, Y.; Li, X. 3D-hierarchical $MoSe_2$ nanoarchitecture as a highly efficient electrocatalyst for hydrogen evolution. *2D Mater*. **2017**, 4025092.

[20] Ramadoss, M.; Chen, Y.; Hu, Y.; Yang, D. Three-dimensional porous nanoarchitecture constructed by ultrathin $NiCoBO_x$ nanosheets as a highly efficient and durable electrocatalyst for oxygen evolution reaction. *Electrochim. Acta* **2019**, *321*, 134666.

[21] Xie, F.; Wu, H.; Mou, J.; Lin, D.; Xu, C.; Wu, C.; Sun, X. Ni_3N@Ni-Ci nanoarray as a highly active and durable non-noble-metal electrocatalyst for water oxidation at near-neutral Ph. *J. Catal.* **2017**, *356*, 165–172.

[22] Andersen, N. I.; Serov, A.; Atanassov, P. Metal oxides/CNT nano-composite catalysts for oxygen reduction/oxygen evolution in alkaline media. *Appl. Catal. B: Environ*. **2015**, *163*, 623-627.

[23] Li, H.; Zhou, Q.; Liu, F.; Zhang, W.; Tan, Z.; Zhou, H.; Huang, Z.; Jiao, S.; Kuang, Y. Biomimetic design of ultrathin edge-riched FeOOH@Carbon nanotubes as high-efficiency electrocatalysts for water splitting. *Appl. Catal. B: Environ*. **2019**, *255*, 117755.

[24] Huang, R.; Chen, W.; Zhang, Y.; Huang, Z.; Dai, H.; Zhou, Y.; Wu, Y.; Lv, X. Well-designed cobalt-nickel sulfide microspheres with unique peapod-like structure for overall water splitting. *J. Colloid Interface Sci*. **2019**, *556*, 401-410.

[25] Wang, J.; Cui, W.; Liu, Q.; Xing, Z.; Asiri, A. M.; Sun, X. Re-cent Progress in Cobalt-Based Heterogeneous Catalysts for Electro-chemical Water Splitting. *Adv. Mater*. **2016**, *28*, 215-230.

[26] Ge, Y.; Wu, J.; Xu, X.; Ye, M.; Shen, J. Facile synthesis of $CoNi_2S_4$ and $CuCo_2S_4$ with different morphologies as prominent catalysts for hydrogen evolution reaction. *Int. J. Hydrogen Energy* **2016**, *41*, 19847-19854.

[27] Zhang, F.; Ge, Y.; Chu, H.; Dong, P.; Baines, R.; Pei, Y.; Ye, M.; Shen, J. Dual-Functional Starfish-like P‑Doped Co−Ni−S Nanosheets Supported on Nickel Foams with Enhanced Electrochemical Performance and Excellent Stability for Overall Water Splitting. *ACS Appl. Mater. Interfaces* **2018**, *10*, 7087-7095.

[28] Zequine, C.; Bhoyate, S.; Wang, F.; Li, X.; Siam, K.; Kahol, P. K.; Gupta, R. K. Effect of solvent for tailoring the nanomorphology of multinary $CuCo_2S_4$ for overall water splitting and energy storage. *J. Alloy. Compd*. **2019**, *784*, 1-7.

[29] Luo, H.; Lei, H.; Yuan, Y.; Liang, Y.; Qiu, Y.; Zhu, Z.; Wang, Z. Engineering Ternary Copper-Cobalt Sulfide Nanosheets as High-performance Electrocatalysts toward Oxygen eVolution Reaction. *Catalysts* **2019**, *9*, 459.

[30] Chen, B. B.; Ma, D. K.; Ke, Q. P.; Chen, W.; Huang, S. M. In-dented Cu_2MoS_4 nanosheets with enhanced electrocatalytic and photocatalytic activities realized through edge engineering. *Phys. Chem. Chem. Phys*. **2016**, *18*, 6713-6721.

[31] Lin, Y.; Chen, S.; Zhang, K.; Song, L. Recent Advances of Ternary Layered Cu_2MX_4 (M = Mo, W; X = S, Se) Nanomaterials for Photocatalysis. *Solar RRL* **2019**, *3*, 1800320.

[32] Wang, B.; Hu, Y.; Yu, B.; Zhang, X.; Yang, D.; Chen, Y. Heterogeneous CoFe–Co_8FeS_8 nanoparticles embedded in CNT networks as highly efficient and stable electrocatalysts for oxygen evolution reaction. *J. Power Sources* **2019**, *433*, 126688.

[33] Zhou, Y.; Luo, M.; Zhang, Z.; Li, W.; Shen, X.; Xia, W.; Zhou, M.; Zeng, X. Iron doped cobalt sulfide derived boosted electrocatalyst for water Oxidation. *Appl. Surf. Sci*. **2018**, *448*, 9-15.

[34] Huang, L.; Wu, H.; Liu, H.; Zhang, Y. Phosphorous doped cobalt-iron sulfide/carbon nanotube as active and robust electrocatalysts for water splitting. *Electrochim. Acta* **2019**, *318*, 892-900.

[35] Liu, T.; Yang, F.; Cheng, G.; Luo, W. Reduced Graphene Oxide-Wrapped $Co_{9-x}Fe_xS_8$/Co, Fe-N-C Composite as Bifunctional Electrocatalyst for Oxygen Reduction and Evolution. *Small* **2018**, *14*, 1703748.

[36] Shit, S.; Jang, W.; Bolar, S.; Murmu, N. C.; Koo, H.; Kuila, T. Effect of Ion Diffusion in Cobalt Molybdenum Bimetallic Sulfide toward Electrocatalytic Water Splitting. *ACS Appl. Mater. Interfaces* **2019**, *11*, 21634-21644.

[37] Quan, B.; Tong, H.; Liu, C.; Li, D.; Meng, S.; Chen, M; Zhu, J.; Jiang, D. Integration of $ZnCo_2S_4$ nanowires arrays with NiFe-LDH nanosheet as water dissociation

promoter for enhanced electrocatalytic hydrogen evolution. *Electrochim. Acta* **2019**, 324, 134861.

[38] S, Chandrasekaran.; L, Yao.; L, Deng.; C, Bowen.; Y, Zhang.; S, Chen.; Z, Lin.; F, Peng.; P, Zhang. Recent advances in metal sulfides: from controlled fabrication to electrocatalytic, photocatalytic and photoelectrochemical water splitting and beyond. *Chem. Soc. Rev*. **2019**, *48*, 4178-4280.

[39] Yu, X. Y.; Lou, X. W. D. Mixed Metal Sulfides for Electrochemical Energy Storage and Conversion. *Adv. Energy Mater*. **2018**, *8*, 1701592.

[40] Fu, G.; Lee, J. M. Ternary metal sulfides for electrocatalytic energy Conversion. *J. Mater. Chem. A* **2019**, *7*, 9386-9405.

[41] Shen, M.; Ruan, C.; Chen, Y.; Jiang, C.; Ai, K.; Lu. L. Covalent Entrapment of Cobalt−Iron Sulfides in N‑Doped Mesoporous Carbon: Extraordinary Bifunctional Electrocatalysts for Oxygen Reduction and Evolution Reactions. *ACS Appl. Mater. Interfaces* **2015**, *7*, 1207−1218.

[42] Mani, S.; Ramaraj, S.; Chen, S. M.; Dinesh, B.; Chen, T. W. Two-dimensional metal chalcogenides analogous $NiSe_2$ nanosheets and its efficient electrocatalytic performance towards glucose sensing. *J. Colloid Interface Sci*. **2017**, *507*, 378-385.

[43] Zheng, Y-R.; Gao, M-R. Gao, Q.; Li, H-H.; Xu, J.; Wu, Z-Y.; Yu. S-H.; An Efficient CeO_2/$CoSe_2$ Nanobelt Composite for Electrochemical Water Oxidation. *Small* **2015**, *11*, 182-188.

[44] Toh, R. J.; Martinez, C. C. M.; Sofer, Z.; Pumera, M. $MoSe_2$ Nanolabels for Electrochemical Immunoassays. *Anal. Chem*. **2016**, *88*, 12204-12209.

[45] Mi, L.; Sun, H.; Ding, Q. Chen, W.; Liu, C.; Hou, H.; Zheng, Z.; Shen, C. 3D hierarchically patterned tubular NiSe with nano-/microstructures for Li ion battery design. *Dalton Trans*. **2012**, *41*, 12595.

[46] Xu, R.; Wu, R.; Shi, Y.; J. Zhang, Zhang, B. Ni_3Se_2 nanoforest/Ni foam as a hydrophilic, metallic, and self-supported bifunctional electrocatalyst for both H_2 and O_2 generations. *nano energy* **2016**, *24*, 103-110.

[47] Eftekhari, A. Molybdenum diselenide ($MoSe_2$) for energy storage, catalysis, and optoelectronics. *Appl. Mater. Today* **2017**, *8*, 1-17.

[48] Tan, S. M.; Sofer, Z.; Luxa, J.; Pumera, M. Aromatic-Exfoliated Transition Metal Dichalcogenides: Implications for Inherent Electrochemistry and Hydrogen Evolution. *ACS Catal*. **2016**, *6*, 4594-4607.

[49] Bo, Z.; Mao, S.; Han, Z. J.; Cen, K.; Chen, J.; Ostrikov, K. Emerging energy and environmental applications of vertically oriented graphenes. *Chem. Soc. Rev*. **2015**, *44*, 2108-2121.

[50] Gilic, M.; Petrovic, M.; Cirkovic, J.; Paunovic, N.; SavicSevic, S.; Nikitovic, Ž.; Romcevic, M.; Yahia, I.; Romcevic, N. Low-temperature photoluminescence of $CuSe_2$ nano objects in selenium thin films. *Processing and Application of Ceramics* **2017**, *11*, 127-135.

[51] Qiao, L. N.; Wang, H. C.; Shen, Y.; Lin, Y. H.; Nan, C. W. Enhanced Photocatalytic Performance under Visible and Near-Infrared Irradiation of $Cu_{1.8}Se/Cu_3Se_2$ Composite via a Phase Junction. *Nanomaterials* **2017**, *7*, 19.

[52] Xiao, H.; Wang, S.; Wang, C.; Li, Y.; Zhang, H.; Wang, Z.; Zhou, Y.; An, C.; Zhang, J. Lamellar structured $CoSe_2$ nanosheets directly arrayed on Ti plate as an efficient electrochemical catalyst for hydrogen evolution. *Electrochim. Acta* **2016**, *217*, 156-162.

[53] Zhao, F.; Shen, S.; Cheng, L.; Ma, L.; Zhou, J.; Ye, H.; Han, N.; Wu, T.; Li, Y.; Lu, J. Improved Sodium-Ion Storage Performance of Ultrasmall Iron Selenide Nanoparticles. *Nano Lett*. **2017**, *17*, 4137-4142.

[54] Sakthivel, M.; Ramaraja, S.; Chena, S-M.; Dinesh, B.; Rama-samy, H. V.; Lee, Y.S. Entrapment of bimetallic $CoFeSe_2$ nanosphere in functionalized carbon nanofiber for

selective and sensitive electrochemical detection of caffeic acid in wine samples. *Analytica Chimica Acta* **2018**, *1006*, 22-32.

[55] Jiang, Y.; Qian, X.; Niu, Y.; Shao, L.; Zhu, C.; Hou, L. Cobalt iron selenide/sulfide porous nanocubes as high-performance electrocatalysts for efficient dye-sensitized solar cells. *J. Power Sources* **2017**, *369*, 35-41.

[56] Pandit, M. A.; Billakanti, S.; Muralidharan, K. A simplistic approach for the synthesis of CuS-CdS heterostructure: A Novel photo catalyst for oxidative dye degradation. *J. Environ. Chem. Eng*. **2020**, *8*, 103542.

[57] Chiou, J. R.; Lai, B. H.; Hsu, K. C.; Chen, D. H. One-pot green synthesis of silver/iron oxide composite nanoparticles for 4-nitrophenol reduction. *J. Hazard. Mater*. **2013**, *248*, 394-400.

[58] Pandit, M. A.; Kumar, D. S. H.; Billakanti, S.; Ramadoss, M.; Muralidharan, K. Chalcopyrite with Magnetic and Dielectric Properties: An Introductory Catalyst for 4‑Nitrophenol Reduction. *J. Phys. Chem. C* **2020**, *124*, 18010−18019.

[59] Srinivas, B.; Pandit, M. A.; Muralidharan, K. Importance of Clean Surfaces on the Catalyst: SnS_2 Nanorings for Environmental Remediation. *ACS Omega* **2019**, *4*, 14970-14980.

[60] Manigandan, R.; Dhanasekaran, T.; Padmanaban, A.; Giribabu, K.; Suresh, R.; Narayanan, V. Bifunctional hexagonal Ni/NiO nanostructures: influence of the core–shell phase on magnetism, electrochemical sensing of serotonin, and catalytic reduction of 4-nitrophenol. *Nanoscale Adv*. **2019**, *1*, 1531-1540.

[61] Zhang, Z.; Shao, C.; Li, X.; Sun, Y.; Zhang, M.; Mu, J.; Zhang, P.; Guo, Z.; Liu, Y. Hierarchical assembly of ultrathin hexagonal SnS_2 nanosheets onto electrospun TiO_2 nanofibers: enhanced photocatalytic activity based on photoinduced interfacial charge transfer. *Nanoscale* **2013**, *5*, 606−618.

[62] Billakanti, S.; Krishnamurthi, M. Facile preparation of surfactant or support material free CdS nanoparticles with enhanced photocatalytic activity. *J. Environ. Chem. Eng*. **2018**, *6*, 1250−1256.

[63] Padhi, D. K.; Parida, K. Facile fabrication of a-FeOOH nanorod/RGO composite: a robust photo catalyst for reduction of Cr(VI) under visible light irradiation. *J. Mater. Chem. A* **2014**, *2*, 10300–10312.

CHAPTER 6

Summary and Conclusions

Most of the reports dated till now about the synthesis of nanomaterials have involved surfactants in the reactions. Further, the majority of them are multistep reactions and time-consuming. The surfactants usually played the role of controlling morphology, preventing the agglomeration of nanoparticles by forming micelles around the nanoparticles. However, the very explicit role of surfactants for shaping nanomaterial's morphology has a disadvantage of reducing the catalytic activity. The disadvantage is because the presence of surfactants blocks the active sites of catalysts and produces a barrier to substrates reaching to catalysts surface. So the present work portrayed here is wholly and solely surfactants-free synthesis and a single-step procedure. The method described here to synthesize various nanomaterials is a simple wet chemical approach involving hexamethyldisilazane (HMDS) as an initiator for reaction, a reagent, stabilizer, and reducing agent.

Our research group established the HMDS-assisted approach to synthesize various categories of simple and complex nanomaterials. Using this novel approach, we could synthesize various forms of nanomaterials ranging from binary to ternary to composites of metal chalcogenides. We succeeded in synthesizing SnS_2 nanostructures (with and without surfactants), CuS@CdS heterojunctions, $CuFeS_2$ NPs, and $Co_{0.8}Fe_{0.2}L_2$ (L = S, Se) nanoparticles, as already discussed in their respective chapters. These chalcogenides were synthesized without using an external surfactant as HMDS performed the sole purpose and under inert conditions.

In the first study, two types of SnS_2 nanomaterials were synthesized, with (peg-SnS_2NF) and without (sf-SnS_2NR) the involvement of the organic template and the compared their catalytic activities. The synthesis of these materials was achieved in a single-step procedure aided by hexamethyldisilazane (HMDS). These nanoparticles were subjected to X-ray diffraction, transmission electron microscopy, scanning electron microscopy, Raman spectroscopy, and UV−vis spectroscopy analyses to investigate their structural, topographical, surface, and optical properties. The present work suggests that

the surfactant-free SnS_2 nanoring (sf-SnS_2NR) catalyst had lower surface area compared to the poly(ethylene glycol)-stabilized SnS_2 nanoflower (peg-SnS_2NF) catalyst but showed high activity under visible light for the photoreduction of Cr(VI) and the photocatalytic degradation of organic dyes (MO and Rh B). The work exposed the importance of the clean surfaces on the catalyst and is expected to have a high impact on the photocatalytic activity of the SnS_2 nanomaterial. The study also endorses the utility of the HMDS-assisted synthetic method for the production of multifunctional semiconductor tin disulfide nanomaterials with multiple potential applications. The excellent photocatalytic behavior of SnS_2 can be credited to the following factors. (i) The clean surfaces on the catalyst enhanced electron mobility in the nanorings. (ii) The specific 2D morphology of the ring structure also contributed to the efficient charge carrier separation in the material.

In order to improve the catalytic activities of semiconductor nanostructures a heterojunction was formed besides the involvement of surfactant free synthesis. Direct synthesis of CuS-CdS based mesoporous composite materials and determination of their photocatalytic activity was achieved successfully through wet chemical one-pot hexamethyldisilazane (HMDS) assisted synthetic method. In this study, a series of CuS microflowers (mf) decorated with varying amounts of CdS nanoparticles (NP) have been synthesized successfully in a controlled manner. Relatively easy synthesis of material along with its surfactant-free clean surfaced heterojunction accentuates the reliability of the protocol described here. Full characterization of these semiconducting materials was accomplished with a series of analytical techniques, which include powder X-ray diffraction (PXRD), scanning electron microscopy (SEM), tunnelling electron microscopy (TEM), X-ray photoelectron spectroscopy (XPS), UV–vis, IR, BET and lifetime studies. Upon varying the concentration of precursor of Cd in the reactions, the resulting materials exhibited a well-demarcated change in morphologies ranging from undifferentiated mass to well-differentiated flower-like architectures. The thoroughly characterized composite was accessed finally for their potential photocatalytic activity for the degradation of organic dyes. The results showed 96.0% degradation of rhodamine B (Rh B) over 10 min and 94.7% degradation of methylene blue (MB) over 9 min. This observed rate of degradation was much higher compared to that observed in the case of

pure CuS (62.0% of Rh B and 50.2% of MB). Photoluminescence studies also revealed the superior photocatalytic ability of CSD-1. The recyclability tests revealed a long life span of photocatalysts.

For the first time, the synthesis of surfactant-free ternary chalcogenide-chalcopyrite, sf-$CuFeS_2$, by a wet-chemical one-pot hexamethyldisilazane-assisted synthetic method was accomplished. Various analytical and spectroscopic techniques were used for the physical characterization of the material produced. From the observation of magnetic properties, the material chalcopyrite was found to be paramagnetic. The dielectric constant and dielectric loss were also determined and were found to be decreasing with an increase in frequency. The dielectric behavior of the material was explained by the Maxwell−Wagner theory of polarization, and the dielectric constant of the as-synthesized sample was found to be 3.176 at 100 °C and 500 kHz. The potential catalytic activity was confirmed by performing the reduction of 4-nitrophenol (4-NP) to 4-amino phenol (4-AP) in the presence of sodium borohydride ($NaBH_4$) in aqueous medium at room temperature. The catalyst showed about 90% yield in the reduction reactions, which can be attributed to easy access to active sites invigorated by the absence of surfactant molecules. The reusability of the catalyst was checked to find out the stability, and excellent retention of activity up to five cycles was observed.

We have used the hexamethyldisilazane (HMDS) - assisted method constructively to synthesize a novel ternary cobalt and iron based metal chalcogenide $Co_{0.8}Fe_{0.2}L_2$ (L=S, Se) [$Co_{0.8}Fe_{0.2}S_2$ and $Co_{0.8}Fe_{0.2}Se_2$]. These materials behaved as a bifunctional catalyst for both electrochemical OER and photocatalysis for the reduction of Cr(VI). The materials showed good electrochemical water splitting properties for OER performance (345 and 350 mV @η_{10}, 52.4, and 84.5 mV/dec respectively for the Tafel values of $Co_{0.8}Fe_{0.2}Se_2$ and $Co_{0.8}Fe_{0.2}S_2$). Besides electrochemical water splitting, these materials were tested for the photocatalytic reduction of toxic Cr(VI) to Cr(III) on exposure to sunlight irradiations. As photocatalysts, $Co_{0.8}Fe_{0.2}S_2$ and $Co_{0.8}Fe_{0.2}Se_2$ could convert about 96% and 91% of Cr(IV) to Cr(III). While their recyclability tests, both the catalysts presented balanced electro catalysis activities for 1500 CV cycles and

photocatalysis of 5 cycles. This observation is an important criterion governing their usage for large scale applications.

The HMDS-assisted synthetic approach was good enough to produce nanomaterials in a single step compared to complex or multistep methods reported in various literatures. This method yielded high-phase purity materials, which were well crystalline nature, and reasonable control on morphology. However, the nanoparticles synthesized using this method were sparingly soluble in organic media. Interestingly, the heterogeneous catalysts synthesized by the HMDS-assisted approach have shown superior catalytic performances in different areas than the same materials produced by the reported. In this regard, the present work provides new insight into developing photocatalysts with clean surfaces for the effective charge separation and photocatalytic remediation of pollutants from wastewater.

List of Publications

Publications from Thesis

1. Billakanti Srinivas, **Manzoor Ahmad Pandit**, and Krishnamurthi Muralidharan. "Importance of Clean Surfaces on the Catalyst: SnS_2 Nanorings for Environmental Remediation". ***ACS Omega*** 2019, 4, 14970−14980.
2. **Manzoor Ahmad Pandit**, Srinivas Billakanti, Krishnamurthi Muralidharan. "A simplistic approach for the synthesis of CuS-CdS heterostructure: A novel photo catalyst for oxidative dye degradation". ***Journal of Environmental Chemical Engineering*** 8, (2020), 103542.
3. **Manzoor Ahmad Pandit**, Dasari Sai Hemanth Kumar, Srinivas Billakanti, Manigandan Ramadoss and Krishnamurthi Muralidharan. "Chalcopyrite with Magnetic and Dielectric Properties: An introductory catalyst for 4-Nitrophenol reduction". ***J. Phys. Chem. C*** 2020, 124**,** 18010−18019.
4. **Manzoor Ahmad Pandit**, Dasari Sai Hemanth Kumar, Manigandan Ramadoss and Krishnamurthi Muralidharan. "Boosting the Bifunctional Catalytic Role of Cobalt Iron Chalcogenide- $Co_{0.8}Fe_{0.2}L_2$ (L = S and Se) as an Electrochemical OER Performer and a Photocatalyst for Cr(VI) Reduction" (Manuscript communicated).

Other Publications

5. **Manzoor Ahmad Pandit**, Dasari Sai Hemanth Kumar, Mohan Varkola, Satyanarayana Moru, and Krishnamurthi Muralidharan. Base tunable morphology dependent electrochemical hydrogen evolution performances of ternary chalcogenide-Cu_3BiS_3 synthesized by hydrothermal method (Manuscript under preparation).
6. **Manzoor Ahmad Pandit**, Dasari Sai Hemanth Kumar and Krishnamurthi Muralidharan. Single step deposition of CuS nanoparticles on ultrathin g-C_3N_4 nanosheets as a novel composite photocatalyst for Bisphenol A oxidation. (Manuscript under preparation).

7. **Manzoor Ahmad Pandit**, Dasari Sai Hemanth Kumar and Krishnamurthi Muralidharan. One-pot hexamethyldisilazane assisted synthesis of Ppy/$NiCo_2S_4$ heterostructures as a superior electrode for electrocatalytic OER performances (Manuscript under prepration).
8. Dasari Sai Hemanth Kumar, **Manzoor Ahmad Pandit** and Krishnamurthi Muralidharan. Magnetic properties tuning of nickel ferrites by doping with Co and Mn synthesized by hydrothermal method and there charge-discharge properties (manuscript under preparation).
9. Dasari Sai Hemanth Kumar, **Manzoor Ahmad Pandit**, Dolly Ramakrishna and Krishnamurthi Muralidharan. Microflower deposition of ZnS on g-C_3N_4 nanosheets by one-pot method and their photocatalytic activitiy. (Manuscript under preparation).

Poster and Oral Presentations

1. Presented a poster entitled **"Synthesis of Template Free Pervoskites Materials for Photovoltaic Applications"** at 8th International Collaborative and Cooperative Chemistry Symposium (ICCCS-8) organized by School of Chemistry, University of Hyderabad, held on December 18-19, 2017.

2. Presented a poster entitled **"The hexamethyldisilazane (HMDS) assisted synthesis of pervoskites materials for photovoltaic applications"** at National Symposium on Convergence of Chemistry and Materials held at BITS Pilani, Hyderabad on 21-22 December, 2017.

3. Presented a poster entitled **"One pot HMDS-assisted synthesis of CdS decorated CuS microflowers for photocatalytic activity"** in Chem Fest-2018 organised by School of Chemistry, University of Hyderabad, from March 9-10, 2018.

4. Presented a poster entitled **"One pot wet chemical method for the synthesis of CdS decorated CuS microflowers for photocatalytic degradation of organic contaminants"** in ICMST organized by Indian Institute of Space Science and Technology jointly with Materials Research Society of India, Thiruvananthapuram, Kerala, held in October 10-13, 2018.

5. Presented a poster entitled **"Synthesis of CdS decorated CuS hierarachical architectures by wet chemical method for photocatalytic degradation of organic contaminants"** in 5th International Conference on Nanoscience and Nanotechnology (ICONN 2019) organized by SRM Institute of Science and Technology, Chennai, 28-30 January 2019.

6. Delivered an oral talk and presented a poster entitled **"A simplistic approach for the synthesis of CuS-CdS heterostructure: A novel photo catalyst for oxidative dye degradation"** in Chem Fest-2019 held by School of Chemistry, University of Hyderabad, from 22-23 February, 2019.

7. Presented a poster entitled **"Importance of Clean Surfaces on the Catalyst: SnS_2 Nanorings for environmental remediation"** at International Conference on Advanced Materials (ICAM-2019) organized by Centre for Nano science and Nanotechnology, Jamia Millia Islamia, New Delhi, held on 6-7 March 2019.

8. Presented a poster entitled **"Chalcopyrite: An Introductory Catalyst for 4-Nitrophenol Reduction, With Magnetic and Dielectric Properties"** at national conference on advanced functional materials organized by Department of Chemistry, Jamia Millia Islamia, New Delhi, held on 19-21 november 2019.

ACS OMEGA

Article

Cite This: ACS Omega 2019, 4, 14970−14980

http://pubs.acs.org/journal/acsodf

Importance of Clean Surfaces on the Catalyst: SnS_2 Nanorings for Environmental Remediation

Billakanti Srinivas, Manzoor Ahmad Pandit, and Krishnamurthi Muralidharan*

School of Chemistry, University of Hyderabad, Hyderabad 500046, India

Supporting Information

ABSTRACT: The focus of the work is the synthesis of SnS_2 nanomaterials with (**peg-SnS_2NF**) and without (**sf-SnS_2NR**) the involvement of the organic template and the comparative study of their catalytic activities. The synthesis of these materials was achieved in a single-step procedure aided by hexamethyldisilazane (HMDS). These nanoparticles were subjected to X-ray diffraction, transmission electron microscopy, scanning electron microscopy, Raman spectroscopy, and UV−vis spectroscopy analyses to investigate their structural, topographical, surface, and optical properties. The present work suggests that the surfactant-free SnS_2 nanoring (**sf-SnS_2NR**) catalyst has lower surface area compared to the poly(ethylene glycol)-stabilized SnS_2 nanoflower (**peg-SnS_2NF**) catalyst but shows high activity under visible light for the photoreduction of Cr(VI) and the photocatalytic degradation of organic dyes. The work exposed the importance of the clean surfaces on the catalyst and is expected to have a high impact on the photocatalytic activity of the SnS_2 nanomaterial. The study also endorses the utility of the HMDS-assisted synthetic method for the production of multifunctional semiconductor tin disulfide nanomaterials with multiple potential applications.

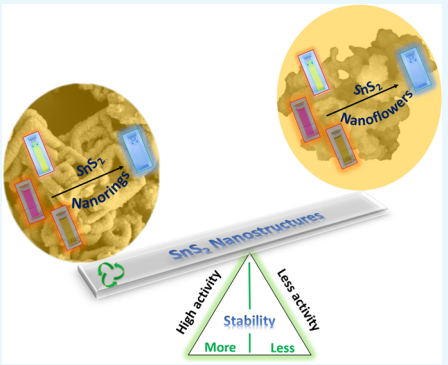

INTRODUCTION

The scientific community is always working for the development of an efficient and economical method for the elimination of pollutants such as organic dye molecules and heavy metal ions from aqueous solutions.[1] Among the heavy metal ions, especially, hexavalent chromium compounds Cr(VI) are highly lethal, carcinogenic, and pollutants found recurrently in wastewater from industrial processes.[2−4] The semiconductor-based photocatalytic reduction of Cr(VI) and disintegration of organic pollutants have gained importance due to its remarkable advantages, such as direct use of clean and safe solar energy, reusability, and low cost.[5−8] The multifunctional materials possessing more than one property are more attractive for potent technological applications.[9]

Among the semiconducting metal sulfides, tin disulfide (SnS_2) can harvest visible light, which makes them promising sensitizers for wide band gap semiconductors and photocatalysts.[10] Until now, numerous morphologies of SnS_2 nanostructures, such as fullerene-like nanoparticles,[11] nanobelts,[12] nanosheets,[13] and nanoflakes,[14] have been produced successfully. Synthesis of these materials was achieved by adopting various methods such as laser ablation,[15] template-assisted solvothermal processes,[12] coevaporation,[16] and the sol−gel synthetic route.[17] However, almost all these materials were covered by either organic surfactant molecules or other inorganic materials. Such a covering of the surfaces precludes any interaction that supposed to happen on their surfaces and thus leading to the reduced catalytic activity compared to the potential expected from the materials. There are efforts to increase the activity and performance of the SnS_2 catalyst by modifying their properties with dopants and by making nanocomposites.[10b−h] However, there are no reports on synthesizing and using SnS_2 nanomaterials with unhindered free surfaces.

Herein, we report the synthesis of surfactant-free SnS_2 nanorings (**sf-SnS_2NR**) having free surfaces by adopting a modified HMDS-assisted chemical synthetic procedure. The systematic studies on the effect and importance of the clean surface on the catalyst and morphology-controlled synthesis of SnS_2 at nanolevel are also being performed. The unique multifunctional ability of the tin sulfide nanorings as photocatalysts in both removals of organic dyes, rhodamine B (RhB) and methyl orange (MO), and the reduction of the polluting inorganic system like Cr(VI) are explored. We have also produced SnS_2 nanoflowers (**peg-SnS_2NF**) with the poly(ethylene glycol) (PEG) template, carried out a comparative study, and explained the superiority of **sf-SnS_2NR** over **peg-SnS_2NF** toward the reduction of Cr(VI) and degradation of organic dye molecules.

RESULTS AND DISCUSSION

Synthesis, Characterization, and Morphological Analysis. For the present study, we have synthesized SnS_2 nanostructures without any organic surfactant molecules

Received: June 14, 2019
Accepted: August 21, 2019
Published: September 4, 2019

Scheme 1. Schematic Illustration of Synthesis of sf-SnS_2 NR and peg-SnS_2 NF

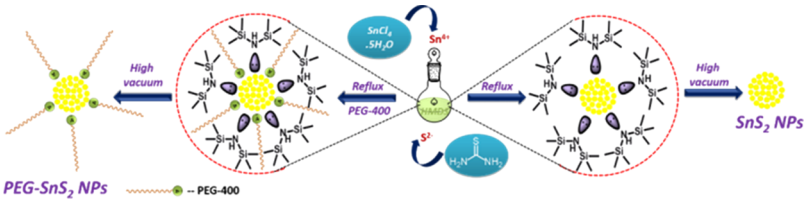

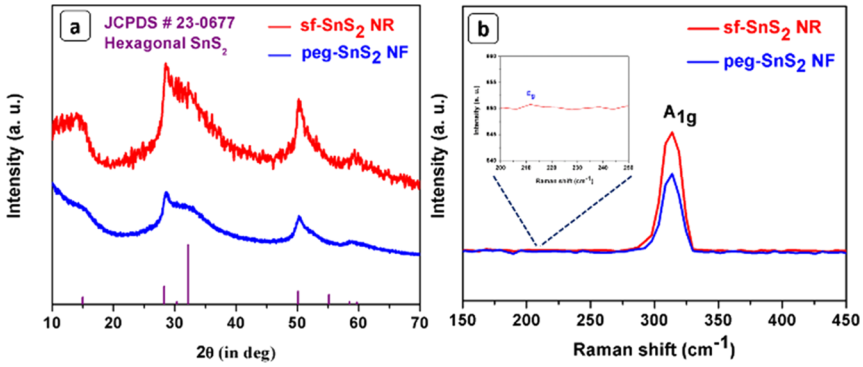

Figure 1. Primary characterization of SnS_2 nanocatalyst. (a) XRD pattern of **sf-SnS_2NR** and **peg-SnS_2NF**. (Hexagonal SnS_2 (JCPDS no. 23-0677)). (b) Raman spectroscopy of the SnS_2 nanostructures.

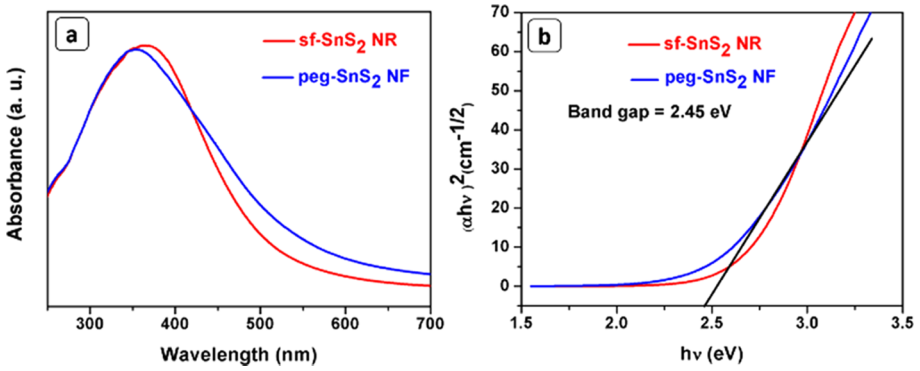

Figure 2. Optical study of SnS_2 nanostructures. (a) UV−vis DRS spectra of **sf-SnS_2NR** and **peg-SnS_2NF** samples. (b) Band gap calculations of the SnS_2 nanostructures.

covering their surfaces as well as the particles with a known amount of polymer (PEG) covering the surfaces of the particles. Simple reactants/reagents were used to synthesize these materials by single-step procedures to minimize residuals and impurities (Scheme 1). The hexamethyldisilazane (HMDS)-assisted method yielded **sf-SnS_2NR** where there were no surfactant molecules and yielded **peg-SnS_2NF** where PEG was used in the reaction. In these reactions, the role of HMDS was multiple since it acted as the solvent, reducing agent and also provided surroundings like the capping agent during the reaction. In the presence of metal sources and thiourea, HMDS led to the formation of a polymeric network by preventing the aggregation of the nanostructures. After completion of the reaction, by applying high vacuum, HMDS was removed, and finally, SnS_2 nanostructures were obtained. In these reactions, the HMDS molecules involved in the reaction but not a part of either source materials or the product, and therefore, the reaction was termed as the HMDS-assisted synthesis.

The typical X-ray diffraction patterns aided us to explore the structural properties of the as-synthesized SnS_2 nanostructures (Figure 1a). The peaks were indexed according to JCPDS data card no. 23-0677, and the corresponding peaks confirmed the formation of the hexagonal structure of SnS_2.[18] No impurities were identified in the XRD pattern demonstrating the phase purity of nanostructures. The samples were further investigated by Raman spectra (Figure 1b) for the signature of vibrational modes of the SnS_2 material. The spectra of both samples showed the strong characteristic peaks at 313.78 and 313.56 cm^{-1} for the **sf-SnS_2 NR** and **peg-SnS_2 NF** samples, respectively, which could be assigned to the A_{1g} mode of SnS_2.[19]

Figure 2a displays optical absorption by SnS_2 nanostructures within the UV and visible light spectra of wavelength ranging 250−700 nm. The absorption maximum of the materials was around 385 nm.[20] The broad spectrum in the visible region suggested that both the SnS_2 nanomaterials described here have the capability of harvesting visible light and hence can act as the photocatalyst while exposed to visible light. The band gap of both the SnS_2 nanostructures by the Tauc method was found to be around 2.50 eV predicting its ability to work as the photocatalyst on irradiation of visible light. The band gaps

DOI: 10.1021/acsomega.9b01766
ACS Omega 2019, 4, 14970−14980

determined from DRS spectra recorded both the nanorings and nanoflowers were 2.55 and 2.45 eV, respectively.[21]

The morphology of the resulting powdered sample from the reaction was analyzed by field emission scanning electron microscopy (FESEM) and transmission electron microscopy (TEM). The typical low-magnification FESEM image of the **sf-SnS_2** (Figure 3a and Figure S1) revealed clearly that the

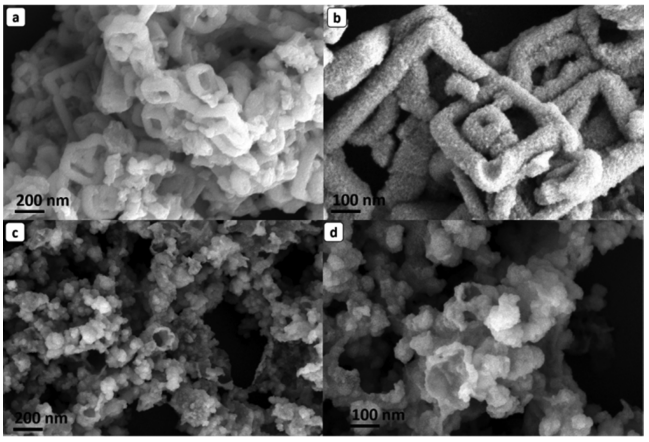

Figure 3. Morphological study of SnS_2 nanostructures. (a, b) FESEM micrographs of **sf-SnS_2NR**. (c, d) FESEM micrographs of **peg-SnS_2NF**.

sample has consisted of nanorings (**sf-SnS_2NR**) with an average diameter of 50 nm. Further, a high-magnification FESEM image was recorded (Figure 3b), which highlighted the ring pattern of the **sf-SnS_2**. The low- and high-magnification FESEM images of the as-synthesized **peg-SnS_2** (Figure 3c,d, and Figure S1) showed the nanoflower (**peg-SnS_2NF**) morphology with an average diameter of 100 nm. Even after the vigorous ultrasonic treatment, the hierarchical structures maintained their integrity showing the structural stability of the products.

Analysis by TEM also confirmed the formations of nanorings of the **sf-SnS_2** and nanoflowers of **peg-SnS_2** nanostructures (Figure 4 and Figure S3). A diffraction pattern (Figure 4c) consists of polycrystalline rings that can be indexed to the SnS_2 phase (standard diffraction file no. 23-0677). The

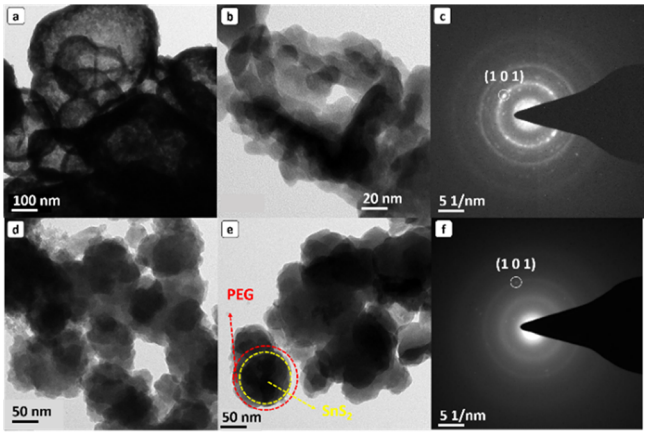

Figure 4. TEM data for the SnS_2 nanostructures: (a, b) **sf-SnS_2NR**, (d, e) **peg-SnS_2NF**, and (c, f) selected area diffraction pattern for both SnS_2 nanostructures.

rings were continuous and devoid of any separate bright spots indicating the crystalline nature of **sf-SnS_2NR**. A diffraction pattern (Figure 4f) for **peg-SnS_2NF** showed the amorphous ring pattern indicating that the PEG had indeed stabilized the **SnS_2NF**.

The X-ray photoelectron spectroscopy (XPS) was recorded to conclude the chemical composition and bonding configuration of the as-synthesized materials. The XPS spectrum (Figure 5) revealed the presence of Sn and S elements only,

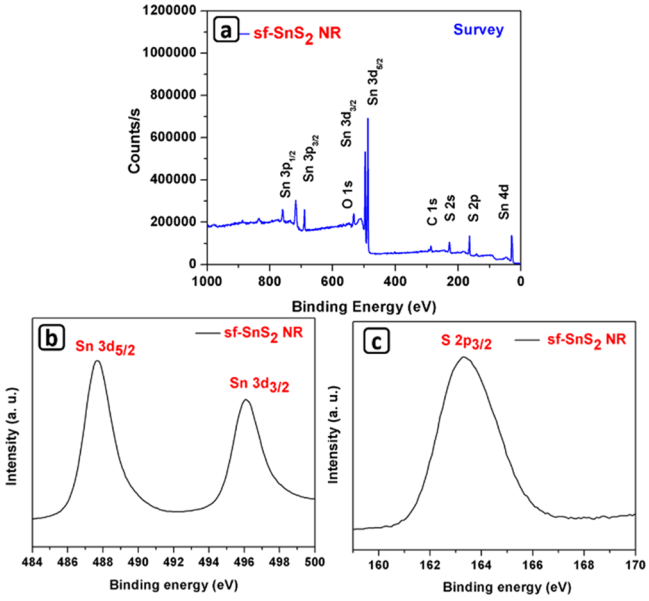

Figure 5. XPS spectrum of the as synthesized **sf-SnS_2NR** for the elements: (a) survey spectrum, (b) Sn 3d, and (c) S 2p.

and no other elements like N or Si were noticed. These findings showed that as-synthesized materials were free from the surfactant on the surfaces of the catalyst. The obtained results were in consistent with the XRD and EDS results. Characteristic high-resolution XPS spectra of Sn 3d and S 2p are shown in Figure 5b,c. The binding energies of Sn $3d_{5/2}$ (487.66 eV), Sn $3d_{3/2}$ (496.12 eV), and S $2p_{3/2}$ (163.30 eV) in SnS_2 nanostructures were in agreement with the reported characteristic values of Sn^{4+} and S^{2-} in SnS_2.[22]

The broad band peak at 545 cm^{-1} in the FTIR spectrum of **sf-SnS_2NR** was due to the vibration of Sn−S bands (Figure 6). The absence of any peak related to HMDS in the FTIR spectrum of Figure 6a confirmed the complete absence of the

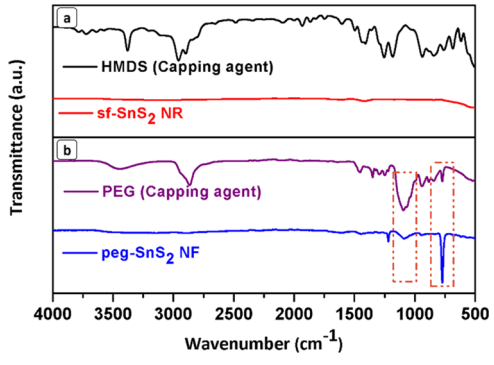

Figure 6. FTIR spectra of the as synthesized SnS_2 nanostructures: (a) **sf-SnS_2NR** and (b) **peg-SnS_2NF**.

DOI: 10.1021/acsomega.9b01766
ACS Omega 2019, 4, 14970−14980

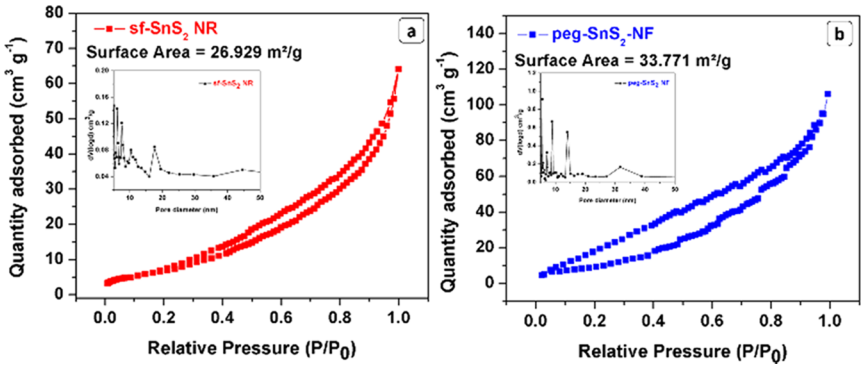

Figure 7. Nitrogen adsorption−desorption isotherm of the SnS_2 nanomaterial: (a) **sf-SnS_2NR** and (b) **peg-SnS_2NF**.

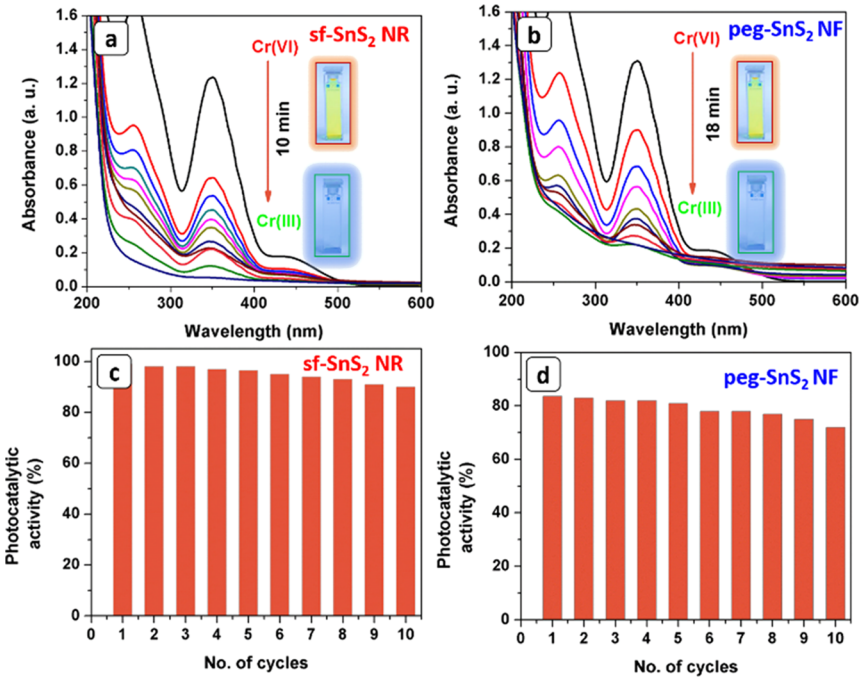

Figure 8. Photocatalytic reduction of Cr(VI) to Cr(III) using **SnS_2 Nanostructures** as the photocatalyst. (a, b) The absorption spectra showing a gradual decrease in the typical peak intensity at λ_{max} = 350 nm, by using **sf-SnS_2NR**, corroborating 99% reduction of Cr(VI) in 10 min and by using **peg-SnS_2NF**, 84% reduction of Cr(VI) in 18 min. (c, d) The recyclability of the SnS_2 nanostructures.

capping agent on the surfaces of SnS_2 nanorings.[23] The presence of the signature of PEG (Figure 6b) in the FTIR spectrum confirmed that PEG has effectively worked as a surfactant to stabilize **SnS_2NF**.

The photocatalytic application is mainly dependent on surface contact, and hence, the surface area of the materials is an essential factor. We have determined the surface area by the nitrogen adsorption−desorption isotherm for both the SnS_2 nanostructures (Figure 7). It was observed clearly that both the materials were mesoporous, and the BET surface areas for **sf-SnS_2NR** and **peg-SnS_2NF** were 26.33 and 33.60 m^2 g^{-1}, respectively. The surface area of the flower-like nanostructures was found to be higher than that of the ring-like nanostructure. This observation was quite the opposite of the catalytic activity performance (vide infra).

Photoreduction of Cr(VI) to Cr(III). The results displayed in Figure 8 elucidate the photocatalytic reduction of aqueous Cr(VI) (at pH 3) using **sf-SnS_2 NR** and **peg-SnS_2 NF** as catalysts under visible light irradiation. Few controlled reactions wherein (Figure S7) the direct photolysis (in the absence of catalyst) or catalysis (in the absence of light) alone could not drive the reduction of Cr(VI). Therefore, the reduction of aqueous Cr(VI) was the photocatalytically driven reaction completely rather than simple physical adsorption of Cr(VI). The formation of photoreduced product Cr(III) from the toxic Cr(VI) in all these reactions was confirmed by coordinating it with PDCA (Figure S8).[23]

In the presence of the **sf-SnS_2NR** catalyst, the toxic Cr(VI) reduction happened swiftly with a reaction rate of 0.244 min^{-1}, approached 99% reduction, and reached the equilibrium in 10 min. While in the case of **peg-SnS_2NF**, a reaction rate of 0.0982 min^{-1} was observed and approached only 84% reduction in 18 min. Hence, the **sf-SnS_2NR** acts as a more active photocatalyst for the reduction of Cr(VI) compared to photocatalysts in earlier reports (Table 1). Interestingly, in the case of catalytic decomposition of hydrogen peroxide, Zboril and co-workers also noticed high catalytic activity of iron(III) oxide nanoparticles having relatively lesser surface area.[24] All these results supported our assumption clearly on the

DOI: 10.1021/acsomega.9b01766
ACS Omega 2019, 4, 14970−14980

Table 1. Comparison Table of Numerous Catalysts with Various Dopant Materials for Cr(VI) Reduction

catalyst	Cr(VI) concentration	amount of catalyst (mg)	time (min)	ref
SnS_2	100 mL of 50 mg L^{-1}	100	120	26
SnS_2	50 mL of 50 mg L^{-1}	50	90	27
RGO-SnS_2	300 mL of 100 mg L^{-1}	200	120	28
MOSF-SnS_2	50 mL of 50 mg L^{-1}	50	100	29
CNF-SnS_2	50 mL of 50 mgL^{-1}	50	90	30
g-C_3N_4/SnS_2	100 mL of 50 mg L^{-1}	40	50	31
Ag_2S-SnS2	70 mL of 50 mg L^{-1}	70	60	32
SnO_2-SnS_2	80 mL of 2 $\times 10^{-4}$ M	20	180	33
SnS_2-TiO_2	80 mL of 100 mg L^{-1}	40	100	34
*sf-SnS_2 NR	60 mL of 100 mg L^{-1}	30	10	present work

importance of clean surfaces on catalysts rather than the larger surface area.

Effect of Amount of Catalyst and Pollutant Cr(VI). It was necessary to understand the catalyst loading parameters after the results above of stable and rapid photocatalytic activity of the **sf-SnS_2NR** toward the reduction of toxic Cr(VI). Therefore, the effect of the concentration of Cr(VI) and the amount of catalyst on the rate of the reaction were studied while keeping the other parameters constant. Figure 9 shows

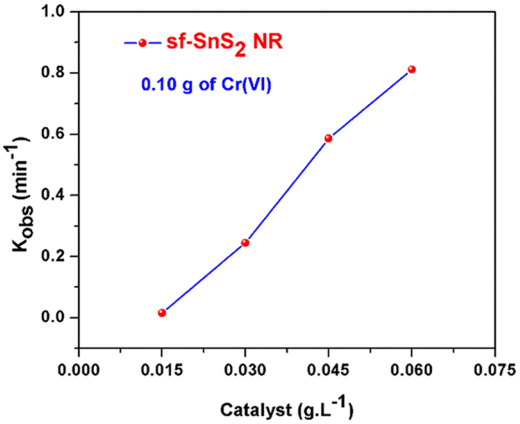

Figure 9. Influence of amount of catalyst on the photocatalytic reduction of toxic Cr(VI) to nontoxic Cr(III) using **sf-SnS_2NR** as the photocatalyst. Catalyst dosage had a linear relationship with the rate constant.

the reduction of Cr(VI) when the catalyst (**sf-SnS_2NR**) quantities were varied. The irradiation time required for the complete reduction of Cr(VI) decreased with increasing initial dosage of the SnS_2 photocatalyst. It was observed that k_{app} depends on the concentration of the Cr(VI) solution and the amount of catalyst added. When the amount (between 0.15 and 0.60 g L^{-1}) of **sf-SnS_2NR** catalyst was varied, there was an incremental change in the photocatalytic performance. The rate constant of the reduction reaction had the linear relationship (from 0.01507 to 0.81122 min^{-1}) with the amount of catalyst dosage. The increase of the efficiencies of Cr(VI) reduction with the increase of the initial amount of SnS_2 can be ascribed to the increase in both absorbed light and the numbers of surface active sites. These results suggested that the photocatalytic activity of **sf-SnS_2NR** could be improved by increasing the amount of catalyst.

Furthermore, Figure 10 depicts the effect of initial concentration of Cr(VI) aqueous solution on the photocatalytic reduction of Cr(VI) while keeping the catalyst dosage (**sf-SnS_2NR**) constant. It was clear that the efficiencies of reduction of Cr(VI) in photocatalytic systems consisting of 100 and 200 mg L^{-1} Cr(VI) were observed to be 99 and 81%, respectively. (Rate constants were 0.244 and 0.088 min^{-1}.) The decrease in the efficiencies of the reduction reaction with the increase of initial Cr(VI) concentration can be attributed to the following two aspects. First, since the reaction occurs on the surface of the photocatalyst, the limited surface active sites of the photocatalyst are not sufficient at higher Cr(VI) concentration. Second, Cr(VI) in a high concentration can absorb the visible light (420−480 nm), thus decreasing the proportion of light received by the SnS_2 photocatalyst.

Effect of pH on Cr(VI) Reduction. The effect of pH on the photocatalytic reduction of Cr(VI) in the presence of **sf-SnS_2NR** was examined by keeping the photocatalyst dosage constant and varying the initial pH from 3 to 5. It was noticed that the photocatalytic reduction of Cr(VI) was retarded with increased pH (Figure S4). There was a gradual decrease in the rate constant: 0.24475 min^{-1} at pH 3 and 0.09406 min^{-1} at pH 5. It was witnessed that the Cr(VI) reduction at low pH was much higher than that in a high pH condition. It was assumed that the increased dissolution of **sf-SnS_2NR** and along with lower concentration of H^+ in high pH was responsible for the decreased photocatalytic activity.

Stability and Reusability. The stability and reusability of any photocatalyst during the photocatalytic reaction are critical factors for its industrial usage. Therefore, it is necessary to study the stability of the as-synthesized **sf-SnS_2NR** in the photocatalytic reduction reactions involving aqueous Cr(VI). The recyclability of the catalyst for photocatalytic reduction of Cr(VI) is illustrated in Figure 8c. The performance of the **sf-SnS_2NR** photocatalyst did not show any significant loss up to 10 cycles. This revealed the durability of **sf-SnS_2NR** as the photocatalyst in the reduction of aqueous Cr(VI). While checking the reusability of both the SnS_2 nanostructures for 10 cycles, it was observed that there was only 5% efficiency loss for **sf-SnS_2NR**, whereas, in the case of **peg-SnS_2NF**, the efficiency loss was 5−10% (Figure 8c,d).

We have analyzed the catalyst after completion of the 10th cycle using SEM and EDX to identify the accumulation of Cr on the catalyst surface. There are no adsorbed chromium ions found over the catalyst surface (Figures S2 and S6). The XRD pattern of the materials was recorded after photocatalytic reduction, and no change in the XRD pattern occurs after the reduction process (Figure S5). It implies that the **sf-SnS_2NR** had high stability and did not corrode during the photocatalytic reduction of Cr(VI), which showed its potential applications for the treatment of polluted water.

Morphology Effect and the Importance of Clean Surface on the Catalyst. In the photocatalytic reduction of Cr(VI), the ring-like nanostructure was more efficient than nanoflower-like morphology (Figure 8). The rates of photocatalytic reduction of Cr(VI) by **sf-SnS_2NR** and **peg-SnS_2NF** were compared by varying the quantity of the catalysts (Figure

DOI: 10.1021/acsomega.9b01766
ACS Omega 2019, 4, 14970−14980

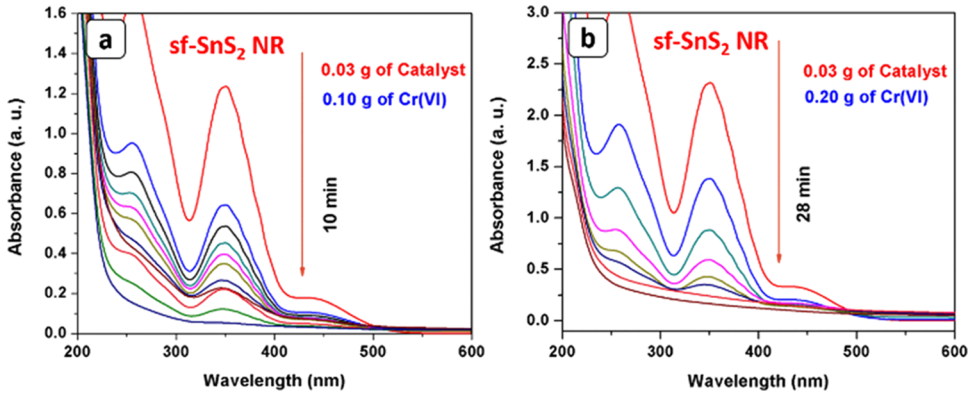

Figure 10. Influence of concentration of Cr(VI) (catalyst dosage constant, 0.03 g) on the photocatalytic reduction of toxic Cr(VI) to nontoxic Cr(III) using **sf-SnS_2NR** as the photocatalyst. (a) 0.10 g of Cr(VI) and (b) 0.20 g of Cr(VI). Concentration of Cr(VI) had an inverse relationship with the rate constants.

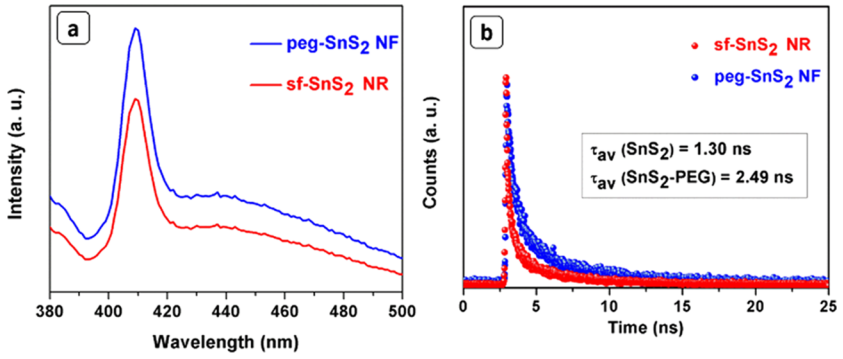

Figure 11. (a) Steady-state PL spectra of **sf-SnS_2NR** and **peg-SnS_2NF**. (b) Time-resolved transient PL decay of **sf-SnS_2NR** and **peg-SnS_2NF**.

9). In every case, the **sf-SnS_2NR** showed superior photocatalytic activity than the **peg-SnS_2NF**. The variance in the photocatalytic activity of both the SnS_2 nanomaterials may be explained by the collective action of several factors. Except the specific surface area, almost all the factors were the same as revealed by the various characterization techniques, and it can be said that the difference in photocatalytic activity of SnS_2 nanomaterials was influenced exclusively by a single parameter, that is, clean surfaces and morphology.

It is known that the adsorption and desorption of molecules on the surface of catalysts directly affect the photocatalytic process. Thus, the clean surfaces on the catalyst and relatively higher surface area of the porous **sf-SnS_2NR** allowed more number of surface coordination sites exposed to the solution than the **peg-SnS_2NF**. Moreover, the presence of clean surfaces on the catalyst surface helped more efficient transportation of the reactant molecules to the active sites and, thus, enhances the efficiency of photocatalysis. The low surface area and surfactant-free surfaces of the **sf-SnS_2NR** make nanorings a better material for the photocatalytic reduction of Cr(VI) compared to the PEG-coated nanoflower, that is, **peg-SnS_2NF**.

SnS_2 having a central metal ion with the d^{10} configuration favors the separation of photogenerated charges due to the highly dispersive conduction band. Afterward, the capture photoexcited electron at the conduction band takes place. In this process, the separated electron involves in the reduction of Cr(VI) to generate Cr(III).[34] As an evidence of the photoinduced interfacial charge transfer process, the photoluminescence (PL) and time-resolved photoluminescence (TRPL) of **sf-SnS_2NR** were recorded and compared with those of **peg-SnS_2NF** (Figure 11).

The **sf-SnS2 NR** showed a less intense PL peak compared to the **peg-SnS2 NF** (Figure 11a). This observation suggested that the interfacial charge transfer on **sf-SnS2 NR** inhibited the recombination of photoinduced charge carriers.[35] Afterward, the time-resolved transient photoluminescence decay (TRPL) spectrum was recorded to understand this process (Figure 11b). The average lifetime ($\langle\tau\rangle$) of **sf-SnS2 NR** (1.30 ns) was found to be less than that of **peg-SnS_2NF** (2.49 ns). This drop in the lifetime points to the effective carrier separation in clean surfaces of **sf-SnS_2NR**. When the transient photocurrent responses are studied, the **sf-SnS_2NR** showed a good response compared to the response of **peg-SnS_2NF** (Figure S9). This phenomenon occurs because of the smooth transfer of generated electrons from the conduction band (CB) to the valence band (VB) of **sf-SnS_2NR**, and this assumption was validated with the quenching of emission.

The clean surfaces remarkably enhanced the separation efficacy of photoinduced charge carriers on **sf-SnS_2 NR** through the photoinduced interfacial charge transfer Figure 9. In the photocatalysis progression, the photogenerated holes were trapped by the hydroxyl groups (or H_2O) on the surface to yield $OH^{\cdot}$ radicals. Meanwhile, the dissolved oxygen molecules react with electrons and yield superoxide radical anions, $O_2^{\cdot-}$, which on protonation generate the hydroperoxy, HO_2, radicals. This radical forms the hydroxyl radical $OH^{\cdot}$, which involves the decomposition of the organic dye. Altogether, the efficient charge separation on the clean surfaces affords the enhanced photocatalytic activities. Therefore, all

DOI: 10.1021/acsomega.9b01766
ACS Omega 2019, 4, 14970−14980

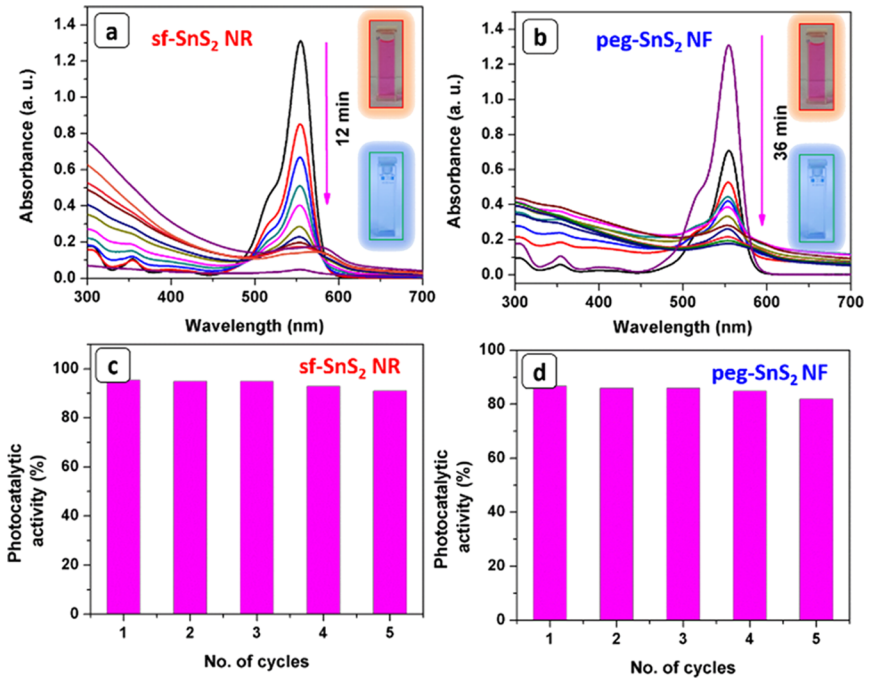

Figure 12. Photocatalytic activities of the SnS_2 nanostructures in the degradation of Rh B dye. (a, b) Photocatalytic reduction of Rh B using **sf-SnS_2NR** and **peg-SnS_2NF** as the photocatalyst. (c, d) The recyclability of the SnS_2 nanostructures.

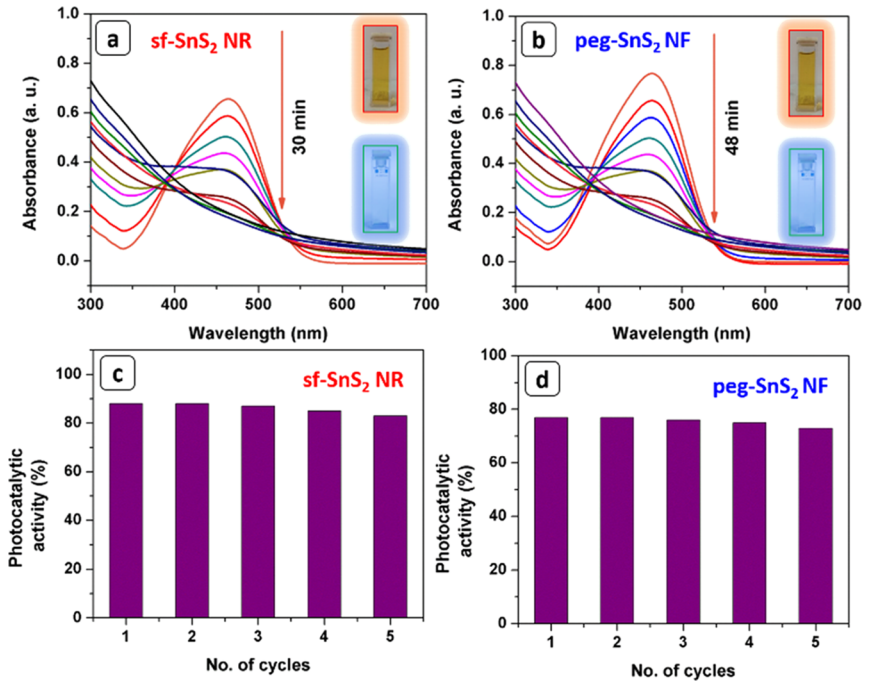

Figure 13. Photocatalytic activities of the SnS_2 nanostructures in the degradation of MO dye.(a, b) Photocatalytic reduction of MO using **sf-SnS_2NR** and **peg-SnS_2NF** as the photocatalyst. (c, d) The recyclability of the SnS_2 nanostructures.

these findings undoubtedly express the importance of clean surfaces on catalysts to achieve high catalytic performance.[36]

Photocatalytic Degradation of Dyes. Apart from toxic Cr(VI) reduction reactions, the photocatalytic activity of the synthesized **sf-SnS_2NR** was found to have practical application in the degradation of some water pollutants like organic dyes (RhB and MO). Figure 12 reveals the results of the degradation of RhB by visible light irradiation (sunlight) in the presence of the **sf-SnS_2NR**. In the controlled reactions, no reaction happened in the absence of light and SnS_2 catalyst samples, indicating the importance of the photocatalyst for the degradation of the dye (Figure S7). After addition of the photocatalyst, a rapid decrease in peak intensity was observed. The complete degradation of 60 mL of 5 mg L^{-1} RhB with 30 mg of **sf-SnS_2NR** was observed in only 12 min. The apparent rate constant (k_{app}) calculated from the linear plot of $\ln[A_t]/[A_0]$ versus time was found to be 0.1744 min^{-1}. While in the case of **peg-SnS_2NF**, it took nearly 36 min to degrade the dye,

DOI: 10.1021/acsomega.9b01766
ACS Omega 2019, 4, 14970−14980

and the rate constant (k_{app}) was calculated as 0.04695 min^{-1} (Figure 12a,b). The decrease in absorption intensity of RhB at λ_{max} with progression of the reaction time without any shift of the absorption wavelength suggested complete cleavage of the RhB chromophores.

The efficiency of the **sf-SnS_2NR** photocatalyst for the degradation of the MO dye was also tested (Figure 13). Exceptional efficiency was observed in the case of MO with a rate constant (calculated from the linear plot of $\ln[A_t]/[A_0]$ vs time) of 0.06752 min^{-1} and dye degradation time of 30 min for 60 mL of 5 mg L^{-1} MO dye with 30 mg of **sf-SnS_2NR** (Figure 13a,b). While in the case of **peg- SnS_2NF**, it took nearly 48 min to degrade the dye, and the apparent rate constant (k_{app}) was calculated as 0.03313 min^{-1}. In these cases, no noticeable degradation and no shift in peak positions were observed in the absence of the SnS_2 catalyst under the same experimental conditions. Hence, we found that the **sf-SnS_2NR** is the best photocatalyst for the photocatalytic reactions.

The mechanism of photoreduction of Cr(VI) and degradation of pollutants like RhB and MO is illustrated in Figure 14. Due to the narrow band gap, the **sf-SnS_2NR** can be

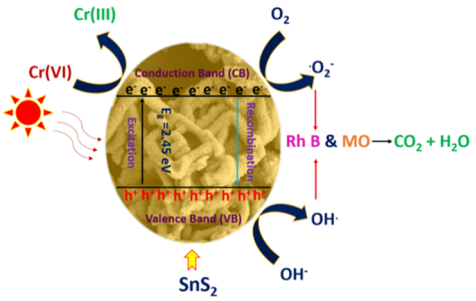

Figure 14. Schematic representation of mechanism of the SnS_2 photocatalyst.

excited by sunlight efficiently to produce electron−hole pairs. Due to the availability of free and clean surfaces on the catalyst, the generated charges will quickly be promoted to the excited state. Simultaneously, the recombination of electron−hole pairs was suppressed owing to the direct oxidization of pollutants.

The catalysts were reused in the water purification to determine the durability of the photocatalyst. For this purpose, the reaction mixture was centrifuged after each run of the reactions to separate the catalyst. Then, the regenerated catalyst was reused with the fresh reactants in the subsequent cycle of the photocatalytic reaction under the same experimental conditions. The results showed that the **sf-SnS_2NR** could be used repeatedly for at least 10 times without significant deactivation. However, the **peg-SnS_2NF** displayed a gradual decrease in dye degradation after five cycles. The **peg-SnS_2NF** was not robust since it contained big-sized SnS_2 nanoflowers that may perhaps be leached easily in the liquid phase reaction.

CONCLUSIONS

By the simple wet chemical approach, surfactant-free SnS_2 nanorings (**sf-SnS_2NR**) and PEG-stabilized SnS_2 nanoflowers (**peg-SnS_2NF**) were prepared at gram scale. The developed semiconductor tin disulfide nanomaterials showed multiple potential applications, especially in photoreduction and photodegradation. It was emphasized that as-synthesized SnS_2 nanostructures exhibited great photocatalytic activity in the reduction of carcinogenic Cr(VI) to nontoxic Cr(III) under ambient conditions. The SnS_2 nanostructures efficiently degraded mutagenic dyes (MO and RhB) to nontoxic products in a shorter period. The improved photoactivities are ascribed to the effective charge transfer across the clean surfaces of the catalyst, as evidenced by the electron microscopic analyses and steady-state and time-resolved transient photoluminescence decay studies. In all cases, the reusability of the **sf-SnS_2NR** photocatalyst was excellent over many cycles.

The excellent photocatalytic behavior of SnS_2 can be credited to the following factors. (i) The clean surfaces on the catalyst enhanced electron mobility in the nanorings. (ii) The specific 2D morphology of the ring structure also contributed to the efficient charge carrier separation in the material. Therefore, the present work provides new insight into developing photocatalysts with clean surfaces for the effective charge separation and photocatalytic remediation of pollutants from wastewater.

EXPERIMENTAL SECTION

Materials. Tin(IV) chloride ($SnCl_4{\cdot}5H_2O$, 99%), hexamethyldisilazane (HMDS, 99%), and thiourea (TU) (99%) were purchased from Sigma-Aldrich, USA. Potassium dichromate ($K_2Cr_2O_7$, 99%), RhB (99%), and MO (99%) were obtained from Merck, India. All chemicals were used without any further purification.

Instrumentation. XRD patterns of the products were collected at room temperature using a Bruker D8 X-ray diffractometer (XRD) with a scan rate of 1° min^{-1} in a 2θ range from 10° to 80° (Cu Kα = 1.54 Å; operating current = 30 mA; operating voltage = 40 kV). Surface morphology, particle size, and energy-dispersive spectroscopy (EDS) were studied using an Ultra 55 Carl Zeiss instrument (operating voltage = 10 kV). To do TEM measurements, the as-synthesized nanomaterials were suspended in isopropanol followed by sonication for 3 min and then dispersed on carbon-coated copper grids (200 mesh). Images were acquired using an FEI Technai G^2 20 STEM with a 200 kV acceleration voltage.

The Raman spectra were recorded using a Renishaw microscope at a wavelength of 632 nm. A JASCO 5300 spectrophotometer was used to record the Fourier transform infrared (FT-IR) spectra on the KBr pellet containing the samples. Solid-state UV−vis absorption spectra were recorded with a Shimadzu UV-3600 UV−vis spectrometer. UV−vis diffuse reflectance spectra of the as-synthesized SnS_2 materials were recorded and transformed into the absorption spectra using the Kubelka−Munk function. The direct band gaps of SnS_2 nanostructures were obtained from the Tauc plot (where n = 1/2). Solution-phase UV spectra during photocatalysis reactions were recorded using a JASCO-V770 UV−vis spectrophotometer. Surface area and pore size analyses were determined from the BET studies, and BET analysis was recorded by the Quantachrome Instruments.

Synthesis Section. *Synthesis of Surfactant Free-SnS_2 Nanorings (**sf-SnS_2 NR**).* Surfactant-free tin disulfide (**sf-SnS_2**) nanomaterials were prepared by a one-pot approach using standard Schlenk line techniques under an inert atmosphere. The typical procedure is as follows. The precursors of tin ($SnCl_4{\cdot}5H_2O$ = 0.200 g, 0.57 mmol) and sulfur (thiourea = 0.086 g, 1.14 mmol) were added in a 1:2 ratio and were mixed with excess hexamethyldisilazane

DOI: 10.1021/acsomega.9b01766
ACS Omega 2019, 4, 14970−14980

(HMDS) (5 mL, 23.85 mmol) in a 100 mL two-necked flask under a N_2 atmosphere (Table 2). The temperature was raised

Table 2. Reaction Conditions for the Synthesis of SnS_2 Diverse Nanoarchitectures

SL no.	amount of tin source (g)	amount of sulfur source (g)	amount of HMDS (mL)	amount of PEG (mL)	morphology
1	0.2	0.08	5	0	rings
2	0.2	0.08	5	10	flowers
3	0.2	0.08	0	0	no reaction

and refluxed for 3 h to complete the reaction. After cooling, the obtained yellow particles were collected by centrifugation and washed with abundant deionized water and methanol to remove unreacted starting materials. Finally, the product was dried under vacuum at 120 °C for 3 h before further analysis.

*Synthesis of PEG-SnS_2 Nanoflowers (**peg-SnS_2 NF**).* To prepare **peg-SnS_2NF**, we have followed the same experimental procedure as mentioned above. Additionally, poly(ethylene glycol) (PEG-400) (10 mL) was added to the reaction flask containing other reactants: tin and sulfur sources, (Table 2) and HMDS. After completion of the reaction, the resultant yellow powder was isolated and washed many times with deionized water (3 × 20 mL) followed by methanol (3 × 20 mL) repeatedly, separated by centrifugation, and dried at 120 °C for 3 h for analysis.

Photocatalytic Activity. *General Description of Photocatalytic Activity Test.* The photocatalytic activities of both **sf-SnS_2NR** and **peg-SnS_2NF** were assessed from the experiment of degradation/reduction of different pollutants. All of the photocatalytic tests were performed under standard conditions at room temperature with exposure to natural sunlight, which covered the entire wavelength distribution of the light in the visible region.

The photocatalyst (SnS_2 or peg-SnS_2; 30 mg) was added to 60 mL of either Rh-B (5 mg/L), MO (5 mg/L), or Cr(VI) (100 mg/L of pH 3) aqueous solution separately. Then, the reaction mixtures were stirred under dark for 1 h under the open environment at room temperature to ensure the formation of the adsorption−desorption equilibrium between the catalyst and reactants. Then, from the stock solution, 60 mL of suspension was positioned inside a beaker and irradiated with the sunlight. After regular intervals of time, 3 mL of a sample was taken and centrifuged at 3000 rpm to remove the catalyst. The concentrations of the reaction mixture in the supernatant solution were determined by recording absorption spectra. A gradual decrease in the characteristic absorption peak at 550 nm (Rh B), 450 nm (MO), and 350 nm (Cr(VI)) was noted, and each experiment was repeated twice.

The reduction and degradation efficiency was calculated by using the following eq 1:

$$\eta = (C_0 - C)/C_0 \times 100\% \quad (1)$$

The photocatalytic degradation rate of Cr(VI) and organic dyes followed the Langmuir−Hinshelwood eq 2

$$\ln(C_0/C) = k_{app}t \quad (2)$$

where k_{app} is the apparent rate constant of the pseudo-first order, t is the irradiation time, and C_0 and C are the initial and instant residual concentrations of the Cr(VI), Rh B, and MO solution. Reduction and degradation experiments were carried out on a recycled SnS_2 sample to study the stability of the SnS_2 photocatalyst.

Cr(VI) Reduction Test. The photocatalytic reaction was performed at room temperature. In a beaker, 30 mg of photocatalyst and 60 mL of 100 mg L^{-1} $K_2Cr_2O_7$ aqueous solution (pH = 3) were stirred for a sufficient amount of time to reach the adsorption−desorption equilibrium. Then, it was exposed to sunlight to initiate the reaction.

To confirm the photocatalytic reduction of Cr(VI), we have performed few controlled reactions by following our previous article.[23,25] The reduced product Cr(III) was confirmed by forming a metal complex with 2,6-pyridine dicarboxylic acid (PDCA). The controlled reactions were monitored by UV−vis spectra, and the results are displayed in Figure S8.

Degradation of Organic Dyes. The photocatalytic dye degradation experiments were performed by measuring the optical absorption of the organic pollutants. By determining the peak intensity of the dye against time in the presence of catalyst under visible light irradiation, the photocatalytic activity was studied. Thirty milligrams of **sf-SnS_2NR or peg-SnS_2NF** was utilized for the degradation of 60 mL of 5 mg L^{-1} solutions of RhB and MO, respectively.

Catalyst Reproducibility and Stability. Initially, the stability of synthesized SnS_2 nanostructures was checked by execution of XRD studies on the samples stored up to 1 month. All the photocatalytic experiments were repeated several times by varying the amounts of catalyst and concentrations of the substrates. The reduction of Cr(VI) and dye degradation were carried out up to 10 times with the recycled SnS_2 catalyst to check the stability of the catalyst and reproducibility of the obtained results. After completion of each cycle, the photocatalyst was recovered by centrifugation, washed with 1 M nitrite acid solution and deionized water to diminish the amount of Cr(III) deposited on the surface of the catalyst, and dried under vacuum at 60 °C for 4 h.

■ ASSOCIATED CONTENT

Supporting Information

The Supporting Information is available free of charge on the ACS Publications website at DOI: 10.1021/acsomega.9b01766.

XRD pattern, FESEM and TEM images, pH effect on dichromate reduction, photoreduction of dichromate, degradation of organic dyes in the absence of catalyst, and proof of Cr(III) formation (PDF)

■ AUTHOR INFORMATION

Corresponding Author

*E-mail: murali@uohyd.ac.in; murali@uohyd.ernet.in.

ORCID

Krishnamurthi Muralidharan: 0000-0003-0529-2447

Funding

DST-SERB of India funded the work through award no. SB/S1/IC-47/2013.

Notes

The authors declare no competing financial interest.

■ ACKNOWLEDGMENTS

The authors thank DST-SERB, India (project no. SB/S1/IC-47/2013) and UGC-CAS for funding. B.S. gratefully acknowledges the DST-SERB for Research Associate fellowship. We

DOI: 10.1021/acsomega.9b01766
ACS Omega 2019, 4, 14970−14980

thank Centre for Nanotechnology at the University of Hyderabad for providing the TEM facility.

REFERENCES

(1) Qu, J.; Fan, M. The current state of water quality and technology development for water pollution control in China. *Crit. Rev. Environ. Sci. Technol.* **2010**, *40*, 519−560.

(2) (a) Chen, C.; Ma, W.; Zhao, J. Semiconductor-mediated photodegradation of pollutants under visible-light irradiation. *Chem. Soc. Rev.* **2010**, *39*, 4206−4219. (b) Wittbrodt, P.-R.; Palmer, C.-D. Reduction of Cr(VI) in the Presence of Excess Soil Fulvic Acid. *Environ. Sci. Technol.* **1995**, *29*, 255−263.

(3) Wang, W.; Tadé, M. O.; Shao, Z. Research progress of perovskite materials in photocatalysis- and photovoltaics-related energy conversion and environmental treatment. *Chem. Soc. Rev.* **2015**, *44*, 5371−5408.

(4) Wang, Z.; Bush, R. T.; Sullivan, L. A.; Liu, J. Simultaneous Redox Conversion of Chromium(VI) and Arsenic(III) under Acidic Conditions. *Environ. Sci. Technol.* **2013**, *47*, 6486−6492.

(5) Nasrallah, N.; Kebir, M.; Koudri, Z.; Trari, M. Photocatalytic reduction of Cr(VI) on the novel hetero-system CuFe(2)O(4)/CdS. *J. Hazard. Mater.* **2011**, *185*, 1398−1404.

(6) Pawar, R. C.; Lee, C. S. Sensitization of CdS nanoparticles onto reduced graphene oxide (RGO) fabricated by chemical bath deposition method for effective removal of Cr(VI). *Mater. Chem. Phys.* **2013**, *141*, 686−693.

(7) Zhang, N.; Yang, M.-Q.; Tang, Z.-R.; Xu, Y.-J. CdS−graphene nanocomposites as visible light photocatalyst for redox reactions in water: A green route for selective transformation and environmental remediation. *J. Catal.* **2013**, *303*, 60−69.

(8) Liu, S.; Zhang, N.; Tang, Z.-R.; Xu, Y.-J. Synthesis of One-Dimensional CdS@TiO_2 Core−Shell Nanocomposites Photocatalyst for Selective Redox: The Dual Role of TiO_2 Shell. *ACS Appl. Mater. Interfaces* **2012**, *4*, 6378−6385.

(9) (a) Jana, S.; Srivastava, B. B.; Jana, S.; Bose, R.; Pradhan, N. Multifunctional Doped Semiconductor Nanocrystals. *J. Phys. Chem. Lett.* **2012**, *3*, 2535. (b) Xia, Q. N.; Cuan, Q.; Liu, X.-H.; Gong, X.-Q.; Lu, G.-Z.; Wang, Y.-Q. Pd/NbOPO4Multifunctional Catalyst for the Direct Production of Liquid Alkanes from Aldol Adducts of Furans. *Angew. Chem., Int. Ed.* **2014**, *53*, 9755. (c) Kumar, M.; Deka, S. Multiply Twinned AgNi Alloy Nanoparticles as Highly Active Catalyst for Multiple Reduction and Degradation Reactions. *ACS Appl. Mater. Interfaces* **2014**, *6*, 16071.

(10) (a) Lai, C. H.; Lu, M. Y.; Chen, L. J. Metal sulfide nanostructures: synthesis, properties and applications in energy conversion and storage. *J. Mater. Chem.* **2012**, *22*, 19−30. (b) Zhang, Y. C.; Du, Z. N.; Li, K. W.; Zhang, M. Size-controlled hydrothermal synthesis of SnS_2 nanoparticles with high performance in visible light-driven photocatalytic degradation of aqueous methyl orange. *Sep. Purif. Technol.* **2011**, *81*, 101−107. (c) Wei, H.; Hou, C.; Zhang, Y.; Nan, Z. Scalable low temperature in air solid phase synthesis of porous flower-like hierarchical nanostructure SnS_2 with superior performance in the adsorption and photocatalytic reduction of aqueous Cr(VI). *Sep. Purif. Technol.* **2017**, *189*, 153−161. (d) Wang, S.; Peng, T.; Zhang, Y. NH_4Cl-assisted in air, low temperature synthesis of SnS_2 nanoflakes with high visible-light-activated photocatalytic activity. *Mater. Lett.* **2019**, *234*, 361−363. (e) Zhang, Y. C.; Yao, L.; Zhang, G.; Dionysiou, D. D.; Li, J.; Du, X. One-step hydrothermal synthesis of high-performance visible-light-driven SnS_2/SnO_2 nanoheterojunction photocatalyst for the reduction of aqueous Cr(VI). *Appl. Catal., B* **2014**, *144*, 730−738. (f) Zhang, Y. C.; Li, J.; Xu, H. Y. One-step in situ solvothermal synthesis of SnS_2/TiO_2 nanocomposites with high performance in visible light-driven photocatalytic reduction of aqueous Cr(VI). *Appl. Catal., B* **2012**, *123-124*, 18−26. (g) Zhang, Y.; Zhang, F.; Yang, Z.; Xue, H.; Dionysiou, D. D. Development of a new efficient visible-light-driven photocatalyst from SnS_2 and polyvinyl chloride. *J. Catal.* **2016**, *344*, 692−700. (h) Zhang, F.; Zhang, Y.; Zhang, G.; Yang, Z.; Dionysiou, D. D.; Zhu, A. Exceptional synergistic enhancement of the photocatalytic activity of SnS_2 by coupling with polyaniline and N-doped reduced graphene oxide. *Appl. Catal., B* **2018**, *236*, 53−63.

(11) Hong, S. Y.; Popovitz-Biro, R.; Prior, Y.; Tenne, R. Synthesis of SnS_2/SnS fullerene-like nanoparticles: A superlattice with polyhedral shape. *J. Am. Chem. Soc.* **2003**, *125*, 10470−10474.

(12) Ji, Y.; Zhang, H.; Ma, X.; Xu, J.; Yang, D. Single-crystalline SnS_2 nano-belts fabricated by a novel hydrothermal method. *J. Phys.: Condens. Matter* **2003**, *15*, L661−L665.

(13) Chen, X.; Hou, Y.; Zhang, B.; Yang, X. H.; Yang, H. G. Low-cost SnSx counter electrodes for dye-sensitized solar cells. *Chem. Commun.* **2013**, *49*, 5793.

(14) Chen, D.; Shen, G.; Tang, K.; Lei, S.; Zheng, H.; Qian, Y. Microwave-assisted polyol synthesis of nanoscale SnSx (x=1, 2) flakes. *J. Cryst. Growth* **2004**, *260*, 469−474.

(15) Johny, J.; Sepulveda-Guzman, S.; Krishnan, B.; Avellaneda, D.; Shaji, S. Facile and fast synthesis of SnS2 nanoparticles by pulsed laser ablation in liquid. *Appl. Surf. Sci.* **2018**, *435*, 1285−1295.

(16) Yang, Y.-B.; Dash, J. K.; Littlejohn, A. J.; Xiang, Y.; Wang, Y.; Shi, J.; Zhang, L. H.; Kisslinger, K.; Lu, T.-M.; Wang, G.-C. Large Single Crystal SnS_2 Flakes Synthesized from Coevaporation of Sn and S. *Cryst. Growth Des* **2016**, *16*, 961−973.

(17) Ludi, B.; Olliges-Stadler, I.; Rossell, M. D.; Niederberger, M. Extension of the benzyl alcohol route to metal sulfides: "non-hydrolytic" thio sol-gel synthesis of ZnS and SnS_2. *Chem. Commun.* **2011**, *47*, 5280−5282.

(18) Lakshmi, V.; Chen, Y.; Mikhaylov, A. A.; Medvedev, A. G.; Sultana, I.; Rahman, M. M.; Lev, O.; Prikhodchenko, P. V.; Glushenkov, A. M. Nanocrystalline SnS_2 coated onto reduced graphene oxide: demonstrating the feasibility of a non-graphitic anode with sulfide chemistry for potassium-ion batteries. *Chem. Commun.* **2017**, *53*, 8272−8275.

(19) Bharatula, L. D.; Erande, M. B.; Mulla, I. S.; Rout, C. S.; Late, D. J. SnS_2 nanoflakes for efficient humidity and alcohol sensing at room temperature. *RSC Adv.* **2016**, *6*, 105421−105427.

(20) (a) Lin, C.; Zhu, M.; Zhang, T.; Liu, Y.; Lv, Y.; Li, X.; Liu, M. Cellulose/SnS_2 composite with enhanced visible-light photocatalytic activity prepared by microwave-assisted ionic liquid method. *RSC Adv.* **2017**, *7*, 12255−12264. (b) Liu, Y.; Chen, P.; Chen, Y.; Lu, H.; Wang, J.; Yang, Z.; Lu, Z.; Li, M.; Fang, L. In situ ion-exchange synthesis of $SnS_2/g\text{-}C_3N_4$ nanosheets heterojunction for enhancing photocatalytic activity. *RSC Adv.* **2016**, *6*, 10802−10809.

(21) (a) Xia, J.; Zhu, D.; Wang, L.; Huang, B.; Huang, X.; Meng, X.-M. Large-Scale Growth of Two-Dimensional SnS_2 Crystals Driven by Screw Dislocations and Application to Photodetectors. *Adv. Funct. Mater.* **2015**, *25*, 4255−4261. (b) Li, X.; Zhu, J.; Li, H. Comparative study on the mechanism in photocatalytic degradation of different-type organic dyes on SnS_2 and CdS. *Appl. Catal. B* **2012**, *123-124*, 174−181. (c) Zhang, Y. C.; Du, Z. N.; Li, S. Y.; Zhang, M. Novel synthesis and high visible light photocatalytic activity of SnS_2 nanoflakes from $SnCl_2.2H_2O$ and S powders. *Appl. Catal., B* **2010**, *95*, 153−159. (d) Wu, Z.; Xue, Y.; Zhang, Y.; Li, J.; Chen, T. SnS_2 nanosheet-based microstructures with high adsorption capabilities and visible light photocatalytic activities. *RSC Adv.* **2015**, *5*, 24640−24648. (e) Wei, R.; Zhou, T.; Hu, J.; Li, J. Glutatione modified ultrathin SnS_2 nanosheets with highly photocatalytic activity for wastewater treatment. *Mater. Res. Express* **2014**, *1*, No. 025018.

(22) Lei, Y.; Song, S.; Fan, W.; Xing, Y.; Zhang, H. Facile synthesis and assemblies of flowerlike SnS_2 and In^{3+}-doped SnS_2: Hierarchical structures and their enhanced photocatalytic property. *J. Phys. Chem. C* **2009**, *113*, 1280−1285.

(23) (a) Zhang, Z.; Shao, C.; Li, X.; Sun, Y.; Zhang, M.; Mu, J.; Zhang, P.; Guo, Z.; Liu, Y. Hierarchical assembly of ultrathin hexagonal SnS_2 nanosheets onto electrospun TiO_2 nanofibers: enhanced photocatalytic activity based on photoinduced interfacial charge transfer. *Nanoscale* **2013**, *5*, 606−618. (b) Kumar, B. G.; Srinivas, B.; Prasad, M. D.; Muralidharan, K. Ag/Ag_2S heterodimers: tailoring the metal−semiconductor interface in a single nanoparticle. *J. Nanopart. Res.* **2015**, *17*, 325−336. (c) Srinivas, B.; Kumar, B. G.; Muralidharan, K. Stabilizer free copper sulphide nanostructures for

DOI: 10.1021/acsomega.9b01766
ACS Omega 2019, 4, 14970−14980

rapid photocatalytic decomposition of rhodamine B. *J. Mol. Catal. A: Chem.* **2015**, *410*, 8−18. (d) Billakanti, S.; Baskaran, G. K.; Muralidharan, K. Recyclable Ni_3S_4 Nanocatalyst for Hydrogenation of Nitroarenes. *ChemistrySelect* **2017**, *2*, 4753−4758. (e) Billakanti, S.; Krishnamurthi, M. Facile preparation of surfactant or support material free CdS nanoparticles with enhanced photocatalytic activity. *J. Environ. Chem. Eng.* **2018**, *6*, 1250−1256.

(24) Gregor, C.; Hermanek, M.; Jancik, D.; Pechousek, J.; Filip, J.; Hrbac, J.; Zboril, R. The Effect of Surface Area and Crystal Structure on the Catalytic Efficiency of Iron(III) Oxide Nanoparticles in Hydrogen Peroxide Decomposition. *Eur. J. Inorg. Chem.* **2010**, 2343−2351.

(25) Chen, Z.; Naidu, R.; Subramanian, A. Separation of chromium (III) and chromium (VI) by capillary electrophoresis using 2,6-pyridinedicarboxylic acid as a pre-column complexation agent. *J. Chromatogr. A* **2001**, *927*, 219−227.

(26) Zhang, Y. C.; Li, J.; Zhang, M.; Dionysiou, D. D. Size-Tunable Hydrothermal Synthesis of SnS_2 Nanocrystals with High Performance in Visible Light-Driven Photocatalytic Reduction of Aqueous Cr(VI). *Environ. Sci. Technol.* **2011**, *45*, 9324−9331.

(27) Mondal, C.; Ganguly, M.; Pal, J.; Roy, A.; Jana, J.; Pal, T. Morphology Controlled Synthesis of SnS2Nanomaterial for Promoting Photocatalytic Reduction of Aqueous Cr(VI) under Visible Light. *Langmuir* **2014**, *30*, 4157−4164.

(28) Yuan, Y.-J.; Chen, D.-Q.; Shi, X.-F.; Tu, J.-R.; Hu, B.; Yang, L.-X.; Yu, Z.-T.; Zou, Z.-G. Facile fabrication of "green" SnS_2 quantum dots/reduced graphene oxide composites with enhanced photocatalytic performance. *Chem. Eng. J.* **2017**, *313*, 1438−1446.

(29) Qu, J.; Chen, D.; Li, N.; Xu, Q.; Li, H.; He, J.; Lu, J. Coral-Inspired Nanoscale Design of Porous SnS_2 for Photocatalytic Reduction and Removal of Aqueous Cr (VI). *Appl. Catal., B* **2017**, *207*, 404−411.

(30) Zhong, Y.; Qiu, X.; Chen, D.; Li, N.; Xu, Q.; Li, H.; He, J.; Lu, J. Flexible Electrospun Carbon Nanofiber/Tin(IV) Sulfide Core/Sheath Membranes for Photocatalytically Treating Chromium(VI)-Containing Wastewater. *ACS Appl. Mater. Interfaces* **2016**, *8*, 28671−28677.

(31) Sun, M.; Yan, Q.; Yan, T.; Li, M.; Wei, D.; Wang, Z.; Wei, Q.; Du, B. Facile fabrication of 3D flower-like heterostructured g-C_3N_4/SnS_2 composite with efficient photocatalytic activity under visible light. *RSC Adv.* **2014**, *4*, 31019−31027.

(32) Liu, J.; Jing, L.; Gao, G.; Xu, Y.; Xie, M.; Huang, L.; Ji, H.; Xie, J.; Li, H. Ag_2S quantum dots in situ coupled to hexagonal SnS_2 with enhanced photocatalytic activity for MO and Cr(VI) removal. *RSC Adv.* **2017**, *7*, 46823−46831.

(33) Zhang, X.; Zhang, P.; Wang, L.; Gao, H.; Zhao, J.; Liang, C.; Hu, J.; Shao, G. Template-oriented Synthesis of Monodispersed SnS_2@SnO_2 hetero-nanoflowers for Cr(VI) photoreduction. *Appl. Catal., B* **2016**, *192*, 17−25.

(34) Wang, J.; Li, X.; Li, X.; Zhu, J.; Li, H. Mesoporous yolk−shell SnS_2−TiO_2 visible photocatalysts with enhanced activity and durability in Cr(VI) reduction. *Nanoscale* **2013**, *5*, 1876−1881.

(35) (a) Ye, S.; Qiu, L.-G.; Yuan, Y.-P.; Zhu, Y.-J.; Xia, J.; Zhu, J.-F. Facile fabrication of magnetically separable graphitic carbon nitride photocatalysts with enhanced photocatalytic activity under visible light. *J. Mater. Chem. A* **2013**, *1*, 3008−3015. (b) Yang, C.; Wang, W.; Shan, Z.; Huang, F. Preparation and photocatalytic activity of high-efficiency visible-light-responsive photocatalyst SnS_x/TiO_2. *J. Solid State Chem.* **2009**, *182*, 807−812.

(36) Zhang, Z.; Huang, J.; Zhang, M.; Yuan, Q.; Dong, B. Ultrathin hexagonal SnS_2 nanosheets coupled with g-C_3N_4 nanosheets as 2D/2D heterojunction photocatalysts toward high photocatalytic activity. *Appl. Catal., B* **2015**, *163*, 298−305.

DOI: 10.1021/acsomega.9b01766
ACS Omega 2019, 4, 14970−14980

A simplistic approach for the synthesis of CuS–CdS heterostructure: A Novel photo catalyst for oxidative dye degradation

Article *in* Journal of Environmental Chemical Engineering · November 2019

DOI: 10.1016/j.jece.2019.103542

CITATIONS
0

READS
32

3 authors:

Manzoor Pandit
University of Hyderabad
2 PUBLICATIONS **1** CITATION
SEE PROFILE

Srinivas Billakanti
University of Hyderabad
11 PUBLICATIONS **33** CITATIONS
SEE PROFILE

Krishnamurthi Muralidharan
University of Hyderabad
57 PUBLICATIONS **683** CITATIONS
SEE PROFILE

Journal of Environmental Chemical Engineering 8 (2020) 103542

Contents lists available at ScienceDirect

Journal of Environmental Chemical Engineering

journal homepage: www.elsevier.com/locate/jece

A simplistic approach for the synthesis of CuS-CdS heterostructure: A novel photo catalyst for oxidative dye degradation

Manzoor Ahmad Pandit, Srinivas Billakanti, Krishnamurthi Muralidharan*

School of Chemistry, University of Hyderabad, India

ARTICLE INFO

Keywords:
Heterojunctions
Photo catalyst
Clean surfaces
Water purification
Copper sulphide
Cadmium sulphide

ABSTRACT

Direct synthesis of CuS-CdS based mesoporous composite materials and their photocatalytic activity are delineated. In this study, a series of CuS micro flowers (mf) decorated with varying amounts of CdS nanoparticles (NP) have been synthesized successfully in a controlled manner. Relatively easy synthesis of material along with its surfactant-free clean surfaced heterojunction accentuates the reliability of the protocol described here. Full characterization of these semiconducting materials was accomplished with a series of analytical techniques, which include powder x-ray diffraction (PXRD), scanning electron microscopy (SEM), tunnelling electron microscopy (TEM), x-ray photoelectron spectroscopy (XPS), UV–vis, IR, BET and lifetime studies. Upon varying the concentration of precursor of Cd in the reactions, the resulting materials exhibited a well-demarcated change in morphologies ranging from undifferentiated mass to well-differentiated flower-like architectures. The thoroughly characterized composite was accessed finally for its potential photocatalytic activity for the degradation of organic dyes. The results showed 96.0% degradation of rhodamine B (RhB) over 10 min and 94.7% degradation of methylene blue (MB) over 9 min. This observed rate of degradation was much higher compared to that observed in the case of pure CuS (62.0% of RhB and 50.2% of MB).

1. Introduction

Nefarious chemical by-products from various small as well as large industrial units have created menace of environmental pollution, and the problem is aggravating at an alarming rate. For instance, the contamination of water by various industrial sewages, including the organic dyes, pose a difficult task to handle [1–4]. Towards a viable solution, many biological, as well as physical treatment procedures, including adsorption, ultrafiltration, and coagulation, were developed. Unfortunately, all strategies were limited either by their complicacy or expensiveness [5,6], and therefore, for a practical solution to these hazards, there is a need to develop more specific and environmentally benign strategies.

Among the many treatment protocols developed over the years for the treatment of contaminated water, the semiconductor-based catalytic treatment materials picked up full acceptance. In this context, metal chalcogenides, especially CuS and CdS, which exhibited peculiar properties including suitable band gap and required electronic band position, makes them ideal visible light active semiconducting photo catalysts for wastewater treatment [6–8]. Although, CuS, a p-type semiconductor having a narrow bandgap (Eg = 2.0–2.2 eV) is an efficient visible-light photo catalyst for wastewater treatment [9–11]. Nevertheless, the immediate recombination of charge carriers that are generated on exposure to visible light limits the efficiency as a photo catalyst. Therefore, many modified CuS based composite nanostructures were synthesized with different synthetic modifications, including heterojunction formation, doping with some other active metals.

The materials obtained by various modifications exhibited better photocatalytic activity applications compared to the parent compounds. For instance, Liu et al. reported the synthesis of CuS-modified Bi_2S_3, which showed enhanced visible-light photocatalytic performance towards rhodamine B (RhB) degradation [12]. Similarly, Lee et al. carried a successful fabrication of CuS (p-type) and ZnO (n-type) nanoarrays using stainless steel mesh as support. This material exhibited the ability to function as a photo catalyst for the decomposition of acid orange under visible light irradiation [7,13]. Soltani et al. produced ZnS and CdS nanoparticles with absorption spanning into the visible region that showed better durability towards photo-erosion [14]. Sunita et al. synthesized TiO_2/CuS core-shell nanostructure that was useful to degrade methylene blue in a time of 60 min of exposure to radiations [15]. Basu et al. synthesized ZnO/CuS heterojunction, which worked as an excellent catalyst for the photodecomposition of methylene blue (MB) at room temperature [16]. These composite materials eased the charge

* Corresponding author.
E-mail address: murali@uohyd.ac.in (K. Muralidharan).

https://doi.org/10.1016/j.jece.2019.103542
Received 25 September 2019; Received in revised form 7 November 2019; Accepted 12 November 2019
Available online 13 November 2019

transfer through heterojunctions by means of increasing the separation of electron-hole pairs [17].

Zhu et al. performed efficient photocatalytic degradation of the tetracycline hydrochloride on the α-Fe_2O_3@CN composite under the visible light [18]. Wei et al. synthesized a series of different nanostructures like SiO_2 nanoparticles, MoS_2 based polymer composites, and magnetic graphene oxide composites via mussel inspired chemistry and were used successfully for the removal of toxic organic dyes like Congo red, methylene blue respectively [19]. They used these materials as the catalysts for photocatalytic degradation of rhodamine B, photocatalytic decontamination of phenol and petrochemical wastewater, and photocatalytic degradation of 4-chlorophenol (4-CP) respectively [20]. The observations described above explain that the creation of heterostructure between semiconductors leads to the improved catalytic activities in photo catalysis.

It is propounded that a heterostructure between CuS and CdS would establish better contact between these two materials through the formation of heterojunction. CuS and CdS are active individually, under visible light irradiation. Further, the synthetic procedure with better control over tuning the bandgap of these individual materials has been well established in the literature. However, the faster recombination rate of photo generated excitons reduces their catalytic activity. The presence of heterojunction can lead to an enhanced charge separation by transferring charge carriers. This process could induce an increase in the mobility of charge carriers and the stability of the material, and so finally, its photocatalytic activity [21–26]. Moreover, the availability of free and unprotected surfaces is critical to enhance the catalytic activity of nanoparticles further. Therefore, a method that can deliver the nanocomposites devoid of stabilizing molecules like surfactants, which otherwise hamper their photocatalytic activity is worth to look for [27].

This paper describes a novel approach for the synthesis of well-constructed micro/nano composite materials of CuS micro flowers (**mf**) decorated with CdS nanoparticles (**NP**). The work includes the preparation of a series of CuS-CdS composites (CSD-0, CSD-0.5, CSD-1, CSD-2, and CSD-3) and investigation of their potential catalytic activity towards the degradation of organic dyes like rhodamine B and methylene blue. We observed that the catalytic performance shown by as-synthesized composites towards the reduction of organic dyes is far better as compared to pure CuS nanomaterials. Further, enhancement in the catalytic activity of nanocomposites has also been verified by studying the lifetime of photo generated charge carriers using the FLTM technique. The presence of a clean-surface path for photo generated charges in these highly stable CSD composites extended the recyclability of the catalyst in the degradation reactions [27]. Therefore, this work is expected to sensitize newer ways for the improvement of a low-cost and competent photo catalysts for wastewater treatment.

2. Experimental section

2.1. Materials

Copper nitrate ($Cu(NO_3)_2{\cdot}3H_2O$), cadmium chloride ($CdCl_2$, anhydrous), thiourea [$H_2NC(S)NH_2$] and hexamethyldisilazane [$(Me_3Si)_2NH$] (HMDS) were procured from Sigma Aldrich. The chemicals of analytical grade were used as such without further purification.

2.2. Synthesis of CuS decorated with CdS micro/nano composite materials

In a typical reaction, cadmium chloride ($CdCl_2$, anhydrous), (n mmol; where n = 0, 0.5, 1, 2, and 3) copper (II) nitrate trihydrate ($Cu(NO_3)_2{\cdot}3H_2O$) (4 mmol) and thiourea [$H_2NC(S)NH_2$] (3 mmol) were added into 7 mL of HMDS in a reaction vessel. The reagents in the vessel were stirred continuously for 6 h at 140 °C using a magnetic stirrer under continuous supply of nitrogen gas using Schleck lines. Subsequently, the assimilated precipitate was separated by centrifugation, filtered, and then washed using deionized water and ethanol for 3–4 times each. At final, the products were dried by applying vacuum. The products, CuS mf decorated with CdS NP (CuS-CdS micro/nano composites) were named as CSD-0, CSD-0.5, CSD-1, CSD-2, and CSD-3 respectively for the products obtained from the reactions wherein the amounts of $CdCl_2$ used in these reactions were 0, 0.5, 1, 2, and 3 mmol.

2.3. Instrumentation

XRD patterns of the synthesized products were collected at room temperature using Bruker D8 X-ray diffractometer (XRD) at a scan rate of $1^{\circ}min^{-1}$ ($CuK_{\alpha} = 1.54$ Å; operating voltage = 40 kV; operating current = 30 mA) measurements with Cu Kα radiation in a 2θ range from 1Å to 8Å. The morphological texture (FESEM), energy dispersive spectroscopy (EDS) were studied using an Ultra 55 Carl Zeiss instrument at an operating voltage of 10 kV. The synthesized materials were made into suspension in isopropanol by sonicating for 2 − 3 min. It was drop cast on carbon-coated copper grids (200 mesh) for the TEM analyses. FEI Technai G^2 20 STEM with a 200 kV acceleration voltage was used to capture TEM images. JASCO 5300 spectrophotometer was used to analyse the Fourier transform infrared (FT-IR) spectra (KBr pellet). The optical properties were confirmed by studying the UV/Vis absorption spectra of samples in the solid and liquid states (for photo catalysis) using JASCO-V770 UV/Vis spectrometer, wherein barium sulphate was used as the filler. BET studies were carried to determine surface area and pore size analysis, which were conducted on the Quantachrome instruments. The X-ray photoelectron spectra (XPS) were obtained using a Thermo scientific Escalab 250Xi spectrometer with Al − Kα radiation. The lifetime studies were performed by using MicroTime 200 resolved confocal fluorescence setup from PicoQuant equipped with an inverted microscope, a 485 nm pulsed laser source used for excitation.

2.4. Photocatalytic activity

The aqueous solutions of rhodamine B (RhB) and methylene blue (MB) were separately prepared by adding each 10 mg L^{-1} in deionized water. From this stock solution of dyes, 60 mL was placed in a beaker for the experiment, which was then supplemented with 30 mg of CuS-CdS micro/nano composites [CSD-0, CSD-0.5, CSD-1, CSD-2, and CSD-3]. Afterwards, the solution was stirred in dark for about 30 min to ensure the establishment of an adsorption–desorption equilibrium before being illuminated to sunlight. Then the dispersion was exposed to sunlight while being continuously stirred. At a regular time interval, about 3 mL of the suspension was removed, centrifuged for catalyst separation and the liquid then placed in cuvette to study absorption properties.

The UV–vis absorption spectra were recorded by continuously repeating the above procedure, the characteristic absorption peaks at 553 nm for RhB and 660 nm for MB were monitored to follow the catalytic degradation process. The decrease in the intensity of colour of toxic organic dyes while carrying photo catalysis reaction was noticed. This reaction was found to follow a first order reaction kinetics and the rate of degradation was calculated by the following formula;

$$\text{Degradation (\%)} = (1 - C_t/C_0) \times 100\% \quad (1)$$

Here, C_0 is the initial concentration and C_t the concentration of the dye at time t. To highlight the stability and reusability of the catalyst, the same materials used one time were centrifuged from the solution and washed to be reused as in aforementioned steps.

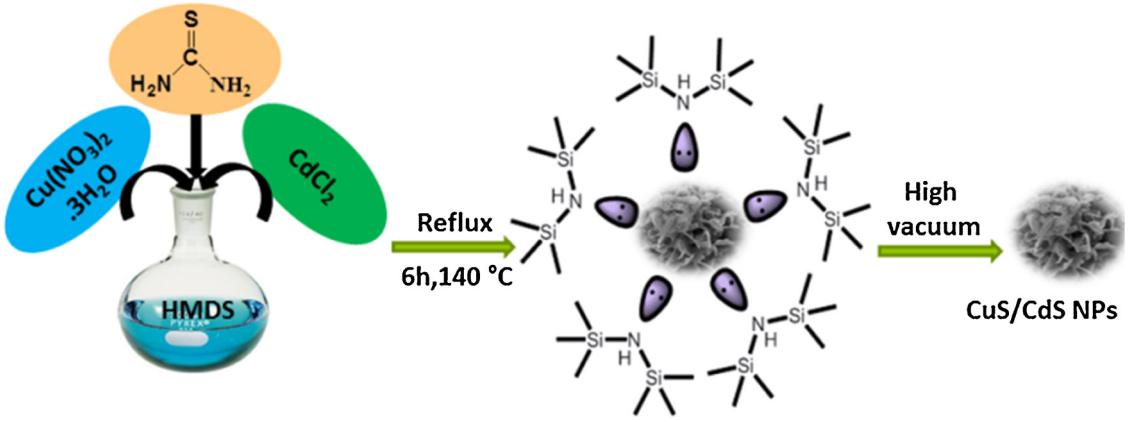

Scheme 1. Schematic illustration of surfactant free CdS decorated CuS nanostructures.

3. Results and discussion

3.1. Synthesis and characterization

Using HMDS-assisted synthetic method, we have synthesized (Scheme 1) five different CuS mf decorated by CdS NP by varying the amount of cadmium source (anhydrous $CdCl_2$) and fixing the amounts of copper and sulphur sources [$Cu(NO_3)_2{\cdot}3H_2O$, 4 mmoL and $H_2NC(S)NH_2$, 3 mmol] in the synthesis. Accordingly, for the amounts of $CdCl_2$ of 0, 0.5, 1, 2 and 3 mmol, the products (CuS mf decorated by CdS NP) obtained were named as CSD-0, CSD-0.5, CSD-1, CSD-2, and CSD-3 respectively. In this synthetic process, HMDS was proven to react with sulphur in presence of metal salts to form $[S\text{-}N(SiMe_3)]_n$ polymer as an intermediate, which would release S^{2-} ion. Also, this intermediate controls the growth of the particles during the reaction. Formation of stable Si-Cl bond drives this reaction and yields Me_3SiCl as a side product. Although HMDS played manifold roles; as a solvent, a reducing agent, as the stabilizing agent since it behaves like surfactant and halts the growth of the particles during the synthesis, yet no atom of HMDS forms the composition of the product materials. Therefore, the reaction is termed as the HMDS –assisted synthesis.

Powder X-ray diffraction (XRD) data confirmed the formation of the CuS-CdS micro/nano composite materials in the HMDS-assisted synthesis. Fig. 1 portrays the XRD patterns of the samples of nanocomposites with different Cd concentrations. All the peaks in the figure correspond to the hexagonal CuS phase (JCPDS No. 65–3556). The XRD patterns of synthesized composites did not specify the characteristic peaks related to other materials, hence confirming high phase purity embedded with lesser loadings of CdS on CuS. However, XRD analysis provided subtle proof for the presence of detached CdS in the materials even for the samples obtained in presence of 1 – 3 mol % Cd source. Nevertheless, the presence of cadmium was confirmed by X-ray photoelectron spectroscopy (XPS) and energy-dispersive X-ray spectroscopy (EDS) analysis (vide infra). Only the difference observed in the PXRD patterns was the increase of intensity of (102) peak and the decrease in the intensity of (110) and (116) peaks. This change in the peak intensity can be attributed to the addition of Cd^+ and Cl^- ions while synthesizing the composite materials that resulted in a subtle change in the stoichiometry of copper sulphides. No change in phase as well as in the composition of synthesized composites was observed [28]. Based on Scherer equation, the peak-width analysis of PXRD spectra showed an average crystallite size of ~30 – 40 nm.

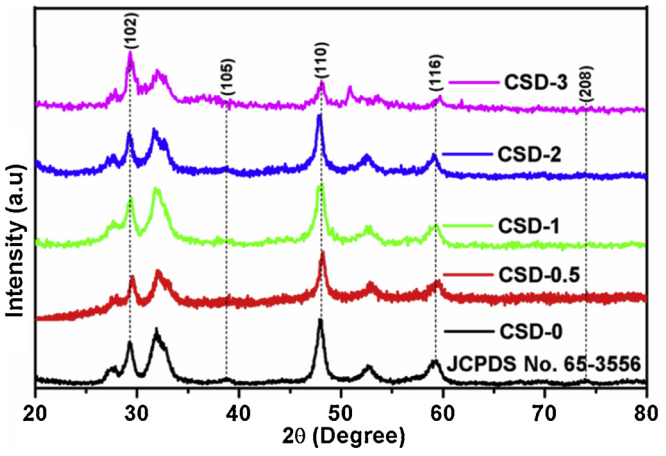

Fig. 1. XRD patterns of CSD-0, CSD-0.5, CSD-1, CSD-2, and CSD-3 with varying amounts of $CdCl_2$ in the reaction while keeping all other reaction conditions same.

The elemental distribution of the synthesized composites was analysed by energy dispersive X-ray spectroscopy (EDS) analysis, which revealed that Cu, Cd and S elements were homogeneously distributed throughout the composite (Fig. S1). The atomic weight ratios of Cu, Cd and S were found 45.6, 25.3 and 29.12 for CSD-1 respectively. The valence states of Cu and Cd atoms in the composite were investigated with X-ray photoelectron spectroscopy (XPS) (Fig.2). The survey (Fig. 2a) scans show that all main peaks, though the intensities were different, could be indexed to Cu, Cd and S of CSD-1 sample, which was the most active catalyst examined in this work. The XPS spectrum of Cd 3d shown in Fig. 2b revealed a doublet at 404.6 and 411.4 eV corresponding to Cd^{2+} $3d_{5/2}$ and $3d_{3/2}$ core-levels in CdS confirming the presence of Cd^{2+} in CdS. Similarly, Fig. 2c displays XPS spectrum of Cu 2p for CSD-1 mf, showing the binding energies of Cu $2p_{3/2}$ and Cu $2p_{1/2}$ core-level signals at 932.6 and 952.4 eV respectively. These peaks are being characteristic for Cu^{2+} in CuS compound, existence as Cu(II) was confirmed. For Cu 2p, the symmetrical shape of peaks confirms the existence of copper in the catalyst as CuS. Besides two main peaks, a weak satellite peak approximately at 943.2 eV further confirmed the paramagnetic nature of Cu^{2+}. The core-level XPS spectra of S 2p is shown in Fig. 2d. For the sample of CSD-1 obtained with the addition of $CdCl_2$, two foremost peaks located at 161.85 eV (S $2p_{3/2}$) and 162.6 eV (S $2p_{1/2}$) were observed. These peaks were ascribed to S^{2-}, specifying the presence of two different metal sulphides (CuS and CdS) in the composite. For Cu $2p_{1/2}$ and S 2p the peaks observed at 951.9 eV for former and 161.8 eV for latter were found to be slightly shifted to lower binding energy region due to $CdCl_2$ addition, confirming the presence of more Cu^+ on the surface in CSD-1 [29,30].

3.2. Structural and morphological analysis

From the FESEM (Fig. 3) images of CSD-0 (where there was no Cd) showed nanofiber like particles and developing of mf (Fig. 3a-b).

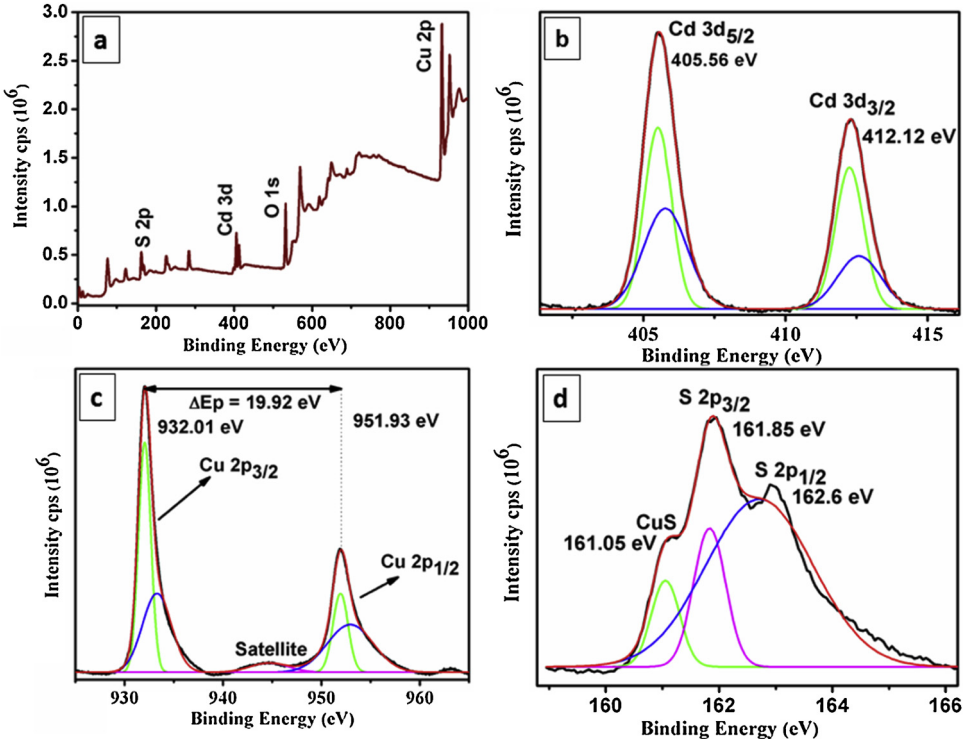

Fig. 2. XPS analysis of CSD-1 in the Cu 2p, Cd 3d and S 2p regions. (a) Survey spectrum of the composite material. (b–d) showing the binding energies of Cd, Cu and S respectively for CSD-1.

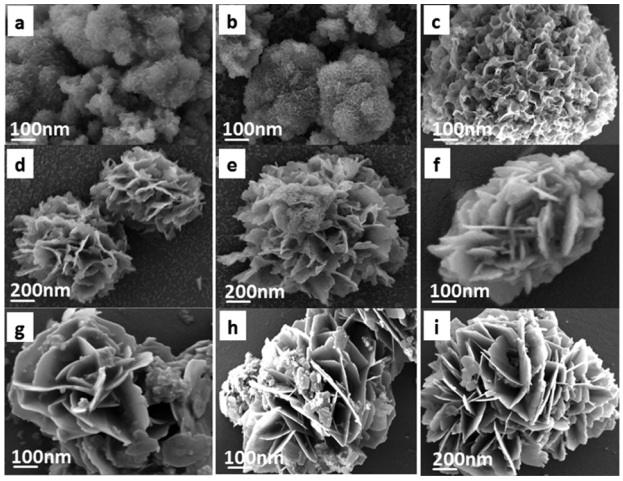

Fig. 3. SEM images of different CSD composites: (a–b) CSD-0, (c) CSD-0.5, (d–e) CSD-1, (f–g) CSD-2 and (h–i) CSD-3.

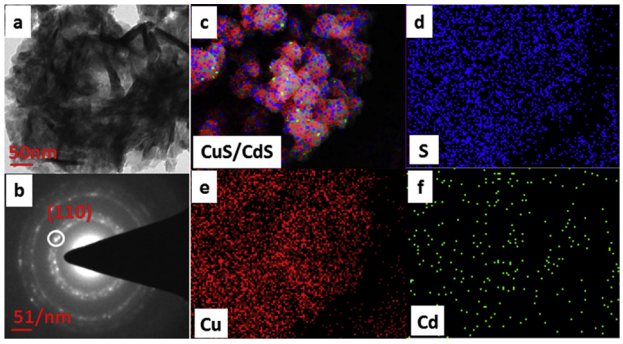

Fig. 4. TEM image, SAED patterns and Elemental mapping from SEM of CSD-1 composite: (a, b) TEM images and SAED patterns of CSD-1. (c, d, e and f) elemental mapping of CSD-1.

Interestingly, after the addition of Cd precursor to the reaction, the morphology transformed into flower-like structure for the sample of CSD-0.5 but with inhomogeneous sizes and thin petals (Fig. 3c). Further increase in the amount of $CdCl_2$ to the reaction [for CSD-1, Fig. 3d-e] resulted in the formation of well-developed microflower-like structure with highly thin porous petals. With another increment in CdS content, the mf developed to somewhat relaxed structure with its petals seeming to expand in space but associated with the decrease in density of pores [sample CSD-2, Fig. 3f and g]. After the addition of final increment of CdS, the mf grew to highly dense and thick sheet like diverse flowers accompanied with reduction in the density of pores of CSD-3 (Fig. 3h and i). These stepwise incremental changes in the CdS addition clearly highlighted the change in morphology from messy to thin porous like microflowers. These changes finally ended up by completely transforming morphology to well-developed thick sheet and high particle density flowers confirming the regular deposition of CdS particles on flowers.

Further evaluations about morphological transformation were confirmed from studying TEM measurements (Fig. 4). Fig. (4 a, b for CSD-1 and Fig.S2a, c, e and g for CSD-0, CSD-0.5, CSD-2, and CSD-3) shows the TEM images of CSD composite materials. From the figure, it is clear that all the TEM images are almost in close confirmation with their corresponding SEM images with flowers becoming more porous and thin up to CSD-1 and after that with further enhancement in CdS concentration the overall thickness increases but with the decrease in porosity. The elemental mapping (Fig. 4c, d, e, and f- for CSD-1) further confirms the distribution of elements (Cu, Cd, and S) present in the composite materials. To understand the crystalline nature of the mesoporous network, the synthesized composites were subjected to selected-area electron diffraction (SAED), which presented (Fig. 4b for CSD-1 and Fig. S2b, d, f, and h for CSD-0, CSD-0.5, CSD-2 and CSD-3) a sequence of diffused Debye-Scherer rings corresponding to the zinc-blende structure of CdS, agreeing well with XRD results. These results confirmed the successful deposition of CdS particles on the CuS surface.

Consistency in all data from XRD, XPS, SEM and TEM confirmed the well-defined synthesis of mesoporous composite materials compromising of covellite (CuS) and cubic CdS nanostructures [29].

3.3. Clean surface area and optical properties

As discussed earlier, the availability of free surface of the micro and nanoparticles for the catalytic activity is the key for their success in catalysis. The main side product in the synthesis described here is Me_3SiCl and it can be removed from the reaction mixture by vacuum along with HMDS used in the reactions. Since no other surfactant molecules are used in the synthesis, and starting materials [thiourea, $Cu(NO_3)_2{\cdot}3H_2O$ and $CdCl_2$] are removed by washing with water and ethanol, the product is supposed to have clean surfaces. EDS analysis did not show any signature of silicon in the products. As exemplified in different works of literature that an external surfactant hinders the catalytic activity of a catalyst by decreasing the generation of electron-hole pairs, their mobility. For better catalytic activity, to circumvent the problem of surfactant molecules, it is necessary to develop surfactant-free nanostructures. In this regard, the FTIR spectrum of CSD-1 material (Fig. S3) showed that there are no significant signals for the materials. For visual comparison, the FTIR spectrum (Fig. S3a) of the HMDS is presented as well. These observations explain clearly that CSD materials discussed here have clean surfaces and can be suitable materials for catalysis.

In order to evaluate the specific surface area and corresponding pore structure, we have carried out the nitrogen adsorption-desorption isotherms (BET) for the CSD materials (Fig. S4). A sample of CSD-1 exhibited type IV isotherms and its specific surface area was calculated to be 18.1 $m^2 g^{-1}$. The obtained surface area is not so much higher but still CSD-1 showed the best photocatalytic activity among all these composite catalysts. This is due to the existence of special hierarchical structure and highly porous nature of petals, providing a good number of active sites for catalytic activities, together. These results are in good agreement with the FTIR analysis which states that the as synthesized catalysts are having clean and free (free from surfactants) surfaces.

The optical properties of composite catalysts were confirmed from UV–vis absorption spectra (Fig. S5). It is observed that all the catalysts show similar absorption, mostly in the visible region with broad peak absorption. Still, CSD-1 shows superior photocatalytic activity as compared to other samples. This increased activity might be due to some morphological changes giving CSD-1 a particular hierarchical type structure which might cause some slight changes in the absorption spectra, but overall the absorption spectra of all the samples remain unaffected [31]. The average band gap values calculated from the absorption data was 2.29 eV for CSD materials.

3.4. Photocatalytic properties

Rh B and MB represent the most commonly used organic dyes at industrial scale and therefore are used as probe molecules predominantly while studying the heterogeneous catalysis. Therefore, to evaluate the photocatalytic potential of CSD materials, the time dependent photo degradation of Rh B and MB dyes was studied. The schematic illustration of overall photo catalysis performed by CSD materials is shown in Scheme 2. A set of control experiments for CSD-1 material (Fig S6a) which include one without catalyst (photolysis) and another one without the visible light intervention but in the presence of a catalyst (catalysis). These reactions revealed the photocatalytic potential of CSD materials in the presence of visible light, divulging the importance of both catalyst and light to impact the dye degradation.

The photocatalytic ability of CSD composite materials (CSD-0, CSD-0.5, CSD-1, CSD-0.2, CSD-0.3) were tested individually. All the composite materials showed varying photocatalytic activity towards the degradation of toxic organic dyes RhB and MB. The lowest photo degradation efficiency was observed for CSD-0 sample compared to the other CSD materials that are having definite amounts of CdS, which could be attributed to the effect of morphology. From above analysis, it is clear that the photocatalytic activities were enhanced obviously by loading CdS on to CuS surfaces. However the trend was not followed regularly with a series of CSD materials. Among these composite materials, the sample CSD-1 showed the highest photocatalytic activity towards RhB and MB dyes which is matching well with the photocatalytic degradation kinetics. With CSD-1 catalyst, there was a rapid decrease in the intensity of absorption peak with increasing time of exposure. The degradation of RhB and MB dye solutions was observed to be 96.04% after 10 min for former and 94.69% after 9 min for latter respectively (Fig. 5a, c) and remained at a relatively stable level after this time. The photocatalytic activity of other composite materials (CSD-0, CSD-0.5, CSD-0.2, CSD-0.3) towards the degradation of RhB and MB shown by their UV–vis absorption spectrum are represented in fig. S6b, c.

The photocatalytic degradation of RhB and MB using CSD composite materials were found to follow the first order kinetics. The first-order rate constant is calculated by the following equation [32]

$$\ln(C/C_0) = -kt \quad (2)$$

Where C_0 is the initial concentration of organic dyes, C is the concentration at time t, and k is the first-order rate constant (min^{-1}), and t is the irradiation time (min). From Fig. 6a c, it is observed that the samples prepared by adding different amounts of Cd, have different photocatalytic abilities. The rate constant of photodecomposition when plotted against time as per Eq. 2 gave a straight line for CSD-1 (Fig. 6b and d**)** and in general for all CSD materials (**Fig. S7**), confirming the first order kinetics of the degradation of organic dyes. The correlation between the reaction rate constant and the amount of CdS in the composite materials was also plotted (**Fig. S8**). Data in Table 1 and plots (Fig. 6) explain that CSD-1 with the appropriate CdS amount can achieve the optimal photo degradation efficiency. The first-order rate constant (K/min) of CSD-1 mf for the degradation of RhB (0.22205/min) is much higher than that of CSD-0 (0.05659/min) and CSD-0.5 (0.0676/min). A similar trend was observed for MB degradation, were the rate constant for CSD-1 mf (0.17709/min) was much higher than that of CSD-0 (0.04072/min).

The durability of the catalyst was evaluated by recycling the catalyst in the photo degradation reactions of RhB and MB in aqueous solutions. Again CSD-1 holds the best durability than others (Fig. 5b and d). Table 2 compares the catalytic efficiencies of many catalysts with CSD composite materials and shows increased catalytic activity of CSD-1 compared to other reported systems [33–37]. The data clearly explains that the heterostructures between two binary metal chalcogenides will increase the catalytic activity towards organic dye degradation experiments and the importance of clean surfaces on the catalyst surfaces.

3.5. Structural influence of the degradation reactions

The mechanism for the performed photo degradation of organic dyes by using CSD composite materials is presented in Fig. 7 [38]. According to this mechanism, irradiation of CSD composite materials with natural light resulted in the generation of electron and hole pairs. Owing to the driving force attained from the heterostructures with reduced potential energy, the electrons were transferred easily to the conduction band of CdS. This whole process, in turn, resulted in the formation of super oxygen radicals ($\cdot O_2$) because of the combining of these electrons with absorbed O_2 on the surface. At the same time, the photo generated holes were transferred to CuS from CdS and generated hydroxyl radicals (·OH). At the end, the organic dyes (RhB and MB) could be degraded efficiently into smaller molecules such as CO_2 and H_2O by these strongly oxidizing species generated in the process.

The photocatalytic activity of any synthesized catalyst has both the synergistic as well as antagonistic contributions from many underlying

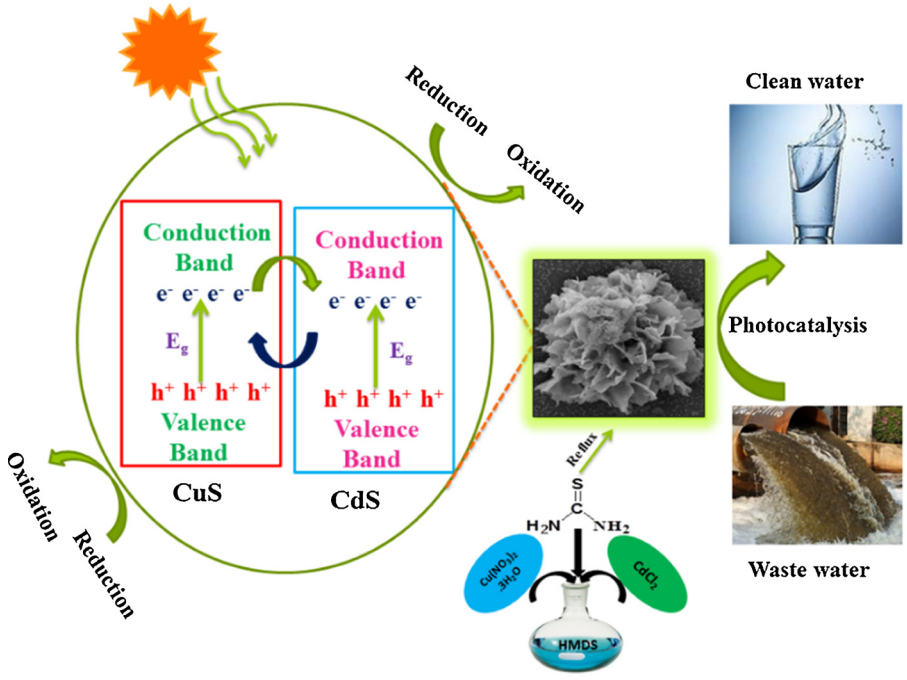

Scheme 2. Schematic illustration of photo catalysis by CSD materials.

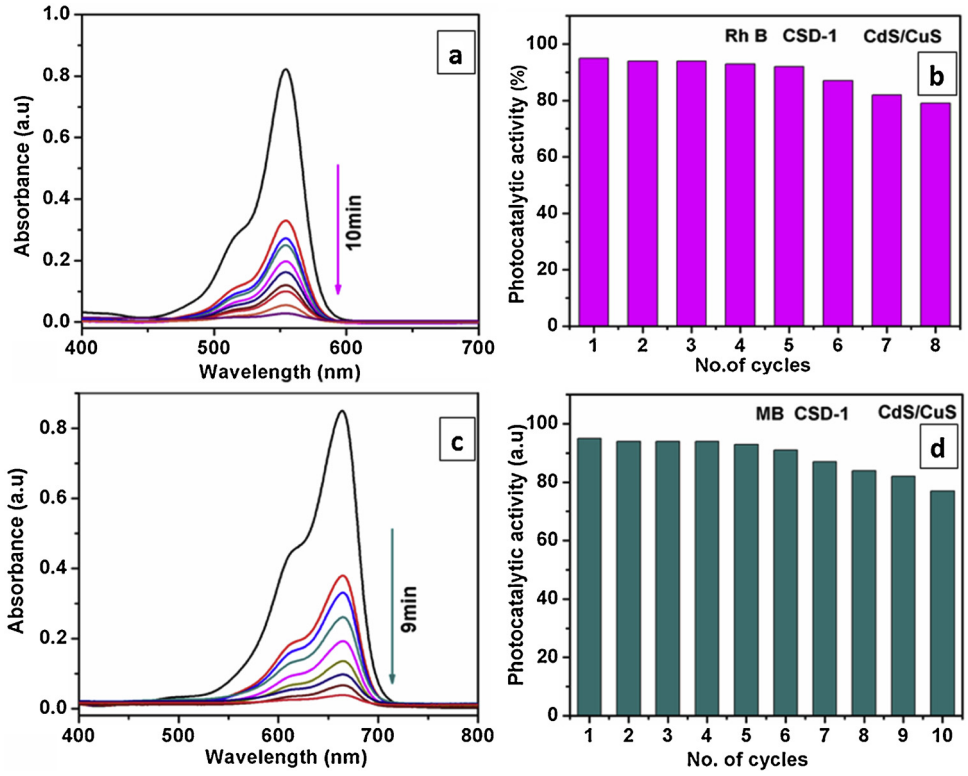

Fig. 5. (a and c) are the optical absorption profiles for the RhB and MB dyes under visible light irradiation using the CSD-1 sample. (b and d) are the recyclability studies for the composite material [CSD-1] in the photodecomposition of RhB and MB respectively.

factors. Concerning the catalyst described here, there is also scope for both types of factors to operate. For instance, (1) If individual CuS or CdS generate photo-induced charges, those charges can recombine easily resulting in the decreased photocatalytic activity; (2) specific surface area of the catalyst is the main influencing factor of the efficiency of photo degradation; (3) The formation of heterostructure due to its synergistic effect plays a pivotal role in facilitating the parting away of photo induced charges, thus resulting in the enhancement of mobility of charge carriers, hence an overall increase in photocatalytic activity [39].

In the newly created CuS-CdS heterojunction described here, there was an increase in sizes of flower petals with the addition of CdS loadings and a simultaneous increase in porosity from CSD-0 to CSD-1. Further, there was a decrease (CSD-2 to CSD-3) in the porous cavities of

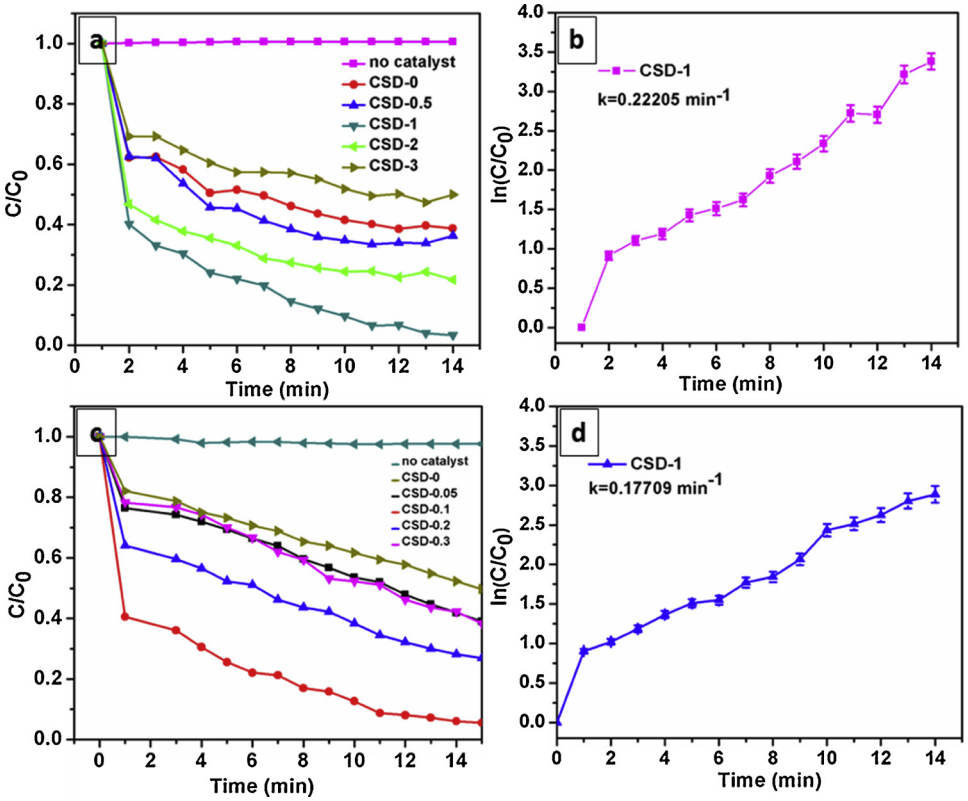

Fig. 6. (a and c) Relative concentration (C/C_0) of RhB and MB using as prepared composite materials by varying $CdCl_2$ concentrations under visible light. (b and d) The linear fit plots of $\ln(C/C_0)$ *vs*. time of the data in (a and c) for CSD-1.

the petals with a further increase in CdS loading. This decrease in the porosity reflected as the lowest adsorption and catalytic activities in relation with their less surface area. Even though CSD-1 has relatively low BET surface area, the adsorption capability of CSD-1 was slightly higher than others. This increased activity was due to highly porous nature and clean surfaces on the catalyst, which provided more catalytic active sites. The availability of surfactant free-surface of photo catalyst facilitates efficient contact with organic contaminants and enhanced charge carrier transfer and thereby presenting the highest photocatalytic decomposition of organic dyes (RhB and MB) [40]. The enhanced photocatalytic activity was further authenticated from the lifetime studies, as shown in (Fig. S9). The lifetime studies supported our activity performance; the average lifetime for the CSD-1 is less (2.78 ns) compared to other materials [CSD-0, 3.22 ns; CSD-0.5, 3.08 ns; CSD-2, 3.12 ns, and CSD-3, 2.82 ns] [40,41] which shows its better photocatalytic potential.

For broad spectrum applicability, the recyclability of catalyst is decisive and in this regard, we have tested the reusability of our CSD heterostructure material by repeating the photocatalytic decomposition of organic dyes using the recovered catalyst under the same experimental procedure. For this purpose, after the experiment, the catalyst was separated by centrifugation (3000 rpm), sequentially washed with distilled water and acetone and then finally dried over vacuum for 2 h at 60 °C. The well-dried catalyst was reused in the procedure, as mentioned above. Interestingly, the heterostructure showed higher stability with no decrease in the activity until the 5th cycle, as can be seen from (Fig. 6). Although a slight decrease in activity was noticed after 5th catalytic cycle, the photo catalyst was stable until 8 cycles in the case of

Table 2
Comparison table for the various heterostructure catalysts for the photocatalytic degradation of organic dyes.

Catalyst	Pollutant Conc.	Catalyst amount	Time (min)	ref
CuS/Bi_2S_3	10 mg/L	0.1 g/L	300	9
CuS/ZnO	(1.0×10^{-5} M)	2 cm x 2 cm/50 m L	300	10
CdS/ZnS	10 mg/L	100 mg/L	360	11
CuS/TiO_2	10^{-5}M	30 mg/L	60	12
CuS/ZnO	2×10^{-5} M	20 mg/50 m L	40	13
CuS/Bi_2S_3	2×10^{-5} 10 mg/L	0.050 g/L	150	33
CuS/ZnS	10^{-5} 10 mg/L	0.050 g/L	60	34
CuS/TiO_2	10 mg/L	0.100 g /L	180	35
CuS-rgo	4mg/L	0.1 g/L	120	36
CdS-rGo	10 mg/L	0.160 g/L	150	37
CuS/CdS	10 mg/L	0.030 g/L	10	Present work

Table 1
The first order rate constants, R^2 values, maximum degradation < %) and time required for maximum degradation for the RhB and MB by CSD mf.

Sample	K_{app} (CuS/CdS)		R^2		Maximum Degradation (%)		Time taken for maximum degradation (min)	
	RhB	MB	RhB	MB	RhB	MB	RhB	MB
CSD-0	0.0566	0.0407	0.76371	0.95213	62.04	50.21	17	14
CSD-0.5	0.0676	0.0480	0.73335	0.89161	66.99	58.57	12	11
CSD-1	0.2221	0.1771	0.96082	0.94981	96.04	94.69	10	9
CSD-2	0.0839	0.0775	0.70341	0.93671	78.76	73.18	13	12
CSD-3	0.0415	0.0597	0.68105	0.97541	53.03	62.13	15	13

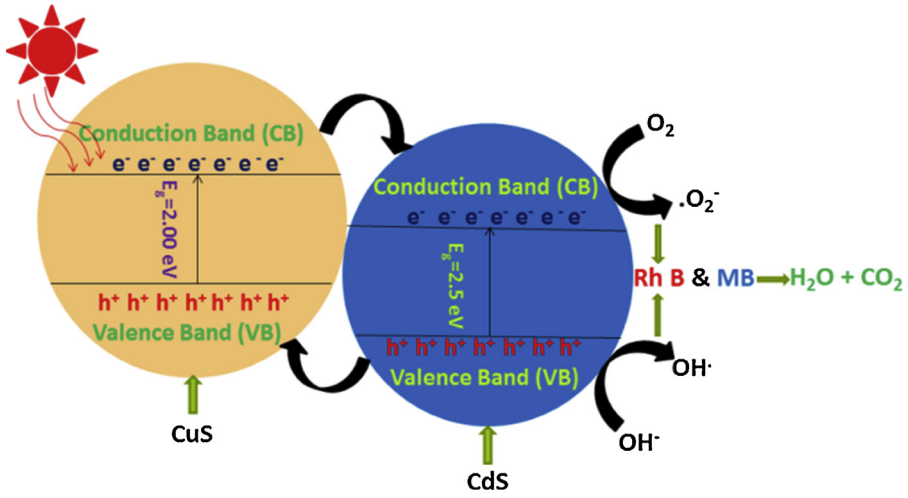

Fig. 7. The sketch of the band energy level and charge transfers involved in CSD photo catalysts.

RhB and 10 cycles for MB. Further, we have performed morphological (Fig. S10) studies and obtained XRD spectrum (Fig. S11) of the reused catalyst (CSD-1). From FESEM images and XRD plots, it was clear that the catalyst was stable with no appreciable changes in the morphology and peak intensities were observed even after 10 cycles. These studies highlight the importance of the heterostructures and clean surfaces on the catalyst for the secure promotion of charges, which directly affects the activity and durability of the photo catalyst.

4. Conclusions

In summary, we have demonstrated the formation of a simple CuS-CdS heterojunction resulting from decorating CuS micro flowers (**mf**) with CdS nanoparticles (**NP**). These heterojunctions helped to substantially enhance their photocatalytic activity compared to individual binary CuS and CdS nanostructures. These materials, which resulted from a one-pot HMDS-assisted synthesis, were unambiguously characterized by a series of analytical techniques which include PXRD, SEM, EDX, TEM, XPS, and BET. Their incisive structural and morphological investigations revealed that $CdCl_2$ loading decisively affects the composition and morphological transformation from irregular to petals through micro flowers, probably because of the induction of Cl^- ions and the formation of CuS-CdS heterojunction.

Investigation of photocatalytic activity interpreted that these nanocomposites possess better photocatalytic efficiency compared to pure CuS and CdS nanostructures, with sample CSD-1 having 1 mmoL $CdCl_2$ loading being the best hit for the degradation of RhB and MB dyes. Moreover, the post-experimental analysis points to that as-prepared catalysts were highly stable (10 cycles) for the photo degradation of organic dyes, which provided it with excellent potential for further photocatalytic applications.

Declaration of Competing Interest

There are no conflicts to declare.

Acknowledgements

The project is funded partially by UGC-CAS and DST-PURSE grants. The authors thank the Centre for Nanotechnology at the University of Hyderabad for the TEM facility. M. A. P thanks UGC-BSR for fellowship.

Appendix A. Supplementary data

Supplementary material related to this article can be found, in the online version, at doi:https://doi.org/10.1016/j.jece.2019.103542.

References

[1] (a) E. Eltzov, V. Pavluchkov, M. Burstin, R.S. Marks, Creation of a fiber optic based biosensor for air toxicity monitoring, Sens. Actuators B Chem. 155 (2011) 859–867; (b) C. Chen, W. Ma, J. Zhao, Semiconductor-mediated photodegradation of pollutants under visible-light irradiation, Chem. Soc. Rev. 39 (2010) 4206–4219.
[2] L.J. Zhou, Y.C. Zou, J. Zhao, P.P. Wang, L.L. Feng, L.W. Sun, D.J. Wang, G.D. Li, Facile synthesis of highly stable and porous Cu_2O/CuO cubes with enhanced gas sensing properties, Sens. Actuators B Chem. 188 (2013) 533–539.
[3] B. Kumar, S. Saha, A. Ganguly, A.K. Ganguli, A facile low temperature (350 °C) synthesis of Cu_2O nanoparticles and their electrocatalytic and photocatalytic properties, RSC Adv. 4 (2014) 12043–12049.
[4] P. Basnet, G.K. Larsen, R.P. Jadeja, Y.C. Hung, Y.P. Zhao, A-Fe_2O_3 nanocolumns and nanorods fabricated by Electron beam evaporation for visible light photocatalytic and antimicrobial applications, ACS Appl. Mater. Interfaces 5 (2013) 2085–2095.
[5] L.L. Ma, J.L. Li, H.Z. Sun, M.Q. Qiu, J.B. Wang, J.Y. Chen, Y. Yu, Self-assembled Cu_2O flowerlike architecture: polyol synthesis, photocatalytic activity and stability under simulated solar light, Mater. Res. Bull. 45 (2010) 961–968.
[6] P. Basnet, Y.P. Zhao, Tuning the Cu_xO nanorod composition for efficient visible light induced photocatalysis, Catal. Sci. Technol. 6 (2016) 2228–2238.
[7] A. Kudo, Y. Miseki, Heterogeneous photo catalyst materials for water splitting, Chem. Soc. Rev. 38 (2009) 253–278.
[8] (a) L.L. Wang, J. Ge, A.L. Wang, M.S. Deng, X.J. Wang, S. Bai, R. Li, J. Jiang, Q. Zhang, Y. Luo, Y.J. Xiong, Designing p-Type semiconductor–Metal hybrid structures for improved photocatalysis, Angew. Chem. Int. Ed 53 (2014) 5107–5111;
(b) C. Zhu, B. Lu, Q. Su, E. Xie, W. Lan, A simple method for the preparation of hollow ZnO nanospheres for use as a high performance photo catalyst, Nanoscale 4 (2012) 3060–3064;
(c) G. Zhang, H. Duan, B. Lu, Z. Xu, Electrospinning directly synthesized metal nanoparticles decorated on both sidewalls of TiO_2 nanotubes and their applications, Nanoscale 5 (2013) 5801–5808;
(d) M. Zhang, C. Shao, J. Mu, Z. Zhang, Z. Guo, P. Zhang, Y. Liu, One-dimensional Bi_2MoO_6/TiO_2 hierarchical heterostructures with enhanced photocatalytic activity, Cryst. Eng. Comm 14 (2012) 605–612;
(e) L. Zhang, D. Jing, X. She, H. Liu, D. Yang, Y. Lu, J. Li, Z. Zheng, L. Guo, Heterojunctions in g-C_3N_4/TiO_2(B) nanofibres with exposed (001) plane and enhanced visible-light photoactivity, J. Mater. Chem. A Mater. Energy Sustain. 2 (2014) 2071–2078;
(f) X. Chen, C. Li, M. Gratzel, R. Kostecki, S.S. Mao, Nanomaterials for renewable energy production and storage, Chem. Soc. Rev. 41 (2012) 7909–7937.
[9] M. Basu, A.K. Sinha, M. Pradhan, S. Sarkar, Y. Negishi Govind, T. Pal, Evolution of hierarchical hexagonal stacked plates of CuS from liquid-Liquid interface and its photocatalytic application for oxidative degradation of different dyes under indoor lighting, Environ. Sci. Technol. 44 (2010) 6313–6318.
[10] X. Liu, M.T. Mayer, D. Wang, Negative differential resistance and resistive switching behaviors in Cu_2S nanowire devices, Appl. Phys. Lett. 96 (2010) 223103.
[11] X. Meng, G. Tian, Y. Chen, R. Zhai, J. Zhou, Y. Shi, X. Cao, W. Zhou, H. Fu, Hierarchical CuS hollow nanospheres and their structure-enhanced visible light photocatalytic properties, Cryst. Eng. Comm. 15 (2013) 5144–5149.
[12] Z.Q. Liu, W.Y. Huang, Y.M. Zhang, Y.X. Tong, Facile hydrothermal synthesis of Bi_2S_3 spheres and CuS/Bi_2S_3 composites nanostructures with enhanced visible-light photocatalytic performances, Cryst. Eng. Comm. 14 (2012) 8261–8267.
[13] M. Lee, K. Yong, Highly efficient visible light photocatalysis of novel CuS/ZnO heterostructure nanowire arrays, Nanotechnology. 23 (2012) 194014.
[14] N. Soltani, E. Saiona, W.M.M. Yunus, M. Erfani, M. Navasery, G. Bahmanrokh,

K. Rezaee, Enhancement of visible light photocatalytic activity of ZnS and CdS nanoparticles based on organic and inorganic coating, Appl. Surf. Sci. 290 (2014) 440–447.
[15] S. Khanchandani, S. Kumar, A.K. Ganguli, Comparative study of TiO_2/CuS Core/Shell and composite nanostructures for efficient visible light photocatalysis, ACS Sustainable Chem. Eng. 4 (2016) 1487–1499.
[16] M. Basu, N. Garg, A.K. Ganguli, A type-II semiconductor (ZnO/CuS heterostructure) for visible light photocatalysis, J. Mater. Chem. A Mater. Energy Sustain. 2 (2014) 7517–7525.
[17] S. Thangavel, K. Krishnamoorthy, S.J. kim, G. Venugopal, Designing ZnS decorated reduced graphene-oxide nanohybrid via microwave route and their application in photocatalysis, J. Alloys. Compd. 683 (2016) 456–462.
[18] H.U. Rasheed, X. Lv, W. Wei, D.K. Sam, N. Ullah, J. Xie, W. Zhu, Highly efficient photocatalytic degradation of the Tetracycline hydrochloride on the α-Fe_2O_3@CN composite under the visible light, J. Environ. Chem. Eng. 7 (2019) 103322.
[19] (a) Q. Huang, M. Liu, L. Mao, D. Xu, G. Zeng, H. Huang, R. Jiang, F. Deng, X. Zhang, Y. Wei, Surface functionalized SiO_2 nanoparticles with cationic polymers via the combination of mussel inspired chemistry and surface initiated atom transfer radical polymerization: characterization and enhanced removal of organic dye, J. Colloid Interface Sci. 499 (2017) 170–179;
(b) Q. Huang, M. Liu, J. Chen, Q. Wan, J. Tian, L. Huang, R. Jiang, Y. Wen, X. Zhang, Y. Wei, Facile preparation of MoS_2 based polymer composites via mussel inspired chemistry and their high efficiency for removal of organic dyes, Appl. Surf. Sci. 419 (2017) 35–44;
(c) Y. Liu, H. Huang, D. Gan, L. Guo, M. Liu, J. Chen, F. Deng, N. Zhou, X. Zhang, Y. Wei, A facile strategy for preparation of magnetic graphene oxide composites and their potential for environmental adsorption, Ceram. Int. 44 (2018) 18571–18577.
[20] (a) A.A. Isari, A. Payan, M. Fattahi, S. Jorfi, B. Kakavandi, Photocatalytic degradation of rhodamine B and real textile wastewater using Fe-doped TiO_2anchored on reduced graphene oxide (Fe-TiO_2/rGO): Characterization and feasibility, mechanism and pathway studies, Appl. Surf. Sci. 462 (2018) 549–564;
(b) F. Hayati, A.A. Isari, M. Fattahi, B. Anvaripour, S. Jorfi, Photocatalytic decontamination of phenol and petrochemical wastewater through ZnO/TiO_2 decorated on reduced graphene oxide nanocomposite: influential operating factors, mechanism, and electrical energy consumption, RSC Adv. 8 (2018) 40035–40053;
(c) A. Shojaie, M. Fattahi, S. Jorfi, B. Ghasemi, Synthesis and evaluations of Fe_3O_4–TiO_2–Ag nanocomposites for photocatalytic degradation of 4-chlorophenol (4-CP): effect of Ag and Fe compositions, Int. J. Ind. Chem. 9 (2018) 141–151.
[21] X. Wan, X.Y. Liang, C.R. Zhang, X.X. Li, W.W. Liang, H.S. Xu, S. Lan, S.L. Tie, Morphology controlled syntheses of Cu-doped ZnO, tubular Zn(Cu)O and Ag decorated tubular Zn(Cu)O microcrystals for photocatalysis, Chem. Eng. J. 272 (2015) 58–68.
[22] X. Xu, Z.H. Gao, Z.D. Cui, Y.Q. Liang, Z.Y. Li, S.L. Zhu, X.J. Yang, J.M. Ma, Synthesis of Cu_2O Octadecahedron/TiO_2 quantum dot heterojunctions with high visible light photocatalytic activity and high stability, ACS Appl. Mater. Interfaces 8 (2016) 91–101.
[23] (a) L. Chen, S.F. Yin, S.L. Luo, R. Huang, Q. Zhang, T. Hong, P.C.T. Au, $Bi_2O_2CO_3$/BiOI photocatalysts with heterojunctions highly efficient for visible-light treatment of dye-containing wastewater, Ind. Eng. Chem. Res. 51 (2012) 6760;
(b) L. Chen, Q. Zhang, R. Huang, S.F. Yin, S.L. Luo, C.T. Au, Porous peanut-like Bi_2O_3–$BiVO_4$ composites with heterojunctions: one-step synthesis and their photocatalytic properties, Dalton Trans. 41 (2012) 9513;
(c) M. Xiong, L. Chen, Q. Yuan, J. He, S.L. Luo, C.T. Au, S.F. Yin, Facile fabrication and enhanced photosensitized degradation performance of the g-C_3N_4– $Bi_2O_2CO_3$ composite, Dalton Trans. 43 (2014) 8331;
(d) L. Chen, R. Huang, Y.J. Ma, S.L. Luo, C.T. Au, Controllable synthesis of hollow and porous Ag/$BiVO_4$ composites with enhanced visible-light photocatalytic performance, RSC Adv. 3 (2013) 24354;
(e) S.G. Kumar, K.S.R.K. Rao, Zinc oxide based photocatalysis: tailoring surface-bulk structure and related interfacial charge carrier dynamics for better environmental applications, RSC Adv. 5 (2015) 3306–3351.
[24] Q. Wang, G. Yun, Y. Bai, N. An, Y. Chen, R. Wang, Z. Lei, W.S. Guan, CuS, NiS as co-catalyst for enhanced photocatalytic hydrogen evolution over TiO2, Int. J. Hydrogen Energy 39 (2014) 13421–13428.
[25] X.H. Guan, L. Yang, X. Guan, G.S. Wang, RSC Adv. 5 (2015) 36185–38191.
[26] (a) C. Mondal, A. Singh, R. Sahoo, A.K. Sasmal, Y. Negishi, T. Pal, Preformed ZnS nanoflower prompted evolution of CuS/ZnS p–n heterojunctions for exceptional visible-light driven photocatalytic activity, New J. Chem. 39 (2015) 5628–5635;
(b) V. Dzhagana, B. Kempken, M. Valakh, J. Parisi, J. Kolny- Olesiak, D.R.T. Zahn, Probing the structure of $CuInS_2$-ZnS core-shell and similar nanocrystals by Raman spectroscopy, Appl. Surf. Sci. 395 (2017) 24–28.
[27] (a) B.G. Kumar, K. Muralidharan, Hexamethyldisilazane-assisted synthesis of indium sulphide nanoparticles, J. Mater. Chem. 21 (2011) 11271–11275;
(b) B.G. Kumar, K. Muralidharan, Organic-free self-assembled copper sulfide microflowers, Eur. J. Inorg. Chem. (2013) 2102–2108;
(c) B.G. Kumar, K. Muralidharan, S_4N_4 as an intermediate in Ag_2S nanoparticle synthesis, RSC Adv. 4 (2014) 28219–28224;
(d) B.G. Kumar, B. Srinivas, M.D. Prasad, K. Muralidharan, Ag/Ag_2S heterodimers: tailoring the metal–semiconductor interface in a single nanoparticle, J. Nanopart. Res. 17 (2015) 325–336;
(e) B. Srinivas, B.G. Kumar, K. Muralidharan, Stabilizer free copper sulphide nanostructures for rapid photocatalytic decomposition of rhodamine, B. J. Mol. Catal. A: Chem 410 (2015) 8–18;
(f) S. Billakanti, G.K. Baskaran, K. Muralidharan, Recyclable Ni_3S_4 nanocatalyst for hydrogenation of nitroarenes, Chem. Select 2 (2017) 4753–4758;
(g) S. Billakanti, K. Muralidharan, Facile preparation of surfactant or support material free CdS nanoparticles with enhanced photocatalytic activity, J. Environ. Chem. Eng. 6 (2018) 1250–1256;
(h) S. Billakanti, M.A. Pandit, K. Muralidharan, Importance of clean surfaces on the catalyst: SnS_2 nanorings for environmental remediation, ACS Omega 4 (2019) 14970–14980.
[28] P. Kumar, M. Gusain, R. Nagarajan, Synthesis of $Cu_{1.8}S$ and CuS from copper-thiourea containing precursors; Anionic (Cl^-, NO^{3-}, SO_4^{2-}) influence on the product stoichiometry, Inorg. Chem. 50 (2011) 3065–3070.
[29] L.J. Zhang, T.F. Xie, D.J. Wang, S. Li, L.L. Wang, L.P. Chen, Y.C. Lu, Noble-metal-free CuS/CdS composites for photocatalytic H_2 evolution and its photogenerated charge transfer properties, Int. J. Hydrogen Energy 38 (2013) 11811–11817.
[30] (a) X. Zong, J.F. Han, G.J. Ma, H.J. Yan, G.P. Wu, C. Li, Photocatalytic H_2 evolution on CdS loaded with WS_2 as cocatalyst under visible light irradiation, J. Phys. Chem. C 115 (2011) 12202–12208;
(b) P. Kar, S. Farsinezhad, X. Zhang, K. Shankar, Anodic Cu_2S and CuS nanorod and nanowall arrays: preparation, properties and application in CO_2 photoreduction, Nanoscale 6 (2014) 14305–14318.
[31] (a) M. Saranya, R. Ramachandran, S.K. Jeong, A.N. Grace, Enhanced visible light photocatalytic reduction of organic pollutant and electrochemical properties of CuS catalyst, Powder Technol. (2015) 209–220;
(b) Z. Hosseinpour, S. Hosseinpour, M. Maaza, A. Scarpellini, Co^{2+} and Ho^{3+} doped CuS nanocrystals with improved photocatalytic activity under visible light irradiation, RSC Adv. 6 (2016) 42581–42588.
[32] (a) S. Xiong, B. Xi, Y. Qian, CdS hierarchical nanostructures with tunable morphologies: preparation and photocatalytic properties, J. Phys. Chem. C 114 (2010) 14029–14035;
(b) Q.Y. Tian, W. Wu, L.G. Sun, S. Yang, M. Lei, J. Zhou, Y. Liu, X.G. Xiao, F. Ren, C.Z. Jiang, V.A.L. Roy, Tube-like ternary α-Fe_2O_3@SnO_2@Cu_2O sandwich heterostructures: synthesis and enhanced photocatalytic properties, ACS Appl. Mater. Interfaces 6 (2014) 13088–13097.
[33] L. Chen, J. He, Q. Yuan, Y.W. Zhang, F. Wang, C.T. Au, S.-F. Yin, CuS–Bi_2S_3 hierarchical architectures: controlled synthesis and enhanced visible-light photocatalytic performance for dye degradation, RSC Adv. 5 (2015) 33747–33754.
[34] J. Yu, J. Zhang, S. Liu, Ion-exchange synthesis and enhanced visible-light photoactivity of CuS/ZnS nanocomposite hollow spheres, J. Phys. Chem. C 114 (2010) 13642–13649.
[35] G. Hou, Z. Cheng, L. Kang, X.J. Xu, F. Zhang, H. Yang, Controllable synthesis of CuS decorated TiO_2 nanofibers for enhanced photocatalysis, Cryst. Eng. Comm. 17 (2015) 5496–5501.
[36] Y. Zhang, J. Tian, H. Li, L. Wang, X. Qin, A.M. Asiri, A.O.Al. Youbi, X. Sun, Biomolecule-Assisted, Environmentally Friendly, One-Pot Synthesis of CuS/Reduced Graphene Oxide Nanocomposites with Enhanced Photocatalytic Performance, Langmuir. 28 (2012) 12893–12900.
[37] X. Wang, H. Tian, Y. Yang, H. Wang, S. Wang, W. Zheng, Y. Liu, Reduced graphene oxide/CdS for efficiently photocatalystic degradation of methylene blue, J. Alloys. Compd. 524 (2012) 5–12.
[38] (a) M. Tanveer, C.B. Cao, I. Aslam, Z. Ali, F. Idrees, M. Tahir, W.S. Khan, F.K. Butt, A. Mahmood, Effect of the morphology of CuS upon the photocatalytic degradation of organic dyes, RSC Adv. 4 (2014) 63447–63456;
(b) J. Kundu, D. Pradhan, Controlled synthesis and catalytic activity of copper sulfide nanostructured assemblies with different morphologies, ACS Appl. Mater. Interfaces 6 (2014) 1823–1834.
[39] Z. Khan, T.R. Chetia, A.K. Vardhaman, D. Barpuzary, C.V. Sastri, M. Qureshi, Visible light assisted photocatalytic hydrogen generation and organic dye degradation by CdS–metal oxide hybrids in presence of graphene oxide, RSC Adv. 2 (2012) 12122–12128.
[40] R.C. Shen, J. Xie, P. Guo, L. Chen, X. Chen, X. Li, Bridging the g-C_3N_4 nanosheets and robust CuS cocatalysts by metallic acetylene black interface mediators for active and durable photocatalytic H_2 production, ACS Appl. Energy Mater. 1 (5) (2018) 2232–2241.
[41] H. Chauhan, K. Soni, M. Kumar, S. Deka, Tandem photocatalysis of graphene-stacked SnS_2 nanodiscs and nanosheets with efficient carrier separation, ACS Omega 1 (2016) 127–137.

THE JOURNAL OF PHYSICAL CHEMISTRY C

pubs.acs.org/JPCC Article

Chalcopyrite with Magnetic and Dielectric Properties: An Introductory Catalyst for 4-Nitrophenol Reduction

Manzoor Ahmad Pandit, Dasari Sai Hemanth Kumar, Srinivas Billakanti, Manigandan Ramadoss, and Krishnamurthi Muralidharan*

Cite This: J. Phys. Chem. C 2020, 124, 18010−18019 Read Online

ACCESS | Metrics & More | Article Recommendations | Supporting Information

ABSTRACT: The progress for the development of active, stable, and economic catalysts for the chemical transformation of noxious chemicals to benign is of primary importance. The synthesis of surfactant-free chalcopyrite, **sf-$CuFeS_2$**, by a wet-chemical one-pot hexamethyldisilazane-assisted synthetic method was accomplished. Various analytical and spectroscopic techniques were used for the physical characterization of the material produced. From the observation of magnetic properties, the material chalcopyrite was found to be paramagnetic. The dielectric constant and dielectric loss were also determined and were found to be decreasing with an increase in frequency. The dielectric behavior of the material was explained by the Maxwell−Wagner theory of polarization, and the dielectric constant of the as-synthesized sample was found to be 3.176 at 100 °C and 500 kHz. The potential catalytic activity was confirmed by performing the reduction of 4-nitrophenol (**4-NP**) to 4-amino phenol (**4-AP**) in the presence of sodium borohydride ($NaBH_4$) in aqueous medium at room temperature. The catalyst showed about 90% yield in the reduction reactions, which can be attributed to easy access to active sites invigorated by the absence of surfactant molecules. The reusability of the catalyst was checked to find out the stability, and excellent retention of activity up to five cycles was observed.

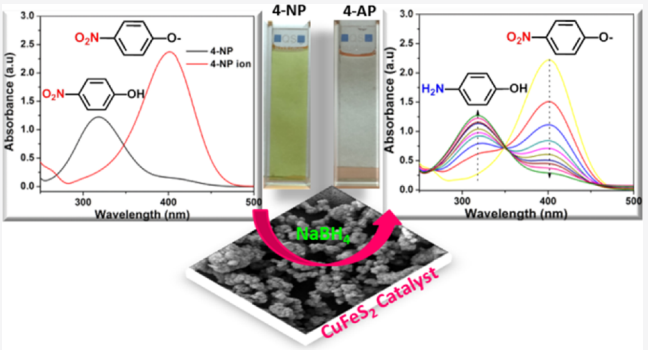

1. INTRODUCTION

Ternary chalcogenides of transition metals of type $CuMX_2$ (where M = Al, In, Ga, and Fe and X = S and Se) that are behaving as semiconductors have attracted immense research interest because of their characteristic physical and chemical properties. These materials have shown potential applications in spintronics and photoconversion in solar cells.[1−8] Among these transition metal chalcogenides, chalcopyrite ($CuFeS_2$) has been studied widely. Chalcopyrite with an elemental composition of earth-abundant elements like Cu and Fe, besides S, lags in the race of literature of semiconductors of Cu-based nanocrystals.[9,10] Chalcopyrite has a zinc blende-type structure with a coordination number of four for both cations and anions forming distinct corner-sharing tetrahedra.[11]

The chalcopyrite mineral having a dazzling golden surface is considered the most capable semiconductor material with unusual optical, electrical, and magnetic properties.[12,13] It also possesses high values of thermoelectric power[14] and rectification,[15] with an optical band gap[16,17] in the range of 0.5−0.6 eV behaving as an n-type semiconductor. Chalcopyrite exhibits a magnetic property changing from antiferromagnetic behavior to paramagnetic depending on temperature. It displays an antiferromagnetic property achievable at a Néel temperature of 823 K while a paramagnetic arrangement at around 50 K. The probable reason for this complicated magnetic behavior is as follows. Neutron diffraction studies of $CuFeS_2$ showed an effective magnetic moment of 3.85 μB for Fe, which is lower compared to the expected value for Fe^{3+} ions (~5.0 μB).[12] The lesser magnetic moment was attributed to the significant Fe−S covalent interactions.[18−20] The magnetic moment of Cu in chalcopyrite could not be calculated accurately in the vicinity of a large moment of the iron ion.[21,22]

For many nanostructured materials, the exciting variation in properties is observed based on the crystal structure and morphology of materials, which in turn depends on the synthetic procedures. $CuFeS_2$ nanostructures have received tremendous research interest. Silvester et al. synthesized colloidal sols of $CuFeS_2$ nanocrystals by a hydrothermal method under the controlled conversion of iron(III) oxide. These materials were optically transparent, and their properties

Received: March 27, 2020
Revised: July 28, 2020
Published: July 28, 2020

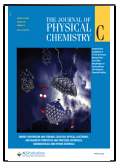

https://dx.doi.org/10.1021/acs.jpcc.0c02697
J. Phys. Chem. C 2020, 124, 18010−18019

were closely matching that of the bulk material.[23,24] Wang et al.[25] and Liang et al.[26] independently developed prominent colloidal methods to synthesize $CuFeS_2$ nanocrystals. Various types of nanostructures of $CuFeS_2$, including thin films,[27] (nanowires, nanorods, and spherical particles)[16,17] and nanocrystals[25,26,28] have been synthesized for probable applications in photovoltaics,[29] thermoelectric[26] and spintronic devices, and as catalysts for dye degradation.[30]

One of the biggest challenges and concerns in front of researchers is to make the environment pollutant-free. Large quantities of toxic and carcinogenic chemical byproducts like organic dyes[31−33] and nitro-based aromatic compounds[34] and heavy metal ions[35−37] are continuously being released into water bodies from industrial units. These pollutants contaminate water as well as create environmental menace at an alarming rate and are becoming a difficult task to handle.[38−46] Nitrophenols are considered to be the most common pollutants in both industrial and agricultural wastewaters, particularly among them, 4-nitrophenol (**4-NP**), which is highly soluble and stable in water. It is the most tarnished pollutant and has made life vulnerable upon exposure, causing severe health problems.[47−50]

Various treatment methods, like adsorption[51,52] and catalytic reduction,[53,54] were designed to remove **4-NP** from water. Adsorption is a useful remedial method for wastewater treatment from nitro compounds. Adsorption involves the use of an adsorbent, which can adsorb the adsorbate, mostly contaminating its surface. Adsorption is also an economical and efficient approach for the removal of **4-NP**. Nevertheless, the adsorption process mostly depends on the nature of the adsorbent, like its morphology, surface area, and size.[49] Besides these, temperature, pH, and time are the critical factors deciding the fate of the adsorption process.[55] On the other hand, the catalytic approach is considered a simple, versatile, and cost-effective process, involving the use of a reducing agent like $NaBH_4$ in the presence of nanomaterials as catalysts for the reduction of **4-NP**.[56]

The present work aims to produce chalcopyrite nanoparticles in a simplified method and determine their unique magnetic and dielectric properties in comparison with the same materials known in the literature. Also, it is of interest to test the hitherto unknown catalytic ability of $CuFeS_2$ in organic functional group transformation reactions. We are able to synthesize surfactant-free $CuFeS_2$ nanoparticles (**sf-$CuFeS_2$**) using a realistic HMDS-assisted synthetic approach. The synthesized nanostructures were characterized by powder X-ray diffraction, scanning electron microscopy (SEM), and high-resolution transmission electron microscopy (HRTEM). The magnetic property measurement (at room temperature and 100 K) confirms the paramagnetic nature of the chalcopyrite material. Dielectric studies showed a substantial decrease in the value of both dielectric constant and dielectric loss at low frequency, but at a higher frequency, it remains unchanged. After confirming the properties of **sf-$CuFeS_2$** nanoparticles without any organic molecules in their surroundings, the synthesized chalcopyrite was assessed for its potential catalytic ability in the reduction of **4-NP** to 4-aminophenol (**4-AP**). It is important to mention here that there is no report yet on the catalytic reduction of **4-NP** to **4-AP** using $CuFeS_2$ nanoparticles. The catalyst developed consists of naturally abundant and low-cost non-noble elements that make the easy availability of the catalyst on a large scale.

2. EXPERIMENTAL SECTION

2.1. Materials. Copper chloride ($CuCl_2$ anhydrous), ferric chloride ($FeCl_3$ anhydrous), thiourea [$H_2NC(S)NH_2$], and hexamethyldisilazane [$(Me_3Si)_2NH$] (HMDS) were purchased from Sigma-Aldrich. All the above reagents were of analytical grade and used without further purification.

2.2. Synthesis of sf-$CuFeS_2$. For the synthesis of **sf-$CuFeS_2$** nanoparticles, a hexamethyldisilazane (HMDS)-assisted wet-chemical method was employed. In a typical reaction, 1.48 mmol of $CuCl_2$, 1.48 mmol of $FeCl_3$, and 2.56 mmol of thiourea were added one by one to an RB flask connected to the Schlenk lines to maintain the inert conditions. Then, 6 mL HMDS of (26 mmol) was injected by a syringe under a continuous supply of nitrogen gas. The reaction mixture was set to reflux at 160 °C for 3 h with continuous stirring. After the completion of reaction, the precipitates were separated by centrifugation at 2500 rpm, decanted, and then washed by deionized water and ethanol each 3−4 times. The material collected was subjected to high vacuum for the complete removal of any residual solvents. The product was dried at 70 °C overnight in a vacuum oven.

2.3. Catalytic Reduction of 4-Nitrophenol. In order to perform the catalytic reduction of **4-NP**, a general procedure was applied. A 0.5 mL $NaBH_4$ (0.1 M) aqueous solution was added to 2.5 mL of 4-nitrophenol (0.1 mM) aqueous solution. To this mixture was added 0.8 mL of **sf-$CuFeS_2$** suspension (8 mg/100 mL) to perform the catalysis. The reduction of 4-nitophenol to **4-AP** was regularly monitored using the UV−Vis absorption spectrum within a range of 200−600 nm. The conversion percentage of the **sf-$CuFeS_2$** catalyst is given by eq 1.

$$\%\text{Conversion} = (C_0 - C_t/C_0) \times 100 \quad (1)$$

Here, C_0 is the initial concentration (corresponding to absorbance) of 4-nitrophenol at λ_{max}, and C_t is the concentration at time t.

2.4. Instrumentation. Various analytical techniques used for the characterization of $CuFeS_2$ are described as follows. The X-ray diffraction measurements for determining crystal structure and phase purity were performed using a Bruker D8 X-ray diffractometer equipped with Cu Kα radiation (λ = 1.54056 Å, 2θ ranges from 20 to 70°).The surface morphology, particle size, and elemental analysis were carried out by FESEM, and EDAS studies were performed using an Ultra 55 Carl Zeiss instrument with an operating voltage of 10 kV. The TEM images were acquired using an FEI Tecnai G^2 20 STEM with a 200 kV acceleration voltage. The samples were prepared by drop casting of a colloidal suspension of chalcopyrite on carbon-coated copper grids (200 meshes). Optical properties and catalysis were recorded with a JASCO-V770 UV−Vis spectrometer; barium sulfate was used as a standard. The specific surface area and the pore size of the material were estimated by a Nova 2000e, Quantachrome Instruments Limited, USA, using liquid nitrogen (77 K).

The specific surface area and the average pore size distribution were determined by using a multipoint BET equation and from BJH plots, respectively. The oxidation state and elemental compositions were determined by X-ray photoelectron spectra (XPS) using a Thermo Scientific Escalab 250Xi spectrometer with Al Kα radiation. Magnetic properties were studied by the VSM instrument at two different temperatures. For studying dielectric properties, the principle

https://dx.doi.org/10.1021/acs.jpcc.0c02697
J. Phys. Chem. C 2020, 124, 18010−18019

of a parallel plate capacitor was applied, and the measurements were carried out on an HF-LCR meter (6505 P, Wayne Kerr Electronics, U.K.) instrument. An 8 mm, thick disk-shaped pellet of 0.5 mm thickness was prepared under a uniaxial pressure of 5 tons and 5% polyvinyl alcohol as a binder. The prepared pellet was sintered at 500 °C for the removal of the binder. A thin paste of silver acting as a conducting layer was applied on the pellet to function as an electrode.

3. RESULTS AND DISCUSSION

3.1. Synthesis and Characterization. The chalcopyrite material (**sf-$CuFeS_2$**) was synthesized (Scheme 1) by a one-pot HMDS-assisted wet-chemical approach supplemented with Schlenk lines to maintain the continuous inert atmosphere. The PXRD pattern confirmed the crystalline nature and phase purity of the prepared sample. As shown in Figure 1, all the peaks can be indexed to the tetragonal structure of chalcopyrite with JCPDS no. 37-0471.[57] The peaks at 2θ of 29.4, 49.01, and 57.8° can be indexed to the planes of (112), (220), and (312), respectively. No other characteristic peaks were found in the PXRD pattern that can be indexed to either pure CuS or FeS_2 phases or any other stoichiometry of both, hence confirming the single phase and high purity of the material.

Scheme 1. Schematic Illustration of the Reaction Showing Chalcopyrite Formation

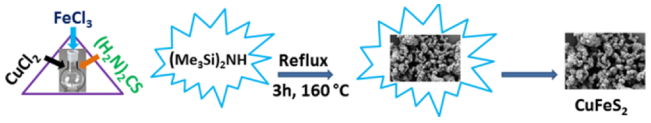

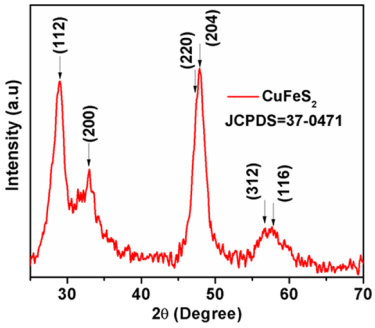

Figure 1. PXRD pattern of **sf-$CuFeS_2$** showing high crystalline nature with high intensity peaks. All the peaks correspond to JCPDS no. 37-0471.

SEM and EDAS images revealed the morphology and elemental distribution. As shown in Figure 2a, scanning electron microscopy (SEM) confirms that the nanostructures have particle-type morphology with almost all the particles of similar size. The particles formed clusters probably because of the surfactant-free synthesis. The high-magnification SEM image depicts the cluster formation (Figure S1a). The study aims to develop surfactant-free materials in order to exhibit excellent properties. The elemental distribution analysis spectra (EDAS) (Figure S2) reveal that all three elements (Cu, Fe, and S) are distributed well in stoichiometric ratios.

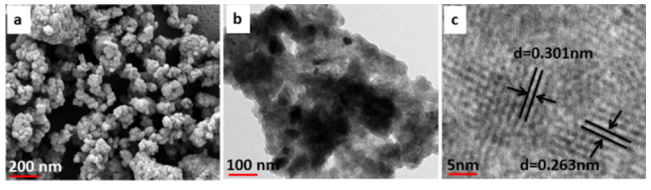

Figure 2. Microscopic investigation of **sf-$CuFeS_2$** particles. (a) FESEM, (b) TEM, and (c) HRTEM images.

Further confirmation about the particle morphology of synthesized materials was performed by TEM analysis. Figure 2b represents the distinctive TEM image of **sf-$CuFeS_2$** nanoparticles. From the figure, it is clear that the particles are of nano dimensions with the average particle size approximately equals to ~65 nm. The high-resolution TEM image (HRTEM) is shown in Figure 2c. It shows that the distances between two crystal facet planes are 0.301 and 0.263 nm, which correspond well to planes (112) and (200), respectively, of the synthesized material. The dark-field TEM image (Figure S1b) shows bright spots corresponding to the particle nature of synthesized materials, hence agreeing well with the SEM. The SAED pattern (Figure S1c) shows some diffraction rings corresponding to (112), (200), and (204) crystal planes, which matches well with the PXRD pattern, so confirming the well crystalline nature of **sf-$CuFeS_2$** nanoparticles.

The further validity of chalcopyrite formation and the elemental composition with valance states was confirmed by performing XPS analysis (Figure 3). The survey spectrum (Figure 3a) shows that all the elements Cu, Fe, and S are well present in the chalcopyrite. The spectrum shows that Cu 2p split into two dominant peaks, Cu $2p_{1/2}$ and Cu $2p_{3/2}$, at binding energies of 955.15 and 935.20 eV, indicating the presence of Cu as Cu^+ ions (Figure 3b). Besides this, two weak satellite peaks located at 944.93 and 963.8 eV are observed clearly in the Cu 2p spectrum, which is reliable with the presence of Cu^{2+} rather than Cu (0).[58] Similarly, an Fe peak (Figure 3c) split into two peaks, Fe $2p_{1/2}$ and Fe $2p_{3/2}$, at 726.03 and 712.05 eV, respectively, revealing[59] the existence of Fe as Fe^{3+}. The S 2p spectrum (Figure 3d) shows two peaks, one at 164.9 eV for S $2p_{3/2}$ and the other peak at 169.5 eV assigned for the S−O bond showing oxidized sulfur-related species, but since there is no proof for the oxidation of S in $CuFeS_2$ happening, it indicates the presence of S as S^{2-}.[60,61]

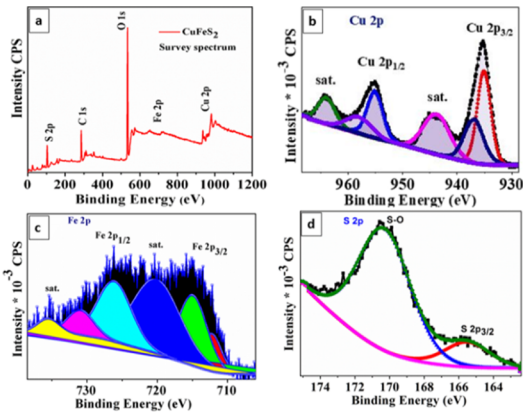

Figure 3. XPS spectrum of **sf-$CuFeS_2$**. (a) Survey spectrum showing the presence of all requisite elements Cu, Fe, and S. (b–d) Binding energy values of Cu, Fe, and S, respectively.

https://dx.doi.org/10.1021/acs.jpcc.0c02697
J. Phys. Chem. C 2020, 124, 18010−18019

3.2. Magnetic Property. The chalcopyrite, $CuFeS_2$, is known for its magnetic properties and related applications. Therefore, it is required to study the magnetic property of **sf-CuFeS$_2$** prepared in this study. Figure 4a shows magnetization

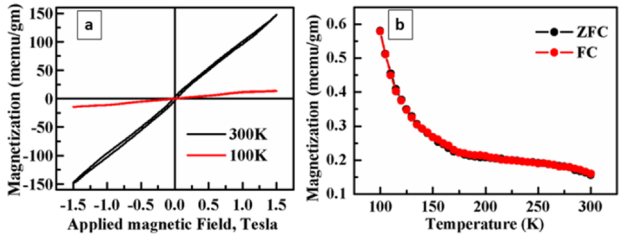

Figure 4. (a) Magnetization vs. applied magnetic field plots for the samples at 300 and 100 K. (b) Magnetization vs. temperature plots for the samples.

vs. applied magnetic field $[M(H)]$ plots for the samples of **sf-CuFeS$_2$** at 300 and 100 K. An almost straight line behavior of the $M(H)$ curve indicates the paramagnetic behavior of the sample. Magnetization values at 1.5 Tesla are 148 and 17 memu/gm at 300 and 100 K, respectively. Coercivity values are 23 and 48 mTesla at 300 and 100 K, respectively. A decrease in magnetization is noticed at 100 K, while coercivity values are increased at lower temperature. Even though coercivity and remanent magnetization values are very small, the existence of these parameters indicates the presence of small ferromagnetism in **sf-CuFeS$_2$**. However, the ferromagnetism in the samples is suppressed with the dominating paramagnetic nature of the samples.

Figure 4b shows the magnetization vs. temperature $(M(T))$ plots in the temperature range of 100−300 K in zero field-cooled (ZFC) and field-cooled (FC) mode at an applied field of 500 Oe. Bifurcation between the ZFC and FC curve is very narrow and indicates that paramagnetism is dominating in the synthesized **sf-CuFeS$_2$** material.[62]

3.3. Dielectric Constant Properties. For many minerals, finding out the dielectric properties has become a topic of discussion. Since the dielectric property depends on the conductivity, it is of curiosity to understand the frequency-dependent variation in the dielectric constant of **sf-CuFeS$_2$**. The following formula is used to determine the dielectric constant of a mineral

$$\varepsilon'' = Cd/A\varepsilon_0 \quad (1)$$

and

$$\varepsilon'' = \varepsilon' \tan(\delta) \quad (2)$$

Here, d represents the thickness, A is area of the sample, and C is capacitance.

The dielectric properties of the **sf-CuFeS$_2$** pellet sintered at 500 °C were studied by varying the frequency from 20 Hz to 1 MHz within a temperature range of 100−400 °C (Figure 5). From Figure 5a, it is clear that the dielectric constant values decrease continuously with the increase in frequency.[63] Up to 100 kHz, there is a regular decrease, but after then, with the further increase in frequency, it remains constant without any fluctuation, which is a significant observation attributed to the surfactant-free nature of the material. Also, it is seen that the dielectric loss of the material shows similar behavior like the dielectric constant (Figure 5b). This behavior of the synthesized sample could be explained based on the Maxwell−Wagner polarization theory of dielectrics. Space charge polarization is a factor responsible for the decrease in values of dielectric properties, which is associated with the charge concentrated at the grain boundaries or grain deficiencies of the sample particles of various dielectric properties.[64] The contribution from grain sizes mostly controls the low-frequency values of ε. From the figure, we see that the values of both dielectric constant and dielectric loss drop with the increase in frequency for this **sf-CuFeS$_2$** material.

According to the Maxwell−Wagner theory, at lower frequencies, different polarization mechanisms, including space charge, dipolar, and ionic polarization, contribute to the dielectric properties of the material.[65] However, with an increase in frequency, the space charge polarization does not get enough time to follow the applied external frequency and is therefore relaxed, leading to the reduction of dielectric properties of the material with an increase in the frequency. It was found that the dielectric constant determined at different temperatures remains unchanged at higher frequencies, indicating that the dielectric property does not vary with the change in temperature. The dielectric loss at higher frequencies was found to be relatively low because the electric wave frequency was not found to be in proper comparison to the natural frequency of the bounded charge, so the reason for weak radiation. The dielectric constant of **sf-CuFeS$_2$** at 100 °C and 500 kHz is 3.176; the low value might be presumably because of the particle-type morphology as compared to bulk or sheet morphology as reported previously.[66]

3.4. Surface Area and Photophysical Properties. The active surface area and photophysical properties of catalysts are the most critical parameter to determine the catalytic activity. A general sense prevailing in the catalysts related to the surface area is that the larger the surface area, the higher will be the catalytic activity. The reason is that a material with a large

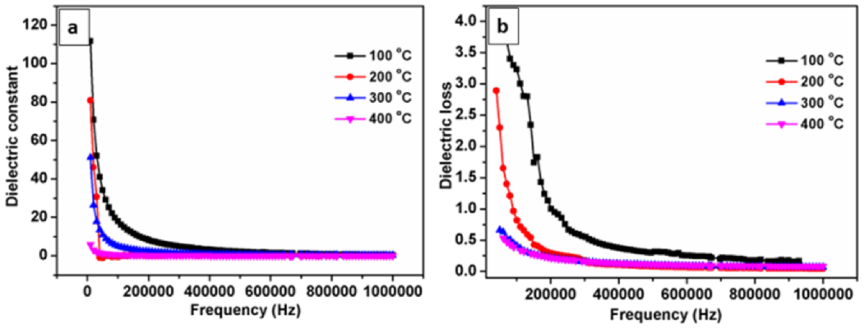

Figure 5. Plots showing variation of (a) dielectric constant and (b) dielectric loss with frequency at different temperatures.

https://dx.doi.org/10.1021/acs.jpcc.0c02697
J. Phys. Chem. C 2020, 124, 18010−18019

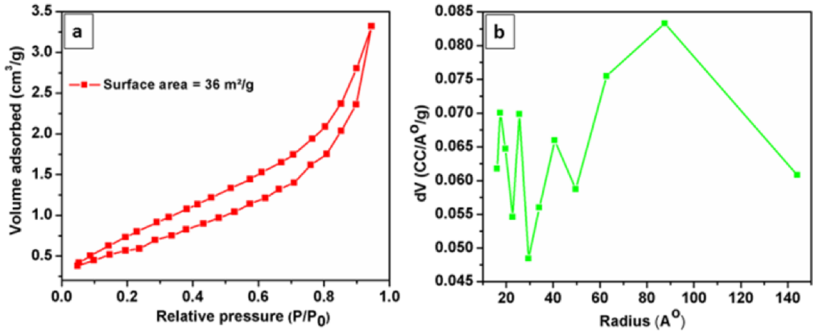

Figure 6. Active surface area of **sf-CuFeS$_2$**. (a) Nitrogen adsorption−desorption isotherm. (b) BJH average pore size distribution plot of chalcopyrite.

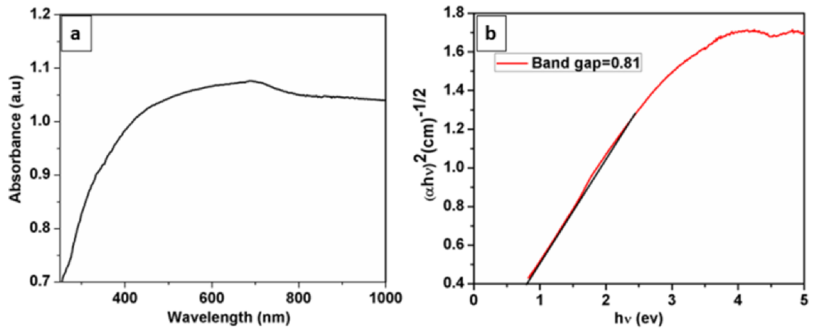

Figure 7. UV−Vis diffuse reflectance spectra of **sf-CuFeS$_2$**. (a) Absorption spectrum. (b) Band gap.

surface area will be having a sufficient amount of active sites that will undergo maximum adsorption, hence higher catalytic activity. In this scenario, it is imperative to determine the surface area of **sf-CuFeS$_2$** (Figure 6). From Figure 6a, it is evident that the N_2 adsorption−desorption curves of chalcopyrite follow the type III isotherm. The isotherm shows an excellent interface that is formed between the adsorbent and the adsorbed layer, suggesting a strong interaction between these two, showing multilayer adsorption taking place.[67]

The specific surface area of **sf-CuFeS$_2$** was found to be 36 m^2/g. The average pore size of chalcopyrite, as calculated from BJH plots (Figure 6b), was found to be ca. 17 Å. From the observations (high surface area and average pore size), it is clear that the nature of the sample is mesoporous, and the enhancement in the porosity is because of the surfactant-free synthesis. Since there is no other organic surfactant molecules surrounding **sf-CuFeS$_2$**, the whole surface area is available for catalytic activity.

The photophysical properties of the material were determined from the UV−Vis absorption spectrum. As is clear from Figure 7a, the chalcopyrite shows absorption mostly in the range of 300−800 nm, and the maximum absorption onset is at 480 nm. As discussed above, the $CuFeS_2$ band gap mostly varies in the range of 0.5−0.6 eV. The energy band gap (E_g) can be determined by extrapolating the linear region of the plot $(\alpha h\nu)^2$ vs. $h\nu$ to zero absorption as shown in eq 2.[41−43]

$$\alpha h\nu = A(h\nu - E_g)^2 \quad (2)$$

Where α is the optical adsorption coefficient, h is the Planck constant; ν is the frequency of light; E_g is the band gap energy. The band gap corresponding to the absorption onset calculated for **sf-CuFeS$_2$** by the Tauc plot given in eq 2 was found to be 0.81 eV (Figure 7b). Since the band gap is of a high value as depicted for chalcopyrite, the possible reason may be the quantum confinement.[68] This result showed that the removal of the surfactant is not affecting the band gap of **sf-CuFeS$_2$** nanoparticles significantly compared to $CuFeS_2$ nanoparticles reported earlier.

3.5. Catalytic Reduction of 4-NP. The potential of catalytic application of **sf-CuFeS$_2$** was confirmed by the reduction of toxic **4-NP** using $NaBH_4$. The schematic representation of **4-NP** reduction is shown in Scheme 2. The

Scheme 2. The Reduction of 4-NP on the Surface of the sf-CuFeS$_2$ Catalyst

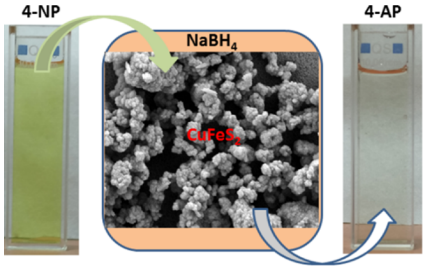

treatment of water contaminated with **4-NP** by this way of catalytic reduction is a realistic approach to deal with it. The reduction reaction is confirmed by the changes in the absorption spectrum of **4-NP** to **4-AP**. The UV−Vis spectrum of **4-NP** has strong absorption in the 317 nm range with a light yellow color. By the addition of $NaBH_4$, the light yellow color changed to bright yellow with the concomitant shift in the absorption peak to the 400 nm region (Figure 8a). This change in color is due to the transformation of 4-nitrophenol to its

https://dx.doi.org/10.1021/acs.jpcc.0c02697
J. Phys. Chem. C 2020, 124, 18010−18019

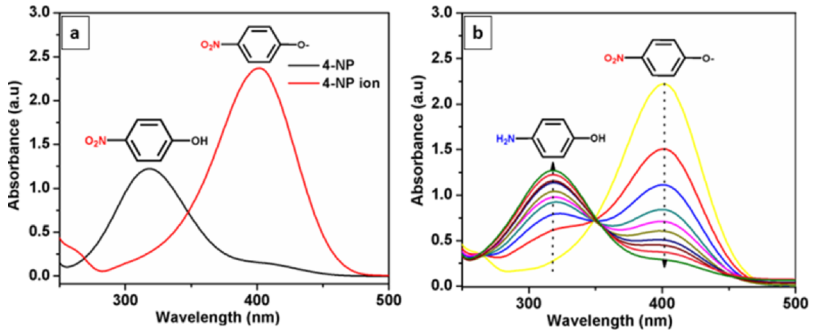

Figure 8. Effective role of the catalyst for **4-NP** reduction to **4-AP** with $NaBH_4$. (a) UV−Vis spectra of **4-NP** before and after adding $NaBH_4$ solution. (b) Continuous reduction of **4-NP** to **4-AP** in the presence of the **sf-$CuFeS_2$** catalyst.

corresponding phenoxide ion, 4-nitrophenolate ion, by the subsequent addition of $NaBH_4$.

When the solution with $NaBH_4$ was kept for a long time, it was observed that upon checking the UV spectra, there was no further decrease in intensity of the peak obtained at 400 nm (Figure S3a) for the phenolate ion, which indicates that without the addition of a catalyst (**sf-$CuFeS_2$**), no further reaction is possible. By the addition of a proper amount of the catalyst to the solution, the intensity of the peak at 400 nm was found to decrease swiftly, whereas another peak at the 318 nm region was found to increase in intensity as time progresses (Figure 8b).[69] The new peak at the 318 nm region gives an indication of the reduction of **4-NP**; the new peak corresponds to amine, thereby suggesting the formation of **4-AP**. On the other hand, the complete change of the color from yellow to colorless also indicates the formation of **4-AP** by the reduction of **4-NP**.

For studying the reaction kinetics of the reduction reaction, the change in concentration is determined from C_t/C_0 (Figure 9a), which in turn are measured from A_t/A_0 in terms of the

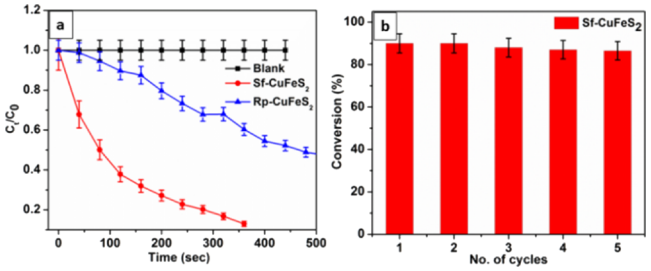

Figure 9. Plots showing the kinetics and stability of the synthesized **sf-$CuFeS_2$** for the reduction of **4-NP** with $NaBH_4$ and its comparison with Rp-$CuFeS_2$. (a) C_t/C_0. (b) Reusability of the catalyst.

change in relative intensity in the absorption spectrum at 400 nm. Here, C_t and C_0 are the **4-NP** concentration at time t and the initial concentration, respectively. The linear correlation between $\ln(C_t/C_0)$ and the reaction time shows that it is a first-order kinetics as given by eq 3.[70]

$$\ln(C_t/C_0) = -kt \tag{3}$$

Here, k indicates the first-order rate constant (s^{-1}), and t is the reaction time. The calculated value of k (Figure S3c) is found to be 5.21×10^{-3} s^{-1}, and the total time taken for the completion of reduction reaction is 6 min. Since this type of catalysis by $CuFeS_2$ is the first time reported by our group in this manuscript, a comparison of the catalytic activity of **sf-$CuFeS_2$** with other materials reported in the literature is given in Table 1. The data in the table clearly shows the superior

Table 1. Comparison List of 4-NP Reduction with Catalysts Reported in the Literature

catalyst	amount of the catalyst used	time of completion (min)	ref
Ag/Fe_3O_4	0.20 g/L	40	48
Au/AC	0.20 g/L	30	74
Au	0.15 g/L	30	75
Ag/PAN	10 mg	70	76
S-Ag	6 mg/5 mL	15	77
g-C_3N_4/CuS	10 mg	50	78
Cu catalyst	12.5 mg	50	79
$CuFe_2O_4$−G	20 mg	9	80
$Ag@CeO_2$	0.25 mg	2.1	81
sf-$CuFeS_2$	8 mg	6	this work

catalytic activity of **sf-$CuFeS_2$** in the reduction of **4-NP** to **4-AP**. For explaining the role of the catalyst, a controlled reaction (Figure S3a) was performed in the presence of an excess of $NaBH_4$, where there was no influence on the reaction by $NaBH_4$ besides serving as an electron donor.

The attractiveness of the HMDS-assisted synthetic approach is that the reaction yields materials without any surfactant molecules post-synthesis. In this method, HMDS itself serves the multiple roles of being a solvent, a stabilizing agent, and a reducing agent. Here, no external surfactants are added during reaction. Since the surface of the catalyst is free from any capping, **sf-$CuFeS_2$** showed better catalytic activity compared to the same materials prepared using a method reported in the literature. For comparison, we have prepared $CuFeS_2$ (named as Rp-$CuFeS_2$) by a known method and tested its catalytic activity in the reduction of **4-NP** (Figure 9a and Figure S3b).[71] The calculated value of k (Figure S3c) is 2.01×10^{-3} s^{-1}, which is much lower than the k observed for **sf-$CuFeS_2$**. This result highlights the advantages of the preparation of $CuFeS_2$ without a surfactant as well as the supremacy of the HMDS-assisted synthesis.

The mechanism of reduction of **4-NP** in the presence of **sf-$CuFeS_2$** using $NaBH_4$ can be explained as follows. When the catalyst is added to the reaction medium, both $NaBH_4$ and **4-NP** adsorb on the surface of the catalyst. The catalyst initiates the reduction process by the electron accepted from BH_4^- to **4-NP**. The adsorbed borohydride ion transfers surface hydrogen to the catalyst surface. Once the hydride gets adsorbed on the catalyst surface, it transfers its electron to the catalyst. In this electron transfer process, a hydrogen atom is

https://dx.doi.org/10.1021/acs.jpcc.0c02697
J. Phys. Chem. C 2020, 124, 18010−18019

generated, which attacks the nitro group of the **4-NP** molecule adsorbed on the catalyst surface. Through this electron transfer process from the catalyst to **4-NP**, the reduction of **4-NP** to **4-AP** takes place. The mechanistic pathway proposed here for the catalytic reduction of **4-NP** is similar to previously stated mechanisms including Langmuir−Hinshelwood mechanisms.[72,73]

The stability of the catalyst is the paramount factor for its application on a large scale. Therefore, to determine stability, the reusability of the catalyst was checked by repeating the catalytic reduction of **4-NP** using the recuperated catalyst. While performing the reusability test, the catalyst was separated by centrifugation (3000 rpm) and repeatedly washed with water and acetone and dried in a vacuum. Attractively, the chalcopyrite presented excellent stability with no appreciable reduction in activity until the 5th cycle (Figure 9b). Only after the fifth catalytic cycle, a slight reduction in activity was observed. The structural analysis and morphological observations of the used catalyst revealed (Figure S4) the good stability of **sf-CuFeS$_2$** as a catalyst for **4-NP** reduction.[82]

The effect of changes in the amount of the catalyst on the conversion efficiency was tested. The catalyst amounts were increased from 4 to 8 mg by keeping other parameters constant. As shown in Figure 10, with the increase in the

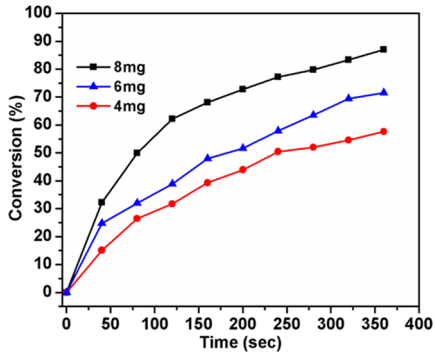

Figure 10. Effect of the catalyst dosage on the conversion efficiency of **4-NP**.

catalyst dosage, the rate of conversion efficiency also increased. The efficiency was found to increase from 58 to 89%. The increase in efficiency with catalyst dosage is probably because of the increase in the number of active sites.

Besides this, the effect of initial concentrations of **4-NP** on the conversion efficiency of the catalytic process was tested, keeping the amount of the catalyst constant at 8 mg/100 mL as well as 0.1 M $NaBH_4$. As shown in Figure S5, with the increase in substrate concentration from 0.1 to 0.3 mM, the conversion efficiency decreased from 89 to 46%, showing that the initial concentration of the substrate has a significant influence on the conversion efficiency of the catalyst. The figure shows that conversion efficiency directly depends on both the amount of the catalyst and pollutant concentration used. The decrease in efficiency might be due to a decrease in the number of active sites on the catalyst. Because of the increase in substrate concentration due to easy access, more of the active sites on the catalyst are occupied, leaving fewer active sites for the new entrant on the catalyst.

4. CONCLUSIONS

In summary, chalcopyrite with a high surface area was synthesized by an HMDS-assisted wet-chemical method. After a successful synthesis, the materials were subjected to various analytical characterizations. The **sf-CuFeS$_2$** is of a highly crystalline nature with no other phase impurities, as confirmed by PXRD. Both SEM and TEM determined and confirmed the particle morphology of nanostructures. The study of magnetic properties of **sf-CuFeS$_2$** revealed its paramagnetic nature. Measurement of dielectric properties showed a reduction in the values initially at low frequencies, which then remains unchanged at higher frequencies. The chalcopyrite exhibited superior catalytic activity on the reduction of **4-NP** most likely because of clean surfaces on the catalyst and high surface area. This work corroborates new ways for the designing of materials with multiple roles like in catalysis and energy storing devices.

■ ASSOCIATED CONTENT

Supporting Information

The Supporting Information is available free of charge at https://pubs.acs.org/doi/10.1021/acs.jpcc.0c02697.

High-magnification FESEM, dark-field TEM images, and SAED patterns of **sf-CuFeS$_2$**; EDAX of **sf-CuFeS$_2$**; controlled reaction by using $NaBH_4$, kinetics confirming the first-order rate constant; structural and morphological studies after catalysis (PDF)

■ AUTHOR INFORMATION

Corresponding Author

Krishnamurthi Muralidharan − *School of Chemistry, University of Hyderabad, Hyderabad 500046, India;* orcid.org/0000-0003-0529-2447; Email: murali@uohyd.ac.in

Authors

Manzoor Ahmad Pandit − *School of Chemistry, University of Hyderabad, Hyderabad 500046, India*

Dasari Sai Hemanth Kumar − *School of Chemistry, University of Hyderabad, Hyderabad 500046, India*

Srinivas Billakanti − *School of Chemistry, University of Hyderabad, Hyderabad 500046, India*

Manigandan Ramadoss − *School of Chemistry, University of Hyderabad, Hyderabad 500046, India;* orcid.org/0000-0001-9633-0220

Complete contact information is available at: https://pubs.acs.org/10.1021/acs.jpcc.0c02697

Notes

The authors declare no competing financial interest.

■ ACKNOWLEDGMENTS

M.A.P thanks the UGC-BSR for fellowship. We thank the Centre for Nano Science and Technology (for TEM) and School of Physics (for PXRD), University of Hyderabad. Financial and infrastructure support from the University Grants Commission, New Delhi, India (through the UPE and CAS programs) and the Department of Science and Technology, New Delhi, India (through the PURSE and FIST programs) are gratefully acknowledged.

REFERENCES

(1) Berends, A. C.; Mangnus, M. J. J.; Xia, C.; Rabouw, F. T.; de Mello Donega, C. Optoelectronic Properties of Ternary I−III−VI_2 Semiconductor Nanocrystals: Bright Prospects with Elusive Origins. *J. Phys. Chem. Lett.* **2019**, *10*, 1600−1616.

(2) Zhang, Y.; Yang, Y.; Hou, Z.; Jiang, X.; Zhang, L.; Yang, Y.; Wang, Y. The Effect of Reaction Temperature and Time on $CuInSe_2$ Quantum Dots by Solvothermal Method. *AIP Adv.* **2020**, *10*, No. 035313.

(3) Matthews, P. D.; McNaughter, P. D.; Lewis, D. J.; O'Brien, P. Shining a Light on Transition Metal Chalcogenides for Sustainable Photovoltaics. *Chem. Sci.* **2017**, *8*, 4177−4187.

(4) Marrón, D. F.; Martí, A.; Luque, A. Thin-Film Intermediate Band Photovoltaics: Advanced Concepts for Chalcopyrite Solar Cells. *Phys. Status Solidi A* **2009**, *206*, 1021−1025.

(5) Tu, X.; Li, M.; Su, Y.; Yin, G.; Lu, J.; He, D. Self-Templated Growth of $CuInS_2$ Nanosheet Arrays for Photoelectrochemical Water Splitting. *J. Alloys Compd.* **2019**, *809*, 151794.

(6) Kolny-Olesiak, J.; Weller, H. Synthesis and Application of Colloidal $CuInS_2$ Semiconductor Nanocrystals. *ACS Appl. Mater. Interfaces* **2013**, *5*, 12221−12237.

(7) Yarema, O.; Yarema, M.; Wood, V. Tuning the Composition of Multicomponent Semiconductor Nanocrystals: The Case of I−III−VI Materials. *Chem. Mater.* **2018**, *30*, 1446−1461.

(8) van der Stam, W.; Berends, A. C.; de Mello Donega, C. Prospects of Colloidal Copper Chalcogenide Nanocrystals. *ChemPhysChem* **2016**, *17*, 559−581.

(9) Aldakov, D.; Lefrançois, A.; Reiss, P. Ternary and Quaternary Metal Chalcogenide Nanocrystals: Synthesis, Properties and Applications. *J. Mater. Chem. C* **2013**, *1*, 3756−3776.

(10) Gabka, G.; Bujak, P.; Żukrowski, J.; Zabost, D.; Kotwica, K.; Malinowska, K.; Ostrowski, A.; Wielgus, I.; Lisowski, W.; Sobczak, J. W.; Przybylski, M.; Pron, A. Non-Injection Synthesis of Monodisperse Cu-Fe-S Nanocrystals and Their Size Dependent Properties. *Phys. Chem. Chem. Phys.* **2016**, *18*, 15091−15101.

(11) Nasluzov, V.; Shor, A.; Romanchenko, A.; Tomashevich, Y.; Mikhlin, Y. DFT + U and Low-Temperature XPS Studies of Fe-Depleted Chalcopyrite ($CuFeS_2$) Surfaces: A Focus on Polysulfide Species. *J. Phys. Chem. C* **2019**, *123*, 21031−21041.

(12) Zhang, Z.; Xu, B.; Zhang, L.; Ren, S. Hybrid Chalcopyrite−Polymer Magnetoconducting Materials. *ACS Appl. Mater. Interfaces* **2016**, *8*, 11215−11220.

(13) Conejeros, S.; Alemany, P.; Llunell, M.; Moreira, I. d. P. R.; Sánchez, V.; Llanos, J. Electronic Structure and Magnetic Properties of $CuFeS_2$. *Inorg. Chem.* **2015**, *54*, 4840−4849.

(14) Zhang, P.; Zhang, Y.-X.; Lai, H.; Deng, J.; Feng, J.; Ge, Z.-H. Enhanced Thermoelectric Properties of Natural Chalcopyrite by Vacuum Annealing. *Mater. Lett.* **2019**, *253*, 430−433.

(15) Sherbini, M. A. E.; Yousef, Y. L. The Effect of Cooling and of Magnetic Fields on Crystal Rectification. *Proc. Phys. Soc.* **1939**, *51*, 449−455.

(16) Wang, M. X.; Wang, L. S.; Yue, G. H.; Wang, X.; Yan, P. X.; Peng, D. L. Single Crystal of $CuFeS_2$ Nanowires Synthesized Through Solventothermal Process. *Mater. Chem. Phys.* **2009**, *115*, 147−150.

(17) Disale, S. D.; Garje, S. S. A Convenient Synthesis of Nanocrystalline Chalcopyrite, $CuFeS_2$ using Single-Source Precursors. *Appl. Organomet. Chem.* **2009**, *23*, 492−497.

(18) Boekema, C.; Krupski, A. M.; Varasteh, M.; Parvin, K.; Van Til, F.; Van Der Woude, F.; Sawatzky, G. A. Cu and Fe Valence States in $CuFeS_2$. *J. Magn. Magn. Mater.* **2004**, *272-276*, 559−561.

(19) Sato, K.; Harada, Y.; Taguchi, M.; Shin, S.; Fujimori, A. Characterization of Fe 3d States in $CuFeS_2$ by Resonant X-ray Emission Spectroscopy. *Phys. Status Solidi A* **2009**, *206*, 1096−1100.

(20) Engin, T. E.; Powell, A. V.; Hull, S. A High Temperature Diffraction-Resistance Study of Chalcopyrite, $CuFeS_2$. *J. Solid State Chem.* **2011**, *184*, 2272−2277.

(21) Woolley, J. C.; Lamarche, A. M.; Lamarche, G.; Quintero, M.; Swainson, I. P.; Holden, T. M. Low Temperature Magnetic Behaviour of $CuFeS_2$ from Neutron Diffraction Data. *J. Magn. Magn. Mater.* **1996**, *162*, 347−354.

(22) Knight, K. S.; Marshall, W. G.; Zochowski, S. W. The LowTemperature and High-Pressure Thermoelastic and Structural Properties of Chalcopyrite, $CuFeS_2$. *Can. Mineral.* **2011**, *49*, 1015−1034.

(23) Silvester, E. J.; Healy, T. W.; Grieser, F.; Sexton, B. A. Hydrothermal Preparation and Characterization of Optically Transparent Colloidal Chalcopyrite ($CuFeS_2$). *Langmuir* **1991**, *7*, 19−22.

(24) Oguchi, T.; Sato, K.; Teranishi, T. Optical Reflectivity Spectrum of a $CuFeS_2$ Single Crystal. *J. Phys. Soc. Jpn.* **1980**, *48*, 123−128.

(25) Wang, Y.-H. A.; Bao, N.; Gupta, A. Shape-Controlled Synthesis of Semiconducting $CuFeS_2$ Nanocrystals. *Solid State Sci.* **2010**, *12*, 387−390.

(26) Liang, D.; Ma, R.; Jiao, S.; Pang, G.; Feng, S. A Facile Synthetic Approach for Copper Iron Sulfide Nanocrystals with Enhanced Thermoelectric Performance. *Nanoscale* **2012**, *4*, 6265−6268.

(27) Barkat, L.; Hamdadou, N.; Morsli, M.; Khelil, A.; Bernède, J. C. Growth and Characterization of $CuFeS_2$ Thin Films. *J. Cryst. Growth* **2006**, *297*, 426−431.

(28) Wang, C.; Xue, S.; Hu, J.; Tang, K. Raman, Far Infrared, and Mössbauer Spectroscopy of $CuFeS_2$ Nanocrystallites. *Jpn. J. Appl. Phys.* **2009**, *48*, No. 023003.

(29) Wu, Y.; Zhou, B.; Yang, C.; Liao, S.; Zhang, W.-H.; Li, C. $CuFeS_2$ Colloidal Nanocrystals as an Efficient Electrocatalyst for Dye Sensitized Solar Cells. *Chem. Commun.* **2016**, *52*, 11488−11491.

(30) Dalui, A.; Pradhan, B.; Thupakula, U.; Khan, A. H.; Kumar, G. S.; Ghosh, T.; Satpati, B.; Acharya, S. Insight into the Mechanism Revealing the Peroxidase Mimetic Catalytic Activity of Quaternary CuZnFeS Nanocrystals: Colorimetric Biosensing of Hydrogen Peroxide and Glucose. *Nanoscale* **2015**, *7*, 9062−9074.

(31) Gan, D.; Liu, M.; Huang, H.; Chen, J.; Dou, J.; Wen, Y.; Huang, Q.; Yang, Z.; Zhang, X.; Wei, Y. Facile Preparation of Functionalized Carbon Nanotubes with Tannins Through Mussel-Inspired Chemistry and their Application in Removal of Methylene Blue. *J. Mol. Liq.* **2018**, *271*, 246−253.

(32) Huang, Q.; Liu, M.; Mao, L.; Xu, D.; Zeng, G.; Huang, H.; Jiang, R.; Deng, F.; Zhang, X.; Wei, Y. Surface Functionalized SiO_2 Nanoparticles with Cationic Polymers Via the Combination of Mussel Inspired Chemistry and Surface Initiated Atom Transfer Radical Polymerization: Characterization and Enhanced Removal of Organic Dye. *J. Colloid Interface Sci.* **2017**, *499*, 170−179.

(33) Huang, Q.; Liu, M.; Chen, J.; Wan, Q.; Tian, J.; Huang, L.; Jiang, R.; Wen, Y.; Zhang, X.; Wei, Y. Facile Preparation of MoS_2 Based Polymer Composites Via mussel Inspired Chemistry and their High Efficiency for Removal of Organic Dyes. *Appl. Surf. Sci.* **2017**, *419*, 35−44.

(34) Zeng, G.; Huang, L.; Huang, Q.; Liu, M.; Xu, D.; Huang, H.; Yang, Z.; Deng, F.; Zhang, X.; Wei, Y. Rapid Synthesis of MoS2-PDA-Ag Nanocomposites as Heterogeneous Catalysts and Antimicrobial Agents via Microwave Irradiation. *Appl. Surf. Sci.* **2018**, *459*, 588−595.

(35) Dou, J.; Gan, D.; Huang, Q.; Liu, M.; Chen, J.; Deng, F.; Zhu, X.; Wen, Y.; Zhang, X.; Wei, Y. Functionalization of Carbon Nanotubes With Chitosan Based on MALI Multicomponent Reaction for Cu^{2+} Removal. *Int. J. Biol. Macromol.* **2019**, *136*, 476−485.

(36) Gan, D.; Huang, Q.; Dou, J.; Huang, H.; Chen, J.; Liu, M.; Wen, Y.; Yang, Z.; Zhang, X.; Wei, Y. Bioinspired Functionalization of MXenes (Ti_3C_2TX) with Amino Acids for Efficient Removal of Heavy Metal Ions. *Appl. Surf. Sci.* **2020**, *504*, 144603.

(37) Huang, Q.; Liu, M.; Zhao, J.; Chen, J.; Zeng, G.; Huang, H.; Tian, J.; Wen, Y.; Zhang, X.; Wei, Y. Facile Preparation of Polyethylenimine-Tannins Coated SiO_2 Hybrid Materials for Cu^{2+} Removal. *Appl. Surf. Sci.* **2018**, *427*, 535−544.

(38) Pandit, M. A.; Billakanti, S.; Muralidharan, K. A Simplistic Approach for the Synthesis of CuS-CdS Heterostructure: A Novel Photocatalyst for Oxidative Dye Degradation. *J. Environ. Chem. Eng.* **2020**, *8*, 103542.

https://dx.doi.org/10.1021/acs.jpcc.0c02697
J. Phys. Chem. C 2020, 124, 18010−18019

(39) Srinivas, B.; Pandit, M. A.; Muralidharan, K. Importance of Clean Surfaces on the Catalyst: SnS_2 Nanorings for Environmental Remediation. *ACS Omega* **2019**, *4*, 14970−14980.
(40) Lei, Y.; Cui, Y.; Huang, Q.; Dou, J.; Gan, D.; Deng, F.; Liu, M.; Li, X.; Zhang, X.; Wei, Y. Facile Preparation of Sulfonic Groups Functionalized Mxenes for Efficient Removal of Methylene Blue. *Ceram. Int.* **2019**, *45*, 17653−17661.
(41) Manigandan, R.; Dhanasekaran, T.; Padmanaban, A.; Giribabu, K.; Suresh, R.; Narayanan, V. Bifunctional Hexagonal Ni/NiO Nanostructures: Influence of the Core−Shell Phase on Magnetism, Electrochemical Sensing of Serotonin, and Catalytic Reduction of 4-Nitrophenol. *Nanoscale Adv.* **2019**, *1*, 1531−1540.
(42) Zhang, X.; Huang, Q.; Liu, M.; Tian, J.; Zeng, G.; Li, Z.; Wang, K.; Zhang, Q.; Wan, Q.; Deng, F.; Wei, Y. Preparation of Amine Functionalized Carbon Nanotubes via a Bioinspired Strategy and their Application in Cu^{2+} Removal. *Appl. Surf. Sci.* **2015**, *343*, 19−27.
(43) Huang, Q.; Zhao, J.; Liu, M.; Li, Y.; Ruan, J.; Li, Q.; Tian, J.; Zhu, X.; Zhang, X.; Wei, Y. Synthesis of Polyacrylamide Immobilized Molybdenum DiSulfide (MoS_2@PDA@PAM) Composites via Mussel-Inspired Chemistry and Surface-Initiated Atom Transfer Radical Polymerization for Removal of Copper (II) Ions. *J. Taiwan Inst. Chem. Eng.* **2018**, *86*, 174−184.
(44) Liu, Y.; Huang, H.; Gan, D.; Guo, L.; Liu, M.; Chen, J.; Deng, F.; Zhou, N.; Zhang, X.; Wei, Y. A Facile Strategy for Preparation of Magnetic Graphene Oxide Composites and their Potential for Environmental Adsorption. *Ceram. Int.* **2018**, *44*, 18571−18577.
(45) Zeng, G.; Liu, X.; Liu, M.; Huang, Q.; Xu, D.; Wan, Q.; Huang, H.; Deng, F.; Zhang, X.; Wei, Y. Facile Preparation of Carbon Nanotubes Based Carboxymethyl Chitosan Nanocomposites Through Combination of Mussel Inspired Chemistry and Michael Addition Reaction: Characterization and Improved Cu^{2+} Removal Capability. *J. Taiwan Inst. Chem. Eng.* **2016**, *68*, 446−454.
(46) Huang, Q.; Zhao, J.; Liu, M.; Chen, J.; Zhu, X.; Wu, T.; Tian, J.; Wen, Y.; Zhang, X.; Wei, Y. Preparation of Polyethylene Polyamine@Tannic Acid Encapsulated MgAl-Layered Double Hydroxide for the Efficient Removal of Copper (II) Ions from Aqueous solution. *J. Taiwan Inst. Chem. Eng.* **2018**, *82*, 92−101.
(47) Chang, Y.-C.; Chen, D.-H. Catalytic Reduction of 4-Nitrophenol by Magnetically Recoverable Au Nanocatalyst. *J. Hazard. Mater.* **2009**, *165*, 664−669.
(48) Chiou, J.-R.; Lai, B.-H.; Hsu, K.-C.; Chen, D.-H. One-Pot Green Synthesis of Silver/Iron Oxide Composite Nanoparticles for 4-Nitrophenol Reduction. *J. Hazard. Mater.* **2013**, *248-249*, 394−400.
(49) Yao, Y.-X.; Li, H.-B.; Liu, J.-Y.; Tan, X.-L.; Yu, J.-G.; Peng, Z.-G. Removal and Adsorption of p-Nitrophenol from Aqueous Solutions Using Carbon Nanotubes and Their Composites. *J. Nanomater.* **2014**, *2014*, 1−9.
(50) Hamidouche, S.; Bouras, O.; Zermane, F.; Cheknane, B.; Houari, M.; Debord, J.; Harel, M.; Bollinger, J.-C.; Baudu, M. Simultaneous Sorption of 4-Nitrophenol and 2-Nitrophenol on a Hybrid geocomposite Based on Surfactant Modified Pillared-Clay and Activated Carbon. *Chem. Eng. J.* **2015**, *279*, 964−972.
(51) Ivančev-Tumbas, I.; Hobby, R.; Küchle, B.; Panglisch, S.; Gimbel, R. p-Nitrophenol Removal by Combination of Powdered Activated Carbon Adsorption and Ultrafiltration-Comparison of Different Operational Modes. *Water Res.* **2008**, *42*, 4117−4124.
(52) Mehrizad, A.; Zare, K.; Aghaie, H.; Dastmalchi, S. Removal of 4-Chloro-2-Nitrophenol Occurring in Drug and Pesticide Waste by Adsorption onto Nano-Titanium Dioxide. *Int. J. Environ. Sci. Technol.* **2012**, *9*, 355−360.
(53) Das, S. K.; Khan, M. M. R.; Guha, A. K.; Naskar, N. Bio-Inspired Fabrication of Silver Nanoparticles on Nanostructured Silica: Characterization and Application as a Highly Efficient Hydrogenation Catalyst. *Green Chem.* **2013**, *15*, 2548−2557.
(54) Holden, M. S.; Nick, K. E.; Hall, M.; Milligan, J. R.; Chen, Q.; Perry, C. C. Synthesis and Catalytic Activity of Pluronic Stabilized Silver−Gold Bimetallic Nanoparticles. *RSC Adv.* **2014**, *4*, 52279−52288.
(55) Magdy, Y. M.; Altaher, H.; ElQada, E. Removal of Three Nitrophenols from Aqueous Solutions by Adsorption onto Char Ash: Equilibrium and Kinetic Modeling. *Appl. Water Sci.* **2018**, *8*, 26.
(56) Veisi, H.; Kazemi, S.; Mohammadi, P.; Safarimehr, P.; Hemmati, S. Catalytic reduction of 4-nitrophenol Over Ag nanoparticles Immobilized on Stachys Lavandulifolia Extract-Modified Multi Walled Carbon Nanotubes. *Polyhedron* **2019**, *157*, 232−240.
(57) Gabka, G.; Bujak, P.; Ostrowski, A.; Tomaszewski, W.; Lisowski, W.; Sobczak, J. W.; Pron, A. Cu−Fe−S Nanocrystals Exhibiting Tunable Localized Surface Plasmon Resonance in the Visible to NIR Spectral Ranges. *Inorg. Chem.* **2016**, *55*, 6660−6669.
(58) Yu, J.; Ran, J. Facile Preparation and Enhanced Photocatalytic H_2-Production Activity of $Cu(OH)_2$ Cluster Modified TiO_2. *Energy Environ. Sci.* **2011**, *4*, 1364−1371.
(59) Naik, S. R.; Salker, A. V. Change in the Magnetostructural Properties of Rare Earth Doped Cobalt Ferrites Relative to the Magnetic Anisotropy. *J. Mater. Chem.* **2012**, *22*, 2740−2750.
(60) Girma, W. M.; Tzing, S.-H.; Tseng, P.-J.; Huang, C.-C.; Ling, Y.-C.; Chang, J.-Y. Synthesis of Cisplatin(IV) Prodrug-Tethered $CuFeS_2$ Nanoparticles in Tumor-Targeted Chemotherapy and Photothermal Therapy. *ACS Appl. Mater. Interfaces* **2018**, *10*, 4590−4602.
(61) Jeyagopal, R.; Chen, Y.; Ramadoss, M.; Marimuthu, K.; Wang, B.; Li, W.; Zhang, X. A Three-Dimensional Porous CoSnS@CNT Nanoarchitecture as a Highly Efficient Bifunctional Catalyst for Boosted OER Performance and Photocatalytic Degradation. *Nanoscale* **2020**, *12*, 3879−3887.
(62) Kobayashi, K.; Azuma, Y.; Kawashima, K.; Horigane, K.; Akaki, M.; Tokunaga, M.; Akimitsu, J. Magnetic Properties of Chalcopyrite $Cu_{1-x}FeS_2$ at Low Temperatures. *JPS Conf. Proc.* **2014**, *3*, No. 017020.
(63) Farooq, U.; Phul, R.; Alshehri, S. M.; Ahmed, J.; Ahmad, T. Electrocatalytic and Enhanced Photocatalytic Applications of Sodium Niobate Nanoparticles Developed by Citrate Precursor Route. *Sci. Rep.* **2019**, *9*, 4488.
(64) Lesmes, D. P.; Morgan, F. D. Dielectric Spectroscopy of Sedimentary Rocks. *J. Geophys. Res.: Solid Earth* **2001**, *106*, 13329−13346.
(65) Ahmad, T.; Lone, I. H. Citrate Precursor Synthesis and Multifunctional Properties of $YCrO_3$ Nanoparticles. *New J. Chem.* **2016**, *40*, 3216−3224.
(66) Prameena, B.; Anbalagan, G.; Gunasekaran, S.; Ramkumaar, G. R.; Gowtham, B. Structural, Optical, Electron Paramagnetic, Thermal and Dielectric Characterization of Chalcopyrite. *Spectrochim. Acta, Part A* **2014**, *122*, 348−355.
(67) Thommes, M.; Kaneko, K.; Neimark, A. V.; Olivier, J. P.; Rodriguez-Reinoso, F.; Rouquerol, J.; Sing, K. S. W. Physisorption of Gases, with Special Reference to the Evaluation of Surface Area and Pore Size Distribution (IUPAC Technical Report). *Pure Appl. Chem.* **2015**, *87*, 1051−1069.
(68) Tonpe, D.; Gattu, K.; More, G.; Upadhye, D.; Mahajan, S.; Sharma, R. Synthesis of $CuFeS_2$ Thin Films From Acidic Chemical Baths. *AIP Conf. Proc.* **2016**, *1728*, No. 020676.
(69) Yuan, M.; Yang, R.; Wei, S.; Hu, X.; Xu, D.; Yang, J.; Dong, Z. Ultra-Fine Pd Nanoparticles Confined in a Porous Organic Polymer: A Leaching-and-Aggregation-Resistant Catalyst for the Efficient Reduction of Nitroarenes by $NaBH_4$. *J. Colloid Interface Sci.* **2019**, *538*, 720−730.
(70) Dong, Z.; Le, X.; Li, X.; Zhang, W.; Dong, C.; Ma, J. Silver Nanoparticles Immobilized on Fibrous Nano-Silica as Highly Efficient and Recyclable Heterogeneous Catalyst for Reduction of 4-Nitrophenol and 2-Nitroaniline. *Appl. Catal., B* **2014**, *158-159*, 129−135.
(71) Hu, J.; Lu, Q.; Tang, K.; Qian, Y.; Zhou, G.; Liu, X. A Solvothermal Reaction Route for the Synthesis of $CuFeS_2$ Ultrafine Powder. *J. Mater. Res.* **1999**, *14*, 3870−3872.
(72) Baruah, B.; Gabriel, G. J.; Akbashev, M. J.; Booher, M. E. Facile Synthesis of Silver Nanoparticles Stabilized by Cationic Polynorbornenes and Their Catalytic Activity in 4-Nitrophenol Reduction. *Langmuir* **2013**, *29*, 4225−4234.

(73) Wunder, S.; Polzer, F.; Lu, Y.; Mei, Y.; Ballauff, M. Kinetic Analysis of Catalytic Reduction of 4-Nitrophenol by Metallic Nanoparticles Immobilized in Spherical Polyelectrolyte Brushes. *J. Phys. Chem. C* **2010**, *114*, 8814−8820.
(74) Kumar, A.; Belwal, M.; Maurya, R. R.; Mohan, V.; Vishwanathan, V. Heterogeneous Catalytic Reduction of Anthropogenic Pollutant, 4-Nitrophenol by Au/AC Nanocatalysts. *Mater. Sci. Energy Technol.* **2019**, *2*, 526−531.
(75) Guo, P.; Tang, L.; Tang, J.; Zeng, G.; Huang, B.; Dong, H.; Zhang, Y.; Zhou, Y.; Deng, Y.; Ma, L.; Tan, S. Catalytic Reduction−Adsorption for Removal of p-Nitrophenol and its Conversion p-Aminophenol from Water by Gold Nanoparticles Supported on Oxidized Mesoporous Carbon. *J. Colloid Interface Sci.* **2016**, *469*, 78−85.
(76) Gao, S.; Zhang, Z.; Liu, K.; Dong, B. Direct Evidence of Plasmonic Enhancement on Catalytic Reduction of 4-Nitrophenol Over Silver Nanoparticles Supported on Flexible Fibrous Networks. *Appl. Catal., B* **2016**, *188*, 245−252.
(77) Kalantari, K.; Afifi, A. B. M.; Bayat, S.; Shameli, K.; Yousefi, S.; Mokhtar, N.; Kalantari, A. Heterogeneous Catalysis in 4-Nitrophenol Degradation and Antioxidant Activities of Silver NanoParticles Embedded in Tapioca Starch. *Arabian J. Chem.* **2019**, *12*, 5246−5252.
(78) Ayodhya, D.; Veerabhadram, G. Influence of g-C_3N_4 and g-C_3N_4 Nano Sheets Supported CuS Coupled System with Effect of pH on the Catalytic Activity of 4-NP Reduction Using $NaBH_4$. *FlatChem* **2019**, *14*, 100088.
(79) Deka, P.; Deka, R. C.; Bharali, P. In Situ Generated Copper Nanoparticle Catalyzed Reduction of 4-Nitrophenol. *New J. Chem.* **2014**, *38*, 1789−1793.
(80) Zhang, H.; Gao, S.; Shang, N.; Wang, C.; Wang, Z. Copper Ferrite−Graphene Hybrid: A Highly Efficient Magnetic Catalyst for Chemoselective Reduction of Nitroarenes. *RSC Adv.* **2014**, *4*, 31328−31332.
(81) Shi, Y.; Zhang, X.; Zhu, Y.; Tan, H.; Chen, X.; Lu, Z.-H. Core−Shell Structured Nanocomposites Ag@CeO_2 as Catalysts for Hydrogenation of 4-Nitrophenol and 2-Nitroaniline. *RSC Adv.* **2016**, *6*, 47966−47973.
(82) Lu, Z.-H.; Li, J.; Zhu, A.; Yao, Q.; Huang, W.; Zhou, R.; Zhou, R.; Chen, X. Catalytic Hydrolysis of Ammonia Borane via Magnetically Recyclable Copper Iron Nanoparticles for Chemical Hydrogen Storage. *Int. J. Hydrogen Energy* **2013**, *38*, 5330−5337.

https://dx.doi.org/10.1021/acs.jpcc.0c02697
J. Phys. Chem. C 2020, 124, 18010−18019

Surfactant-Free Synthesis of Metal Chalcogenides and their Role as Catalyst for Environmental Remediation and Electrochemical Oxygen Evolution Reaction (OER)

by Manzoor Ahmad Pandit

Surfactant-Free Synthesis of Metal Chalcogenides and their Role as Catalyst for Environmental Remediation and Electrochemical Oxygen Evolution Reaction (OER)

ORIGINALITY REPORT

K. Mur 16/9/2020

53% SIMILARITY INDEX

.K. MURALIDHARAN Professor School of Chemistry University of Hyderabad Hyderabad - 500 046.

% INTERNET SOURCES

% PUBLICATIONS

% STUDENT PAPERS

PRIMARY SOURCES

1	Manzoor Ahmad Pandit, Srinivas Billakanti, Krishnamurthi Muralidharan. "A simplistic approach for the synthesis of CuS-CdS heterostructure: A novel photo catalyst for oxidative dye degradation", Journal of Environmental Chemical Engineering, 2020 Publication	18% Self plagiarism K. Mur 16/9/2020 .K. MURALIDHARAN Professor School of Chemistry University of Hyderabad Hyderabad - 500 046.
2	Billakanti Srinivas, Manzoor Ahmad Pandit, Krishnamurthi Muralidharan. " Importance of Clean Surfaces on the Catalyst: SnS Nanorings for Environmental Remediation ", ACS Omega, 2019 Publication	17% Self plagiarism K. Mur 16/9/2020 .K. MURALIDHARAN Professor School of Chemistry University of Hyderabad Hyderabad - 500 046.
3	Manzoor Ahmad Pandit, Dasari Sai Hemanth Kumar, Srinivas Billakanti, Manigandan Ramadoss, Krishnamurthi Muralidharan. "Chalcopyrite with Magnetic and Dielectric Properties: An Introductory Catalyst for 4-Nitrophenol Reduction", The Journal of Physical	10% Self plagiarism K. Mur 16/9/2020 .K. MURALIDHARAN Professor School of Chemistry University of Hyderabad Hyderabad - 500 046.

Chemistry C, 2020
Publication

4	Manzoor Ahmad Pandit, Sai Hemanth Kumar Nil Dasari, Srinivas Billakanti, Manigandan Ramadoss, Krishnamurthi Muralidharan. "Chalcopyrite with Magnetic and Dielectric Properties: An Introductory Catalyst for 4-Nitrophenol Reduction", The Journal of Physical Chemistry C, 2020 Publication	7%
5	www.ncbi.nlm.nih.gov Internet Source	1%
6	Submitted to University of Hyderabad, Hyderabad Student Paper	<1%
7	Srinivas Billakanti, Muralidharan Krishnamurthi. "Facile preparation of surfactant or support material free CdS nanoparticles with enhanced photocatalytic activity", Journal of Environmental Chemical Engineering, 2018 Publication	<1%
8	scholarbank.nus.edu.sg Internet Source	<1%
9	Mani Sakthivel, Sukanya Ramaraj, Shen-Ming Chen, Bose Dinesh, Hari Vignesh Ramasamy, Y.S. Lee. "Entrapment of bimetallic CoFeSe2 nanosphere on functionalized carbon nanofiber	<1%

Self plagiarism
K. [illegible] 16/9/2020

K. MURALIDHARAN
Professor
School of Chemistry
University of Hyderabad
Hyderabad - 500 046.

Surfactant-Free Synthesis of Metal Chalcogenides and their Role as Catalyst for Environmental Remediation and Electrochemical Oxygen Evolution Reaction (OER)

by Manzoor Ahmad Pandit

Surfactant-Free Synthesis of Metal Chalcogenides and their Role as Catalyst for Environmental Remediation and Electrochemical Oxygen Evolution Reaction (OER)

ORIGINALITY REPORT

60%	%	%	%
SIMILARITY INDEX	INTERNET SOURCES	PUBLICATIONS	STUDENT PAPERS

K. MURALIDHARAN Professor School of Chemistry University of Hyderabad Hyderabad - 500 046.

PRIMARY SOURCES

1	Manzoor Ahmad Pandit, Srinivas Billakanti, Krishnamurthi Muralidharan. "A simplistic approach for the synthesis of CuS-CdS heterostructure: A novel photo catalyst for oxidative dye degradation", Journal of Environmental Chemical Engineering, 2020 Publication	22% Self plagiarism
2	Billakanti Srinivas, Manzoor Ahmad Pandit, Krishnamurthi Muralidharan. " Importance of Clean Surfaces on the Catalyst: SnS Nanorings for Environmental Remediation ", ACS Omega, 2019 Publication	20% Self plagiarism
3	Manzoor Ahmad Pandit, Dasari Sai Hemanth Kumar, Srinivas Billakanti, Manigandan Ramadoss, Krishnamurthi Muralidharan. "Chalcopyrite with Magnetic and Dielectric Properties: An Introductory Catalyst for 4-Nitrophenol Reduction", The Journal of Physical	10% Self plagiarism

Chemistry C, 2020
Publication

4	Manzoor Ahmad Pandit, Sai Hemanth Kumar Nil Dasari, Srinivas Billakanti, Manigandan Ramadoss, Krishnamurthi Muralidharan. "Chalcopyrite with Magnetic and Dielectric Properties: An Introductory Catalyst for 4-Nitrophenol Reduction", The Journal of Physical Chemistry C, 2020 Publication	7%
5	www.ncbi.nlm.nih.gov Internet Source	1%
6	Submitted to University of Hyderabad, Hyderabad Student Paper	<1%
7	www.picoquant.com Internet Source	<1%
8	scholarbank.nus.edu.sg Internet Source	<1%
9	Submitted to Imperial College of Science, Technology and Medicine Student Paper	<1%
10	Srinivas Billakanti, Ganesh Kumar Baskaran, Krishnamurthi Muralidharan. " Recyclable Ni S Nanocatalyst for Hydrogenation of Nitroarenes ", ChemistrySelect, 2017	<1%

Sel/t plagiarism
K. M 16/9/2020

K. MURALIDHARAN
Professor
School of Chemistry
University of Hyderabad
Hyderabad - 500 046.

Publication

11	"Eco-friendly Polymer Nanocomposites", Springer Science and Business Media LLC, 2015 Publication	<1%
12	Srinivas Billakanti, Muralidharan Krishnamurthi. "Facile preparation of surfactant or support material free CdS nanoparticles with enhanced photocatalytic activity", Journal of Environmental Chemical Engineering, 2018 Publication	<1%
13	Chanchal Mondal, Mainak Ganguly, Jaya Pal, Anindita Roy, Jayasmita Jana, Tarasankar Pal. " Morphology Controlled Synthesis of SnS Nanomaterial for Promoting Photocatalytic Reduction of Aqueous Cr(VI) under Visible Light ", Langmuir, 2014 Publication	<1%
14	K. Sridharan. "NMR Spectroscopy", Elsevier BV, 2016 Publication	<1%

Exclude quotes	On	Exclude matches	< 14 words
Exclude bibliography	On		